UNIVERSIDADE ESTADUAL DE CAMPINAS
Faculdade de Engenharia Mecânica

ALESSANDRO JOSÉ TRUTA BESERRA DE LIMA

Thermodynamic optimization focused on direct injection of wet ethanol in spark-ignition engines

Otimização termodinâmica focada à injeção direta de etanol super-hidratado em motores de ignição por centelha

Campinas

2022

ALESSANDRO JOSÉ TRUTA BESERRA DE LIMA

Thermodynamic optimization focused on direct injection of wet ethanol in spark-ignition engines

Otimização termodinâmica focada à injeção direta de etanol super-hidratado em motores de ignição por centelha

Thesis presented to the School of Mechanical Engineering of the University of Campinas in partial fulfillment of the requirements for the degree of Doctor in Mechanical Engineering, in the area of Thermal and Fluids.

Tese de Doutorado apresentada à Faculdade de Engenharia Mecânica da Universidade Estadual de Campinas como parte dos requisitos exigidos para a obtenção do título de Doutor em Engenharia Mecânica, na Área de Térmica e Fluidos.

Orientador: Prof. Dr. Waldyr Luiz Ribeiro Gallo

ESTE TRABALHO CORRESPONDE À VERSÃO FINAL DA TESE DE DOUTORADO DEFENDIDA PELO ALUNO ALESSANDRO JOSÉ TRUTA BESERRA DE LIMA, E ORIENTADA PELO PROF. DR. WALDYR LUIZ RIBEIRO GALLO.

Campinas

2022

Ficha catalográfica
Universidade Estadual de Campinas
Biblioteca da Área de Engenharia e Arquitetura
Rose Meire da Silva - CRB 8/5974

L628t
Lima, Alessandro José Truta Beserra de, 1991-
Thermodynamic optimization focused on direct injection of wet ethanol in spark-ignition engines / Alessandro José Truta Beserra de Lima. – Campinas, SP : [s.n.], 2022.

Orientador: Waldyr Luiz Ribeiro Gallo.
Tese (doutorado) – Universidade Estadual de Campinas, Faculdade de Engenharia Mecânica.

1. Motores de combustão interna. 2. Injeção direta. 3. Etanol. 4. Gotas. 5. Otimização. 6. Exergia. I. Gallo, Waldyr Luiz Ribeiro, 1954-. II. Universidade Estadual de Campinas. Faculdade de Engenharia Mecânica. III. Título.

Informações para Biblioteca Digital

Título em outro idioma: Otimização termodinâmica focada à injeção direta de etanol super-hidratado em motores de ignição por centelha
Palavras-chave em inglês:
Internal combustion engines
Direct injection
Ethanol
Drops
Optimization
Exergy
Área de concentração: Térmica e Fluídos
Titulação: Doutor em Engenharia Mecânica
Banca examinadora:
Waldyr Luiz Ribeiro Gallo [Orientador]
Rogério Gonçalves dos Santos
Carlos Eduardo Keutenedjian Mady
Silvia Azucena Nebra de Pérez
Thompson Diórdinis Metzka Lanzanova
Data de defesa: 25-03-2022
Programa de Pós-Graduação: Engenharia Mecânica

Identificação e informações acadêmicas do(a) aluno(a)
- ORCID do autor: https://orcid.org/0000-0002-3458-2278
- Currículo Lattes do autor: http://lattes.cnpq.br/6604265274201801

UNIVERSIDADE ESTADUAL DE CAMPINAS
FACULDADE DE ENGENHARIA MECÂNICA

TESE DE DOUTORADO

Thermodynamic optimization focused on direct injection of wet ethanol in spark-ignition engines

Otimização termodinâmica focada à injeção direta de etanol super-hidratado em motores de ignição por centelha

Autor: Alessandro José Truta Beserra de Lima

Orientador: Prof. Dr. Waldyr Luiz Ribeiro Gallo

A Banca Examinadora composta pelos membros abaixo aprovou esta Tese de Doutorado:

Prof. Dr. Waldyr Luiz Ribeiro Gallo
DE/FEM/UNICAMP

Prof. Dr. Rogério Gonçalves dos Santos
DE/FEM/UNICAMP

Dr. Carlos Eduardo Keutenedjian Mady
Centro Universitário da FEI

Dr. Silvia Azucena Nebra de Pérez

Dr. Thompson Diórdinis Metzka Lanzanova
DEM/UFSM

A Ata de Defesa com as respectivas assinaturas dos membros encontra-se no SIGA/Sistema de Fluxo de Dissertação/Tese e na Secretaria do Programa da Unidade.

Campinas, 25 de Março de 2022

ACKNOWLEDGEMENTS

Agradeço primeiramente aos meus pais, Erivaldo e Maria de Fátima, e a minha irmã Nathália por todo o apoio, amor e carinho que me deram ao longo da vida.

Agradeço também ao professor Waldyr Luiz Ribeiro Gallo, meu orientador, que me orientou com muita qualidade nos aspectos acadêmico, profissional e pessoal durante todos estes anos. Espero um dia poder ser um docente com tanta qualidade como o senhor.

Agradeço aos membros do laboratório LMB e da FEM, Caio, Felipe, Giovanna e Jair, que por mais que tenhamos tomado caminhos diferentes durante este tempo, cada um de vocês me apoiou com esta fase da vida.

Não posso deixar de agradecer a Letícia, minha esposa, que sempre esteve ao meu lado desde que nos conhecemos e foi a minha principal incentivadora nesta fase da vida. Muito obrigado por tudo!

Agradeço a todas as amigas e amigos que fiz durante todos estes anos neste incrível ambiente universitário em que convivemos! Vocês colaboraram para que eu tivesse experiências únicas na minha vida!

Agradeço a FEM-UNICAMP pela oportunidade de trabalho, experiência e o conhecimento, todos eles fornecidos em um ambiente que estimula adequadamente o aprendizado.

O presente trabalho foi realizado com apoio do Conselho Nacional de Desenvolvimento Científico e Tecnológico (CNPq), processo no 168894/2018-1.

“Quem nunca errou, nunca experimentou nada novo.”

(Albert Einstein, Físico)

RESUMO

O advento dos motores de combustão interna proveu à humanidade avanços no estilo de vida a respeito dos aspectos de capacidade de realização de trabalho e mobilidade. Contudo, sua operação desenfreada com combustíveis fósseis é insustentável, com restrições atuais no seu uso em algumas regiões do planeta. Esta tendência mundial de substituição destes motores enfrenta questionamentos de origem energética, ambiental, material e financeira acerca do atual processo de electrificação veicular. Tópicos como justiça social mundial também estão na balança, principalmente para países emergentes como Brasil, Índia, África do Sul, etc. Sendo assim, a literatura especializada tem discutido a aplicação contextualizada de diferentes sistemas de potência no setor de transporte baseado na disponibilidade de recursos naturais de cada país ou região, a fim de nos movermos em direção a uma sociedade mais sustentável. Por exemplo, alguns sistemas de motores de ignição por centelha com injeção direta tem adotado etanol super-hidratado como alternativa para a sustentabilidade. Artigos científicos vem reportando benefícios na operação de motores com injeção direta com esta mistura de combustível, já que este sistema utiliza melhor as propriedades termodinâmicas tanto do etanol quanto da água. O uso de etanol super-hidratado também beneficia o ciclo de vida do etanol como um todo, já que evita a necessidade de um intenso processo de desidratação, portanto reduz a quantidade de energia requisitada pelo processo de produção de etanol. Portanto, o objetivo desta tese envolve a otimização termodinâmica de um motor de ignição por centelha com injeção direta alimentado com etanol super-hidratado. Este conceito de motor adota algumas tecnologias modernas, assim como propriedades do combustível para melhorar sua eficiência, como por exemplo turbocarregamento, redução de dimensão (*downsizing*), resfriamento evaporativo, fluxo adicional de massa para o cilindro e maiores razões de compressão. Esta pesquisa cobriu o modelamento e análise de diferentes escalas de tamanho do fenômeno de injeção direta (uma gotícula, um spray de gotículas e a operação de um motor com injeção direta) baseados na teoria de evaporação de gotículas multi-componente, com informações especiais obtidas pela aplicação da segunda lei da termodinâmica em tal fenômeno. Todos os códigos computacionais estão disponíveis em MATLAB®, onde eles simulam tanto cada gotícula como os gases em si através de abordagens Lagrangeana e Euleriana, respectivamente. O modelo de variação do tamanho das gotículas adota uma função de distribuição de probabilidade de Rosin-Rammler para representar o jato de spray injetado. O simulador de motores desenvolvido acopla diversos fenômenos relacionados à operação de um motor com injeção direta, portanto destaca as principais características do etanol super-hidratado neste tipo de máquina térmica. A validação do simulador é desenvolvida pela comparação de seus resultados para diferentes modos de injeção de combustível (homogêneo e estratificado) com resultados disponíveis na literatura. Esta tese sugere alguns novos parâmetros relacionados à evaporação de gotículas (ou sprays), como por exemplo eficiências de primeira e segunda leis, que enriquecem a discussão a respeito destes fenômenos em tais motores ou outros sistemas. O cálculo da geração de entropia mostra uma conexão com parâmetros fundamentais da evaporação de gotículas, indicando assim uma oportunidade para otimizar este processo nos motores previamente mencionados. Por fim, os resultados do processo de otimização mostram que eficiências teóricas energéticas e exergéticas de até 45% e 42%, respectivamente, são atingíveis com o uso de E80W20 através de uma combinação apropriada dos parâmetros de entrada sem prejudicar o consumo específico de etanol. Além disso, a otimização também destacou diversas condições nas quais o motor pode operar com misturas de etanol super-hidratado substituindo tanto etanol anidro quanto comercial (E100W0 e E95W5, respectivamente) sem prejudicar o desempenho do motor.

Palavras–chave: Motores de combustão interna, injeção direta, etanol super-hidratado, evaporação de gotículas & sprays, otimização termodinâmica, exergia.

ABSTRACT

The advent of internal combustion engines has provided humanity with advances in lifestyle concerning aspects of work ability and mobility. However, its rampant operation with fossil fuels is unsustainable, with current restrictions on its usage in some regions of the planet. The current trend of replacing these engines faces energy, environmental, material, and financial issues regarding the ongoing vehicle electrification process. Topics such as worldwide social justice have also been discussed, especially in emerging countries like Brazil, India, South Africa, etc. Thus, specialized literature has examined the contextualized application of different power systems in the transport sector based on each country's availability of natural resources to move towards a more sustainable society. For example, some direct-injection spark-ignition engine systems have adopted wet ethanol (i.e., super-hydrated ethanol fuel blends) as an alternative to sustainability. Papers have reported benefits in direct-injection engine operation with this fuel blend, as this system makes better use of both thermodynamic properties of ethanol and water. Wet ethanol usage also benefits the ethanol lifecycle because it avoids the need for intense ethanol distillation; therefore, it reduces the total energy required by the ethanol production process. So, the main objective of this thesis involves the thermodynamic optimization of a direct-injection spark-ignition engine fueled with wet ethanol. This engine concept adopts some modern technologies and fuel properties to improve its efficiency, such as turbocharging, downsizing, evaporative cooling effect, additional in-cylinder mass flow, and higher compression ratios. This research covered the modeling and analysis of different size scales of the direct-injection phenomenon (a single droplet, a droplet spray, and an engine operation with direct injection) based on the theory of multi-component droplet evaporation with special information revealed by the application of the second law of thermodynamics. All computer codes are available in MATLAB®, where they simulate each droplet and the gases by Lagrangian and Eulerian approaches, respectively. The droplet size variation model adopts a Rosin-Rammler probability distribution function to represent the injected spray jet. The developed engine simulator couples several phenomena related to the operation of a direct-injection engine, thus highlighting the main characteristics of wet ethanol usage in this thermal engine. The validation of the simulator is performed by comparing its results for different fuel injection modes (homogeneous and stratified) with results available in the literature. This thesis suggests some new parameters related to droplet and spray evaporation, such as first and second law efficiencies, which enrich the discussion about these phenomena in such engines or other systems. The entropy generation calculation shows a connection with the fundamental parameters of droplet evaporation, indicating an opportunity to optimize this process in the previously mentioned engines. Finally, the optimization process results show that theoretical energetic and exergetic efficiencies up to 45% and 42%, respectively, are achievable for E80W20 by an appropriate combination of input parameters without worsening the specific consumption of ethanol. In addition, this optimization highlighted several cases in which the engine can operate with wet ethanol fuel blends replacing both anhydrous and commercial ethanol (E100W0 and E95W5, respectively) without harming the engine performance.

Keywords: Internal combustion engines, direct injection, wet ethanol, droplets & sprays evaporation, thermodynamic optimization, exergy.

LIST OF FIGURES

LIST OF TABLES

LIST OF ABBREVIATIONS AND ACRONYMS

ASTM	American Society of Testing and Materials
BDC	Bottom-dead center
BIP	Binary interaction parameters
BP	British Petroleum
BSFC	Brake specific fuel consumption
BTDC	Before top-dead center
BZ	Burned zone
CA	Crank angle
CCS	Carbon dioxide capture and sequestration
CEM	Classical evaporation model
CERES	Congresso nacional de energias renováveis, exergia e sustentabilidade
CFD	Computational fluid dynamics
CI	Compression ignition
CMC	Continuous multi-component model
COVID	Corona virus disease
CRDI	Common rail direct-injection
DIN	German organization for standardization
DISI	Direct-injection spark-ignition
DMC	Discrete multi-component model
DCM	Discrete component model
DNS	Direct numerical simulation

ExWy	Hydrous ethanol with $x\%$ v/v of ethanol and $y\%$ v/v water in a ethanol-water liquid solution/mixture
ECU	Electronic computer unit
EDI	Early direct injection or Ethanol direct-injection
EEDI	Early ethanol direct injection
EEE	Effective expansion efficiency
EER	Ethanol-gasoline energy ratio or effective expansion ratio
EGM	Entropy generation minimization
EGR	Exhaust gas recirculation
ENCIT	Congresso Brasileiro de Engenharia e Ciências Térmicas
EOC	End of combustion
EoS	Equation of state
ETC	Effective thermal conductivity model
EV	Electrical vehicles
EVC	Exhaust valve closure
EVO	Exhaust valve opening
FEV	Finite volume method
GCI	Gasoline compression-ignition
GDI	Gasoline direct-injection
GHG	Greenhouse gases
GPI	Gasoline port-fuel injection
HCCI	Homogeneous charge compression ignition
HEV	Hybrid electric vehicles

HMC	Hybrid multi-component model
HoV	Heat of vaporization
ICE	Internal combustion engines
IMEP	Indicated mean effective pressure
ISFC	Indicated specific fuel consumption
ISO	International Organization for Standardization
IVC	Inlet valve closure
IVO	Inlet valve opening
KIVA	KIVA software
LDI	Late direct injection
LDV	Light-duty vehicles
LEDI	Later ethanol direct injection
LES	Large eddy simulation
LHV	Lower heating value
LIF	Laser induced fluorescence
LMB	Laboratório de motores biocombustíveis
LPG	Liquid petroleum gas
LTC	Low-temperature combustion
MBT	Maximum brake torque or maximum spark for best torque
MDQD	Multi-dimensional quasi-discrete model
MON	Motor octane number
N-S	Navier-Stokes equation
NA	Naturally aspirated

NIMEP	Net indicated mean effective pressure
NVO	Negative valve overlap
ODE	Ordinary differential equation
OECD	Organization for Economic Cooperation and Development
PDA	Phase Doppler Anemometry
PDE	Partial differential equation
PDF	Probability distribution function
PFI	Port-fuel injection
PHEV	Plug-in hybrid electric vehicles
PM	Particulate matter
PR	Peng-Robinson
PVO	Positive valve overlap
RANS	Reynolds-averaged Navier-Stokes
RHS	Right-hand side
RK	Runge-Kutta
RON	Research octane number
RTT	Reynolds transport theorem
R-R	Rosin-Rammler
RGF	Residual gas fraction
SFC	Specific fuel consumption
SI	Spark ignition
SIDI	Spark-ignition direct-injection
SOC	Start of combustion

SRK	Soave-Redlich-Kwong
TSCI	Thermally Stratified Compression Ignition
TDC	Top-dead center
UBZ	Unburned zone
US	United States of America
VLE	Vapor-liquid equilibrium
VOC	Volatile organic compound
VOF	Volume of fluid
VVT	Variable valve timing
WG	Wall-guided
WOT	Wide-open throttle

LIST OF SYMBOLS

Common symbols

A	Area - [m^2]
a	Activity coefficient
Ar	Argon
	b Specific exergy - [J/kg]
	b_f Specific flow exergy - [J/kg]
B	Spalding transfer number
	$\dot{B}_d$ Rate of destroyed exergy - [W]
C	Correlation constant
C_d	Drag coefficient
c	Specific heat - [$J/(kg.K)$]
c_p	Constant-pressure specific heat - [$J/(kg.K)$]
c_v	Constant-volume specific heat - [$J/(kg.K)$]
C_2H_5OH	Ethanol
CO_2	Carbon Dioxide
CO	Carbon Monoxide
D	Diameter - [m]
E_{dist}	Total energy spent in ethanol distillation - [J/kg]
F	Correction factor
f_0	Normalized number density function
G	Correction factor

H	Hydrogen atom
H_{UBZ}	Unburned zone gas total enthalpy - $[J]$
H_2	Hydrogen gas
H_2O	Water
h	Specific enthalpy $[J/kg]$
h_{conv}	Convective heat transfer coefficient - $[W/(m^2.K)]$
i	ith Iteration
k	Thermal conductivity - $[W/(m.K)]$
K_{In}	Knock index number
L_k	Knudsen layer thickness
M	Molar mass
m	Mass - $[kg]$
$\dot{m}$	Mass flow rate - $[kg/s]$
n	Spread parameter of the distribution or form factor
N	Nitrogen atom
$N_{classes}$	Number of droplet classes in a PDF
$N_{CV,droplets}$	Number of control volumes representing all droplet classes associated with the fuel spray
$N_{droplet,i}$	Number of droplets in the ith class
N_{engine}	Engine speed - $[RPM]$
N_{layers}	Number of spray layers
N_{nozzle}	Number of fuel injector nozzles
$N_{species}$	Number of chemical species

NEF	Net energy factor
Nu	Nusselt number
NO	Nitric oxide
NO_2	Nitric dioxide
NO_x	Nitric oxides
O	Oxygen atom
O_2	Oxygen gas
OH	Hydroxyl
P	Pressure - $[Pa]$
Pe	Peclet number
Pr	Prandtl number
Q_{LHV}	Lower heating value - $[J/kg]$
$\dot{Q}$	Heat transfer rate - $[W]$
R	Universal gas constant - $[J/(kg.K)]$
r	Radius - $[m]$
Re	Reynolds number
s	Entropy - $[J/(kg.K)]$
Sc	Schmidt number
Sh	Sherwood number
SoI	Start of injection - [°]
T	Temperature $[K]$
t	Time $[s]$
u	Velocity $[m/s]$

UHC	Unburned Hydrocarbons
v	Volumetric fraction
We	Weber number
x	Molar fraction or particle size
$x^{'}$	Location parameter of the distribution
y	Mass fraction
Z	Compressibility factor

Greek symbols

α	Thermal diffusivity - $[m^2/s]$
β	Non-dimensional evaporation parameter
$\mathcal{D}$	Mass diffusivity - $[m^2/s]$
ΔH_{fuel}	Fuel enthalpy of combustion - $[J]$
Δh_v	Heat of vaporization - $[J/kg]$
Δs_v	Entropy of vaporization - $[J/[kg.K]]$
$\Delta\theta_b$	Combustion duration - [°]
δ_g	Gas boundary layer thickness - $[m]$
$\delta_{adm,i}$	Kronecker delta for the inlet direction of the admission valve
$\delta_{adm,o}$	Kronecker delta for the outlet direction of the admission valve
$\delta_{exh,i}$	Kronecker delta for the inlet direction of the exhaust valve
$\delta_{exh,o}$	Kronecker delta for the outlet direction of the exhaust valve
η	Efficiency
ϵ_d	Droplet diameter tolerance - $[m]$
ϵ_i	ith fraction vaporization rate

Γ	Gamma function
λ	Relative Air/fuel ratio - $[kg_{air}/kg_{fuel}]$
μ	Dynamic viscosity - $[Pa.s]$
ω	Engine angular speed - $[rad/s]$
$\dot{\sigma}$	Entropy generation rate - $[W/K]$
σ	Surface tension - $[N/m]$
ρ	Specific mass - $[kg/m^3]$
τ	Characteristic time - $[s]$
θ	Crank angle - $[rad]$
$\cancel{V}$	Volume - $[m^3]$
χ	Recirculation effects coefficient on droplet conductive heat transfer

Superscripts and subscripts

$*$	Corrected
0	Minimum condition, correlation, initial condition or dead-state
$1st$	First law of thermodynamics
$2nd$	Second law of thermodynamics
A	Species A
adm	Admission conditions
air	Air
av	Average
B	Species B
b	Burned
BZ	Burned zone

$classes$	Particle size classes
$comb$	Combustion
$crit$	Critical
$cycle$	Engine cycle
cyl	Cylinder
CV	Control volume
d	Droplet
eff	Effective
$engine$	Engine
eq	Equilibrium
$ethanol$	Hydrous ethanol
EOH	Hydrous ethanol
$evap$	Evaporation
exh	Exhaust conditions
f	Fuel
g	Gas
$gasoline$	Gasoline
H_2O	Water
i	ith element or inlet
inj	Injection
$intake$	Angle referred to the intake/exhaust strokes of an internal combustion engine
j	jth element

jet	Jet
l	Liquid
$layers$	Spray layers
M	Mass transfer
m	Mixture between the droplet surface and the gas environment
min	Minimum
neq	Non-equilibrium
$nozzle$	Fuel injector nozzle
o	Outlet
$part$	Volume equivalent partial diameter
RG	Residual gases
s	Surface
$sens$	Sensible energy
$system$	System
$species$	Total number of species
$stoichiometric$	Stoichiometric
T	Heat transfer
UBZ	Unburned zone
v	Vapor
wb	Wet bulb
$wall$	Cylinder walls
wet	Wet ethanol

CONTENTS

1 INTRODUCTION

1.1 Motivation

1.1.1 Current world and Brazilian contexts for energy demand

The current world situation on energy demand has been in highlight for many years, ever since different energy forms (especially electrical energy) emerged for the majority of humankind. This energy availability directly affected the lifestyle humans have achieved until current days. World energy demand is increasing continuously in every region of the planet especially due to the combination of humankind population growth and advents of individual high energy-demanding novel technologies (e.g., smartphones). For example, more than half of the human population consumed near 100 GJ/head in 2019 (Fig.1.1); a fact that can be justified by the economical growth of many emerging countries from 40 years ago until nowadays, such as Brazil, China, India, etc. More affordable energy sources have allowed many underdeveloped countries to increase their standard of living during most recent decades by using fossil and/or bio-originated fuels as their main energy sources.

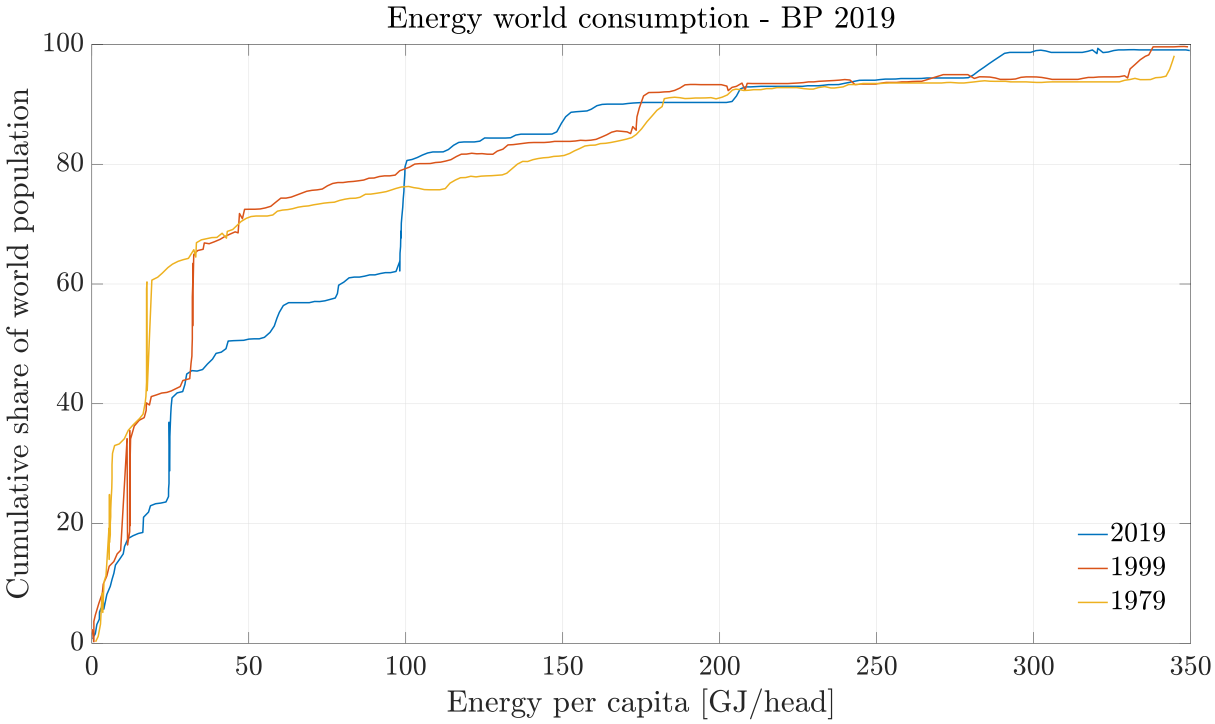

Figure 1.1 – Energy consumption per capita from 1979 to 2019. Adapted from Looney (2020).

In terms of renewable energy perspective, a recent annual British Petroleum (BP) world energy report (Looney, 2020) indicated a relative growth in the primary renewable energy sector during the last decades (Fig. 1.2), although oil production and consumption continue to grow in absolute quantities. Also, liquid fuel consumption reached its peak in 2019 and its tendency is to continue growing, despite the existence of several stimuli for the use of electrified vehicles in some regions of the world (e.g., Europe and North America) to deal with this problem in the transport sector. Therefore, it is expected that liquid energy sources will continue to be part of our society for several decades in this century.

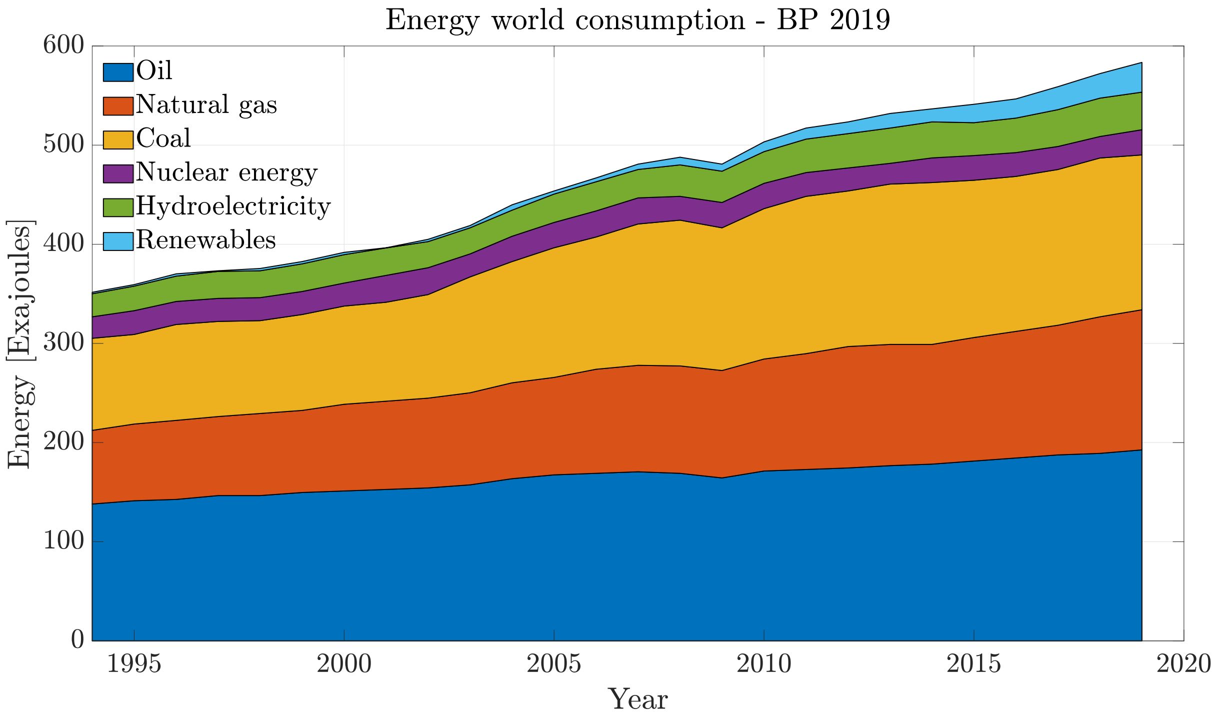

Figure 1.2 – World primary energy consumption from 1994 to 2019. Adapted from Looney (2020).

The current Brazilian energy context is similar, although clear differences in the primary energy sector compared to other countries can be highlighted. A recent Brazilian Energy Balance (Brasil, 2020) presented the national primary energy production. As Fig. 1.3 indicates, Brazil has some ”renewable” energy sources available such as hydro, wind, solar, and biomass (e.g., sugarcane), though current actions have been collaborating to the deforestation of its main forests to the application of unsustainable agriculture techniques in these lands. Thus, these modifications strongly diminish this potential over time towards a more sustainable country in terms of natural resources, such as energy, water, and fertile land.

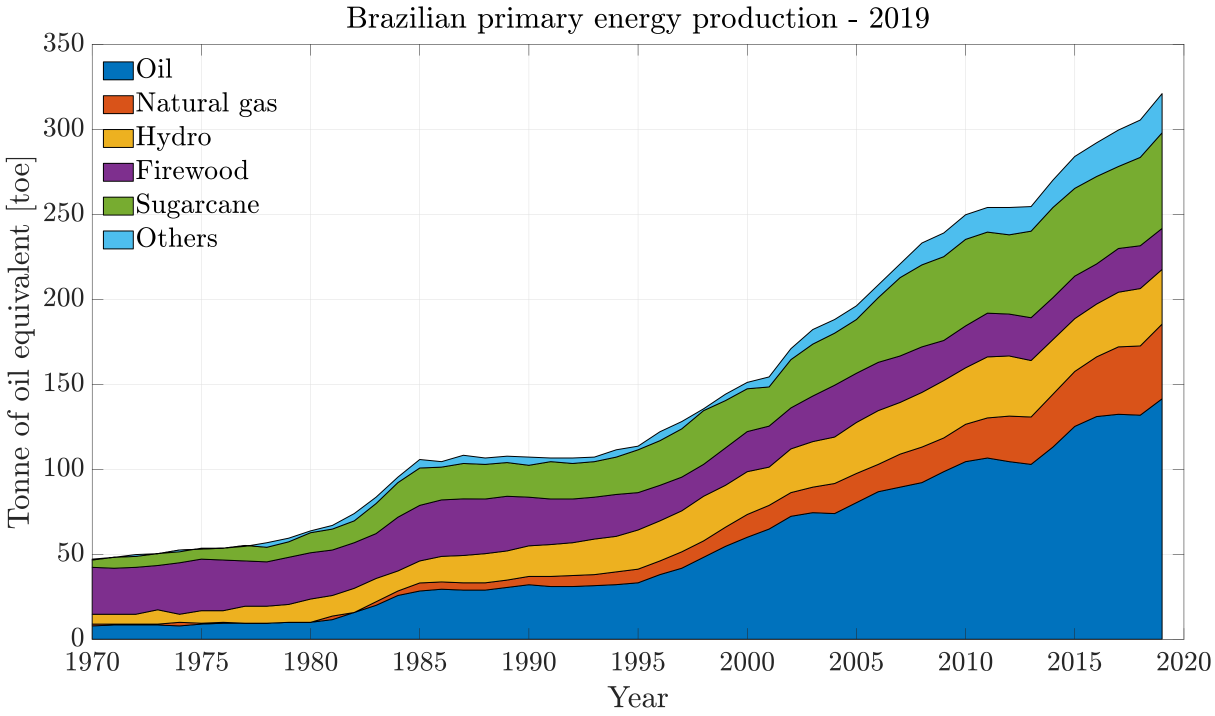

Figure 1.3 – Actual Brazilian primary energy production. Adapted from Brasil (2020).

Ghoniem (2011) contextualized the current worldwide energetic and environmental situation according to the way humankind has been living during the last centuries. For instance, in order to mitigate the CO_2 emissions, four major approaches have been proposed to achieve CO_2 reduction while continuing dependent of fossil fuels for the next decades: improving conversion efficiency on the supply side (conversion from raw sources to the useful form and product); improving conversion efficiency on the demand side (on energy utilization in our society); reducing dependency on high carbon fuels with the application of lower C/H fuels (possible use of nuclear energy) and promoting more reliance on renewable sources; and carbon dioxide capture and sequestration (CCS) directly from power plants by injection in reservoirs, reacting it into stable disposable compounds, or indirectly from biological processes (growing trees, algae, etc).

1.1.2 Current and future perspectives for electric and internal combustion engines

As a current essential part of the world transport sector, internal combustion engines (ICEs) are also included in discussions involving energy usage. Their worldwide adoption with fossil fuels has been releasing both greenhouse and pollutant gases (e.g., NO_x, CO, UHC, etc.) for several decades. Their contribution to global warming is not acceptable anymore in the progress to humankind sustainability. Within this context, the automobile electrification process has been stimulated in order to reduce both the demand of non-renewable fuels and the emission of combustion products on most cities, thus they are presented as environmentally friendly (Costa *et al.*, 2021). This process is usually described as totally capable of overcoming the issues associated with ICEs, although some questions arise about the worldwide economic viability of this substitution (Ahmadi *et al.*, 2014; Jha *et al.*, 2022), the benefits viewed partially only for specific regions in the world (Xu *et al.*, 2021), and its real capacity to mitigate greenhouse gases (GHG) emission without the general adoption of renewable energy sources (Poullikkas, 2015). Another aspect that acts as a barrier to this change of perspective is the consumers attitudes and perceptions to the adoption of electrical vehicles (EV) all over the world (Egbue; Long, 2012).

Underdeveloped countries face additional problems in implementing the replacement of traditional engines to electric ones. Besides the traditional environmental and energetic issues, social-economic and infrastructure problems affect the immediate adoption of electric vehicles on these countries. Some works and reports contextualize how this change of perspective affect South Africa (Dane *et al.*, 2019) and Bolivia (Narins, 2017), for example, emphasizing the challenges they must face, especially for insufficiency of charging station infrastructure (Eltoumi *et al.*, 2021).

Other issues such as current and future rare elements availability are involved in this situation. The stimuli for renewable energy sources (wind, solar, photovoltaic, etc.) electrical devices (vehicles, smartphones, etc.) production stimulates the mining process, which is less publicly discussed, but are as important for humankind sustainability as GHG and fossil fuels usage. For instance, the renovation of the energy sector requires huge amounts of raw materials, with problems associated to those with high supply risks (i.e., material bottlenecks for future demand and geological availability) (Capilla; Delgado, 2014; Valero *et al.*, 2018). There are researchers analyzing the economic and environmental aspects related to the amounts of metal required to this current sustainable energy transition (Tokimatsu *et al.*, 2017). Also, the demand of energy required by the mining process to overcome the demand of specific minerals (e.g., Copper, gold, silver, lead, zinc, etc.) has been thoroughly studied (Calvo *et al.*, 2016). Finally, some additional issues need to be addressed, such as reported by Davidsson e Höök (2017), which evaluated the material requirements and availability required to sustain a multi-terawatt photovoltaic (PV) industry and indicated that a major expansion of solar grade silicon production and significant quantities of silver are necessary to operate as a long-term industry.

While all these new perspectives are evaluated on literature, there are some researches focused on evaluating the effects that hybridization/electrification may cause in the current transportation sector energy consumption and emissions state. For example, Onat *et al.* (2015) presented a comparative analysis of carbon and energy footprint on conventional, hybrid (HEV), plug-in hybrid (PHEV) (i.e.,, hybrids with capacity of recharging their batteries by a plug-in electric source), and electric vehicles (EV) for each state in the US for three different energetic scenarios. PHEV and HEV were presented to be interesting choices regarding the most energy-efficient options, being competitive in the market context with EVs. In terms of emissions, Johnson e Joshi (2017) commented that some projections towards tight CO_2 regulations will require some kind of hybridization and/or high-performance Diesel engines. Also, future gasoline light-duty engine approaches (e.g., Atkinson cycle, stop/start operation, active cylinder deactivation, and variable compression ratio (VCR)) are challenging electric vehicle well-to-wheel (i.e., from the beginning of the primary fuel production to the burning of the vehicle fuel) CO_2 emissions.

Recently, Reitz *et al.* (2020) emphasized the importance of ICEs in many sectors of humankind and how this device will probably continue to exist in many countries for a foreseeable future. A discussion about the capability of several proposed new vehicle propulsion alternatives (e.g., electric vehicles with batteries) to replace traditional vehicles technology in a near future. A realistic possibility presented by the editorial would be the application of highly efficient fully flexible hybrid powertrains in the seek for efficiency improvement in the automotive sector. In addition, (Malaquias *et al.*, 2019) developed a review about the Brazilian ICE-electric vehicle replacement context and presented some questions related to the benefits of such immediate change on the vehicle fleet, as well as on alleged sustainability benefits of EV adoption in exchange of ethanol adoption as a biofuel.

Furthermore, Kalghatgi (2018) indicated that a change of perspective is required thorough an analysis of the energy involved in the transport sector, in order to better comprehend how the future transport sector will operate. Direct-injection spark-ignition (DISI) engines are also included in this change of perspective through the hybridization and electrification processes of the automotive sector in future years. Thus, realistic perspectives about the continuity of ICEs indicate that the humanity still needs their capacities for some decades ahead as better combustion and after-treatment processes are achieved by the evolution of control systems as well as alternatives for petroleum-based fuels get more diffused throughout the world. Kalghatgi (2018) also indicated that more than 90% of the transport energy will still come from combustion engines until 2040, especially powered by petroleum. The main issues that will happen if the actual transport system is dismantled abruptly in several areas (e.g., economic, social, environmental, and political, Fig. 1.4) were also addressed. For example, the available battery capacity must increase by a thousand-fold to cover all light duty vehicles (LDVs) in 2040, and this will only cover half of the global transport demand. Kalghatgi *et al.* (2018) discussed the current search for alternative fuels (ethanol included) to replace humankind dependency on liquid petroleum fuels (which feeds more than 11 billion liters per day). There is an agreement between researchers that future hybrid/electric powertrains will depend on new/better combustion systems with sustainable fuels, which reinforces the application of renewable ethanol fuel depending on the conditions of each specific country.

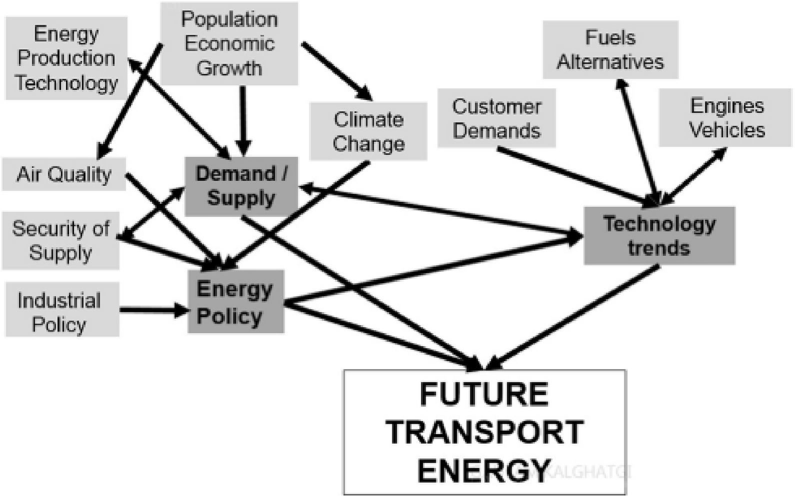

Figure 1.4 – Evolution of the current energy context in the transport sector. Adapted from Kalghatgi (2018).

1.1.3 International and national contextualization of ethanol usage for the transport sector

Bio-ethanol (or ethanol) has always been described as an interesting alternative fuel to replace or complement gasoline in ICEs. It has been tested since the beginning of engines invention and its commercial production was initially stimulated in countries which have proper agricultural conditions for the harvest of crops, such as sugarcane and corn (in Brazil and US, respectively). Baeyens *et al.* (2015) addressed the issues and possible benefits of improving the production of bio-ethanol for all three production generations (sugarcane and corn - first generation, cellulose biomass - second generation, and algal biomass - third generation). Worldwide speaking, Renewable Fuels Association (2020) indicates that the planet ethanol production increased until 2020, when the current pandemic situation caused by COVID-19 strongly affected all economic sectors in the world and caused a reduction in ethanol production. Figure 1.5 indicates that the two main first generation producers of ethanol (US and Brazil) were very affected by the pandemic in 2020. Still, these countries still take advantage of their agricultural resources to yield a renewable fuel which assists on their energy sectors, especially to the automotive transport sector.

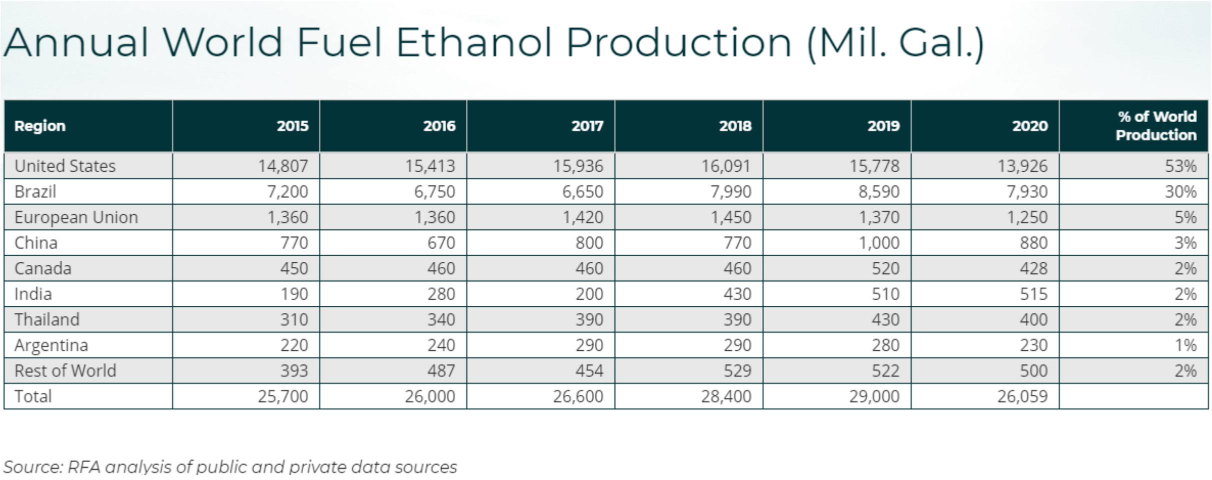

Annual World Fuel Ethanol Production (Mil. Gal.)

Region	2015	2016	2017	2018	2019	2020	% of World Production
United States	14,807	15,413	15,936	16,091	15,778	13,926	53%
Brazil	7,200	6,750	6,650	7,990	8,590	7,930	30%
European Union	1,360	1,360	1,420	1,450	1,370	1,250	5%
China	770	670	800	770	1,000	880	3%
Canada	450	460	460	460	520	428	2%
India	190	280	200	430	510	515	2%
Thailand	310	340	390	390	430	400	2%
Argentina	220	240	290	290	280	230	1%
Rest of World	393	487	454	529	522	500	2%
Total	25,700	26,000	26,600	28,400	29,000	26,059	

Source: RFA analysis of public and private data sources

Figure 1.5 – World ethanol production from 2015 to 2020. Adapted from Renewable Fuels Association (2020).

In terms of Brazil, Nigro e Szwarc (2011) presented the historic background of ethanol usage as a fuel in our country as well as the development of its sector in association to the flex-fuel vehicle technology. Moreover, future possibilities suggested to spread ethanol usage in the country involved economic considerations regarding the vehicle price, cold start and operation, higher knock resistance, and EGR. Távora (2011) followed a similar trend as Nigro e Szwarc (2011), but expanded the analysis to other biofuels (e.g., biodiesel) in Brazil. More recently, the Automotive Vehicle Air Pollutant Control Program (PROCONVE in Portuguese) L7 and L8 phases presented by the Brazilian Government in 2018 (Brazil, 2018) established the new acceptable maximum emission limits for the light-duty vehicles in the country, which will be more restrict from 2022 on. Thus, the requirements for ethanol usage as a fuel will make it harder to be implemented, with special limitation for flex-fuel engines since their efficiency is limited due to its flexible characteristics between gasoline and ethanol.

The 2020 Brazilian sugarcane harvest report (CONAB, 2021) indicated that the yearly ethanol production (derived from sugarcane and corn) reduced 7.9% in season 20/21, due to higher exportation demands for sugar caused by climatic issues that occurred in Thailand (second greatest sugar exporter) and in Brazil during last year, and a worldwide oil price reduction. Additionally, the most recent Brazilian Energy Balance (Brasil, 2020) indicated that ethanol has reached its peak production value (33.800x$10^3 m^3$/year) destined for the transport sector consumption. However, its production usually competes with the worldwide sugar demand which directs part of current sugarcane harvest to this other product. Therefore, current ethanol production in Brazil for vehicles is limited.

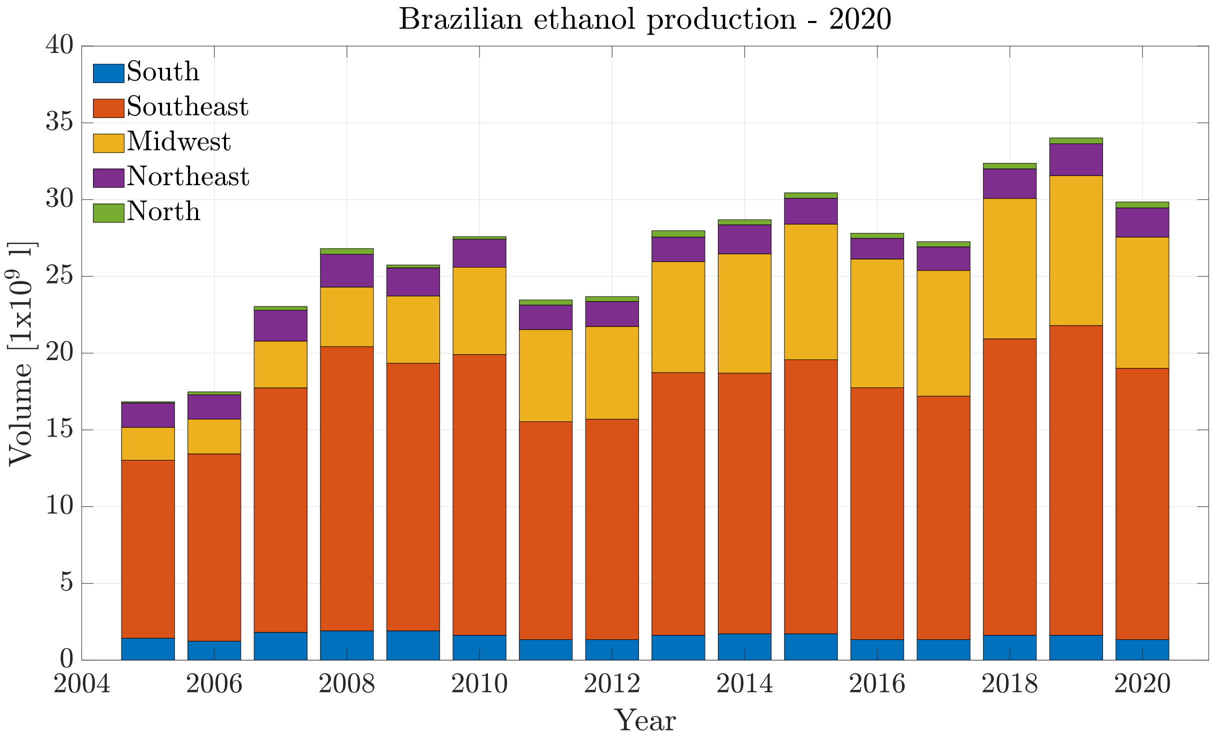

Figure 1.6 – Brazilian ethanol production originated from sugarcane between 2006 to 2021. Adapted from CONAB (2021).

The usage of pure ethanol (i.e., anhydrous ethanol, with at least 99.5% v/v in a ethanol/water solution) as a fuel for spark-ignition (SI) engines has been studied in details, since it gained special support during the 1970s. Brinkman (1981) was one of the first to proper evaluate the main fuel characteristics of ethanol. Results indicated a potential to promote higher engine efficiencies than gasoline (at the same compression ratio), lower NO_x emission, despite the sharp increase of aldehydes emission. Moreover, ethanol higher knock resistance (higher octane number than gasoline) was highlighted by allowing the application of higher compression ratios than it was possible with gasoline in the same engine.

Wet ethanol has been studied by researchers as an alternative for hydrous ethanol due to either cost reduction or to improvements on ethanol life cycle energetic efficiency. Theoretically, in terms of engine operation, higher contents of water in ethanol-water blends absorb more energy when evaporating due to water high heat of vaporization, which reduces the energy transferred to the cooling system as well as the unburned gas zone temperature. This also opens the possibility to improvements in the energy recovered from the exhaust heat recovery system. Moreover, the additional water increases the ratio of specific heats ($k = c_p/c_v$), which is directly proportional to thermal efficiency, thus water may increase the engine efficiency. The water in the fuel also increases the cylinder boundary work, as it occurs in water-injection engines (Bernal, 2019). Lastly, the lower unburned zone temperature suggests the application of higher compression ratios (Zhao, 2010) without damaging the engine structure with the occurrence of knock.

1.1.4 Second law connection with fuel spray and droplet evaporation in DISI engines

Droplet evaporation is a process that occurs right after liquid spray atomization, whose connection with direct fuel injection in ICEs is evident. It involves mass and heat transfer between liquid and gas phases, and it is usually associated with combustion of fuel sprays. The sequence between spray injection towards droplet evaporation has its fundamental aspects clearly understood since the 1980s (Elkotb, 1982; Law, 1982; Sirignano, 1983). Several details of these phenomena were captured by both experimental findings and comprehensive numerical models. Complementary, droplet evaporation always occurs in thermal devices and affects the ignition delay and air-fuel mixture, variables directly related to thermal efficiency in spark-ignition engines, for instance.

Droplet evaporation has been intensely studied throughout the years, although analyses focusing on the second law of thermodynamics view are quite scarce (Som; Datta, 2008). The droplet evaporation modeling is capable of predicting important evaporation characteristics, such as droplet lifetime and evaporation rate (Sazhin, 2017). Thus, works combining these parameters with second law aspects (Dash *et al.*, 1991; Dash; Som, 1991; Hiwase *et al.*, 1998) showed that the main source of irreversibility for droplet evaporation is due to conduction heat transfer and the combined effect of heat and fuel vapor mass transfer in the carrier phase. Moreover, the usage of real fuel blends (i.e., mixture of components) in engines requires the application of multicomponent droplet evaporation effects, which change considerably the evaporation behavior (Law, 1976). These multicomponent effects are important to predict coherently their evaporation on thermal devices (Brenn *et al.*, 2003; Sazhin *et al.*, 2011) and takes into account some differences in comparison to single-component cases, such as differences in volatility between the droplet compounds (Jin; Borman, 1985) and its effect on droplet lifetime and evaporation ratio profiles (Megaridis; Sirignano, 1991). However, independently of the approach, none of these works presented a view on second law analysis of multicomponent effects from droplet vaporization for engines.

Therefore, the application of the second law of thermodynamics in droplet and spray evaporation processes (Som *et al.*, 1990; Dash *et al.*, 1991) is extensive and not new (Som; Datta, 2008), although not quite explored for ICEs. Additionally, even though there is a review paper about exergetic analyses in engines (Rakopoulos; Giakoumis, 2006), works which directly address second law consequences of the spray evaporation process in DI engines (Ismail; Mehta, 2012; Ismail; Mehta, 2014) are very unusual. Moreover, the available information regarding the second law perspective of hydrous ethanol in SI engines (Rufino *et al.*, 2019) does not cover the gap of wet ethanol injection effects on DISI engines.

1.2 Objectives

The main objective of this thesis is to develop a thermodynamic optimization of a DISI engine operating with wet ethanol in a way that both ethanol life cycle and engine efficiency are at optimal conditions. Figure 1.7 illustrates the brainstorming process related to the main ideas of this thesis.

Therefore, the specific objectives associated with this research are the following:

- To understand the behavior of a wet ethanol (multicomponent) droplet injected and evaporating in a thermodinamically finite variable gas phase (engine cylinder during compression) in terms of evaporation and entropy generation by using a zero-dimensional mathematical model;
- To expand the previous model in order to encompass a fuel spray evaporation based on a probability distribution function (PDF) in a similar environment;
- To develop a direct-injection spark-ignition engine simulator and validate it with experimental results from the literature;

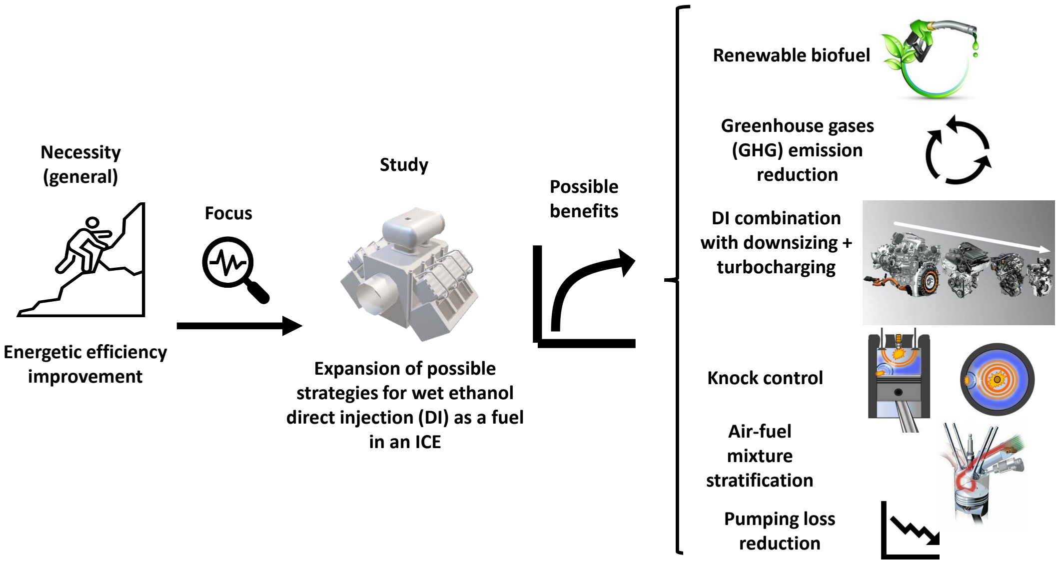

Figure 1.7 – Flowchart contextualizing the main ideas of the thesis.

- To optimize the operation of a DISI engine fueled with wet ethanol in terms of second law of thermodynamics based on its combination with several recent technologies adopted to ICEs.

These objectives lead in the end to an engine simulator capable of optimizing a near state-of-the-art DISI engine operation with a renewable fuel focused on the application in specific regions of the world where enough wet ethanol production is available for usage throughout the year. This simulator also takes into account recent technologies associated with most modern SI engines, such as engine turbocharging and downsizing, and higher compression ratios without knock occurrence; all of which combined with an optimized engine completely adapted to wet ethanol usage and allow the utilization of this engine as the main source of power for a vehicle or coupled with an electric engine as in the case of a hybrid vehicle.

Figure 1.8 compiles the flow sequence related to the mathematical modeling involved in this thesis. Focus is given on direct fuel injection. To further detail the phenomena that occur in our object of study, we focus on specifying the model, trying to deal with the fuel droplets in a Lagrangian way. Therefore, we move from DISI engines, to jet atomization, to droplet spray and finally to individual droplets, until we reach the evaporation of the droplet before the ignition and combustion in the engine cycle. Then it is applied the second law of thermodynamics to the object of study to get a different view on the phenomenon. After this individualized study, the model comes back into the macro scale to assess the macroscopic effects of direct injection of wet ethanol in a DISI engine.

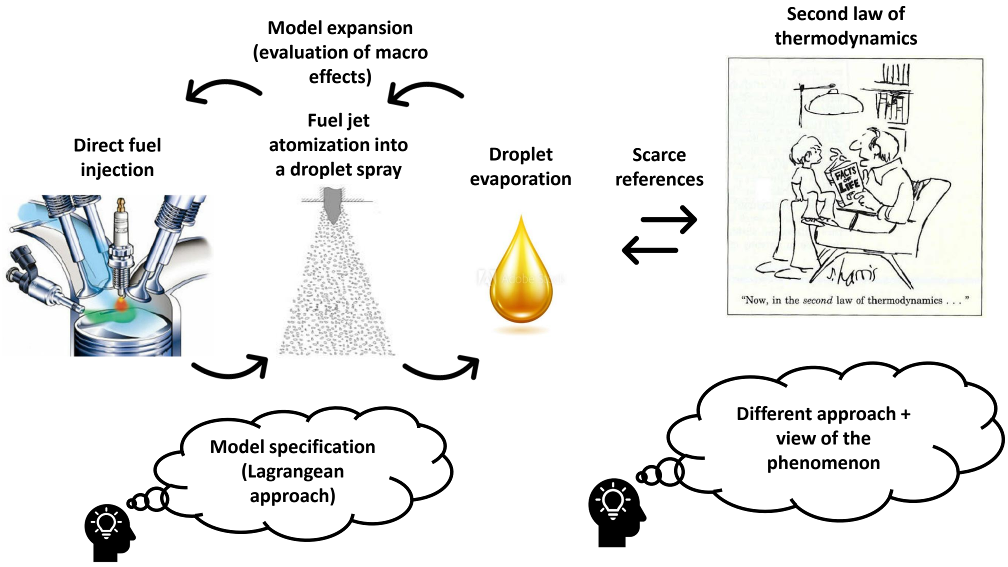

Figure 1.8 – Flowchart describing the modeling flow of the thesis.

1.3 Thesis outline

The outline of this thesis involves chapters detailing all stages of this research. The first chapter presents the introduction of this thesis, where the context related to this work is presented. The second chapter of this thesis involves a literature review about the main fundamentals related to this thesis. Some details required to model the evaporation of a multicomponent droplet are presented, as well as fundamentals of fuel sprays modeling, atomization correlations, probability distribution function (PDF) to represent droplet sprays, and DISI engines with wet ethanol. Also, some aspects related to second law of thermodynamics and these phenomena are also discussed. The third chapter involves the mathematical models and methodology associated to this research. All models are detailed with their description, assumptions, liquid and gas phase modeling, flowchart of the computational model, besides the simulated conditions.

The fourth chapter describes the results involving studies of a wet ethanol droplet in a thermodinamically variable environment. These results are related to two research papers presented in congresses (CERES 2020 and ENCIT 2020) and with one manuscript in final phase to be submitted to a journal of the area. The fifth chapter presents results for a wet ethanol spray injection and evaporation during the compression stroke of a DISI engine. These results covered only the conditions of a conference paper submitted to ECOS 2021.

The sixth chapter encompasses all previously presented models in the DISI engine simulator developed by LMB (Laboratory of Bio-fueled Engines) and compares the simulated results with experimental cases presented by published papers involving direct injection of wet ethanol in an engine operation. The seventh chapter presents the final results of this thesis by detailing the thermodynamic optimization process applied to the developed simulator under several different conditions. Finally, the eighth chapter encompasses all content presented throughout the text by developing the conclusions related to this research. Additionally, the future steps related to this work as well as some suggested ones are also commented in this chapter.

2 LITERATURE REVIEW

2.1 Droplet evaporation

Droplet evaporation is a very common phenomenon in nature: from sprays used for watering plants and harvests, as well as to direct fuel injection in thermal devices, all of them have in common the conversion of higher amounts of liquid jets into small portions of near spherical mass. The break up of liquid jets into these particles enhances significantly the surface area and therefore the interface between liquid and gas phases. It is in this interface where it occurs the exchange of mass, chemical species, momentum, and energy between the two phases. Usually, these exchanges are modeled by the conservation of mass, chemical species, second law of Newton and first law of thermodynamics. The phenomenon of droplet evaporation is associated with all these conservation laws due to the difference between the liquid and gas partial pressures of each component in either phases. Moreover, there is also entropy transfers between the droplet and the surrounding gases, since there is energy transfer associated to this phenomenon.

Figure 2.1 presents a basic schematic diagram of a droplet evaporating in a hot environment. This droplet is moving with a velocity u_d through the gases. The control surface around the droplet is adjacent to the liquid-gas interface, where evaporative mass and heat transfers occur. The surrounding gases heat up the liquid droplet ($\dot{Q}_{conv}$), whereas some energy flows from the droplet to the environment due to mass transfer ($\dot{Q}_{evap}$) associated with evaporation. Basically, the difference between these two energy rates is related to the sensible energy of the droplet, heating up or cooling down the remaining liquid.

2.1.1 Droplet modeling, fundamentals and hypotheses

The fundamentals of droplet evaporation theory are very diffused and usually presented in classical combustion books such as Kuo (2005), Law (2006), Glassman (2008), Turns (2012). The main hypotheses are thoroughly detailed and sub-sequentially a simplified analytical model is provided, based on the model provided by Spalding (1953). Sirignano (2010) presents an expanded view on the area of droplets and sprays, with direct connection with several papers available on literature about this area. Usually, the droplet heating/evaporation models are sorted in terms of ascending complexity levels (Sazhin, 2006), as presented next:

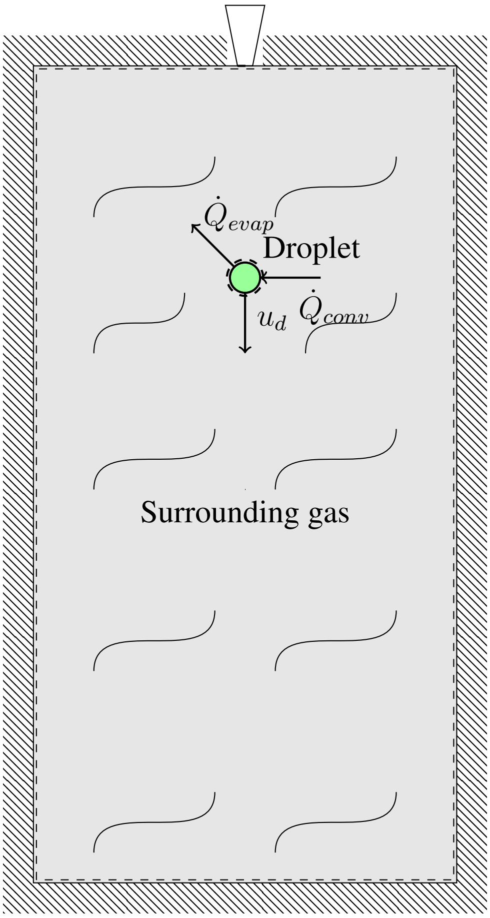

Figure 2.1 – Basic schematic diagram of a droplet evaporating in a hot environment.

1. The droplet surface temperature is uniform and constant over time (i.e., wet-bulb temperature);
2. There is no thermal gradient inside the droplet (infinite liquid thermal conductivity);
3. There is a thermal gradient, but without re-circulation inside the droplets (finite liquid thermal conductivity);
4. The model takes into account both finite liquid thermal conductivity and re-circulation inside the droplets by the usage of a correction factor (effective thermal conductivity - ETC);
5. Vortex dynamics is used to describe the re-circulation inside the droplets (vortex models);
6. The model is based on the full solution of the Navier-Stokes (N-S) equation in the liquid phase;

The first model is usually presented by textbooks as an introduction to droplet vaporization (evaporation/combustion) and it gives an analytical solution to the problem. The second model level requires the solution of a system of ordinary differential equations (ODEs) for the mass, momentum and energy conservation laws. The third and fourth levels require the solution of a system of partial differential equations (PDEs) to solve mainly the equation of energy for the liquid phase, thus it involves an extra complexity (i.e., solution via finite difference or volume methods) to its application in a spray simulation. The last two model levels are not usually solved in most cases, unless it is of interest studying the minimal details about the internal dynamics of liquid phase. Also, their complexity is computationally exhaustive and therefore they are not even applied in combination with CFD codes for the gas phase. After an analysis of computer calculations and phenomenon representation, model 2 was chosen to be used in this research, since its level of complexity offers an acceptable representation of the phenomenon, with enough precision and fast computational calculations to study fuel droplets, especially for great amounts of droplets in sprays.

Based on the previous description of the droplet models, this thesis develops completely the droplet mathematical modeling in Appendix A, in order to avoid presenting an extensive amount of mathematical demonstrations in the main text. All hypotheses are described in the Appendix and in Section 3.1.1 in Chapter 3.

Initially, most theoretical models for droplet evaporation/combustion assumed this particle has a spherical form concentrically surrounded by a spherical surface of a gas (usually air) at a higher temperature than the droplet (Godsave, 1953). It was also postulated that the droplet vapor flows symmetrically radial to the outer surface. In terms of experimental procedures, Nishiwaki (1955) added an study on the evaporation and ignition lag of fuel droplets in several environment conditions (i.e., air temperature) in a furnace combustion chamber. The analysis was composed by photographical methods. Later, Kumagai e Isoda (1957) published some results for ethanol and n-heptane droplets falling in a combustion chamber. The results presented an analysis for the flame boundary layer thickness and its profile around the droplet.

During the 1970s, Law e Williams (1972) specified their study for alkane droplet combustion and analyzed the effects of the chemical kinetics and convection on the phenomenon. Kent (1973) published a well-detailed theoretical study of a mono-component droplet evaporation/condensation model in diffusion-controlled quasi-steady conditions. Next, Hubbard *et al.* (1975) highlighted the initial moment during the process of droplet evaporation when a droplet is usually heated-up (heat-up process) by taking into consideration variable properties for their numerical analysis. The initial transient period represents only the sensible droplet heating, i.e, most of the energy is used to elevate the droplet temperature, instead of evaporating the liquid. Meanwhile, the one-third rule (Eqs. 2.1-2.2) for the property proportion between the droplet saturated vapor and the gas medium was used in the simulations. This rule presents a compromise between numerical analyses and experimental results for droplet evaporation, adjusting thermodynamic and transport properties to values which represent adequately the reality of this phenomenon.

$$T_m = T_{d,s} + \frac{1}{3}(T_g - T_{d,s}) \tag{2.1}$$

$$y_{f,m} = y_{f,s} + \frac{1}{3}(y_{f,g} - y_{f,s}), \tag{2.2}$$

where T_m is the mixture temperature between the droplet surface temperature and the gas environment, $T_{d,s}$ is the droplet surface temperature, T_g is the gas temperature. Eq. 2.2 represents the same terms, but for mass fraction instead of temperature.

Law e Law (1976) took into account the variation of properties such as constant-pressure specific heat (c_p), thermal and mass diffusivities (α and $\mathcal{D}_{A,B}$, respectively) with temperature and species concentration profile in a diffusive flame around a droplet burning. Later, Law e Law (1977) extended the analysis of their previous paper and presented the domain of heat transfer effects on the inner flame region while the mass transfer effects dominated outside the diffusive flame. Faeth (1977) presented a review paper providing novel contents related to spray vaporization (evaporation and/or combustion) in several areas, with a comprehensive presentation of all modeling assumptions on droplet evaporation/combustion and the characteristic times associated with droplet evaporation (Eqs. 2.3-2.5):

$$\tau_l = D_d^2/\alpha_l \tag{2.3}$$

$$\tau_d = (D_d^2 \Delta h_v)/[c_l(T_{wb} - T_g)] \tag{2.4}$$

$$\tau_g = \delta_g^2/\alpha_g \tag{2.5}$$

where τ_l represents the liquid characteristic time, which is the basic time scale involved in this phenomenon, τ_d is the droplet lifetime scale, which involves the amount heat required to evaporate the fuel and the thermal energy to bring the droplet to a condition where mass transfer occurs significantly, and τ_g is the gas characteristic time. At high Reynolds numbers or at low pressures (with $\alpha_g \gg \alpha_l$), the gas time scale is much smaller than the liquid phase transient time, therefore allowing the assumption of gas phase quasi-steadiness on the boundary layer around the droplet. This boundary layer has the same properties as a steady boundary layer and the radial effects of velocity in the interface can be neglected (Faeth, 1977).

Law e Sirignano (1977) exapanded the assumption analysis by focusing on the thermal conduction phenomenon within the droplet during combustion. One important hypothesis on droplet evaporation modeling is that the ratio of liquid/gas density usually indicates high mass and thermal inertia, which justifies the quasi-steady approximation usage on many cases (Sirignano; Law, 1978). Another strong hypothesis is the miscibility of ethanol and water, which indicates a near unitary activity coefficient a_i, therefore it allows the usage of the Raoult law. Tong e Sirignano (1982) presented through a short communication the importance of the thermal boundary layer in the liquid phase of a droplet during its transient heating with internal circulation and some assumptions usually related to its modeling.

Chiang *et al.* (1992) developed a parametric analysis of a cold fuel droplet evaporation process when the droplet is injected in a hot gas flow. The results indicate that higher transfer numbers (B_M and B_T) reduce the droplet drag, whereas at lower values the drag coefficient is dominated by the Reynolds number. Snegirev (2013) analyzed the importance of internal temperature non-uniformity in the evaporation of a mono-component droplet by comparing the performance of simplified methods (power law approximation, higher order polynomial approximation and integral heat balance method) to approximate the temperature gradient within the droplet.

Newer review papers and books on droplet evaporation/combustion are also available in literature. Sazhin (2006) developed a review paper about advanced models of fuel droplet heating and evaporation processes. Sirignano (2014) reviewed works related to a collective number of interactive droplets, classifying these studies in droplet arrays, droplet group, and droplet spray. Sazhin (2017) published the most recent review found in this area of subject. This new review paper presented the context of current unsolved problems in the area of droplet evaporation modeling, such as non-spherical droplets, complex multi-component droplets, etc.

Additionally, Sazhin (2014) presented a text-book about droplets and sprays.

Usually the droplet models take into account the validity of the ideal gas law, although there are studies which used different equations of state to represent the gas phase. Curtis *et al.* (1995) presented a new droplet evaporation model at high pressures for Diesel engine applications. This model adopted the Peng-Robinson equation of state (PR-EOS). Kim e Sung (2003) studied the effects of ambient pressure on the evaporation of a single droplet and a spray, by using the fugacity concept. Later, Qiu *et al.* (2014) developed a thermodynamically consistent phase equilibrium solver with the application of a PR-EOS. Abudour *et al.* (2014) estimated the binary interaction parameters (BIPs) by regression of vapor-liquid equilibrium (VLE) data.

Near state-of-the-art droplet modeling is still researched, despite its complexity and thus application in other codes. For example, Réveillon e Vervisch (2000) presented a sub-model for the behavior of individual droplets to be coupled with a non-premixed turbulent combustion model. This model was projected to be used in conjunction with Direct Numerical Simulation (DNS), Large Eddy Simulation (LES) or Reynolds-Averaged Navier-Stokes (RANS). The Lagrangian approach was adopted to each one of the spray droplets. Yin (2016) presented a complete description of a model for transient heating and evaporation of moving mono-component droplets, where the droplet modeling is coupled with a 3-D solution of the gas phase by a finite volume method (FVM).

2.1.2 Droplet evaporation sub-models

Droplet vaporization modeling was properly initiated near 1950s, although Lord Rayleigh had made an attempt in modeling droplets in XIX century (Strutt; Rayleigh, 1878). Since then, several numerical and analytical solutions for this problem have been presented in literature. These calculations of the droplet vaporization usually take into account sub-models to represent specific parts of the phenomenon, e.g., correlations for non-dimensional numbers as Nusselt and Sherwood.

The first papers related to droplets presented their analyses and results based on combustion conditions. The empirical analyses on this phenomenon indicated that the mass burning rate of droplets is directly proportional to the droplet diameter (Kumagai; Isoda, 1957), therefore it seemed reasonable to better understand the droplet lifetime in order to predict the combustion process (ignition delay, duration, etc.).

Ranz e Marshall Jr. (1952) provided one of the most applied Nusselt and Sherwood (heat and mass transfer, respectively) correlations for a spherical droplet evaporation with different Reynolds numbers. Godsave (1953) published a paper with a initial mathematical model for droplet evaporation or combustion in a stagnant environment (for a sphere, $Nu = Sh = 2$). Another classical paper in droplet modeling is Spalding (1953), that also presented an analytical solution for the problem of a diffusive laminar flow of a component burning in a gaseous medium in steady state. Later, Faeth e Lazar (1971) showed the droplet swelling effect during the early stages of evaporation (i.e, liquid density decreases due to droplet heat-up, which initially increases the droplet volume while the mass evaporates).

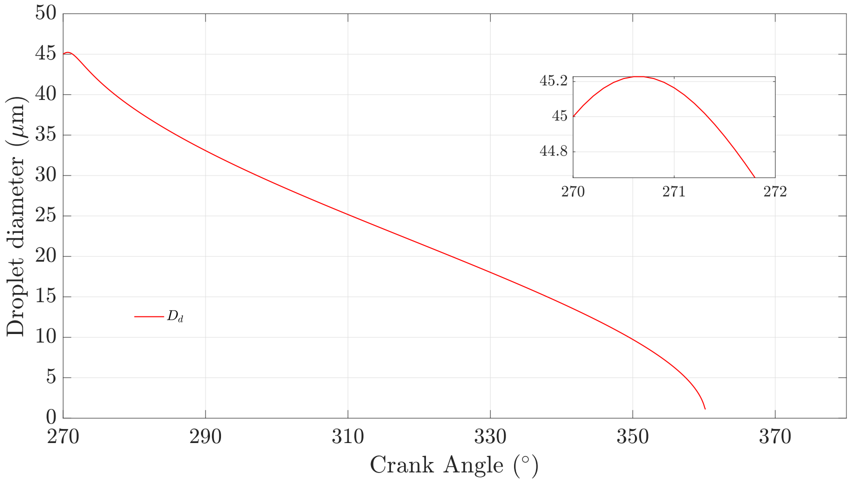

Figure 2.2 – Droplet swelling effect.

Yuen e Chen (1976) approached the droplet evaporation problem by obtaining drag coefficient correlations for their dynamics. The one-third rule was used to average the vapor and gas properties. The drag coefficient are function of the Reynolds number and its comparison with standard drag curves available in literature was successful. Renksizbulut e Yuen (1983) presented a correlation to the drag coefficient over the droplet by introducing the Spalding number in the formula. The emphasis is clear in highlight the droplet evaporation effects on the droplet dynamics and its contribution to the particle deceleration.

Aggarwal *et al.* (1984) compared the effects of different gaseous and liquid phase models on the behavior of an isolated droplet evaporating in a high-temperature environment. The assumption of internal phenomena within the droplet requires a great amount of computational time, which makes the situation unfeasible for sprays, for instance. The spray modeling takes into account the Lagrange-Euler approach. Abramzon e Sirignano (1989) presented a novel model on droplet evaporation which is known by its simplicity without losing significant information of the phenomenon. The paper adopts the film theory on droplet evaporation, i.e. the effects of both thermal and mass boundary layers involving the droplet are considered in the calculations. Also, this paper provides a step-by-step algorithm to a quasi-dimensional droplet evaporation model.

Dombrovsky e Sazhin (2003b) approached the thermal gradient which exists during a droplet heating process with an analytical parabolic solution for the droplet temperature, therefore taking into consideration its thermal conductivity. A comparison of this approach with a finite difference solution is presented and indicates an applicability to predict the droplet heating process in Diesel engines and also for CFD codes. Then, Dombrovsky e Sazhin (2003a) presented an extension of this simplified model, but taking into account evaporation effects. Results were compared to a rigorous solution of this problem based on finite differences and an isothermal model (D_d^2 law). Sazhin e Krutitskii (2003) suggested a new analytical solution to the transient heat conduction problem of a spherical droplet in a infinite medium. Results indicate that the droplet surface reaches its equilibrium temperature faster for a finite thermal conductivity condition in comparison with a infinite condition (i.e. homogeneous temperature). Then, Sazhin *et al.* (2004) presented new solutions to the transient heating of diesel droplets with possibilities to take into account either a constant or variable convective heat transfer conditions. Later, Sazhin *et al.* (2005) suggested new approaches to the modeling of droplet heating and evaporation processes with thermal convection and radiation from a hot surrounding gas. Moreover, Sazhin *et al.* (2007) applied its analytical solution to evaluate the behavior of the transient heating of a semitransparent spherical body, where radiation effects have considerable importance.

Pinheiro (2018) presented a Lagrangian modeling of droplet evaporation for spray calculations. The effects of natural and forced convection on the droplet evaporation rate are studied by the application of the Grashof and Sherwood numbers, respectively. Later, Pinheiro e Vedovoto (2018) indicate that the Abramzon-Sirignano model was the only tested model which does not overestimate the droplet evaporation rate when compared to experimental data.

This review about droplet evaporation and its modeling was intended to clarify the main concepts about them as well as how to computationally simulate this phenomenon. Important attributes related to droplet simulation (e.g., hypothesis, diagram, equations, computational effort, etc.) contextualize the developed model complexity and how it fits on the universe of droplet modeling in specific literature. In short, the combination of the Abramzon-Sirignano model with the one-third rule, the ideal gases assumption, and a Lagrange-Euler approach for spherical droplets offered the conditions to the model developed on Appendix A, which is the base for all subsequent developments presented later in this thesis.

2.2 Multi-component droplets

2.2.1 Fundamentals

Most of the works commented in previous sections of this thesis take into account a single-component droplet, instead of a liquid mixture/solution. Specifically for combustion-related problems, fuels used in thermal devices are not pure substances; actually, they are mixtures of different components, such as gasoline, hydrous ethanol and diesel oil. Therefore, there is a need to consider the multi-component effect in order to predict more closely to reality the evaporation rate of such kind of fuel droplet.

Figure 2.3 describes how the addition of a new component in a droplet affects its evaporation process over time. In this case, ethanol is the less volatile species, so it evaporates slowly than methanol and therefore increase the droplet lifetime as seen in the left sub-figure. Additionally, it also increases the final droplet surface temperature, as shown by the right sub-figure.

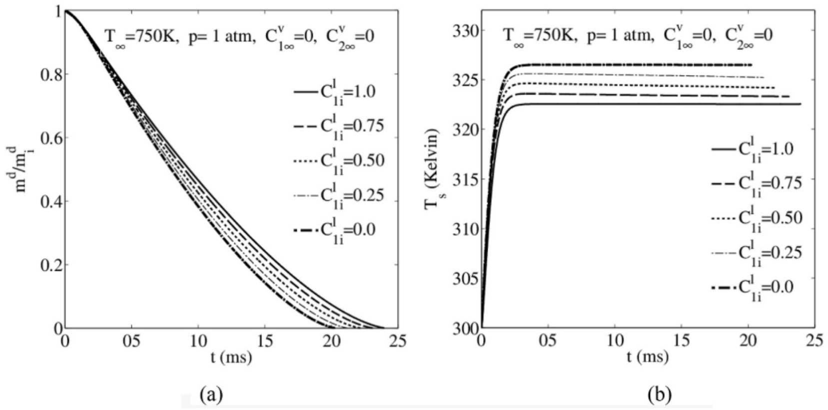

(a) (b)

Figure 2.3 – Differences between compositions of a bi-component (methanol and ethanol) droplet evaporating: (a) mass history; (b) surface temperature. Adapted from (Gavhane *et al.*, 2016).

Some references are presented here to highlight the importance of multi-component evaporation. For example, Newbold e Amundson (1973) provided an accurate model which describe the evaporation of a multi-component droplet (two or three components), especially near its boiling point. Landis e Mills (1974) approached the multi-component droplet problem with the finite difference method for a binary mixture of hydrocarbons. The internal diffusion resistance of the components in the droplet is from the difference between the composition of the liquid phase surface and the average through the droplet, with the highest concentration of the least volatile species in deeper layers of the particle. Law (1976) used two different models to describe the gaseous phase of a multi-component droplet transient combustion in an infinite medium. Sirignano e Law (1978) presented a review paper which emphasized the intrinsically transient nature of the multi-component evaporation. Also, the paper highlights the connection between multi-component evaporation with thermodynamics, fluid mechanics, heat and mass transfer, chemical kinetics and phase equilibrium.

Jin e Borman (1985) highlighted the importance of multi-component droplet vaporization at high pressures. Lower differences between the evaporation rates of different droplet components were found at higher pressures. Megaridis e Sirignano (1991) developed a finite-difference numerical analysis of the fundamental processes governing mass, momentum and energy exchange between liquid and gaseous phases of a multi-component droplet. Hsieh *et al.* (1991) presented a comprehensive analysis of multi-component droplet vaporization near critical conditions. The model considers the gas solubility in the liquid phase, and applies a real gas equation of state.

More recently, Wilms (2005) developed a ph.D thesis with focus on clarifying the understanding of multi-component droplet evaporation models. The necessity was connected to the fuel droplet evaporation process in combustors and automotive engines. Sazhin *et al.* (2005) investigated the effect of thermal gradient inside fuel droplets on the phenomena of evaporation, breakup and vapor/air mixture ignition with a zero-dimensional code. Depredurand (2009) developed a thesis about experimental approaches to multi-component fuel spray evaporation using Laser Induced Fluorescence (LIF) and Phase Doppler Anemometry (PDA) and compared the measurements with models for monocomponent, bicomponent individual droplets and sprays for turbulent conditions.

Different conditions to liquid mixtures evaporation are also dealt by multi-component modeling. For example, Daif *et al.* (1998) developed some experiments related to fuel droplet multi-component vaporization under forced convection conditions and compares the results with the Abramzon and Sirignano droplet model (Abramzon; Sirignano, 1989). Satisfactory results were obtained both for natural convection and forced convection. Kazakov *et al.* (2003)

modeled the combustion of an isolated ethanol-water droplet under microgravity conditions and took into account chemical kinetics effects, gas-phase transport, and non-luminous thermal radiation. Gavhane *et al.* (2016) studied the effects of component composition in multi-component droplets and vapor concentration on droplet evaporation for free convection conditions. For distant volatility blends, both droplet evaporation rate and surface temperature histories are controlled by the heavier component, whereas for close volatility conditions the evaporation rate is controlled by the lighter component while the surface temperature is controlled by the heavier component.

Sazhin *et al.* (2014) modeled the heating and evaporation of a biodiesel fuel droplet and compared the results obtained for taking into account the the contribution of all components of biodiesel (e.g., near 16 components) and a simplified approach assuming one component with averaged transport and thermodynamic coefficients. Oliveira *et al.* (2019) adopted a similar approach to estimate the heat transfer coefficient during the nucleate boiling process by adopting some gasoline surrogates to replace some more complex multicomponent mixtures.

2.2.2 Multi-component sub-models

The specific literature indicates a great variety of multi-component droplet evaporation models which have different levels of mathematical complexity. Depending on the selected approach, these models vary from zero-dimensional equations to partial-differential equation system solutions. For example, Brenn *et al.* (2001) presented an dimensionless equation for the concentration field inside a droplet. This equation represents mass transfer during droplet drying process and takes into consideration the mass transfer through droplet surface. Later, Brenn *et al.* (2003) applied a simplified multi-component droplet evaporation model with a modification of Abramzon and Sirignano model (Abramzon; Sirignano, 1989). This model uses the concept of volume-equivalent partial radius/diameter for each droplet component to represent its droplet ”size” in the component evaporation rate. This partial diameter is obtained by Eq. 2.6:

$$D_{part,i,d} = D_d \left(\frac{\cancel{V}_{i,d}}{\cancel{V}_d} \right)^{1/3} \tag{2.6}$$

where $\cancel{V}_{i,d} = v_{i,d} \cancel{V}_d$ is the volume parcel related to the ith component. Hence, the total evaporation rate is calculated by Eq. 2.7:

$$\dot{m}_d = \sum_{i=1}^{N_{species}} \dot{m}_i = \sum_{i=1}^{n} 2\pi D_{part,i,d}(\rho\mathcal{D})_{i,v} Sh_i \ln(1 + B_{M,i}) \tag{2.7}$$

where $(\rho\mathcal{D})_{i,v}$ and $B_{M,i} = (y_{i,s} - y_{i,g})/(1 - y_{i,g})$ refer to each vapor component. This model was the one adopted on this thesis, due to its simplicity in implementation and to avoid extensive calculations involving more complex models, as some of them are briefly presented in the following text.

Sazhin *et al.* (2010) presented an extension for the analytical solution of spherically symmetric species diffusion equation for droplet heating and evaporation modeling. The work considered both ideal and non-ideal mixtures, with the application of the activity factor. Later, Sazhin *et al.* (2011) take into account the effect of recirculation within the droplet based on the effective thermal conductivity (ETC) model, in which the liquid thermal conductivity is enhanced to represent the additional heat transfer that occurs due to liquid dynamics in the particle:

$$k_{l,\text{eff}} = \chi k_l, \tag{2.8}$$

where $\chi = 1.86 + 0.86tanh[2.225log_{10}(Pe_{d,(l)}/30)]$ and $Pe_{d,(l)} = Re_{d(l)}Pr_l$. χ is a coefficient which represents the effects of recirculation on the conductive heat transfer (Abramzon; Sirignano, 1989). A similar expression for recirculation effects on the diffusion species equation for the droplet exists for the binary diffusion coefficient:

$$\mathcal{D}_{l,\text{eff}} = \chi_y \mathcal{D}_l, \tag{2.9}$$

where $\chi_y = 1.86 + 0.86tanh[2.225log_{10}(Sc_l/30)]$. Its simulation continues until the radius is less than a small number (i.e., 10^{-6} m) in their simulations.

Zeng e Lee (2002) presented a multi-component droplet vaporization model which takes into account the droplet temperature and species concentration non-uniformity inside it. The model presents the advantages of low computational cost and equivalent accuracy as vortex models in droplets. Elwardany *et al.* (2011) made a comparative analysis of the predictions of various models for both mono-component and multi-component droplet heating and evaporation models in ambient air. Yi *et al.* (2016) suggested a novel quasi-dimensional model for multi-component droplets considering finite thermal conductivity and mass diffusivity within the droplet. This model takes into account a parabolic temperature and species profile within the droplet.

Different approaches to solve the multi-component droplet problem are also available in literature. Tamim e Hallett (1995) developed a novel multi-component droplet evaporation model that describes the mixture composition, properties and vapor-liquid equilibrium through the methods of continuous thermodynamics. Some distribution functions are used to calculate these variables based on their compositions. These equations are solved numerically by a finite difference method. Its application is especially focused for fuels with a great amount of components, such as Diesel oil and Gasoline. Later, Tamim (1996) presented a thesis with more details about this novel methodology.

Another approach for complex-composition fuels is based on the distillation curves of each component. Burger *et al.* (2003) presented this new approach to predict multi-component fraction boiling of droplets with special attention given to kerosene. The distillation curve model considers real gas effects and applies the ASTM distillation data of real fuels during their droplet evaporation. Ra e Reitz (2009) described a spray vaporization model for multi-component fuels called discrete multi-component (DMC) fuel approach, which is applied to predict the properties and composition of complex fuels, such as gasoline and diesel. Abianeh e Chen (2012) applied this model to compare the evaporation characteristics of four different ethanol/gasoline blended fuels (E5, E15, E40, E60, and E85) with pure gasoline. Results showed that pure gasoline is more volatile than the blended fuels. Yi *et al.* (2014) developed an improved hybrid multi-component (HMC) vaporization model for realistic fuel droplets. This hybrid approach combines characteristics from the discrete multi-component (DMC) and continuous multi-component (CMC) models by the usage of a PDF to model the properties of each component separately. Al Qubeissi *et al.* (2018) modeled the droplet heating and evaporation processes of ethanol/gasoline fuel blends in conditions representative to ICEs. The discrete component model (DCM) is used to account effects like component transient diffusion, temperature gradient and recirculation inside the droplets. Results indicated that droplets with higher contents of gasoline reached higher surface temperature than pure ethanol. Additionally, the surface temperature is never asymptotic, since the complex multi-component composition of gasoline causes constant change in the droplet surface composition due to different volatilities.

After a brief review about some different multi-component droplet evaporation models, it was clear that the model proposed by Brenn *et al.* (2003) was the right one to this thesis modeling intentions. It is computationally fast (compared to the other approaches) and its equations fit pretty well with the Abramzon-Sirignano model. Despite it does not cover the same features as most of the other models commented previously, it still provides reasonable results for a simple spray evaporation model, as it is the intention in this research, and therefore it is the one adopted for the remaining sections.

2.3 Fuel sprays in thermal devices

2.3.1 Fuel spray injection phenomenology and atomization

A spray is considered as a system of liquid droplets in a fluid continuous phase (Mugele; Evans, 1951). Later, Sirignano (1993) generalized this concept by describing a spray as a type of two-phase flow. It involves a liquid as the dispersed or discrete phase in the form of droplets or ligaments and a gas as the continuous phase. The fundamentals of sprays are usually presented in classical textbook references inside the subject of liquid atomization, such as Lefebvre (2017). Earlier, Kuo (1996) compiled several papers related to the liquid and spray combustion field area in a book with details for both experimental and modeling approaches.

Sprays connect directly with droplets by a sequence of sub-processes involving the disintegration of a liquid jet in an environment. These sub-processes encompass basically how some small disturbances occurring on the jet surface lead to its disintegration into ligaments, and finally into drops (Lefebvre, 2017). Later, these drops goes through the processes of deformation and coalescence, mainly caused by a non-equilibrium situation between surface and shear tensions on the liquid-gas interface. At the end, these instabilities cause a secondary break up, which therefore forms several groups of liquid droplets that compose the spray. Figure 2.4 presents a generic spray atomization process with its different phases:

Borisov *et al.* (1981) focused on clarifying the possible jet break up regimes into droplet sprays/clouds. The criteria to the existence of each one of these regimes are presented in terms of critical Weber Number (We_{crit}). A jet usually breaks up into several droplets because of the aerodynamic forces that act on the liquid surface and causes deformations. Numerical simulations about jet/droplet break-up using a CFD approach are also available in the literature. Reitz e Diwakar (1986) modified the KIVA code to take into account droplet breakup in a hollow cone fuel spray. Their results indicated that this phenomenon alters the spray penetration, vaporization and mixing. Later, Reitz e Diwakar (1987) extended their analysis by evaluating the interactions between spray droplets and gas near to the fuel nozzle in dense high-pressure sprays. Figure 2.5 represents a schematic diagram of a fuel spray in a Diesel engine:

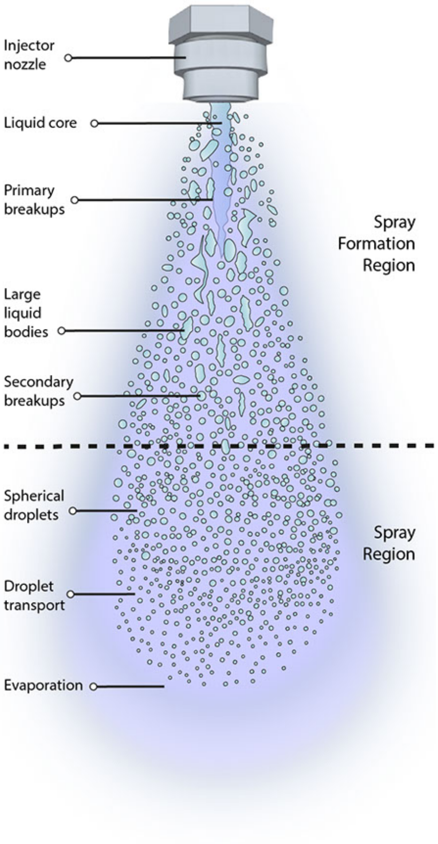

Figure 2.4 – Representation of a spray breakup atomization regimes. Adapted from (Group, 2022).

There are plenty of review papers about experimental and numerical procedures involving fuel spray in the literature: Elkotb (1982) published a review paper presenting the main concepts of fuel atomization for spray modeling and recommended that the fuel injection and its mixture with air must be developed quickly in order to obtain an efficient engine. Faeth (1983) reviewed evaporation and combustion models for sprays, with special attention given to flow structure modeling. Later, Aggarwal (1998) developed a review of theoretical and experimental studies related to spray ignition phenomena. Recently, Aggarwal (2014) indicated that there are three distinctive ignition modes involving droplets, such as droplet ignition (flame surrounding the droplet or on its wake), droplet cluster ignition (ignition around or inside a droplet cloud), and spray ignition (global flame). Before ignition occurs, it is preceded by the fuel droplet evaporation, fuel-air mixing and initiation of the chemical reactions.

The fuel spray dynamics is directly associated with a multiphase flow between the spray droplets (liquid phase) and the environment involving them (gas phase) (Crowe, 1975). Crowe (1976) demonstrates thoroughly the transport equations related to droplets based on the Reynolds Transport Theorem. Young (1995) described the derivation of a set of equations for

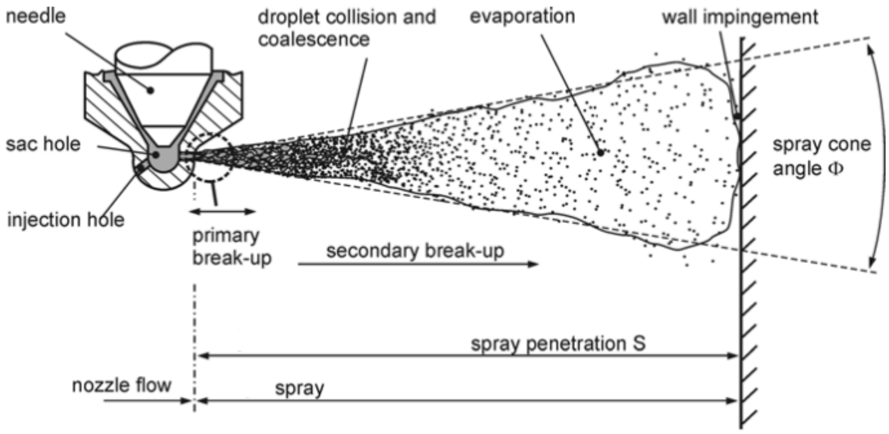

Figure 2.5 – Schematic diagram of a full cone spray in a Diesel engine. Adapted from (Baumgarten, 2006)

a multiphase flow of droplets in a gas phase. Moreover, this equation set has a branch in an entropy analysis. The energy and entropy expressions take into account terms referent to the droplet surface (i.e. energy/entropy related to the droplet surface tension). The Lagrange-Euler modeling is an interesting method to model multi-phase flows. The dispersed phase is usually represented by particles, such as droplets or bubbles, while the continuous phase is composed by some gases or a liquid (Crowe *et al.*, 2012). Dukowicz (1980) developed a numerical technique to represent the combination of Eulerian fluid and Lagrangian particle interactions. Continillo e Sirignano (1991) presented a mathematical model of flame propagation through an air-fuel mixture in a spherical geometry around a spray.

Lapple *et al.* (1967) developed a technical report and conducted a critical review compiling many references in literature in the field of atomization. The usage of correlations to represent this phenomenon for various mechanical atomizing techniques was very common during this period (1960's) and still continues until current days, and therefore it was properly analyzed. More recently, Santos e Moyne (2011) compiled several zero-dimensional correlations for different fuel spray parameters (e.g., spray angle, tip penetration, liquid length, and global SMD) for engine applications. The context of application of these correlations and 1-D dimensional models (i.e. RANS, LES, DNS) is also explored.

Some works involving directly ethanol are also available in literature. For example, Fajgenbaum e Santos (2016) performed some experiments about the fuel temperature effect on the atomization process of ethanol and gasoline in a pressure-swirl atomizer in a port-fuel injector and obtained PDFs for the droplet distribution as function of their diameters and axial positions. Additionally, (Nigra Júnior *et al.*, 2016) developed a similar experiment with a port-fuel single-hole injector and obtained PDFs for the droplet distribution and speed for n-heptane. Olguin e Gutheil (2014) detailed the impact of spray evaporation on the structure of laminar spray flames by combining a theoretical and numerical study for ethanol/air combustion. Earlier, Gu *et al.* (2012) pre-heated different fuels in order to improve their vaporization performance in a crossflow pre-mixer and results pointed out that ethanol SMD changed from 52.8% of initial to 48.2% due to pre-heating near its wet-bulb temperature.

2.3.2 Probability distribution function for droplet sprays

The complexity of representing a spray in numerical calculations is mainly associated to the property variation within the spray. For example, different sizes of droplets are found within a spray, due to their own droplet break up history and interactions with the gas phase. Thus, a stochastic approach represents in a simpler way the behavior of a fuel spray than an deterministic approach, especially in periods before the availability of computers. Therefore, researchers realized that an interesting way of representing this variation on the droplets size is by a probability density function (PDF). For example, Mugele e Evans (1951) presents the fundamentals related with droplet spray variables, such as mean diameters and different representations of droplet distribution. This paper also provides some PDFs for different spray applications, such as Rosin-Rammler, Nukiyama-Tanasawa, log-probability and upper-limit. Later, Simmons (1977a) presented correlations of droplet-size distributions based on PDFs for fuel nozzle sprays both for volume-fraction and number distribution forms (Simmons, 1977b).

A different approach involves the concept of entropy to represent the sprays. Xianguo e Tankin (1987) dealt with this problem by using the information entropy approach to obtain a modified Nukiyama-Tanasawa distribution for droplets. The obtained distribution is said to be independent of the physical terms of the problem. Following a similar path, Li *et al.* (2005) developed a novel model to the initial droplet size distribution based on the maximization of entropy generated during the liquid atomization process. Results were properly compared with experimental data.

Due to the importance of droplet/particle distribution in several scientific fields, some authors presented some subsequent fundamental reviews about this subject. Alderliesten (1990) provides a proper review for concepts of statistics related to particle/droplet mean diameters. Since then, this author focused on present thorough reviews about this theme (Alderliesten, 1991; Alderliesten, 2002; Alderliesten, 2004; Alderliesten, 2006; Alderliesten, 2010). More recently, Alderliesten (2013) presented a detailed analysis about the Rosin-Rammler (R-R) distribution, how it relates to Weibull distribution, and its mathematical and physical properties. The normalized R-R number density function $f_0(x)$ is presented as:

$$f_0(x) = \frac{n x^{n-4}}{x'^{n-3}\Gamma(1-3/n)} \exp\left(-\left[\frac{x}{x'}\right]^n\right) \tag{2.10}$$

where the gamma function $\Gamma(n)$ has acceptable solutions only if $n > 3$. This condition goes in contrast to measured size distributions in literature, where $n \leq 3$ are reported frequently.

2.4 Direct-injection spark-ignition engines

2.4.1 Brief overview

Direct fuel injection occurs differently in Diesel and spark-ignition engines; while the direct fuel injection is a very common process to the former, it was quite uncommon to find the latter in passenger vehicles until late 1970's. The fact that Diesel engines often require higher fuel injection pressures, as well as more complicated and expensive aftertreatment systems to respect the emission regulations created a need to develop more efficient DI gasoline engines with high power output, lower cost fuel injection systems and simpler aftertreatment devices (Zhao, 2010). Direct-injection spark-ignition engines have theoretically the potential of high power outputs and improved fuel economy due to its ability in suppressing the knock phenomenon at full load (FL) conditions and reducing pump losses in partial load (PL) conditions.

Direct injection in gasoline engines has existed since the 1930s; the high cost and inflexibility of the fuel injection system limited the application of this device until the 1990's (Zhao *et al.*, 1997; Zhao *et al.*, 1999; Zhao, 2010) when commercial vehicles obtained reliable electronic control systems capable of operating fuel injection systems with enough precision. Thus, this type of vehicles became popular in the market for certain regions (e.g., Europe). These new engines were developed to operate in the stratified mode (i.e., high air-fuel ratio gradients inside the cylinder before combustion) at part load and low to medium engine speed modes, while at high engine speed and full load it operated in homogeneous mode (i.e., air-fuel completely mixed, similar to port-fuel injection (PFI) engines). Figure 2.6 presents a typical

DISI engine fueled with gasoline, with its auxiliary systems (fuel injector, electronic computer unit (ECU), lambda sensor, catalytic converter, etc.).

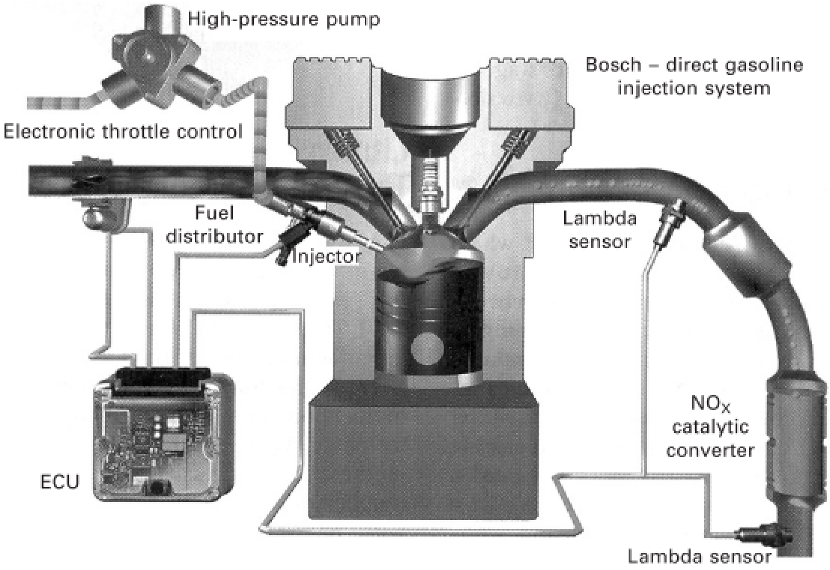

Figure 2.6 – DI gasoline engine. Adapted from (Zhao, 2010).

Heywood (2018) indicates that several advantages are obtained when a liquid fuel is directly injected into the cylinder of a SI engine: the fuel goes directly into the combustion chamber; its distribution can be managed and, if desired, stratified by mixing it with only part of available air in the cylinder. These different procedures cause secondary benefits, such as the evaporative cooling charge caused by fuel vaporization within the air, more air inducted into the cylinder, tighter control of mixing preparation and reduction of specific fuel consumption. This first benefit suppresses the occurrence of auto-ignition/knock and allows the application of higher compression ratios, while the second increases the wide-open-throttle (WOT) torque. Zhao (2010) published a book with a thorough review about advanced techniques related to DISI engines fueled with gasoline and alternative fuels (e.g., ethanol). This book gave special attention to this fuel with a chapter dedicated to it, with a description of its life-cycle, benefits, and questions, besides its potential to fuel engines and CO_2 mitigation under a Brazilian context.

Alternatives towards established fuels and ICE technologies have been constantly investigated throughout the latest decades. Bae e Kim (2017) published a review paper about the seek for alternative fuels for ICEs. Some representative fuels covered in the work were alcohol fuels (methanol and ethanol) and hydrogen (H_2) for SI engines. This paper also commented

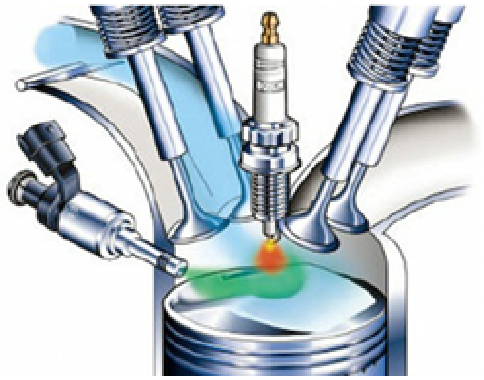

Figure 2.7 – Representation of a fuel direct-injection process in a spark-ignition engine. Adapted from (Ford, 2009).

about other types of combustion engines (GDI, GCI, HCCI, etc.), their technologies, benefits and obstacles they need to overcome.

Furthermore, alternative processes to the classical SI and CI combustion in ICEs are emerging in literature, such as low temperature combustion (LTC) (Agarwal *et al.*, 2017). Its advantages are simultaneous reduction in NO_x, particulate matter (PM), and reduction of specific fuel consumption (SFC), although challenges like controlling ignition timing and combustion rate are still a problem to commercial implementation. The main difference between LTC and classical combustion modes in engines is the occurrence of simultaneous spontaneous ignition of the entire cylinder charge at multiple locations in an auto-ignition temperature with a faster pressure rise, while the cylinder peak temperature remains relatively lower than the other combustion processes.

A new combustion mode called Thermally Stratified Compression Ignition (TSCI) has been recently applied to control both the average temperature and the temperature distribution prior to ignition in HCCI engines (Lawler *et al.*, 2017). This technique amplifies the controllability and the range of operability of LTC by injecting water directly into the cylinders and controlling the start and rate of heat release associated with LTC. The results showed significant thermal stratification in the cylinder caused by local water injection, thereby controlling the rate of heat release, which consequently extended the engine high load limit from 3.6 bar to 8.4 bar gross IMEP.

Some comprehensive reviews and books (Stan *et al.*, 2000; Zhao, 2010) described in details the potential of direct injection engines with gasoline and ethanol. Boretti (2010) analyzed the conditions for pure ethanol engines application in the transport sector and emphasized that direct fuel injection and turbocharging are key features to these engines to reach the maximum potential for ethanol high research octane number (RON) and high heat of evaporation. El-Faroug *et al.* (2016) reviewed experimental results from hydrous ethanol application as a fuel in SI engines (PFI and DI) with blends of gasoline and/or water. Moreover, Wang *et al.* (2017) reviewed knocking combustion in SI engines. Special details about the phenomenology, super-knock occurrence and methods of how to suppress knock (EGR, injection strategy, high EGR-Atkinson/Miller cycle) were presented.

2.4.2 Fuel injection strategies and combustion modes of DISI engine operation

Direct fuels injection in SI engines are intrinsically connected to its operation regime. In an engine cycle, the injection timing has the capacity of completely altering how the combustion process will be in the next cycles, since it basically defines the amount of time the injected fuel has to break into several droplets, evaporate, mixture with air, and then be ignited. Basically, the injection timing is divided into early direct injection (EDI) and late direct injection (LDI), where these instants refer to the intake/admission stroke. Figure 2.8 presents these two modes of operation for DISI engines:

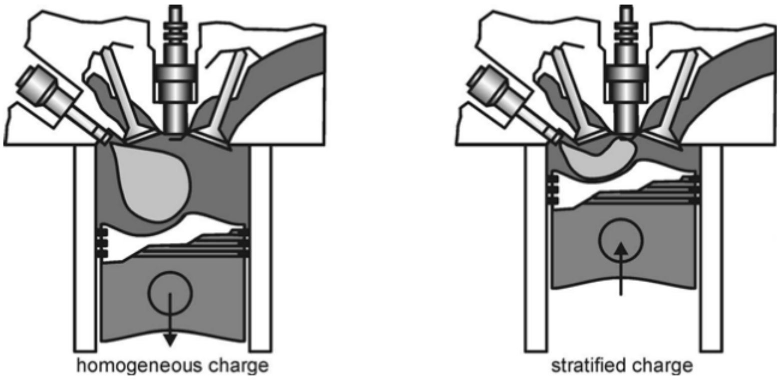

Figure 2.8 – Representations of direct injection modes in DISI engines: Left - nearly homogeneous charge (early injection); right - stratified charge (late injection). Obtained from (Baumgarten, 2006).

An early injection is executed during admission to cause some evaporative charge cooling effect into the gases, therefore reducing their specific volume and enhancing the volumetric efficiency of the engine cycle. Moreover, an early injection also gives enough time to all the fuel completely evaporate and mix with the air and residual gases (depending on the engine speed). The final mixture is nearly homogeneous (Heywood, 2018), which affects the combustion behavior.

On the other hand, a late injection is developed after the admission valve closure. Thus, the fuel has less time to break up, evaporate, and mix before combustion. Therefore, a stratified charge is formed, with several degrees of air-fuel ratios inside the cylinder before the ignition timing. During the first moments of combustion, a near-rich mixture is present near the spark plug, whereas stoichiometric and lean mixtures are encountered around this region; this air-fuel ratio gradient results in an overall lean combustion (up to $\lambda = 1.8$, depending on the fuel and the engine). This reduces peak combustion temperatures and may slow down chemical reactions. Therefore, it affects the formation of gaseous pollutants like NO_x, CO, and UHC, as well as it may reduce both brake specific fuel consumption (BSFC) and knocking tendency. More details are found in review references about mixture preparation and combustion control strategies, such as (Zhao *et al.*, 1997; Zhao *et al.*, 1999).

The newer generations of DISI engines are basically classified into three categories of systems: spray-guided, wall-guided, and air-guided. The former involves using the direction of the fuel spray jet to obtain the desired level of air-fuel mixing before combustion starts. The second normally uses the existence of piston-cups on its crown to facilitate the mixing process. The latter system utilizes different types of air/gas movement inside the cylinder, such as swirl and/or tumble, to amplify the air-fuel mixing quality (Heywood, 2018). Even though most DISI engines currently adopt a hybrid approach of these three categories, the dominant one is the spray-guided system, especially due to the lack of feasibility in realizing the theoretical potential of DISI engines with wall-guided systems, the volumetric efficiency reduction caused by swirl and/or tumble flow on air-guided systems, to avoid the fuel wetting on the pistons or combustion chamber walls (from wall-guided and air-guided systems), besides the benefits provided by this system (Zhao, 2010).

Some reference works are presented here to overview the capacity of the aforementioned fuel injection strategies. Spiegel e Spicher (1992), Yang e Anderson (1998) developed experimental analyses of fuel injection strategies for DISI engines. The former's results indicated only mild differences on the air-fuel mixture homogeneity for early DI fuel injection and port-fuel injection indicated tendencies about early and late injections, while the latter's suggested the application of split injection to compromise between the benefits of early and late injections in DISI engines. Drake e Haworth (2007) published a paper which discuss about optical diagnostics and CFD for five gasoline-engine combustion systems and provides details about different techniques of direct fuel injection in engines (e.g., wall-guided, spray-guided, and air-guided systems), besides homogeneous-charge compression-ignition engines (HCCI). In terms of ethanol, Fournier *et al.* (2016) obtained experimental results for the behavior of fuel blends of ethanol, butanol and acetone both in homogeneous and stratified charge operations for a DISI engine.

Combinations of port-fuel injection for gasoline (GPI) and ethanol direct-injection (EDI) were also explored in order to make the best use of ethanol in DISI engines. The idea of dual-fuel injection was to compromise between the effects of evaporative cooling charge and knock suppression of ethanol with the higher specific energy density of gasoline. For example, Zhuang e Hong (2013a) highlighted the potential of ethanol in improving the engine thermal efficiency and reducing pollutant emissions by exploring this potential in a dual-fuel EDI + GPI strategy. Their results indicated gains in IMEP, knock suppression, CO and UHC reduction, and allowed more advanced spark timings. In a similar study, Zhuang e Hong (2013b) developed a experimental investigation towards the analysis of ethanol injection timing and pressure in a EDI + GPI engine for three different fuel injection pressures (40, 60 and 90 bar). Higher IMEP is obtained for EEDI due to improved volumetric efficiency and combustion. Ethanol fuel injection pressure did not affect the IMEP in EEDI conditions, whereas it increased IMEP at injection timing of 50° BTDC and decreased it at 110° BTDC. Later, Zhuang *et al.* (2017) studied the influence of EDI in suppressing knock in a GPI engine by the means of advancing spark timing and increasing inlet air pressure. Results indicated that increasing the ethanol energy ratio (EER) in gasoline-ethanol fuel blend allowed the advance of knock-limited spark advance (KLSA), which allowed higher cylinder peak pressures and reduced combustion duration (CA$5-90\%$).

Multi-injection strategies are also an interesting alternative for DISI engines. For example, Turkcan *et al.* (2013), Turkcan *et al.* (2014) studied the effects of gasoline-ethanol fuel blends direct-injection strategies on HCCI combustion regime. Results showed that the maximum pressure rise rate occurred with early start of the first injection (SoI_1) timings with fuel blends, instead of gasoline, whereas the start of the second injection (SoI_2) affected the combustion performance. Following a similar trend, Zhuang e Hong (2014) investigated the effect of ethanol SoI timing on knock suppression and lean burn. Following a similar trend, Imaoka *et al.* (2015) studied the application of multistage injection strategies in DI gasoline engines. Multistage benefits the engine cycle by lowering the fuel impingement through reducing the fuel injection momentum, therefore reducing tip penetration and improving the fuel mixing by the fuel spray dispersion. Moreover, the paper showed that retarded injection causes larger cooling effect due to evaporation heat and lower heat transfer from the cylinder walls to the gases. More recently, Duan *et al.* (2020) investigated how injection timing under single and double injection strategies affects performance, combustion and emission of a DISI engine fueled with gasoline/ethanol blend (E10).

2.4.3 Direct fuel injection modeling

Direct fuel injection modeling is directly connected to Diesel engine development, instead of gasoline, due to the aforementioned reasons presented earlier in this chapter. Borman e Johnson (1962)'s work was pioneer in applying the droplet evaporation theory to an open-chamber Diesel engine in order to predict the behavior of the fuel sprays.

Since then, several approaches to modeling the processes of direct fuel injection, break-up, evaporation, mixing and combustion were developed. For example, Hiroyasu e Kadota (1976) proposed a mathematical model capable of predicting the NO_x and soot formation on Diesel engines. Later, Hiroyasu *et al.* (1983) expanded its spray combustion model to predict Diesel engine efficiency and pollutant formation based on a division of the spray in small packages. The spray combustion was broken in terms of some overlapping events (e.g., fuel injection, fuel evaporation and mixing, ignition and combustion, remaining fuel evaporation, mixing and combustion, and final mixing and combustion. Mohammadzadeh (1984) published a thesis presenting a stochastic approach to solve the combustion issue for a direct-injection Diesel engine. More recently, Payri *et al.* (2011) developed a zero-dimensional single-zone thermodynamic predictive model for DI Diesel engines with proper considerations regarding blow-by, fuel injection, engine deformations. Ismail e Mehta (2012) developed a second law analysis of the processes of fuel-air mixing and combustion in a heterogeneous charge compression ignition engine for n-tridecane. The model takes into account several sub-models related to engine operation, such as fuel injection, air swirl, air entrainment, fuel evaporation and mixing, ignition and combustion, etc.

Multi-zone models are an alternative for cases where higher precision is required for pollutant formation prediction, for example. Hountalas e Papagiannakis (2000) developed a two-zone mathematical model for direct injection of dual fuels (Diesel-natural gas) in Diesel engines, with details about the combustion modeling, nitric oxide (NO) prediction, ignition delay model, mass entrainment in the combustion chamber, etc. The combustion model adopted the semi-empirical model of Whitehouse-Way for the liquid Diesel in combination with an Arrhenius type equation, while another Arrhenius type equation modeled the reaction rate of natural gas. Rakopoulos *et al.* (2006) presented a model for the fuel spray development inside a Diesel engine cylinder for bio-diesel, vegetable oil and Diesel fuels. Combinations of multi-component droplet and DI modeling are also available in specific literature. For example, Ra e Reitz (2003) applied a multi-component droplet vaporization model to gasoline direct-injection engines with the application of continuous thermodynamics theory on the droplet's properties. Later, Rakopoulos *et al.* (2008) provided a multi-zone model for the closed cycle of a direct-injection Diesel engine with blends of ethanol/diesel fuel. Krisman *et al.* (2012) explored the potential of ethanol fuel stratification in stratified-charge compression-ignition engines through the application of a multi-zone model validated against experimental data. Ethanol with different quantities of water was studied and results indicated significant reduction of NO production and pressure-rise rate in the engine cycle.

Computational Fluid Dynamics (CFD) is a very strong resource to simulate direct injection engines, despite its requirement for an enormous amount of computational resources, as well as its complexity to be proper developed and analyzed. Puri lng *et al.* (2017) studied the effects of variation of fuel injection timing and pressure in a DI Diesel engine at full load by using the CFD software CONVERGE. Results showed that advancing the ignition timing to 19° BTDC provided the highest pressure peak and the lowest CO formation, although it increased NO_x formation. Gonçalves (2016) studied numerically the effects of internal phenomena in Diesel fuel injectors/nozzles in the process of cavitation in a Diesel engine. Meanwhile, Jadhav e Mallikarjuna (2018) applied a CFD analysis to understand the effect of fuel injector-hole diameter and fuel injection timing on the mixture formation of a gasoline direct injection (GDI) engine. Results indicated that higher diameters cause richer mixtures near the spark plug, while lower diameters and retarded fuel injection timings provide higher indicated mean effective pressures (IMEPs).

After this brief review, this thesis focused on applying the concepts of evaporative cooling effect of fuel early direct injection to amplify the volumetric efficiency of the engine cycle. The advantages mentioned by most references up to this paragraph indicate opportunities for optimal operation of DISI engines. This optimal operation in a hybrid powertrain (with a DISI + Miller cycle) (Zhao, 2017) may allow a sufficient autonomy for many vehicles to drive throughout several regions of a country which do not necessarily have enough infrastructure to electrically charge pure electric vehicles. Thus, the adoption of some DI technologies previously mentioned here in a multi-zone model can emphasize the potential of this engine, especially when fueled with the subject of the next section, ethanol.

2.5 Ethanol and wet ethanol

2.5.1 Overview of ethanol characteristics as a fuel

As commented in Chapter 1, ethanol has been evaluated as a fuel for internal combustion engines since the advent of these machines. References point out that ethanol was present in many important events involving these thermal machines, such as the fuel used on the first American ICE prototype, in an early version of the Otto ICE as well as in the early versions of the Ford model T (Wikipedia, 2022; Hall, 2015). Since then, its properties have been thoroughly studied and analyzed in order to use it as a renewable/sustainable biofuel, thus replacing fossil fuels in some places of the world. An overview of ethanol properties and characteristics (mainly based on Zhao (2010), chapter 9) to be used as a fuel in Brazil is presented in this section.

In terms of production, ethanol can be considered almost 100% renewable (”liquid solar energy”) and therefore almost CO_2 neutral emission. Exceptions involve methane and N_2O for sugar cane production, and Diesel fuel for heavy-duty vehicles in the transport sector. It does not require any energy input to its production, due to the bagasse burn. In addition, its life cycle assessment (LCA) is already available in literature (Macedo *et al.*, 2004; Macedo *et al.*, 2008) and its production is profitable. Besides, its economic impact to food prices is mitigated, when compared to fossil fuel prices impact in this same sector. And lastly, ethanol is biodegradable.

In terms of fuel properties (Zhao, 2010; Moran *et al.*, 2011; Baeyens *et al.*, 2015; Heywood, 2018), despite its lower lower heat value (LHV) (26.8 27.0 *versus* 42.7 43.0 MJ/kg of ”gasoline”), ethanol possess a lower stoichiometric air-fuel ratio (9.0 *versus* 14.7 $\text{kg}_{fuel}/\text{kg}_{air}$), which enhances the specific energy (2.98 *versus* 2.90 MJ/kg_{air}, (Zhao, 2010)) obtainable from combustion. Also, it has a higher H/C ratio (3 *versus* approximately 2.25) and presents similar stoichiometric CO_2 emissions (71.2 *versus* 71.9 $\text{g}_{CO_2}/\text{MJ}_{fuel}$). In spite of ethanol higher specific fuel and volumetric consumption in light-duty vehicles, its dependency can be avoided by adding gasoline in its blend. When burning in an engine, ethanol usually causes lower adiabatic flame temperatures, therefore less heat is lost by convection and radiation to the cooling system. Furthermore, ethanol has a much higher latent heat of vaporization (different literature references indicate 930 (Zhao, 2010), 900 (Heywood, 2018), 910 (Bromberg; Cohn, 2008), 919 (NIST, 2021; Bank, 2022) *versus* 180 (Zhao, 2010), 300 (Bromberg; Cohn, 2008), 350 kJ/kg (Heywood, 2018)), which enhances the evaporative charge cooling effect (in direct-injection systems) and therefore the volumetric efficiency. Moreover, lowering the initial charge temperature enhances the knock limit. Additionally, it has a higher octane number (MON 98 (Zhao, 2010) or 90 (Heywood, 2018), and RON 109 (Zhao, 2010; Heywood, 2018)), thus enabling higher compression ratios with optimal ignition timing and higher boost pressures (via turbocharging or supercharging). These higher anti-knock properties require less enrichment at full load to avoid knock and to lower exhaust temperatures. This evaporative cooling effect also allows a more intense turbocharging, which enables a more aggressive downsizing, reducing volume and surface area, which reduce the vehicle weight and engine friction, respectively. Moreover, ethanol turbocharging usually provides lower exhaust temperatures, thus extending the turbine life expectancy and increasing the efficiency by avoiding/reducing the enrichment at FL to cool down the turbine. Ethanol also has a higher laminar flame speed than gasoline over the usual relative air-fuel ratio (λ) range (Heywood, 2018), which allows possibilities to a more efficient power development due to reduction of negative work (less spark ignition advance for the same angle of peak pressure) (Zhao, 2010; Brusstar; Bakenhus, 2008). Its higher mole ratio of products to reactants (1.061 *versus* 0.937) enhances the cylinder pressure and power output for the same amount of intake air flow (slightly molar expansion, instead of a contraction). The fact that alcohols combustion tolerate significantly high levels of EGR is a key feature to adopt high compression ratios. This fact also leads to higher specific heat ratios ($k = c_p/c_v$), which therefore also increases the engine cycle efficiency (Caton, 2014).

Despite the existence of a considerable number of advantages between its aforementioned characteristics, there are some issues related to ethanol which need to be considered in order to use it as a main fuel in ICEs. For example, material compatibility (corrosive) and engine wear problem require special attention on long-term engine usage (Zhao, 2010). Another question involves the aldehyde emissions due to ethanol combustion (Brinkman, 1981); issue that does not practically happen with gasoline. Also, ethanol has azeotropes (Stein *et al.*, 2013; Baeyens *et al.*, 2015), thus it changes the Reid vapor pressure, therefore enhancing possible evaporative emissions. The ethanol cold start issue is very mentioned throughout the literature, although several approaches such as the combination of variable cam timing and DI with proper strategies (Zhao, 2010; Kapus *et al.*, 2007), heated fuel injectors and split injection have been used to overcome it (Daniel *et al.*, 2012). Finally, lower exhaust temperatures can reduce the catalyst efficiency, especially during start-up operation. In short, all these issues exist and must be taken into account, still they are mostly solved depending on the adopted engine system.

2.5.2 Hydrous ethanol usage in internal combustion engines

Brinkman (1981) was one of the pioneers that highlighted the ethanol main characteristics and potential as a fuel in SI engines (e.g., higher thermal efficiencies, lower NO_x emission, higher knock resistance) when compared to gasoline. However, since 1980s this fuel has faced some limitations on its applications as a main fuel in ICEs in Brazil, especially when the *Proálcool* program was abandoned by the Brazilian government. Other issues involved its cold-start problem in colder regions during the mornings and the sharp increase of aldehydes emission by the engine. Still, ethanol remains until current days as a good alternative renewable fuel in Brazil and has been used in fuel blends with gasoline (27% v/v ethanol) or as hydrous ethanol (approximately 5% v/v water).

Some scientific works have been developed to expand the knowledge of ethanol-gasoline fuel blends to overcome ethanol limitations and especially to highlight its properties. For example, Agarwal (2007) presented a review paper about the application of biofuels (e.g. alcohols and biodiesel) in internal combustion engines. The problems of engine modification, material compatibility, engine performance, pollutant regulation, and environmental effects are addressed, besides economical changes caused by these fuels application. Others (Boretti, 2010; El-Faroug *et al.*, 2016) updated the available information regarding ethanol usage. Later, Melo *et al.* (2012) developed some experimental tests in a flex-fuel engine fueled with gasoline-ethanol blends and calculated several combustion characteristics, such as mass fraction burned, heat release rate (HRR) and combustion duration at maximum brake torque (MBT) conditions for several engine speeds. Results indicated lower CO and THC for higher ethanol contents, in spite of increased CO_2, aldehydes and unburned ethanol emissions. On the other hand, NO_x emissions presented complex tendencies, which cannot be only justified with fuel modification.

Stein *et al.* (2013) overviewed the effects of gasoline-ethanol fuel blends in SI engines for vehicles specifically designed to operate with such blends. Increased ethanol contents are reported to increase knock resistance due to ethanol RON, heat of vaporization (HoV) and sensitivity. These benefits also allow improving fuel efficiency and CO_2 emissions through the application of complementary modifications in the engine, such as downsizing, downspeeding and increased compression ratio. At last, the paper recommends the application of a fuel blend between 20 and 40% v/v for a long-term fuel for the US for vehicles optimized to it. Corsetti *et al.* (2015) studied the evaporation dynamics of ethanol/gasoline blend droplets with single particle manipulation techniques. Different droplet compositions were studied and results indicated that droplets with higher contents of ethanol required longer times to evaporate. Jin *et al.* (2017) compared hazardous air pollutants (HAP) emissions obtained from various ethanol-gasoline fuel blends (from E0 to E85) in a wall-guided (WG) DISI engine. Higher ethanol contents in gasoline reduced dramatically the amount of particulate emission, therefore rare nano-particles were detected during the experimental procedure. On the other hand, ethanol collaborates to increase carbonyl compound emissions, which originate from its incomplete combustion, while volatile organic compounds (VOC) reduced sharply.

Stan *et al.* (2000) investigated the full potentialities of direct-injection systems for spark-ignition engines fueled with ethanol or gasoline. Some years later, Bromberg *et al.* (2006) evaluated the effects of knock suppression caused by direct injection of ethanol as a fuel in a highly turbocharged spark-ignition engine. Results show that the high octane rating of ethanol and its enhanced evaporative cooling effect (due to its high evaporative latent heat) inhibited knock for different conditions, therefore allowing the engine to operate in more intense conditions with higher thermal efficiency. Moreover, these conditions also allow for downsizing with higher compression ratios, obtaining a part-load efficiency increase of more than 30% in comparison to conventional PFI engine operations. Later, Bromberg e Cohn (2008) extended their analysis to present the effective octane rating increase and efficiency advantages of direct-injection alcohol engines.

Some Brazilian researches involving the application of hydrous ethanol and/or DISI engines were published recently. For example, Baêta *et al.* (2015) proposed a new layout for an ethanol direct injection (EDI) engine with turbocharging in order to discover the limits of downsizing for this type of engine. The main objective was to replace high-displacement gasoline engines ($2400 - 3000 cm^3$). The prototype engine ($1400 cm^3$) was capable to reach brake mean effective pressure (BMEP) of $3250 kPa$ at 44% of thermal efficiency. Moreover, a comparison between this prototype and a naturally aspirated (NA) 2.4-l engine showed that the prototype reduced overall fuel consumption on all tested engine cycles in about 18%. Costa *et al.* (2018) investigated the effects of stratified lean burn combustion of Brazilian hydrous ethanol

(E100) in a wall-guided optical DISI engine. Results indicated that specific fuel consumption and fuel conversion efficiency increased 8.1% and 2.6% for $\lambda = 1.4$, while NO_x, THC and CO emissions decreased 66%, 20%, and 20%, respectively. Near state-of-the-art conditions for these fuels could potentially provide an efficiency gain of near 47% for a full-load turbocharged Miller cycle DISI engine (Martins; Lanzanova, 2015).

2.5.3 Wet ethanol as an alternative fuel for internal combustion engines and for transport sustainability

The idea of wet ethanol involves the usage of a biofuel which is capable of reducing the carbon footprint associated with ethanol while it assists to a better transition to a free GHG world economy (Koupaie *et al.*, 2019). The ethanol production of first generation involves sugar-based raw materials like sugarcane crops (in Brazil), which are provided to certain species of yeast or bacteria that metabolize the available sugar into ethanol and CO_2 (Baeyens *et al.*, 2015). After the processes of saccharification, fermentation, distillation, and ethanol dehydration, the final mixture contains 99% of ethanol while the remaining content is water. However, both distillation and dehydration processes require great amounts of energy, especially to overcome the final 20% v/v of water. Mack *et al.* (2009) indicated that E65 (i.e., an ethanol-water mixture with 65% v/v ethanol) decreases water separation cost to only 3% of the total energy of ethanol, and also increases the net energy gain from 21% to 55% of the ethanol energy and coproducts (for corn-based ethanol). Complementary, (López-Plaza *et al.*, 2014) evaluated the cost of wet ethanol production using a conventional distillation column so that it can be used as a fuel in homogeneous charge compression ignition (HCCI) engines and emphasized that wet E80W20 improves the energy balance by a factor of 2.3, CO_2 balance by 1.9, and reduces the cost by 25%. In addition, Fagundez *et al.* (2017) commented that the distillation process accounts for near 13.7% of the total energy cost required to yield ethanol from sugarcane-based production.

Several works are available discussing on how to improve the resources efficiency (i.e., water, energy, CO_2 emission, etc.) on the first-generation ethanol production process (Vane, 2008; Madson; Monceaux, 1995; Lopes *et al.*, 2016). In addition, other aspects to sustainability, such as land use (i.e., food *versus* fuel battle) and the alleged lack of sustainability of ethanol production has already been discussed on the literature (Caspeta *et al.*, 2013), with a proper sustainability assessment already available for Brazil in the last decade (Walter *et al.*, 2011).

Any energy savings obtainable from both distillation and dehydration processes is beneficial to ethanol lifecycle/well-to-wheel energy efficiency (Martinez-Frias *et al.*, 2007). Thus, the compromise between net energy savings from a specific ethanol production process and water-in-ethanol content provides interesting benefits to the ethanol production chain, and therefore would be even more effective if advantages to the ICE operation were obtained as well. Within this context, in order to reach optimal conditions for ethanol lifecycle, it is required that wet ethanol application in ICEs must be thoroughly studied, especially for DISI engines.

The characteristics of wet ethanol as a fuel for engines is quite clear: its higher content of water absorbs more energy (than regular E95) during the fuel atomization and evaporation processes (on direct fuel injection), thus reduces the energy transferred to the cooling system from the gases. Also, it reduces the unburned gases temperature, increases the ratio of specific heats and boundary work, and especially assists on knock control for the engine operation at lower speeds (up to 2000 RPM) (Brewster, 2007; Brewster *et al.*, 2007). For example, Martinez-Frias *et al.* (2007) developed a work where the ethanol life cycle energetic efficiency is improved by promoting the utilization of wet ethanol for HCCI engines. (Munsin *et al.*, 2013) indicated that the amount of energy required to distillate ethanol grows linearly up to 80% v/v and then starts growing exponentially, as shown by Fig. 2.9. Therefore, this significant energy cost growth reduces the lifecycle ethanol energy efficiency and increases its production cost. Results show that the model predicts appropriate engine operation up to 35% v/v of ethanol/water with high efficiency (38.7%), low pollutant emission, besides a net energy gain in the ethanol cycle (up to 55%). Mack *et al.* (2009) studied the HCCI engine operation with ethanol-water mixtures from anhydrous ethanol to 60% v/v water and found proper stability for fuels containing up to 40% v/v water. Also, limiting conditions for wet ethanol combustion were found, which were beyond the capabilities of the experimental apparatus.

More recently, Breaux (2012) published a thesis about the effects of elevated water content in ethanol combustion. Compositions from E100 to E60 were analyzed in a swirl-stabilized combustor and results showed stable combustion for water contents up to 35% v/v water. Lanzanova *et al.* (2013) developed an experimental performance analysis in a PFI SI engine fueled with different ethanol-water mixtures up to 40% and compared their results with simulations developed on GT-Power. Martins *et al.* (2015) presented an investigation about water influence on combustion of water-ethanol fuel blends in a SI engine. Results from this work

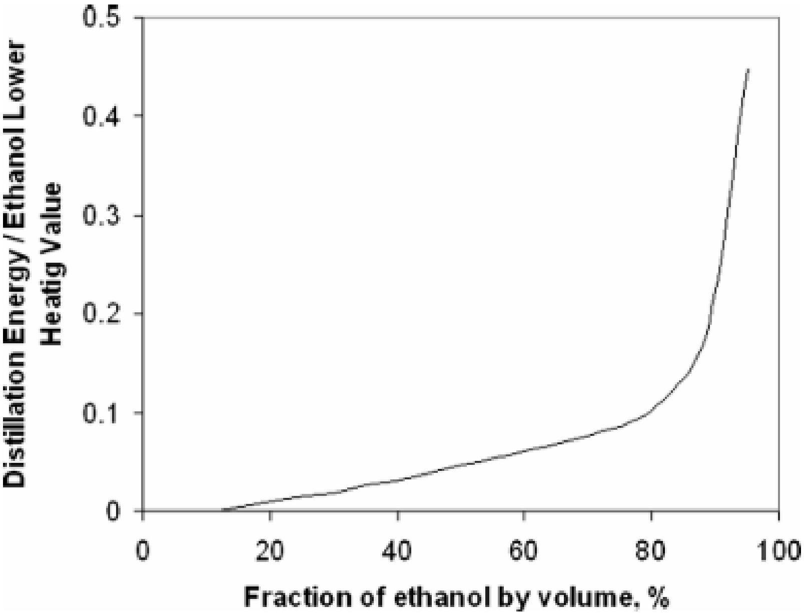

Figure 2.9 – Ethanol distillation energy/lower heating value ratio *versus* fraction of ethanol in volume. Adapted from (Martinez-Frias *et al.*, 2007).

showed higher thermal efficiency, lower maximum rate of pressure rise (i.e., an indirect knock suppression), NO_x production reduction, and an increase in ignition delay for higher water contents of injected fuel. Lanzanova (2017) developed a Ph.D. thesis on experimental investigations of wet ethanol combustion in DISI engines with a deep analysis on positive and negative valve overlaps (PVO and NVO, respectively). Later, Bureshaid *et al.* (2019) applied a turbulent jet ignition to evaluate the combustion and emission characteristics of gasoline, ethanol and wet ethanol in order to extend the lean-burn limits of these fuels. Wet ethanol obtained a higher lean-burn limit than gasoline ($\lambda_{wet} = 1.77$, while $\lambda_{gasoline} = 1.71$ and $\lambda_{ethanol} = 1.77$), whereas NO_x emissions were almost negligible due to lower combustion temperatures of these cases.

After conceiving the TSCI combustion mode (Lawler *et al.*, 2017), Rahimi Boldaji *et al.* (2019) expanded the TSCI application to fuels. However, instead of using direct water injection, the authors decided to inject wet ethanol in different ethanol-water mixtures to discover the effects of applying this combustion mode with this renewable fuel. Wet ethanol fits exceptionally well with the main ideas of TSCI, since it has a high latent heat of evaporation and low equivalence ratio/relative air-fuel ratio sensitivity, both of which collaborate to cause proper thermal stratification without affecting the autoignition timing of various regions (i.e., ethanol has no sensitivity to local relative air-fuel ratio). The results showed that this biofuel provided control over the peak pressure and rate of heat release (i.e., it elongates the combustion process), as well as over the start and rate of combustion in the LTC mode. More recent works applied experimental computational model approaches (e.g., CFD converge or MATLAB subroutines) to relate the pair TSCI and wet ethanol with optimal upstream intake temperature, external cooled exhaust gas recirculation (EGR), multiple split fuel injection strategies, intake boost, injector angle and piston geometry, (Gohn *et al.*, 2020; Gainey *et al.*, 2020; Gainey *et al.*, 2020; Gainey *et al.*, 2020; Gainey *et al.*, 2019; O'Donnell *et al.*, 2020; Gainey *et al.*, 2019).

In terms of direct-injection engines fueled with wet ethanol, Sari *et al.* (2018) seeked to optimal conditions for wet ethanol use as a fuel in DISI engines. Both spark advance and cylinder compression ratio were studied through ignition timing sweep. Fuel blends of 4%, 10%, 20%, and 30% v/v of water in ethanol were tested. Results indicated that all blends offered gains in indicated efficiency, even for E80W20.

Optical techniques have been used to improve the understanding of wet ethanol burning process in ICEs. For example, Koupaie *et al.* (2019) used an optical central DISI engine to study the combustion of wet ethanol in order to improve the understanding of flame propagation using this fuel. Mixtures of 5%, 12% and 20% v/v water in ethanol were studied and compared to baseline results from iso-octane. Higher water contents in ethanol reduced the flame speed ($10.92m/s$ of pure ethanol to $8.2m/s$). Results indicate that the flame unequal propagation caused by higher water contents could be compensated with the spark-plug ideally positioned towards the intake side, which would be of crucial assist to operate the engine under high load knocking conditions. Therefore, higher water contents act as diluents and requires more advanced spark timing to reach MBT (Maximum spark for Best Torque) conditions. Complementary, Augoye e Aleiferis (2014) studied the flame development of anhydrous (E100) and hydrous ethanol (E94W6 and E90W10) mixtures in a optical research engine both for PFI and DI conditions. These results were compared to iso-octane and gasoline and showed that the fuel alcohol blends burned baster (i.e., 11.0 m/s for E100 and approximately 10.0 m/s for E90W10) than the other fuels.

2.6 Second law of thermodynamics in transport phenomena

The second law of thermodynamics is usually associated with thermodynamic processes in order to provide information about the entropy generation or the degree of irreversibility of these processes. For example, Moran *et al.* (2011) presents the fundamentals related to an analysis based on the second law of thermodynamics to macroscopic thermodynamic cycles and thermal devices. Still, no information is provided to the application of such subject in transport phenomena. On the other hand, Bejan (2006) presents advanced concepts related to thermodynamics in engineering, such as the entropy generation minimization (EGM) methodology. It is commented that a transport phenomenon can be analyzed based on a second law view, with some practical examples (e.g., laminar flow in a tube and heat transfer in heat exchangers) didactically presented. In terms of exergetic analyses, Lior *et al.* (2006) published a short review about the application of the exergy concept in transport processes, and some examples of application of this methodology are presented.

The connection between second law of thermodynamics with transport phenomena began during the end of 1970's. Bejan (1979) was a pioneer in being one of the first researchers in connecting the areas of convective heat transfer and the second law of thermodynamics by presenting some aspects related to the latter for different fundamental flow configurations (e.g., pipe flow, boundary layer over flat plate, etc.). The concept of entropy generation number is presented and make a connection between dimensionless numbers used in fluid mechanics and heat transfer (e.g., Peclet, Prandtl, Reynolds, etc.) with the amount of entropy generation obtained for specific cases of these flow configurations. Arpaci e Selamet (1992) reviewed the concepts of entropy efficiency for energy systems and highlighted issues about turbulent dissipation and its connection with local entropy production.

2.6.1 Second law related to droplet/spray evaporation/combustion

This thesis intends to present a second law view about droplet and spray evaporation in DISI engines, therefore a deep review in literature was necessary to understand the main principles and references about this subject. Most references involve analyses about droplet or spray combustion processes in diverse thermal devices and only very few studied directly the evaporation effects on entropy production/exergy destruction.

The first references connecting second law of thermodynamics with droplet and spray evaporation processes were published by the end of 1980's. The technical report written by Sengupta (1987) focused in theoretical studies of droplet and spray evaporation processes, with a connection between these processes and their associated irreversibilities. Som *et al.* (1990) developed probably the first study involving a second law analysis of spray evaporation available in literature. The spray evaporates in a parallel uniform hot gas flow. A thermodynamic advantageous condition is obtained at higher temperature differences between the initial spray and the gas. Next, Dash *et al.* (1991) focused in the temporal rate of entropy generated by a droplet evaporation in a convective high temperature environment. Dash e Som (1991) developed a similar analysis, but focusing in a droplet combustion process, instead of evaporation. The main irreversibilities associated to this phenomenon are attributed to the conduction of heat, the mass and heat convection of fuel vapor, and the combustion process in the gaseous phase. Later, Som e Dash (1993) developed an exergetic balance of a spray evaporation process in a hot gaseous environment. A two-phase flow model was adopted to represent the spray and applied to calculate the entropy generation. Puri (1992) studied the droplet burning issue by presenting an exergetic analysis of a fuel droplet burning in a gaseous flow. The optimal point of this process indicates a low Reynolds number which is connected with an optimal transfer number. An expression based on the Entropy Generation Minimization (EGM) method (Bejan, 2016) is presented. More recently, Som e Sharma (2002) extended their analysis for the application in a gas turbine combustor, focusing on several operation conditions in terms of irreversibility and second law efficiency.

There is a deficiency of research papers involving droplet/spray evaporation or combustion processes, even in terms of other transport phenomena subjects. Som e Datta (2008) published a review paper grouping papers about thermodynamic irreversibilities in combustion processes. It is noted the scarce number of works relating this area with the focused subjects of this thesis.

Papers focusing directly on droplet or spray combustion detail partially the entropy flows and their respective irreversibilities that can also be present in the evaporation process. Hiwase *et al.* (1998) developed an exergetic analysis to determine the exergetic efficiency of a fuel droplet combustion process at a high temperature environment. The optimal condition for the available energy involves a low Damköhler number as well as a high gas temperature. Then, Datta e Som (1999) developed an theoretical exergetic analysis of the spray combustion process with the objectives of evaluate the thermodynamic irreversibilities and the second law efficiency of this process. More recently, Pope *et al.* (2010) presented an analysis about entropy generation in the gas-phase during combustion of a methanol droplet, with special attention given to the effect of surface tension on entropy generation. Results indicate that entropy generation due to heat and mass transfer decreases as higher initial Reynolds numbers are considered. Also, the parcels of heat transfer and chemical reaction on the global entropy generation are more important than the parcel related to mass transfer.

Some works have been published recently connecting second law analyses with droplet evaporation process under different gas-phase conditions. de Lima *et al.* (2020) developed a parametric analysis through the view of second law of thermodynamics of a single-component droplet (anhydrous ethanol) evaporation in a variable temperature environment. The parameters evaporative cooling effect, entropy generation, droplet penetration and evaporation time were used to analyze the evaporation behavior. Later, Lima *et al.* (2020) compared four droplet evaporation models for a pure ethanol droplet in the same ambient as the previously mentioned work. The Abramzon-Sirignano model Abramzon e Sirignano (1989) neither underestimate nor overestimate (i.e. an intermediate behavior) the evaporation time and in-cylinder gases entropy generation during the process, since it is the only one selected which takes into account the gas film effects. The lowest specific entropy generation is found for the leanest condition, which opens a possibility to a thermodynamic optimization of the droplet evaporation process on lean conditions (PL) with interesting conditions of droplet lifetime, penetration, and evaporative cooling effect during the fuel direct-injection process

2.6.2 Second law related to fuel sprays in direct injection spark-ignition engines

Exergetic analyses of ICEs have been quite studied for some time. For example, Gallo (1990) compared the engine performance of SI engines with a carburetor and fueled with gasoline or ethanol through the application of an exergetic analysis. Calculations involved the exergetic efficiency of each engine stroke. Rakopoulos e Giakoumis (2006) reviewed several papers which focused on the application of the second law of thermodynamics in internal combustion engines. Practically all types of ICEs were covered with details about the type of modeling, heat transfer correlations used, parameters studied, experimental validation, etc.

Some researches applied exergetic analyses to pursue extra benefits of ethanol application on ICEs. Khaliq *et al.* (2011) proposed the use of wet ethanol in a conceptual HCCI engine in order to highlight the energy balance towards ethanol. The exergy destruction was presented for all components where the vaporizer (where the fuel evaporates and mixes with air) accounted for 4.39% of total exergy destroyed for the engine operation. Recently, Rufino *et al.* (2019) presented an exergetic analysis of experimental data obtained from a PFI SI engine fueled with ethanol on both partial and full load conditions. Also, the paper presents the exergy components related to an engine cycle (fuel exergy, mechanical losses, exergy flows (admission, exhaust, and cooling water), in-cylinder irreversibilities, and others), as well as the first and second-law efficiencies. Results indicate that ethanol presented lower in-cylinder exergy losses and higher efficiencies than gasohol, although due to its higher pressure peaks caused an increase at the mechanical losses as well.

In terms of DISI engines, the number of studies is quite reduced, especially involving sub-processes inside the engine cycle, such as spray evaporation and mixing before combustion. Ismail e Mehta (2012), Ismail e Mehta (2014) presented second law analyses involving the vaporization process of droplets from engine fuel sprays. Ismail e Mehta (2012) evaluated the availability destruction associated with several sub-processes before combustion, as well as the proper combustion in a heterogeneous mixture (late injection) in a DI Diesel engine. Fuel vaporization was indicated as the main cause of availability destruction before fuel ignition and that fuel injection rate was the controlling factor of this sub-process. Later, Ismail e Mehta (2014) focused specifically in predicting entropy generation due to a droplet evaporating in engine fuel sprays. Recently, Lima e Gallo (2021) developed a thermodynamic analysis of a wet ethanol spray evaporation process in a DISI engine, where a degree of knock suppression (e.g., 10x reduction) was clear when comparing DI with PFI conditions.

3 MATHEMATICAL MODELS AND METHODOLOGY

The methodology section compiles all different methodologies adopted in the development of different work topics associated with this thesis theme. All algorithms/computer codes presented in this chapter for this research were developed in MATLAB®.

The first and second sections deals with the main ideas related to the development and application of a droplet evaporation model. The purpose was to evaluate the behavior and effects of individual droplets through a Lagrangian approach and how it can impact at bigger scales, such as in spray injection and evaporation processes in a engine cylinder. This model takes into account a single-component (ethanol - Section 3.1) as well as a multi-component (wet ethanol - Section 3.2) droplet in a thermodinamically variable environment (i.e, temperature, pressure and/or volume can change during the transient process) similar to thermodynamic states of in-cylinder gases during the compression stroke of a DISI engine. Some aspects of this model were addressed through the application of the second law of thermodynamics by a differential equation for entropy balance for the gases control volume. Some equations were suggested to describe the first and second law efficiencies of a droplet evaporation process in terms of energy and exergy transfers involving the droplet.

The third section expands the study to multiple droplets by considering them as part of a fuel spray in a similar ambient as previously described in the last paragraph (Section 3.3). The phenomena of injection and evaporation of this fuel spray were accounted for the analysis and how they affected the direct fuel injection process during the compression stroke. A mathematical description of the spray is presented, as well as its division into multiple droplet classes by the application of a probability distribution function (PDF) of droplet diameters in sprays. Not only the equations applied to the droplet control volumes (Lagrangian), but also those associated with the surrounding gases (Eulerian) are presented. A second law view of this expanded model is also described. Finally, the efficiencies (first and second laws) of the droplet evaporation process are expanded to cover the spray evaporation.

The fourth section involves all aforementioned processes in a wet ethanol DISI engine simulator, where multiple aspects of the engine operation are emphasized in terms of fuel jet injection, droplet break-up, evaporation, mixing and combustion. The main effects of direct injection (benefits and possible drawbacks) possibly detected by the simulation (e.g., charge cooling and knock suppression), as well as multiple injection strategy, were explored. Moreover, some engine parameters (IMEP, thermal efficiency, engine power, knock occurrence, pollutant emission, etc.) are associated with evaporation characteristics (i.e, droplet lifetime, penetration, evaporative cooling effect) in terms of energy and entropy/exergy transfers balances. The mathematical modeling for all described sub-processes is presented and properly described.

The last section accomplish all knowledge obtained in these studies to perform a thermodynamic optimization of a direct injection of wet ethanol in a turbocharged downsized SI engine. The objective was to gather all benefits associated with direct fuel injection (evaporative cooling, knock suppression, compression ratio increase) and wet ethanol (renewable fuel, ethanol potential, increased cylinder mass, improvement of ethanol lifecycle energy) in a downsized turbocharged SI engine and apply an optimization process in terms of second law of thermodynamics. Some function objectives such as knock index number (K_{In}) are compared to multiple conditions in order to find a near state-of-the-art engine configuration with approaches the maximum potential of wet ethanol as an alternative renewable fuel. The equations involving the exergetic analysis are presented for both closed and open phases. The details about the optimization process are available in Chapter 7.

3.1 Description of a single-component droplet evaporation in thermodynamic variable environments

3.1.1 Model description and assumptions

This initial theoretical model involves a quasi-dimensional thermodynamic analysis of the injection and evaporation processes of a pure ethanol droplet in an environment with thermodynamic conditions similar to in-cylinder gases in the compression stroke of a DISI engine. This particle begins to evaporate at the moment it is injected into this system, as there are both temperature and ethanol concentration gradients in the interface between the droplet surface and the gases. Initially, the gas is at a higher temperature than the droplet as well as it does not contain any traces of the fuel in its composition. Also, there is a relative velocity between the droplet and the gases (which are at rest), thus this relative velocity stimulates further the convective heat and mass transfers that happen between the droplet and the air.

There are two control volumes in this system: one involving the droplet and following the droplet surface variation over time and a second one encompassing the gases, whose volume is also variable. The union of both control volumes represents the cylinder volume (V_t), which is constant during the simulations. Figure 3.1 presents the schematic diagram of this model:

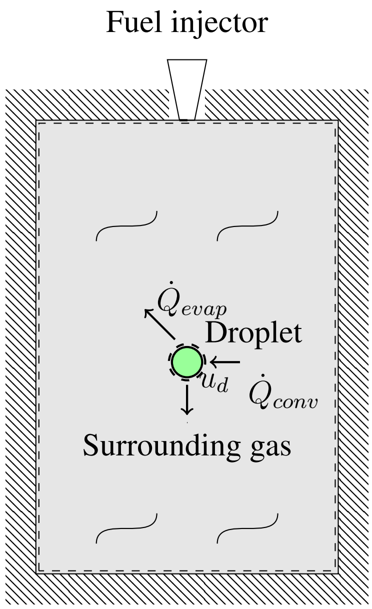

Figure 3.1 – Schematic diagram of a droplet injection and evaporation model in a DISI engine cylinder.

All hypotheses associated with the droplet vaporization theory are available in some review papers of the subject (Faeth, 1977), yet they are also presented here for the sake of completeness. The description of all adopted assumptions to this model follows next:

- The evaporation process occurs in a quasi-steady way. The main reasons are based on the following arguments: the ratio of liquid/gas density is much greater than 1 ($\rho_l/\rho_g \gg 1$), which collaborates to the quasi-steady approximation usage in the liquid phase. Also, it is taken into account that $\delta_g \ll D_d$ and $\alpha_g \gg \alpha_l$, which directs to an hypothesis of the boundary layer involving the droplet has the same properties as a steady layer for the same droplet diameter, temperature, velocity, as well as the gas temperature, thus the radial flow within the liquid phase may be neglected (Faeth, 1977);

- The droplet is the only condensed phase, attains its spherical shape during all evaporation process and does not interact with other droplets. Moreover, it is only composed by fuel and its temperature and specific mass are uniform. The thermodynamic and thermophysical properties, as well as the mass diffusivity are constant at each time step;

- The control volume (CV) which involves the liquid phase follows the droplet diameter reduction, i.e., the control surface is always adjacent and outside the droplet surface.

During evaporation, this control volume keeps adjacent and outside the droplet interface with the surrounding gases. In addition, the CV is adiabatic and rigid on all its control surfaces, with exception on its interface with the particle, where it follows the droplet size variation;

- The initial surrounding gas composition is dry air (N_2 : 78.084% O_2 : 20.946%, Ar : 0.937% and CO_2 : 0.033%) (Way, 1976);
- Due to the evaporation process occurrence in a low oxygen concentration, the oxidation of fuel components in the surrounding gas flow field was considered relatively small so that evaporation process was considered to happen without combustion (Faeth, 1977);
- Secondary droplet break-up modes (e.g., bag, stripping, etc.) are initially neglected;
- The convection effects on the evaporation are taken into account by correcting the results obtained from regular droplet evaporation theory with empirical correlations for Nusselt and Sherwood numbers (heat and mass transfer, respectively);
- The droplet vapor flows symmetrically radial (i.e. unidimensional) from the droplet to the outer surface;
- Film theory considers a spherical symmetric boundary layer between D_d and $D_d + 2\delta$, where δ accounts for the thickness of this boundary layer. Its value is chosen to correct the radial motion for heat and/or mass transfer;
- The vapor pressure of the droplet components (i.e., ethanol and water) do not get near each of their critical conditions (i.e., the gas pressure does not increase to a level which causes these conditions), which allows the application of ideal gas law. Therefore, the model treats both air and ethanol vapor as ideal gases.
- Interface: The surrounding air is insoluble in liquid anhydrous ethanol at cylinder gas conditions; The presence of other gases at the droplet surface does not interfere with the equilibrium vapor pressure of each fuel component vaporizing. Also, the mass transfer rates do not interfere the vapor pressure for a liquid temperature. Surface tension is negligible in this model, since this effect is found to be small for conditions like $D_d > 1\mu m$ and $P > 1atm$;

- Fick's law is assumed valid for droplet evaporation, due to the insolubility assumption in which the fuel vapor is the only species with a non-zero velocity. Soret and Dufour effects are ignored;
- Raoult's law is assumed valid;
- The continuum approximation is valid for droplets with diameters larger than 1 μm;
- Radial pressure gradient: The pressure is assumed constant at each time step for droplets larger than 1 μm;
- The one-third rule (Abramzon; Sirignano, 1989) is used to ponder average mixture properties between the saturated vapor coming from the droplet and the gases involving it;
- The thermodynamic properties used in the model (enthalpy, entropy, free Gibbs energy) are obtained based on NIST thermodynamic tables (Chase Jr., 1998). The droplet properties as well as the fuel vapor specific mass (ethanol and water) are calculated based on correlations from (Green; Perry, 2008), while the gas transport properties (thermal conductivity, dynamic viscosity, mass diffusivity) are obtained utilizing the open source software Cantera. The gas thermodynamic state is determined based on the one-third rule described in Eqs. 2.1-2.2 at the environment pressure to obtain T_m and $y_{i,m}$, respectively. Then the object defined in Cantera software provided the transport properties based on this mixture between the vapor composition over the droplet surface and the environment one.;
- Additional assumptions regarding the energy equation are: there is no shaft or viscous work on control surfaces. There is also no droplet rotation, non-inertial effects on this model. Thermal radiation, chemical reactions and potential energy are considered negligible;

3.1.2 Liquid phase modeling

The conservation laws on their integral forms were applied in order to develop the mathematical model to simulate the aforementioned model of section 3.1.1. The Lagrangian approach was used for the droplet equations, while the Eulerian approach was used for the gases. First, it is presented the final form of the equations for the droplet control volume. Their deduction from Reynolds Transport Theorem and the application of all associated assumptions for the properties (e.g., mass, species, velocity, energy and entropy) are provided in Appendix A to avoid great mathematical developments in the methodology sections. Therefore, Eq. 3.1 presents the Reynolds Transport Theorem (RTT) for the droplet mass conservation:

$$\frac{\mathrm{d}m_d}{\mathrm{d}t} = -\dot{m}_d \tag{3.1}$$

This equation indicates that the droplet mass loss is equal to the mass flow rate that is evaporated from the droplet surface to the surrounding gas. The droplet diameter rate is obtained by Eq. 3.2:

$$\frac{\mathrm{d}D_d}{\mathrm{d}t} = -\frac{2\dot{m}_d}{\pi\rho_d D_d^2} - \frac{\pi D_d}{3\rho_d}\frac{\mathrm{d}\rho_d}{\mathrm{d}t}, \tag{3.2}$$

where the first term on the right hand side (RHS) represents the mass variation due to evaporation, whereas the second one refers to the liquid specific mass variation due to temperature variation (i.e., droplet swelling effect).

The mass flow rate associated with the evaporation process is calculated by Eq. 3.3:

$$\dot{m}_d = \sum_{i=1}^{N_{species}} \dot{m}_i = \sum_{i=1}^{n} \pi D_{part,i} (\rho\mathcal{D})_{i,v} Sh_i \ln(1 + B_{M,i}) \tag{3.3}$$

Equation 3.3 was deduced in Appendix A for multi-component droplet evaporation cases, but for this section it is simplified for a single-component droplet. The term $D_{part,i}$ represents the concept of volume-equivalent partial diameter for each droplet component to represent its droplet ”size” in the component evaporation rate (Brenn *et al.*, 2003), as previously presented in Eq. 2.6.

The term $(\rho\mathcal{D})_{i,v}$ in Eq. 3.3 is evaluated at average mixture conditions based on the aforementioned one-third rule, while $B_{M,i}$ is the Spalding mass transfer number for each droplet component (Tong; Sirignano, 1986):

$$B_{M,i} = (y_{i,fs} - y_{i,fg})/(1 - y_{i,fg}) \tag{3.4}$$

where $y_{i,fs}$ is the mass fraction of the ith droplet component on the vapor droplet surface and $y_{i,fg}$ is the mass fraction of the ith droplet component on surrounding gases. Eqs. 2.6-3.4 reduce to $D_{part,i} = D_d$ and $B_{M,i} = B_M = (y_{fs} - y_{fg})/(1 - y_{fg})$ for this model.

The droplet momentum conservation equation is also obtained from the RTT. The deduction to its final form is based on (Abramzon; Sirignano, 1989; Crowe *et al.*, 2012) and on the aforementioned assumptions. Finally it is obtained Eq. 3.5:

$$\frac{\mathrm{d}u_d}{\mathrm{d}t} = \frac{3}{4}\frac{C_d}{D_d}\frac{\rho_s}{\rho_d}|u_g - u_d|(u_g - u_d) \tag{3.5}$$

The drag coefficient correlation takes into account the evaporation effects and it is calculated by Eq. 3.6 (Abramzon; Sirignano, 1989):

$$C_d = \frac{12.69}{Re_m^{2/3}(1 + B_M)} \tag{3.6}$$

The conservation of energy for the droplet is obtained by applying the assumptions and isolating the temperature differential, as presented in Appendix A. The final form is presented by Eq. 3.7:

$$\frac{\mathrm{d}T_d}{\mathrm{d}t} = \frac{\dot{Q}_{d,conv} - \dot{Q}_{d,evap}}{m_d c_d}, \tag{3.7}$$

where $\dot{Q}_{d,evap} = \dot{m}_d \Delta h_v$ and $\dot{Q}_{d,conv} = A_d h_{conv}(T_\infty - T_d)$. h_{conv} is the convection heat transfer coefficient, which is obtained through the correlations presented later in Sec. 3.1.3. The droplet entropy balance is also obtained based on RTT (Bejan, 2006). The T_s term represents the surface temperature where the heat transfer happens, which in this case is at the surface droplet temperature T_d. Therefore, based on all presented assumptions, the final form is shown by Eq. 3.8:

$$\dot{\sigma}_d = m_d \left.\frac{\mathrm{d}s}{\mathrm{d}t}\right|_d + \dot{m}_d \Delta s_v - \frac{\dot{Q}_{d,conv}}{T_d}, \tag{3.8}$$

where $\Delta s_v = \Delta h_v / T_d$, since the vapor entropy change is in the saturation phase change. The control volume entropy variation, as the droplet is liquid and incompressible, is calculated by Eq. 3.9:

$$\left.\frac{\mathrm{d}s}{\mathrm{d}t}\right|_{droplet} = \frac{c_d}{T_d}\frac{\mathrm{d}T_d}{\mathrm{d}t} \tag{3.9}$$

Comparing Eqs. 3.7 and 3.8, it is noticed that $\dot{\sigma}_d = 0$ for this control volume. This means that the evaporation process is considered reversible for this model.

3.1.3 Heat and mass transfer correlations for droplet heating & evaporation

The presented droplet evaporation model needs the inputs for experimental correlations associated with the phenomena in order to work properly (Faeth, 1977). Some correlations usually presented in specific literature are presented here for the sake of completeness of the model. The classical Ranz-Marshall correlation is used to calculate both Nusselt and Sherwood numbers for the droplet evaporation process (Ranz; Marshall Jr., 1952):

$$Nu = 2 + 0.6(Re_m^{1/2} Pr_m^{1/3}) \tag{3.10}$$

$$Sh = 2 + 0.6(Re_m^{1/2} Sc_m^{1/3}), \tag{3.11}$$

where Reynolds, Prandtl and Schmidt numbers are $Re_m = (\rho_m |u_d - u_g| D_d)/(\mu_m)$, $Pr_m = (c_{p,m}\mu_m)/(k_m)$, and $Sc_m = (\mu_m)/(\rho_m \mathcal{D}_m)$, respectively. The Frossling correlation (Abramzon; Sirignano, 1989) is another one applied to represent droplet evaporation:

$$Nu = 2 + 0.552(Re_m^{1/2} Pr_m^{1/3}) \tag{3.12}$$

$$Sh = 2 + 0.552(Re_m^{1/2} Sc_m^{1/3}) \tag{3.13}$$

These two different correlations tend to overestimate the heat and mass transfers at low Reynolds numbers, with a special issue of enhancing significantly the mass and heat exchange at $Re_m \approxeq 0$. The Clift correlation (Abramzon; Sirignano, 1989) considers the evaporation effects directly in Nusselt and Sherwood evaluations and also avoids the infinity-result:

$$Nu = 1 + (1 + Re_m Pr_m)^{1/3} f(Re_m) \tag{3.14}$$

$$Sh = 1 + (1 + Re_m Sc_m)^{1/3} f(Re_m), \tag{3.15}$$

where $f_{Re_m} = 1 (Re_m \leq 1)$ and $f_{Re_m} = Re_m^{0.077} (Re_m \leq 400)$.

3.1.4 Gas phase modeling

The conservation laws on their integral forms were also applied to the surrounding gases, just as in the case of the droplet control volume. Only mass, energy and entropy equations are used for the gases, since the model consider that the gas is quiescent (Turns, 2012; Kuo, 2005). Therefore, based on aforementioned assumptions and on a similar deduction available in Appendix B, the gas mass conservation provides Eq. 3.16:

$$\frac{\mathrm{d}m_g}{\mathrm{d}t} = \dot{m}_d \tag{3.16}$$

Following the Appendix B, the energy conservation provides Eq. 3.17, which represents the gas temperature temporal rate:

$$\frac{\mathrm{d}T_g}{\mathrm{d}t} = \frac{\dot{m}_d(h_v - u_g) - \pi D_d^2 h_{conv}(T_g - T_d) + P_g \frac{\mathrm{d}\rlap{-}V_d}{\mathrm{d}t}}{m_g c_{v,g}} \tag{3.17}$$

The pressure rate is obtained by the ideal gas equation of state:

$$\begin{aligned} \frac{\mathrm{d}P_g}{\mathrm{d}t} = \frac{1}{\rlap{-}V_{system} - \frac{R_g \rlap{-}V_g}{c_{p,g}} - \rlap{-}V_d} \Bigg\{ R_g T_g \frac{\mathrm{d}m_g}{\mathrm{d}t} + \frac{R_g}{c_{p,g}} \Big[\dot{m}_d(h_v - h_g) - \pi D_d^2 h_{conv}(T_g - T_d) \\ + P_g \frac{\mathrm{d}\rlap{-}V_d}{\mathrm{d}t} \Big] - P_g \left(\frac{\mathrm{d}\rlap{-}V_{system}}{\mathrm{d}t} - \frac{\mathrm{d}\rlap{-}V_d}{\mathrm{d}t} \right) \Bigg\} \end{aligned} \tag{3.18}$$

The entropy balance provides Eq. 3.19, which provides the entropy generation rate on the gas control volume:

$$\dot{\sigma}_g = \dot{m}_d(s_g - s_v) + m_g \frac{\mathrm{d}s_g}{\mathrm{d}t} + \pi D_d^2 h_{conv} \frac{T_g - T_d}{T_d}, \tag{3.19}$$

where s_g is the gas entropy, s_v is the vapor entropy that is crossing the control surface.

3.1.5 Droplet evaporation models

The droplet evaporation models used in this thesis are standard ones, which allows their application with the hypotheses previously presented in this chapter. Within this context, it was selected four evaporation models for this research: the classical evaporation model (CEM), the modified classical evaporation model, the non-equilibrium model, and the Abramzon-Sirignano model. Pinheiro (2018) described these models in terms of their historic importance, assumptions and extensions, therefore only the main equations are presented here for the sake of completeness. The CEM model applies the aforementioned Eqs. 3.1-3.4 and 3.5-3.7. Also, a pair of the Nusselt and Sherwood correlations (e.g., 3.10-3.15) are required for this model to work properly.

The modified classical evaporation model applies the same equations cited in CEM model as well as an expression for a correction factor G required on the classical model, in order to take into account the existence of a gas-liquid film around the droplet (Pinheiro, 2018). Equations (3.20-3.21) describe this correction factor and how it modifies the droplet energy balance:

$$G = \frac{\beta}{e^{\beta} - 1}, \tag{3.20}$$

$$Q^{*}_{d,conv} = GQ_{d,conv} = G\pi D_d^2 h_{conv}(T_g - T_d), \tag{3.21}$$

where $\beta = -\frac{\dot{m}c_{p,m}}{2\pi k_m D_d}$ is a non-dimensional evaporation parameter. The corrected convective heat transfer $Q^{*}_{d,conv}$ substitutes its similar term $Q_{d,conv}$ on Eq. 3.7.

The droplet evaporation non-equilibrium model assumes some non-equilibrium effects on the vapor molar fraction of each fuel component evaporating, thus a deviation term was suggested to employ these effects on these molar fractions (Pinheiro, 2018). Equation 3.22 represents this deviation term based on the calculation of the molar vapor fraction from the partial pressure-total pressure ratio:

$$x_{fs,neq} = x_{fs,eq} - \frac{2L_k\beta}{D_d}, \tag{3.22}$$

where $x_{fs,eq} = P_{fs}/P_g$. L_k is the Knudsen layer thickness and it is obtained by Eq. 3.23:

$$L_k = \frac{\mu_m\sqrt{2\pi T_d R_f}}{\alpha_e Sc_m Pr_m}, \tag{3.23}$$

where α_e is the molecular accommodation coefficient and it is usually approximated to 1.

As presented by Abramzon e Sirignano (1989), the film theory considers that the diffusive effects associated with heat and/or mass transfer resistances are present in only a thin shell film around a droplet with thicknesses δ_T and/or δ_M. These thicknesses are calculated by Eqs. 3.24-3.25:

$$\delta_{T,0} = \frac{D_d}{Nu_0 - 2} \tag{3.24}$$

$$\delta_{M,0} = \frac{D_d}{Sh_0 - 2}, \tag{3.25}$$

where Nu_0 and Sh_0 are the Sherwood and Nusselt numbers obtained from correlations, such as the presented ones in the last sub-section. These thicknesses are valid for non-evaporating droplets, although they can be corrected to take into account the Stefan flow present in droplet evaporation processes. The correction factors F_M and F_T are defined by Eqs. 3.26-3.27, respectively:

$$F_T = \frac{\delta_T}{\delta_{T,0}} \tag{3.26}$$

$$F_M = \frac{\delta_M}{\delta_{M,0}} \tag{3.27}$$

These correction factors are used to obtain corrected Sherwood and Nusselt parameters Sh^* and Nu^*:

$$Nu^* = 2 + \frac{Nu_0 - 2}{F_T} \tag{3.28}$$

$$Sh^* = 2 + \frac{Sh_0 - 2}{F_M} \tag{3.29}$$

The correction parameters are $F_T = (1+B_T)\frac{\ln(1+B_T)}{B_T}$ and $F_M = (1+B_M)\frac{\ln(1+B_M)}{B_M}$, which are correlations obtained from experimental measurements of a laminar boundary flow over an evaporating wedge (Abramzon; Sirignano, 1989). The Spalding heat transfer number is $B_T = (c_{p,f}(T_g - T_d))/(\Delta h_v + \dot{Q}_d/\dot{m}_d)$ and the heat transfer penetrating into the droplet is $\dot{Q}_{d,sens} = \dot{Q}_{d,conv} - \dot{Q}_{d,evap}$. The complete algorithm to apply the film theory on droplet evaporation models is didactically presented in Abramzon e Sirignano (1989).

3.1.6 Liquid-gas interface equations

The phase-equilibrium between liquid and gas phases on the droplet surface is assumed in the presented model. The molar fraction of component i on the droplet surface $x_{i,fs}$ is given by the Raoult law:

$$x_{i,fs} = \frac{P_{i,f}}{P_g}, \tag{3.30}$$

where $P_{i,f}$ is the partial pressure of the ith component on the droplet surface and P_g is the gas pressure. Both ethanol and water vapor pressure correlations are obtained from Green e Perry

(2008), whose constants are available in Table 3.1. The general vapor pressure correlation has the following form (Eq. 3.31):

$$P_{i,f} = \exp\left(C_1 + \frac{C_2}{T_d} + C_3 \ln(T_d) + C_4 T_d^{C_5}\right) \tag{3.31}$$

Table 3.1 – Vapor pressure constants for Eq. 3.31 (Green; Perry, 2008).

	Ethanol	Water
C_1	73.649	273.304
C_2	-7258.2	-7122.3
C_3	-7.3037	-7.1424
C_4	$4.1653\text{x}10^{-6}$	$2.8853\text{x}10^{-6}$
C_5	2	2

The conversion between mass and molar fractions on the droplet surface is given by Eq. 3.32:

$$y_{i,fs} = x_{i,fs}\frac{M_i}{M_{av,s}}, \tag{3.32}$$

where M_i is the molar mass of the ith droplet component and $M_{av,s}$ is the average molar mass of the gases on the droplet surface.

3.1.7 Algorithm procedure

In order to solve the presented set of equations and investigate the droplet evaporation phenomenon, a 4th order Runge-Kutta (RK) ordinary differential equation (ODE) solver was implemented. The solution procedure to develop the simulations is direct and briefly commented. First, the droplet evaporation function is presented (Fig. 3.2):

Basically, this function encompasses the following steps:

1. Initially, some simulation parameters are required as inputs, like the ones involved with the droplet $(m_{d,i}, D_{d,i}, u_{d,i}, T_{d,i}, y_{H_2O})$, with the environment $(T_{g,i}$, $P_{g,i}$ and $m_{g,i}$, besides the constants for the correlations for liquid component properties;

2. Next, the function calculates the liquid component properties $(P_f, \rho_l, c_l, k_l, \mu_l$ and $\Delta h_v)$, besides the molar and mass fractions on droplet surface (Appendix C and Eqs. 3.30-3.32);

3. Then the Spalding mass transfer number and the evaporation rate of the fuel component are evaluated (Eqs. 3.3 - 3.4);

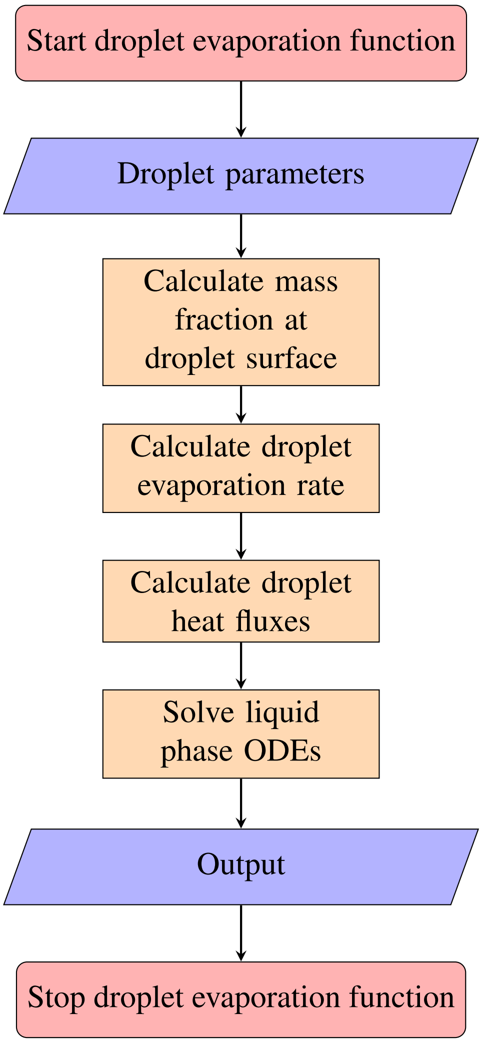

Figure 3.2 – Flowchart of the droplet evaporation function.

4. Later, there is the application of the one-third rule to obtain the physical properties of the gas mixture (ρ_m, μ_m, k_m, $c_{p,m}$, and $D_{j,v}$) to calculate the dimensionless numbers of the mixture (Re_m, Le_m, Pr_m, Sc_m, Nu, and Sh). Also, it is required to evaluate Δh_v and $h_{conv,d}$ to obtain the droplet heat fluxes ($\dot{Q}_{conv}, \dot{Q}_{evap}$) (Eqs. 3.20 - 3.29, 3.10 -3.15);

5. Finally, the function applies a 4th order RK solver to solve the droplet differential equations (mass, diameter, velocity, and temperature) (Eqs. 3.1,3.2, 3.5 - 3.7);

6. The desired outputs are selected and there is the end of the function;

The droplet evaporation function is associated with the algorithm which describes the pure ethanol droplet evaporation modeling, as presented by Fig. 3.3:

Next some brief comments about this algorithm are presented:

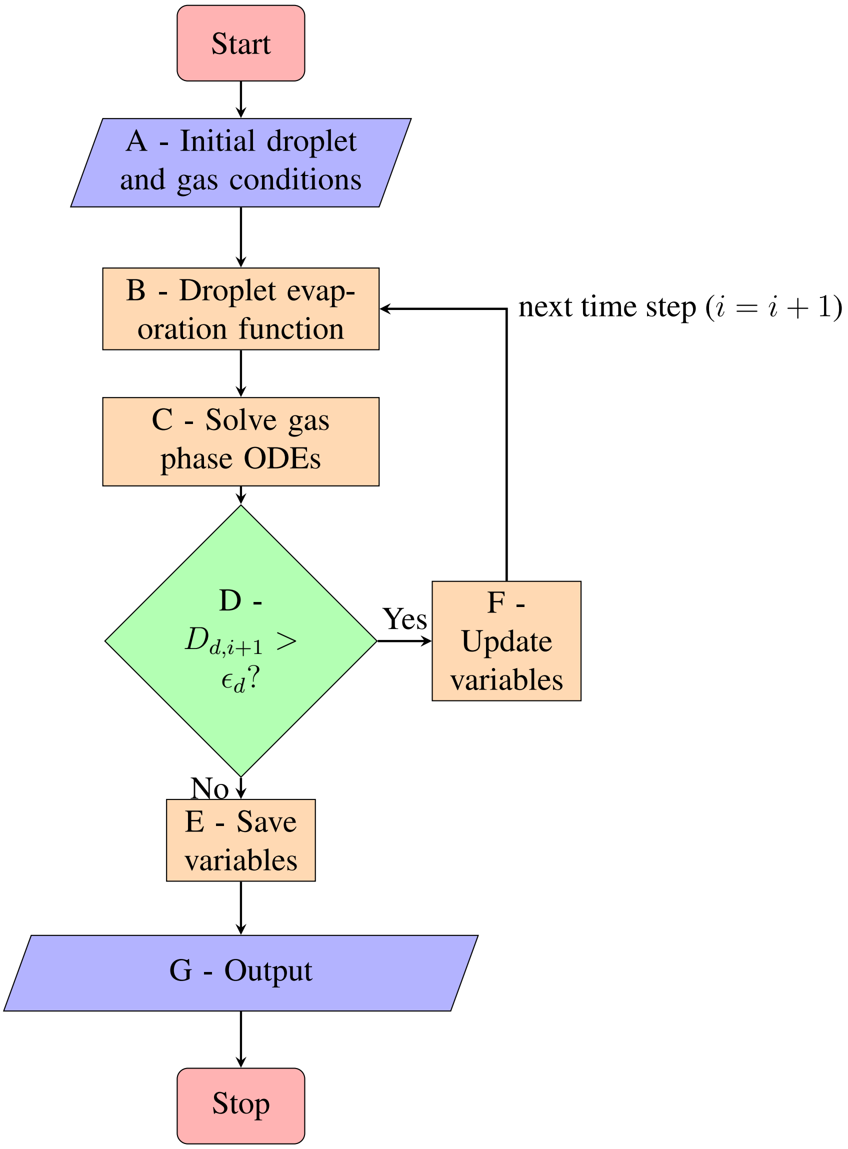

Figure 3.3 – Flowchart of the single-component droplet evaporation algorithm in a thermodynamically variable environment based on section 4.1.1.

1. Step A involves the input of initial parameters, droplet and gas compositions, cylinder geometry, and constants for the property correlations of the fuel components (Appendix C) ($m_{d,i}, D_{d,i}, u_{d,i}, T_{d,i}, T_{g,i}, P_{g,i}$);
2. B is the droplet evaporation function;
3. Step C applies the same numerical method to solve the gas-phase differential equations (mass, temperature, pressure, entropy generation) (Eqs. 3.16-3.19);
4. Step D checks if the droplet criterion is respected, i.e., if the new droplet diameter is higher than $1\mu m$, which is the value adopted to respect the continuum limit;

5. Step F updates the droplet and gas variables for the next time step and returns to step B;
6. Step E saves the final values for the variables of interest;
7. End of the simulation.

3.2 Description of a wet ethanol droplet evaporation in thermodinamically variable environments

3.2.1 Model description and assumptions

The second model presented in this chapter is an extension of the one presented in details in Section 3.1.1. The modifications are related to the droplet initial composition, which now takes into account wet ethanol (i.e., a liquid mixture of ethanol-water in different conditions). A multi-component droplet evaporation modifies significantly the behavior of mass, energy and entropy exchanges between the two control volumes in question, therefore it requires some analysis about the evaporation behavior for direct fuel injection in engines.

Besides the aforementioned assumptions presented in Section 3.1.1, some additional ones are necessary due to the fact of a multi-component droplet is taken into account:

- The droplet composition is considered homogeneous within the droplet, i.e., there are no concentration spatial gradients (infinite diffusivity coefficient).
- Eqs. 3.3-3.4 (Brenn *et al.*, 2003) are also valid under simulated conditions;
- Raoult's law for ideal liquid mixtures is assumed valid;

3.2.2 Liquid phase equations

Based on all aforementioned assumptions, the liquid phase droplet transport equations were developed. These are the same as presented before 3.1-3.9. The Clift correlations 3.14-3.15 The Abramzon-Sirignano model was selected to represent the droplet evaporation modeling (Eqs. 3.24-3.29).

3.2.3 Gas phase equations

A finite amount of gases involving the droplet is assumed in this model, in order to evaluate both evaporative cooling effect and entropy generation on in-cylinder gases caused by droplet evaporation. The mass of the gas is established as a function of the air-fuel ratio. The gas mass conservation is the same as Eq. 3.16, however the energy, pressure and entropy differential equations have some additions on their appearance. Some additional terms are added in the gas phase conservation equations to turn the model more complete. For instance, the cylinder volume variation is now taken into account during the compression stroke. The cylinder wall-gas heat transfer is also considered. The mass fraction variation from the enthalpy chain rule in Appendix B is also present in the energy balance. Finally, the enthalpy form of the energy balance is used as well. Following the same procedure as presented in Appendix B, the gas temperature differential equation is represented by Eq. 3.33:

$$\frac{\mathrm{d}T_g}{\mathrm{d}t} = \frac{1}{m_g c_{p,g}} \left[\dot{m}_d (h_v - h_g) - m_g \sum_{j=1}^{N_{species}} \left(h_{j,g} \frac{\mathrm{d}y_{j,g}}{\mathrm{d}t} \right) - \pi D_d^2 h_{conv} (T_g - T_d) \right. \\ \left. + \rlap{-}V_g \frac{\mathrm{d}P_g}{\mathrm{d}t} + P_g \frac{\mathrm{d}\rlap{-}V_d}{\mathrm{d}t} + \dot{Q}_{g,wall} \right], \quad (3.33)$$

while the pressure rate is obtained through the ideal gas equation of state differential form (Eq. 3.34):

$$\frac{\mathrm{d}P_g}{\mathrm{d}t} = \frac{1}{\rlap{-}V - \frac{R_g \rlap{-}V_g}{c_{p,g}} - \rlap{-}V_d} \left\{ R_g T_g \frac{\mathrm{d}m_g}{\mathrm{d}t} + \frac{R_g}{c_{p,g}} \left[\dot{m}_d (h_v - h_g) - m_g \sum_{j=1}^{N_{species}} \left(h_{j,g} \frac{\mathrm{d}y_{j,g}}{\mathrm{d}t} \right) \right. \right. \\ \left. \left. - \pi D_d^2 h_{conv} (T_g - T_d) + P_g \frac{\mathrm{d}\rlap{-}V_d}{\mathrm{d}t} + \dot{Q}_{g,wall} \right] - P_g \left(\frac{\mathrm{d}\rlap{-}V_{system}}{\mathrm{d}t} - \frac{\mathrm{d}\rlap{-}V_d}{\mathrm{d}t} \right) \right\} \quad (3.34)$$

The second law of thermodynamics provides the entropy generation rate (Eq. 3.35):

$$\dot{\sigma}_g = \dot{m}_d (s_g - s_v) + m_g \frac{\mathrm{d}s_g}{\mathrm{d}t} + \pi D_d^2 h_{conv} \frac{T_g - T_d}{T_d} - \frac{\dot{Q}_{g,wall}}{T_{wall}} \quad (3.35)$$

3.2.4 Droplet evaporation energetic and exergetic efficiencies

In order to evaluate how well the evaporation process of a fuel droplet occurs during its injection in a compression stroke of an engine, the author suggests a definition for this process in terms of the first and second laws of thermodynamics. The suggested energetic efficiency equation for the droplet evaporation process in this model is presented by Eq. 3.36, where the desired effect is the total amount of energy-related to the heat of vaporization from the droplet components during the evaporation process and the main source of energy is cumulative energy associated with the convective heat transfer from surrounding gases to the droplet:

$$\eta_{1st,d} = \frac{\int_0^{t_{evap}} \dot{m}_d \Delta h_v dt}{\int_0^{t_{evap}} \dot{Q}_{conv} dt} \tag{3.36}$$

The exergetic efficiency to droplet evaporation is presented by Eq. 3.37:

$$\eta_{2nd,d} = \frac{\int_0^{t_{evap}} \dot{m}_d (\Delta h_v - T_0 \Delta s_v) dt}{\int_0^{t_{evap}} \dot{Q}_{conv} \left(1 - \frac{T_0}{T_d}\right) dt} = \frac{\int_0^{t_{evap}} \dot{m}_d \Delta h_v \left(1 - \frac{T_0}{T_d}\right) dt}{\int_0^{t_{evap}} \dot{Q}_{conv} \left(1 - \frac{T_0}{T_d}\right) dt}, \tag{3.37}$$

where $T_0 = 293K$ is the dead-state temperature and Δs_v is the vaporization entropy of droplet components.

3.2.5 Multicomponent liquid-gas interface equations

In order to take into account the multicomponent composition of the droplet, Eq. 3.3 provides the total droplet evaporation rate obtained from the sum of each component. The Spalding mass transfer number for each component ($B_{M,i}$) is given by Eq. 3.4 as presented in Section 3.1.2 (Tong; Sirignano, 1986). Moreover, a modified Raoult law is required to deal with liquid mixtures such as the case of wet ethanol droplets. Thus, the molar fraction of component i on the droplet surface $x_{i,fs}$ is given by this Raoult law for ideal liquid mixtures:

$$x_{i,fs} = x_{i,ls} \frac{P_{i,f}}{P_g}, \tag{3.38}$$

where $x_{i,ls}$ is the liquid molar fraction of component i on the droplet. Equations 3.31 and 3.32 are also applicable under described conditions.

3.2.6 Algorithm procedure

In order to solve the presented set of equations and investigate the droplet evaporation phenomenon, an implicit trapezoidal ordinary differential equation (ODE) solver was implemented. The idea of using an implicit method was to cover possible multi-component evaporation complexities that could lead to some stiffness in the ODE system. The solution procedure to develop the simulations is direct and briefly commented, since it follows a very similar sequence as the one presented in Section 3.1.7. Some modifications are required in order to consider the multicomponent effects on the droplet evaporation. The gas-phase solution is very similar to the latest one presented, with differences associated to the cylinder volume geometry, the molar fraction rate necessary for the energy balance and the evaluation of

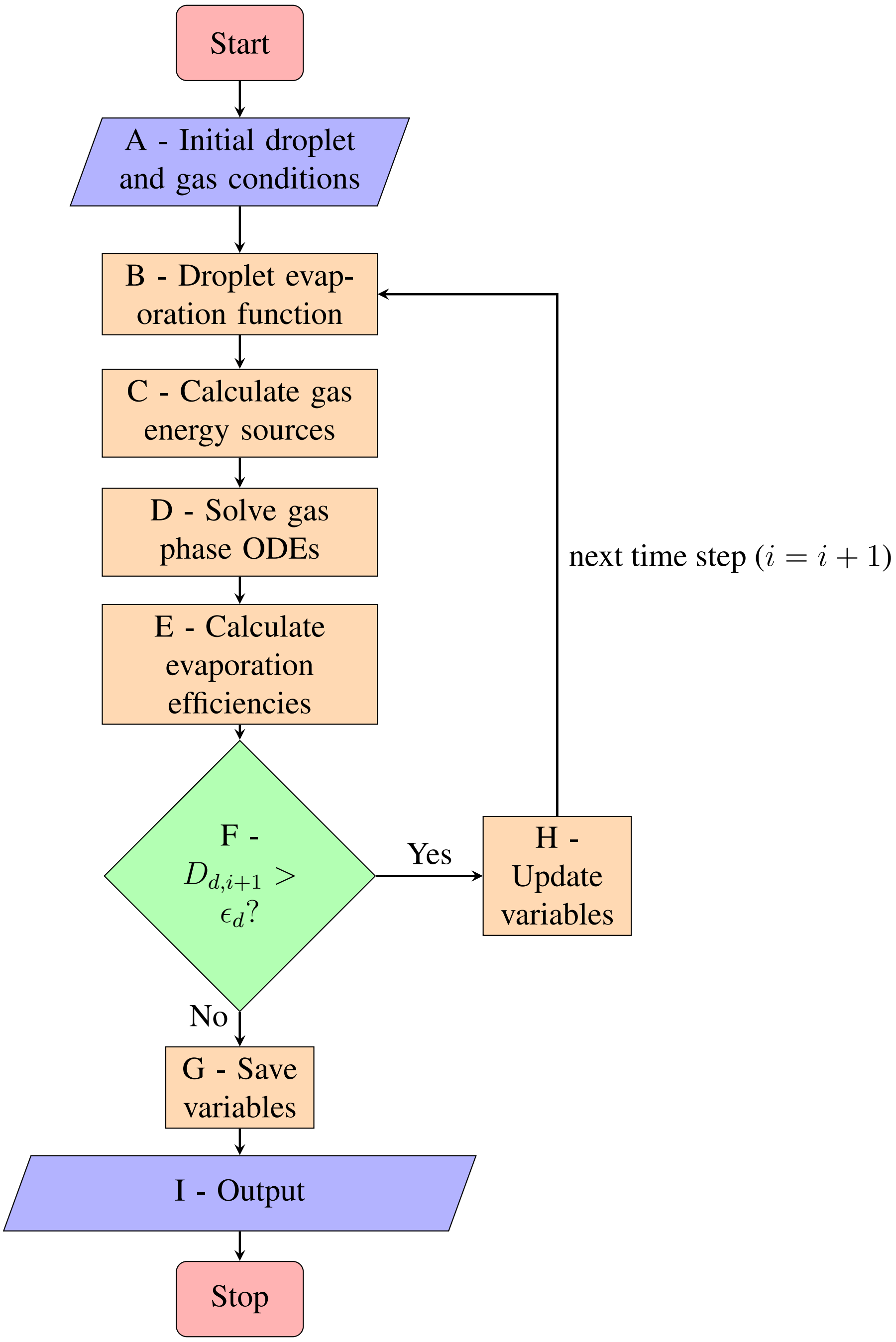

Figure 3.4 – Flowchart of the wet ethanol droplet evaporation algorithm in a thermodynamically variable environment based on section 4.3.1.

the droplet evaporation efficiencies. Thus, the algorithm which describes the multi-component droplet evaporation modeling is presented by Fig. 3.4:

Next some brief comments about this algorithm are presented:

1. Step A here requires the same procedure as presented in Section 3.1.7, besides engine cylinder kinematics (Appendix C);

2. The difference on the droplet evaporation function (Step B) to a multi-component case is the weighting between the liquid properties based on the current liquid composition (Appendix C and Eqs. 3.3 - 3.4, 3.31, 3.32, 3.38);
3. Step C evaluates all energy transfers associated with the gas control volume, such as $\dot{Q}_{conv,cyl}$, h_v, $\mathrm{d}y_g/\,\mathrm{d}t$, etc;
4. Step D applies the same numerical method to solve the gas-phase differential equations (mass, species, temperature, pressure, entropy generation) (Eqs. 3.16, 3.33 - 3.35);
5. Step E calculates the energetic and exergetic droplet evaporation efficiencies for this time step ($\eta_{1st,d}, \eta_{2nd,d}$) (Eqs. 3.36 - 3.37);
6. Step F checks if the droplet criterion is respected, i.e., if the new droplet diameter is higher than $1\mu m$;
7. Step G updates the droplet and gas variables for the next time step and returns to step B;
8. Step H saves the final values for the variables of interest;
9. End of the simulation;

3.3 Wet-ethanol spray direct injection and evaporation during the compression stroke of a DISI engine

3.3.1 Model description and assumptions

The third step to the final model of this thesis involves the direct injection of wet ethanol as a fuel during the compression stroke of a DISI engine. The phenomena of fuel injection, droplet spray evaporation and mixing and consequently combustion are evaluated based on all modeling presented in this chapter so far.

The fuel spray represents a key role in this model: it is formed from the liquid jet from the fuel injector which atomizes after the sequence of processes of droplet break-up and coalescence inside the cylinder gas.

This model is quasi-dimensional and at the beginning of the simulation the compression stroke initiates until the initial fuel injection moment. With the fuel spray injection, evaporation and convective heat transfer initiate between the droplet classes and the gases. The procedure continues until the end of the compression stroke or the spray evaporates completely.

Thus, the main idea of this model is to evaluate the wet ethanol droplet/spray evaporation process on in-cylinder gases in terms of the second law of thermodynamics. Focus is given to the evaporative cooling effect caused by the liquid injection, variation of water content in the compression stroke and also to suggested spray evaporation efficiencies (energetic and exergetic) during the simulation. The in-cylinder gas entropy generation is used to evaluate the degree of irreversibility caused by direct fuel injection during the compression stroke.

All assumptions presented on Sections 3.1.7 and 3.2.6 are valid for this model. Also, some additional hypotheses are necessary to turn the model feasible and are presented next:

- Each representative fuel spray layer is composed by a number of droplet classes whose sizes/diameters are obtained from a probability density function (PDF) developed for sprays;
- Phenomena such as droplet break-up and coalescence, as well as droplet interactions are not taken into account in this model;
- The liquid phase (i.e, droplet spray) only interacts with the unburned zone;

The schematic diagram for this model is presented by Fig. 3.5:

3.3.2 Control volume description

In order to predict the thermodynamic behavior of a direct injection spark-ignition engine during the processes of fuel injection and evaporation, this model takes into account a variable number of control volumes inside the cylinder engine, to represent the different zones and/or phases currently in the engine cylinder. The quantity of control volumes for this model is divided as:

- One control volume for the unburned gases;
- One control volume for the burned gases;
- $N_{CV,droplets}$ control volumes representing all droplet classes associated with the fuel spray.

The concept of unburned and burned gases zones is derived from the two-zone thermodynamic model for SI engines, such as detailed in Rufino (2020). In addition to this approach, a liquid fuel spray is present in the engine cylinder, representing the liquid phase

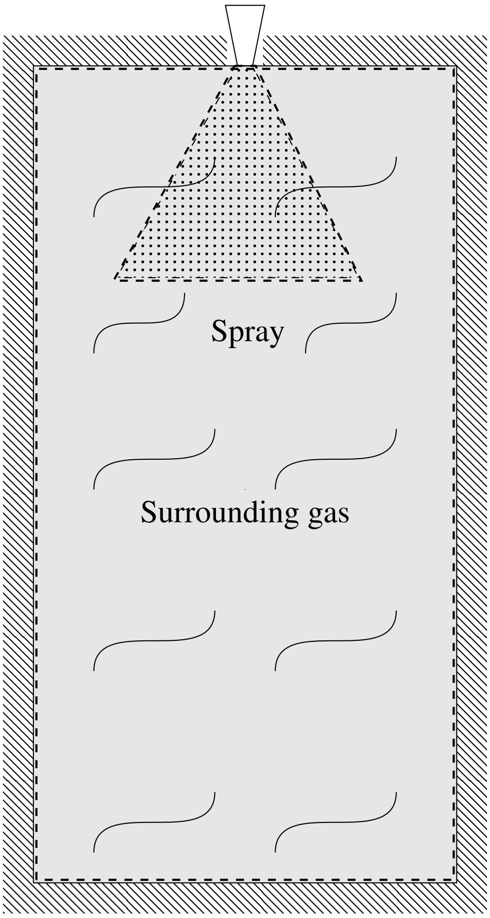

Figure 3.5 – Schematic diagram of a spray injection and evaporation model in a DISI engine cylinder.

from the direct fuel injection. These liquid control volumes involve each droplet available in the spray, such as the discussed models of Sections 3.1 and 3.2. During each time-step at the injection moment, a spray layer arises inside the cylinder from the jet breakup. Each layer is composed by $N_{classes}$ droplet classes, which basically is a representation of a set of droplets with the same droplet diameter.

The mean diameter is applied as a parameter of the selected PDF, which then provides the number of droplets for each droplet size and the droplet diameter range for this specific spray layer. As the simulation goes on, an additional spray layer is created for each time-step until the fuel injection ends. Therefore, a number of spray layers N_{layers} are created during the injection duration, where each of these layers contain $N_{classes}$ different droplet diameters. At the end of fuel injection, the major system contains $N_{CV,droplets}$ different droplet control volumes, such as presented by Eq. 3.39:

$$N_{CV,droplets} = N_{layers} N_{classes} \tag{3.39}$$

Hence, the simulation takes into account $N_{CV,droplets} + 2$ control volumes. As the simulation continues, each droplet class which evaporated completely is removed from the calculations, causing a reduction on the total number of control volumes for the next time-step.

3.3.3 Fuel injection, spray, and droplets relationship

The liquid fuel injection process is detailed in this section, since it has much importance for a DISI engine cycle. Based on previously established injection parameters (e.g., D_{nozzle}, N_{Nozzle}, P_{inj}, θ_{inj}, $m_{f,inj}$, $N_{classes}$, etc.), a certain amount of fuel volume is injected into the engine cylinder, where interactions start happening between the liquid jet and the gases. This spray layer volume is the same as the amount of fuel volume injected during each time-step. In order to simulate the droplet formation process by converting the fuel jet into a fuel spray, this spray layer bulk volume is divided into $N_{classes}$ different droplet diameters with $N_{droplet,class}$ droplets for each size. A Sauter Mean Diameter (SMD) correlation is used to represent the mean diameter of this layer volume and therefore makes the connection between the liquid jet and the spray.

The number of droplets on each class is therefore obtained from the relationship between the amount of fuel volume injected by the fuel nozzle during the ith time-step and this mean droplet diameter. The mass rate of fuel injected during this time step is (Eq. 3.40):

$$\dot{m}_{nozzle} = \rho_f V_{jet} A_{nozzle}, \tag{3.40}$$

where $A_{nozzle} = N_{nozzle} \pi D_{nozzle}^2/4$, $V_{jet} = C_{d,nozzle}\sqrt{\frac{P_{inj}-P_g}{\rho_f}}$ is the mean jet velocity obtained from Bernoulli equation. The volume rate is therefore $\dot{\forall}_{nozzle} = \dot{m}_{nozzle}/\rho_f$ and it is connected with the initial mean droplet diameter, which is assumed as the Sauter Mean Diameter (D_{SMD}) obtained from the Hiroyasu and Arai SMD correlation for Diesel engines (Santos; Moyne, 2011):

$$D_{SMD} = \begin{cases} D_{SMD,LS} = 4.12 D_{nozzle} Re_l^{0.12} We_l^{-0.75} {\frac{\mu_f}{\mu_g}}^{0.54} \left(\frac{\rho_f}{\rho_g}\right)^{0.18} \\ D_{SMD,HS} = 0.38 D_{nozzle} Re_l^{0.25} We_l^{-0.32} {\frac{\mu_f}{\mu_g}}^{0.37} \left(\frac{\rho_f}{\rho_g}\right)^{-0.47} \end{cases} \tag{3.41}$$

where $D_{SMD} = D_{SMD,LS}$ if $D_{SMD,LS} \geq D_{SMD,HS}$, otherwise $D_{SMD} = D_{SMD,HS}$. $Re_l = (\rho_f V_{jet} D_{inj})(\mu_f)$ is the liquid Reynolds number, $We_l = (\rho_f V_{jet}^2 D_{inj})/(\sigma_f)$ is the liquid Weber number, and $We_g = (\rho_g V_{jet}^2 D_{inj})/(\sigma_f)$ is the gas Weber number related to the injection and atomization processes. Hence, the total number of droplets for the ith spray layer is:

$$N_{droplet,i} = \frac{6}{\pi} \frac{N_{nozzle} \dot{V}_{nozzle} \, \mathrm{d}t_{step}}{D_{SMD}^3} \tag{3.42}$$

This number of droplets is divided for each droplet class based on the Rosin-Rammler probability distribution function (PDF) commonly used to droplet sprays and particle phenomena (Alderliesten, 2013). Since droplet coalescence and breakup are not considered in our model, then the number of droplets for each class in each spray layer remains the same during their lifetime. The Rosin-Rammler PDF was selected to represent the fuel spray (Eq. 3.43) (Alderliesten, 2013):

$$f_0(D) = \frac{nD^{n-4}}{D'^{(n-3)}\Gamma\left(1 - \frac{3}{n}\right)} \exp\left[-\left(\frac{D}{D'}\right)^n\right], \tag{3.43}$$

where n represents the PDF shape/spread parameter, D is the droplet diameter class, $D^{'} \approxeq 1.1935 D_{SMD}$ is the location parameter for the function (i.e, droplet size at a volume fraction of 0.368), and $\Gamma(x)$ is the statistical function Gamma. Based on the relative values of $f_0(D)$ for the whole droplet class range ($N_{classes}$) and the total number of droplets $N_{droplet,i}$, the proper amount of droplets $N_{droplet,class}$ is discovered for each droplet class:

$$N_{droplet,class} = N_{droplet,i} f_0(D_{class}) \tag{3.44}$$

These values are truncated to provide an integer number of droplet which respects the correct amount of injected volume on this class. To sum up the aforementioned steps, a flowchart of the fuel injection function is presented here by Fig 3.6:

3.3.4 Droplet & Spray equations

As mentioned earlier, this model takes into account several zones, in which only the unburned zone interacts directly with the liquid phase. This section focuses on the direct fuel injection, evaporation and mixing processes, which happen before the combustion process, therefore the burned zone will only be taken into account on the next section of this chapter.

The Reynolds Transport Theorem is used to develop the Lagrangian conservation equations for the droplets. The modeling for each droplet is equal to the one developed in Section 3.2, with Eqs. 3.2, 3.3, 3.7 used to predict the droplet behavior over time. Also, the Ranz-Marshall correlations 3.10-3.11 are used, as well as the Abramzon-Sirignano model (Eqs. 3.24-3.29).

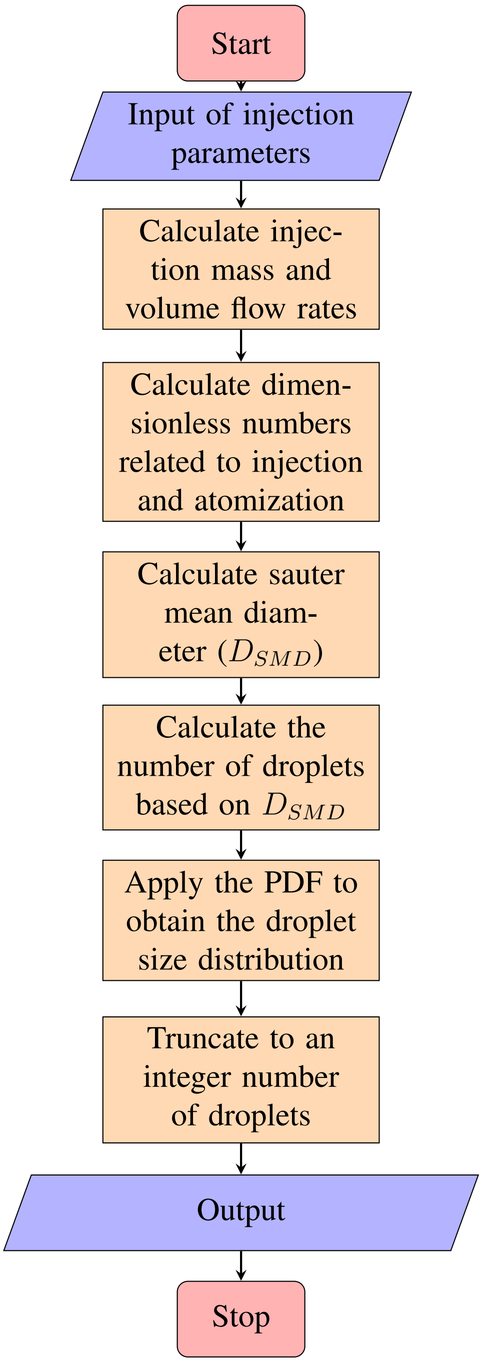

Figure 3.6 – Flowchart of the fuel injection function.

3.3.5 Unburned zone equations

The initial mass of gas is established as a function of the desired air-fuel ratio (A/F) and initial conditions for the inlet valve closing (IVC) moment $(V_{g,IVC}, T_{g,IVC}, P_{g,IVC})$. The amount of air at IVC, as well as the amounts of hydrous ethanol and water that will be injected at the fuel injection period are evaluated by Eqs. 3.45-3.47:

$$m_{air,IVC} = \frac{P_{IVC}V_{IVC}}{R_{g,IVC}T_{g,IVC}} \tag{3.45}$$

$$m_{EOH} = \frac{m_{air,IVC}}{A/F} \tag{3.46}$$

$$m_{H_2O} = \frac{y_{H_2O}}{1 - y_{H_2O}} m_{EOH} \tag{3.47}$$

Usually the known variable for wet ethanol mixtures is the water volumetric fraction (v_{H_2O}), hence the mass-volumetric fraction conversion for liquid mixtures can be obtained by Eq. 3.48:

$$y_{H_2O} = \frac{1}{1 - \left(\frac{\rho_{EOH}}{\rho_{H_2O}}\right)\left(\frac{v_{H_2O}-1}{v_{H_2O}}\right)} \tag{3.48}$$

In order to Eq. 3.48 to be valid, the assumption of liquid volume conservation on liquid mixtures/solutions is required.

Then, the mass conservation for the gases during the compression phase is represented by (3.49):

$$\frac{\mathrm{d}m_g}{\mathrm{d}t} = \sum_{i=1}^{N_{classes}} N_{droplet,i}\dot{m}_{d,i} \tag{3.49}$$

The energy conservation is applied to these gases and provides (3.50):

$$\frac{\mathrm{d}T_g}{\mathrm{d}t} = \frac{1}{m_g c_{p,g}} \left\{ \sum_{i=1}^{N_{classes}} N_{droplet,i}\dot{m}_{d,i}(h_{v,i} - h_g) - m_g \sum_{i=1}^{N_{classes}} \sum_{j=1}^{N_{species}} h_{g,i,j} \frac{\mathrm{d}y_{g,i,j}}{\mathrm{d}t} \right. \\ \left. - \sum_{i=1}^{N_{classes}} N_{droplet,i}\dot{Q}_{conv,i} - \dot{Q}_{wall} + \sum_{i=1}^{N_{classes}} P_g \frac{\pi}{2} N_{droplet,i} D_{d,i}^2 \frac{\mathrm{d}D_{d,i}}{\mathrm{d}t} + \forall_g \frac{\mathrm{d}P_g}{\mathrm{d}t} \right\} \tag{3.50}$$

The first term represents the enthalpy fluxes from saturated vapor and gas enthalpies of the droplet components, the second is the gas enthalpy due to composition variation, the third indicates the sum of convective heat transfer from the surrounding gases to all droplet classes, the fourth is the heat transfer from/to the cylinder walls (Hohenberg correlation (Rufino *et al.*, 2019)), the fifth represents the energy due to all droplets classes volume change, and the sixth indicates the energy related to the gas pressure. Based on the ideal gas law, the pressure rate is calculated by (3.51):

$$\frac{\mathrm{d}P_g}{\mathrm{d}t} = \frac{1}{\frac{R_g \not{V}_g}{c_{p,g}} - \not{V}_g - \not{V}_{spray}} \left\{ -\frac{R_g}{c_{p,g}} \left[\sum_{i=1}^{N_{classes}} P_g \frac{\pi}{2} N_{droplet,i} D_{d,i}^2 \frac{\mathrm{d}D_{d,i}}{\mathrm{d}t} - \sum_{i=1}^{N_{classes}} N_{droplet,i} \dot{Q}_{conv,i} \right.\right.$$
$$\left.\left. - \dot{Q}_{wall} + \sum_{i=1}^{N_{classes}} N_{droplet,i} \dot{m}_{d,i} (h_{v,i} - h_g) - m_g \sum_{i=1}^{N_{classes}} \sum_{j=1}^{N_{species}} h_{g,i,j} \frac{\mathrm{d}y_{g,i,j}}{\mathrm{d}t} \right] - R_g T_g \frac{\mathrm{d}m_g}{\mathrm{d}t} \right\} \tag{3.51}$$

By following the same procedure of the last section, the entropy balance for the surrounding gases is presented by (3.52):

$$\dot{\sigma}_g = \sum_{i=1}^{N_{classes}} N_{droplet,i} \dot{m}_{d,i} (s_{v,i} - s_g) + m_g \frac{\mathrm{d}s_g}{\mathrm{d}t} + \sum_{i=1}^{N_{classes}} N_{droplet,i} \frac{\dot{Q}_{conv,i}}{T_{d,i}} + \frac{\dot{Q}_{wall}}{T_{wall}} \tag{3.52}$$

Equation (3.52) takes into account the entropy flows between the droplets and the gases (first term), the gas entropy variation (second term), and the heat transfers between the gases with the droplets (third term) and with the cylinder walls (fourth term), respectively.

3.3.6 First and second law spray evaporation efficiencies

A first law efficiency for the spray evaporation process is suggested by this work by Eq. (3.53), where the desired effect is the total amount of energy related to the heat of vaporization from droplet components during the evaporation process while the main source of energy is cumulative energy associated with the convective heat transfer from the surrounding gases to the droplets:

$$\eta_{1st,spray} = \frac{\int_0^t \sum_{i=1}^{N_{classes}} N_{droplet,i} \dot{m}_{d,i} \Delta h_{v,i} dt}{\int_0^t \sum_{i=1}^{N_{classes}} N_{droplet,i} \dot{Q}_{conv,i} dt} \tag{3.53}$$

The second law efficiency to the spray evaporation process is presented by Eq. (3.54):

$$\eta_{2nd,spray} = \frac{\int_0^t \dot{m}(\Delta h_v - T_0 \Delta s_v) dt}{\int_0^t \dot{Q}_{conv} \left(1 - \frac{T_0}{T_d}\right) dt} = \frac{\int_0^t \sum_{i=1}^{N_{classes}} N_{droplet,i} \dot{m}_{d,i} \Delta h_{v,i} \left(1 - \frac{T_0}{T_{d,i}}\right) dt}{\int_0^t \sum_{i=1}^{N_{classes}} N_{droplet,i} \dot{Q}_{conv,i} \left(1 - \frac{T_0}{T_{d,i}}\right) dt}, \tag{3.54}$$

where $T_0 = 293K$ is the dead-state temperature.

3.3.7 Algorithm procedure

The set of differential equations is solved by the application of an implicit trapezoidal method, in order to avoid stiffness in these equations, as well as to guarantee a fast and reliable ODE solver procedure. Numerical derivatives were used to obtain the Jacobian matrix required by this method. The reliability of this numerical procedure was tested by comparisons with a fourth order Runge-Kutta solver and the final results for both solvers were equivalent within a tolerance value of $TOL = 1\text{x}10^{-3}$. Also, reductions on the time-step were applied to the implicit method until the same results were obtained for successive time-step reductions. The time-step limit value found for this type of simulation $\Delta t = 1\text{x}10^{-6} s$ and thus, this value was the one adopted in the simulations.

The algorithm presented in Section 3.2.6 was updated to include the models of fuel spray injection and evaporation presented in Section 3.3.3. Thus, the algorithm for this model is presented by Fig. 3.7:

Next some brief comments about this algorithm are presented:

1. Step A requires the inputs of initial parameters for the fuel and the gases, such as composition, thermodynamic variables, air-fuel ratio, engine parameters and constants for the property correlations of the fuel components (Appendix C);
2. Step B calculates the initial mass of in-cylinder gases, besides the mass of ethanol and water that will be injected during the injection period (Eqs. 3.45 - 3.48);
3. Step C checks if the injection occurs during this time step;
4. Step D activates the injection function;
5. Step E is a for-loop for all droplet classes existent at i to actuate the droplet evaporation function. This function will only be active after the beginning of the injection period and it will be active for a specific class until its droplet size becomes lower than the continuum tolerance (ϵ_d);
6. Step F solves the droplet evaporation for the *kth* class;
7. Step G evaluates all energy transfers associated with the gas control volume;
8. Step H applies the same numerical method to solve the gas-phase differential equations (Eqs. 3.49, 3.50 - 3.52);

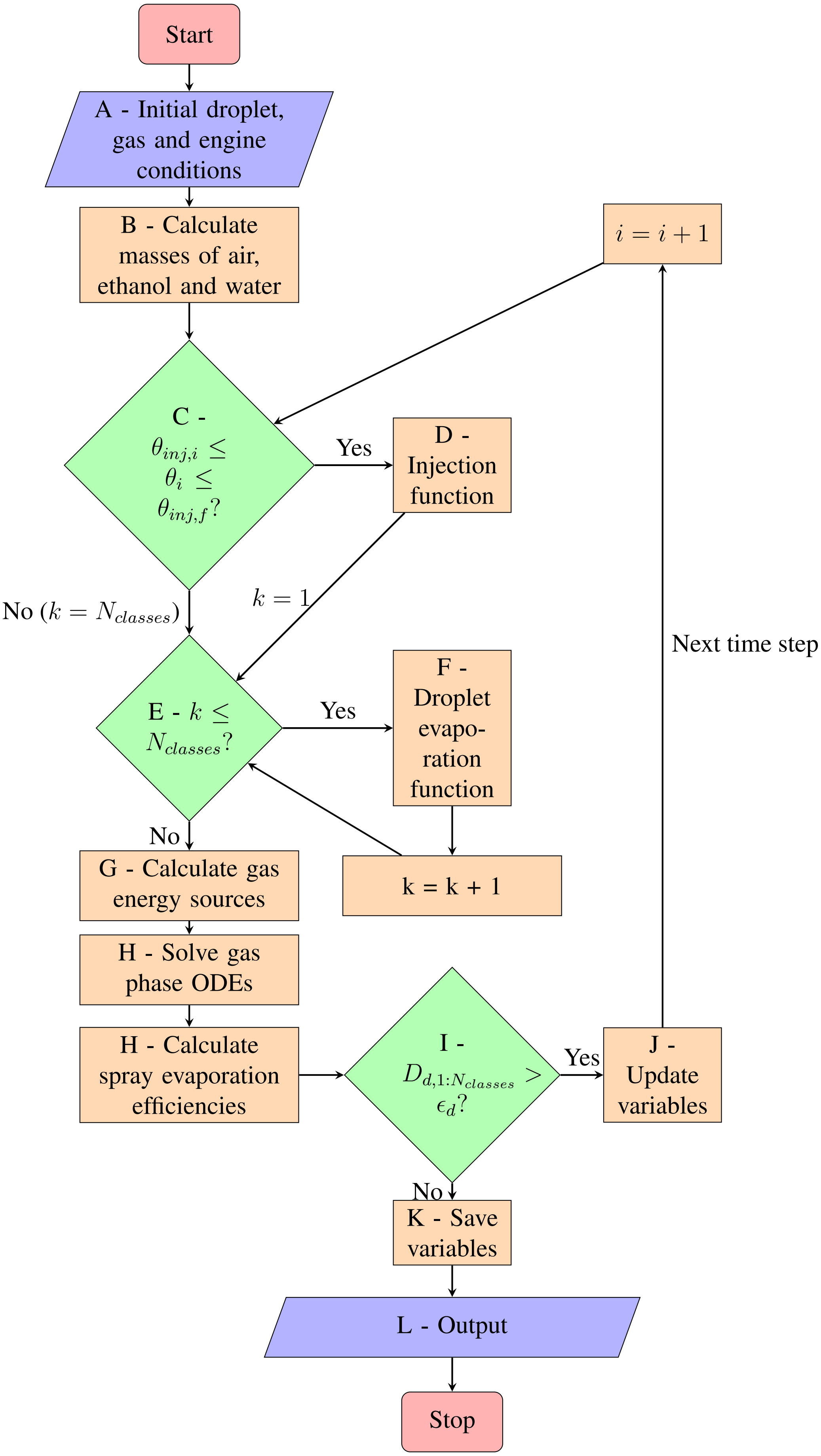

Figure 3.7 – Flowchart of the wet ethanol spray injection and evaporation algorithm during a compression stroke of a DISI engine.

9. Step I calculates the energetic and exergetic droplet evaporation efficiencies for this time step (Eqs. 3.53 - 3.54);
10. Step J checks if the new droplet diameters for all droplet classes are higher than $1 \mu m$, which is the value adopted to allow reasonable computational work;
11. Step J updates the droplet and gas variables for the next time step and returns to step C;
12. Step K actuates when all droplet classes evaporated and saves the final values for the variables of interest;
13. End of the simulation;

3.4 A multi-zone thermodynamic model for the direct injection of wet ethanol as a fuel in a DISI engine

3.4.1 Model description and assumptions

This mathematical model focus on simulating the operation of a DISI engine fueled with wet ethanol. It accomplishes all aforementioned sub-models presented earlier in this chapter (i.e, droplet evaporation, mixing, spray injection, liquid and gas-phase conservation equations) with the combustion process initially indicated by a Wiebe function (Rufino, 2020). The objective is to evaluate how wet ethanol evaporation characteristics (i.e, droplet lifetime, penetration, evaporative cooling effect) impacts the engine operation in terms of fuel injection timing, water content, knock suppression, which generates possibilities to optimal engine operations as a function of some engine parameters like IMEP, thermal efficiency, higher compression ratio, engine power, knock occurrence, pollutant emission, etc. This analysis is developed based on energy and entropy/exergy transfer balances. The mathematical modeling for all described sub-processes is presented and properly described.

This model has the same description as the one presented in Section. 3.3, although there is the addition of the combustion process and the open-phase simulation to fulfill a complete engine simulation. Now there is the formation of a burned zone with the products of the fuel combustion. This new zone grows as combustion evolves over time until it consumes almost all air-fuel mixture available in the unburned zone, thus replacing it in the engine cylinder.

This engine model takes into account here 14 chemical species (Ar, CO, CO_2, H, H_2, H_2O, OH, O, O_2, N, N_2, NO, NO_2, C_2H_5OH). All their thermodynamic properties are calculated by NIST specific heat coefficients and constants (i.e., enthalpy of formation, absolute entropy, free Gibbs energy, etc.) (Chase Jr., 1998), whereas the gas transport properties are obtained by the software Cantera coupled with MATLAB®, just as previously presented in Sec. 3.1.1.

All assumptions presented on Sections 3.1.1, 3.2.1 and 3.3.1 are valid for this model. Also, some additional hypotheses are necessary to turn the model feasible and are presented next:

- The combustion process is simulated by the application of the Wiebe function to the fraction mass burned;
- The ideal gas equation is assumed valid for both zones;
- The initial temperature obtained for the burned zone is the adiabatic flame temperature evaluated for the gas mixture air-fuel-residual gases present in the unburned zone at the first time step of the combustion process;
- The cylinder pressure is assumed homogeneous throughout the process, i.e., the unburned and burned zone are always at the same pressure;
- The unburned and burned zones only exchange mass and energy through the process of combustion;
- There aren't any heat transfer terms between these two zones;
- The liquid phase (i.e, droplet spray) only interacts with the unburned zone, therefore their energy/entropy terms only participate the unburned zone equations;

The schematic diagram for this model is presented by Fig. 3.8:

3.4.2 Liquid phase equations

The conservation equations for the liquid phase (i.e., droplets and spray) follows the same equations as previously presented earlier in this chapter. The main properties associated with a droplet in this model are described by Eqs. 3.1, 3.2, 3.5 and 3.7, which are valid for mass, droplet size, velocity and droplet temperature, respectively. The fractional evaporation rate is defined by 3.3. The Abramzon-Sirignano model as well as the Ranz-Marshall correlations were used to represent the droplet evaporation model and the heat/mass transfer correlations for each

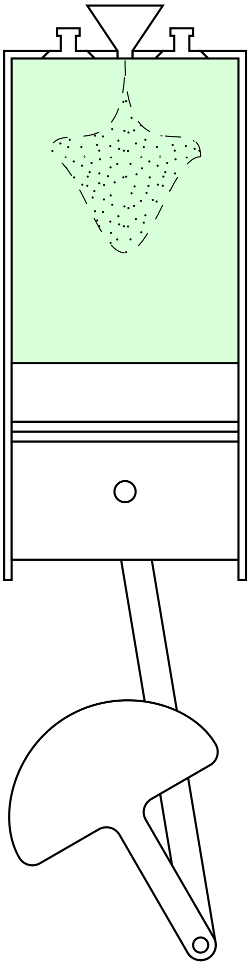

Figure 3.8 – Schematic diagram of a spray injection and evaporation model in a DISI engine cylinder.

droplet, respectively. The spray description is the same as presented in Section 3.3.3. Finally, the initial amount of ethanol-water fuel blend to be injected in the engine cycle is defined by the $lambda = AF_{actual}/AF_{stoichiometric}$ factor. The mass air-fuel ratio (AF) only involves the proportion between fresh air and pure ethanol, although both water and residual gases make part of the global combustion equation.

3.4.3 Closed phase

The four-stroke ICE operation (i.e., admission, compression, combustion, expansion, and exhaust) are usually divided between closed and open phases. The modeling of each phase has some differences due to its own characteristics, thus each one has its own section describing it. Figure 3.9 describes the sequence of engine processes which represents both phases, as well as the combustion period between the start of combustion (SOC) and the end of combustion (EOC), top-dead center (TDC) and Bottom-dead center (BDC):

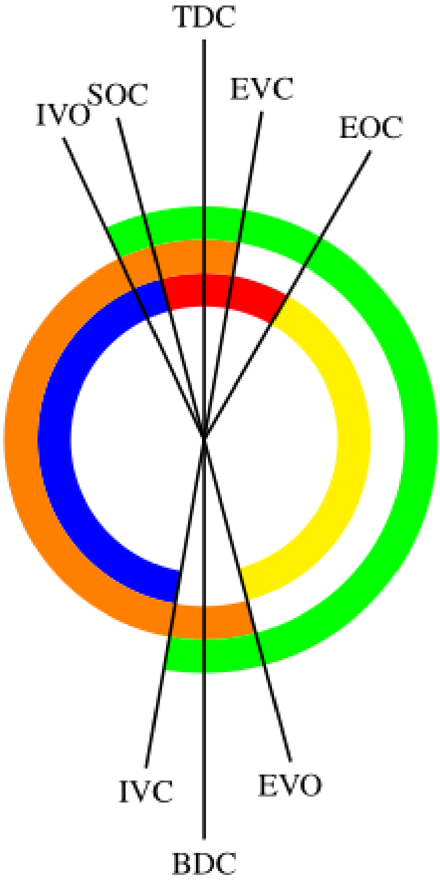

Figure 3.9 – Generic case of the sequence of processes of a spark-ignition engine cycle. Green: air admission; orange: combustion gas exhaust; blue: compression; red: combustion; yellow: expansion. Adapted from (Rufino, 2020).

The closed phase involves the period when both valves (inlet and exhaust) are closed, so it is between the inlet valve closure (IVC) and the exhaust valve opening (EVO). Therefore, it is composed by the compression (blue), combustion (red), and expansion (yellow) strokes. Neglecting possible blow-by effects, the only mass flow that cross the control surface is the fuel injection for direct-injection engines (it depends on the injection timing). During this phase, the composition of the air-fuel gas mixture changes due to the combustion process, which in this case is described in terms of unburned and burned zones.

A complete description of the closed-phase model is presented in Appendix B, while the final forms of the applied equations are presented next.

3.4.3.1 Unburned zone equations

The unburned zone is composed initially by fresh air obtained from the engine intake stroke and by residual gases (i.e., EGR) remaining from the last engine cycle which were not expelled during the exhaust stroke. The initial mass of fresh air is defined by the thermodynamic conditions during IVC, with a discount of the amount of EGR present at this crank angle.

The conservation laws for this zone are described in details in Appendix B, therefore only their final forms are shown here. The mass conservation for this zone is presented by Eq. 3.55:

$$\frac{\mathrm{d}m_{UBZ}}{\mathrm{d}t} = \sum_{k=1}^{N_{classes}} N_{droplet,k}\dot{m}_{d,k} - \dot{m}_{comb}, \tag{3.55}$$

where the mass transfers which involve UBZ are related to the spray evaporation (first term) and with combustion (second term). The chemical species conservation has the following form:

$$\frac{\mathrm{d}m_{UBZ,j}}{\mathrm{d}t} = \sum_{k=1}^{N_{classes}} N_{droplet,k}y_{j,k,evap}\dot{m}_{d,k} - y_{j,UBZ}\dot{m}_{comb}, \tag{3.56}$$

where $y_{j,k,evap}$ is the mass fraction of the *jth* fuel vapor component from the *kth* droplet class of the spray, whereas $y_{j,UBZ}$ is the mass fraction of the *jth* component in the unburned gas zone. The start point is the classical energy conservation equation for ICEs in its differential form Eq. 3.57:

$$\frac{\mathrm{d}U_{UBZ}}{\mathrm{d}t} = \dot{Q}_{wall,UBZ} - P_g\frac{\mathrm{d}V_{UBZ}}{dt} + \sum \dot{m}_{inlet}h_{inlet} - \sum \dot{m}_{outlet}h_{outlet} \tag{3.57}$$

This equation is usually originated from the Reynolds Transport Theorem and has its assumptions detailed in Appendix B. The final form of the unburned zone energy conservation equation is described by Eq. 3.58:

$$\frac{\mathrm{d}T_{UBZ}}{\mathrm{d}t} = \frac{1}{m_{UBZ}c_{p,UBZ}} \left\{ \sum_{k=1}^{N_{classes}} N_{droplet,k}\dot{m}_{d,k}(h_{evap,k} - h_{UBZ}) - m_{UBZ} \sum_{j=1}^{N_{species}} \left(h_{j,UBZ}\frac{\mathrm{d}y_{j,UBZ}}{\mathrm{d}t} \right) \right.$$
$$\left. - \sum_{k=1}^{N_{classes}} N_{droplet,k}\dot{Q}_{conv,k} + \dot{Q}_{UBZ,wall} + P_g \sum_{k=1}^{N_{classes}} N_{droplet,k}\frac{\mathrm{d}V_{d,k}}{\mathrm{d}t} + V_{UBZ}\frac{\mathrm{d}P_g}{\mathrm{d}t} \right\} \quad (3.58)$$

The evaporation process is taken into account in the first, second, third and fifth terms of RHS, while the forth represents the cylinder wall heat transfer from/to UBZ and the sixth is the energy variation due to the gas pressure change. The entropy generation is given by Eq 3.59:

$$\dot{\sigma_{UBZ}} = \sum_{k=1}^{N_{classes}} N_{droplet,k}\dot{m}_{d,k}(s_{UBZ} - s_{evap,k}) + m_{UBZ}\frac{ds_{UBZ}}{dt}$$
$$+ \sum_{k=1}^{N_{classes}} N_{droplet,k}\frac{\dot{Q}_{conv,k}}{T_{d,k}} - \frac{\dot{Q}_{UBZ,wall}}{T_{wall}} \quad (3.59)$$

3.4.3.2 Burned zone equations

Just as it was done on Sec. 3.4.3.1, this section covers only the final forms for the conservation equations of the burned zone. Its mass conservation is given by Eq. 3.60:

$$\frac{\mathrm{d}m_{BZ}}{\mathrm{d}t} = \dot{m}_{comb}, \quad (3.60)$$

where the only mass source for BZ is combustion. The burned zone composition is obtained by the mass fraction of the combustion process from the ethanol-air mixture derived from the unburned zone at each specific time step.

Equation 3.61 describes the energy balance in this new zone:

$$\frac{\mathrm{d}T_{BZ}}{\mathrm{d}t} = \frac{\dot{m}_{comb}(h_{UBZ} - h_{BZ}) + \rlap{-}V_{BZ}\,\frac{\mathrm{d}P_g}{\mathrm{d}t} + \dot{Q}_{BZ,wall} + \Delta H_{fuel}}{m_{BZ}c_{p,BZ}}, \quad (3.61)$$

where the first term refers to the mass inlet and outlet related to the combustion process, whereas the second term is the energy change due to pressure variation, the third is the cylinder wall heat transfer to/from this zone and the last represents the energy variation due to combustion reaction ($\Delta H_{fuel} = \eta_{comb}\omega(\mathrm{d}y_{BZ}/\,\mathrm{d}t)m_{fuel}Q_{LHV,fuel}$). The cylinder gas pressure rate involves terms from the liquid phase, unburned and burned zones and is described by Eq. 3.62:

$$
\begin{aligned}
\frac{\mathrm{d}P_g}{\mathrm{d}t} = \frac{1}{\rlap{-}V_{cyl} - \frac{R_{BZ}\rlap{-}V_{BZ}}{c_{p,BZ}} - \frac{R_{UBZ}V_{UBZ}}{c_{p,UBZ}} - \rlap{-}V_{spray}} \Bigg\{ & R_{UBZ}T_{UBZ}\frac{\mathrm{d}m_{UBZ}}{\mathrm{d}t} + R_{BZ}T_{BZ}\frac{\mathrm{d}m_{BZ}}{\mathrm{d}t} \\
& + \frac{R_{UBZ}}{c_{p,UBZ}} \left[\sum_{k=1}^{N_{classes}} N_{droplet,k}\dot{m}_{d,k}(h_{evap,k} - h_{UBZ}) - m_{UBZ} \sum_{j=1}^{N_{species}} \left(h_{j,UBZ}\frac{\mathrm{d}y_{j,UBZ}}{\mathrm{d}t} \right) \right. \\
& \left. + P \sum_{k=1}^{N_{classes}} N_{droplet,k}\frac{\mathrm{d}\rlap{-}V_{d,k}}{\mathrm{d}t} - \sum_{k=1}^{N_{classes}} N_{droplet,k}\dot{Q}_{conv,k} + \dot{Q}_{UBZ,wall} \right] \\
& + \frac{R_{BZ}}{c_{p,BZ}} \left[\dot{m}_{comb}(h_{UBZ} - h_{BZ}) + \dot{Q}_{BZ,wall} + \Delta H_{fuel} \right] - P_g \left(\frac{\mathrm{d}\rlap{-}V_{cyl}}{\mathrm{d}t} - \frac{\mathrm{d}\rlap{-}V_{spray}}{\mathrm{d}t} \right) \Bigg\}
\end{aligned}
\tag{3.62}
$$

3.4.3.3 Combustion

The combustion process which occurs in this DISI model is initially simulated by the application of Wiebe's function (Rufino, 2020). This function tries to reproduce the behavior of combustion by adjusting some parameters associated with ignition delay, start of combustion (SOC), combustion duration and end of combustion in terms of experimental measurements. Thus, this equation encompasses several influences on the chemical kinetics of combustion in a single semi-empirical equation. A Wiebe function usually has the following form:

$$
y_b(\theta) = 1 - \exp\left[\ln\left(1 - \eta_{comb}\right) \left(\frac{\theta - \theta_0}{\Delta\theta_b} \right)^{n+1} \right], \tag{3.63}
$$

where y_b is the mass fraction burned η_{comb} is a parameter associated with the combustion efficiency (i.e., maximum value of mass fraction burned (MFB)), θ_0 is the SOC (in rad), $\Delta\theta_b$ is the combustion duration, and n is the form factor. All these parameters were obtained as described in Rufino (2020). Moreover, the mass fraction derivative is:

$$
\frac{\mathrm{d}y_b}{\mathrm{d}\theta} = -\frac{\ln\left(1 - \eta_{comb}\right)}{\Delta\theta_b}(n+1)\left(\frac{\theta - \theta_0}{\Delta\theta_b} \right)^{n} \exp\left[\ln\left(1 - \eta_{comb}\right) \left(\frac{\theta - \theta_0}{\Delta\theta_b} \right)^{n+1} \right], \tag{3.64}
$$

3.4.4 Open phase

Based on Fig. 3.9, the open phase is the period when at least one valve is open, thus it initiates at EVO and finalizes at IVC. It covers the exhaust (orange) and admission strokes (green). One observation is made to this phase, since the inlet and exhaust valves periods can overlap, therefore both colors may be present depending on the command valve strategy. In terms of mass flow, there are flows from a possible fuel injection defined during this period and also from the valves to the engine cylinder and vice-versa, depending on the thermodynamic conditions of the in-cylinder gases (i.e., pressure). Therefore, the gas composition is a mixture of fresh air, vapor fuel, and residual gases from past engine cycles. A complete description of the model is presented in Appendix B, while the final forms of the applied equations are presented in the next section.

3.4.4.1 Gas-phase equations

The gas-phase is composed initially by residual gases originated from the combustion process of air-fuel mixture. Between EVO and IVO, gases flow from the cylinder into the exhaust valve as long as the gas pressure overcomes the exhaust pressure. Additionally, the composition does not change during this period. When the inlet valve opens, the admission process can start immediately or not, depending on the pressure gradient between the inlet system and the cylinder gases. Some backflow can occur depending on this pressure gradient. When the admission pressure overcomes the cylinder gas pressure, fresh air starts entering the cylinder and mixing with the remaining residual gas from the latest engine cycle. Another point to take into consideration is if the fuel injection strategy actuates during the open-phase, so there is some liquid during the open phase, thus some vapor fuel mixing in with air-residual gas mixture.

The conservation laws for this zone are described in details in Appendix B, therefore only their final forms are shown here. The mass conservation for the gases is presented by Eq. 3.65:

$$\frac{\mathrm{d}m_g}{\mathrm{d}t} = \sum_{k=1}^{N_{classes}} N_{droplet,k}\dot{m}_{d,k} + (\delta_{adm,i} - \delta_{adm,o})\dot{m}_{adm} + (\delta_{exh,i} - \delta_{exh,o})\dot{m}_{exh}, \tag{3.65}$$

where the mass transfers are related to the spray evaporation (first term) and with valve mass flows (second and third terms). Moreover, $\delta_{adm,i}, \delta_{adm,o}, \delta_{exh,i}, \delta_{exh,o}$ are Kronecker deltas indicating the flow direction from the valves. The mass flow rate modeling related to the valves is properly detailed by Rufino (2020). The chemical species conservation has the following form:

$$\begin{aligned}\frac{\mathrm{d}m_{g,j}}{\mathrm{d}t} = \sum_{k=1}^{N_{classes}} N_{droplet,k}y_{j,k,evap}\dot{m}_{d,k} + (\delta_{adm,i}y_{j,air} - \delta_{adm,o}y_{j,g})\dot{m}_{adm} \\ + (\delta_{exh,i}y_{j,EGR} - \delta_{exh,o}y_{j,g})\dot{m}_{exh},\end{aligned} \tag{3.66}$$

where $y_{j,k,evap}$ is the mass fraction of the *jth* fuel vapor component from the *kth* droplet class of the spray, whereas $y_{j,gas}$ is the mass fraction of the *jth* component in the gas-phase. The final form of the energy conservation equation is described by Eq. 3.67:

$$\begin{aligned}\frac{\mathrm{d}T_g}{\mathrm{d}t} = \frac{1}{m_g c_{p,g}} \Bigg\{ & \sum_{k=1}^{N_{classes}} N_{droplet,k} \dot{m}_{d,k} (h_{evap,k} - h_g) - m_g \sum_{j=1}^{N_{species}} \left(h_{j,g} \frac{\mathrm{d}y_{j,g}}{\mathrm{d}t} \right) \\ & + \delta_{adm,i} \dot{m}_{adm} (h_{adm} - h_g) + \delta_{exh,i} \dot{m}_{exh} (h_{exh} - h_g) \\ & - \sum_{k=1}^{N_{classes}} N_{droplet,k} \dot{Q}_{conv,k} + \dot{Q}_{g,wall} + P_g \sum_{k=1}^{N_{classes}} N_{droplet,k} \frac{\mathrm{d}V_{d,k}}{\mathrm{d}t} + \cancel{V}_g \frac{\mathrm{d}P_g}{\mathrm{d}t} \Bigg\} \end{aligned} \tag{3.67}$$

The evaporation process is taken into account by first, second, and seventh terms of RHS, while the forth and fifth represent the inlet and exhaust valves, the sixth is the cylinder wall heat transfer from/to the gases and the eighth term is the energy variation due to the gas pressure change. The entropy generation is given by Eq 3.68:

$$\begin{aligned}\dot{\sigma}_g = & \sum_{k=1}^{N_{classes}} N_{droplet,k} \dot{m}_{d,k} (s_g - s_{evap,k}) + m_g \frac{ds_g}{dt} + \delta_{adm,i} \dot{m}_{adm} (s_g - s_{adm}) \\ & + \delta_{exh,i} \dot{m}_{exh} (s_g - s_{exh}) + \sum_{k=1}^{N_{classes}} N_{droplet,k} \frac{\dot{Q}_{conv,k}}{T_{d,k}} - \frac{\dot{Q}_{g,wall}}{T_{wall}} \end{aligned} \tag{3.68}$$

3.4.5 Algorithm procedure

The set of differential equations is solved by the application of an implicit trapezoidal method, in order to avoid stiffness in our equations, as well as to guarantee a fast and reliable ODE solver procedure. Numerical derivatives were used to obtain the Jacobian matrix required by this method. The reliability of this numerical procedure was tested by comparisons with a fourth order Runge-Kutta solver and the final results for both solvers were equivalent within a tolerance value of $TOL = 1\text{x}10^{-2}$. Also, reductions on the time-step were applied to the implicit method until the same results were obtained for successive time-step reductions. The time-step limit value found for this type of simulation $\Delta t = 1\text{x}10^{-6}s$ and thus, this value was the one adopted in the simulations.

3.4.6 Validation of the model

In order to corroborate the validity of the presented model, some comparisons with experimental measurements from Lanzanova *et al.* (2016), Brewster *et al.* (2007) are developed. Several ethanol-water mixtures were analyzed by these comparisons. Both partial and full load conditions were also taken into account to a proper direct injection evaluation. The cylinder engine pressure curves, engine thermal efficiency, torque, pressure and temperature peaks, and indicated specific fuel consumption (SFC) were used to compare the model results to the experiment ones. More details about the validation are presented by Chapter 6.

3.5 Thermodynamic optimization of a DISI engine fueled with wet ethanol

The fundamentals related to the thermodynamic optimization involve the same ideas as presented in Sec. 3.4 plus the exergetic analysis presented in Appendix B. The idea is to apply the optimization toolbox of MATLAB by the *fgoalattain* function to find the optimal state. The details are presented in Chapter 7.

3.5.1 Exergetic analysis

Only the main equations for the exergetic analysis will be presented in this Section. The development of all equations and their respective descriptions are available in Appendix B. The closed-phase unburned zone equation is therefore:

$$\begin{aligned}\dot{B}_{d,UBZ} = &\sum_{k=1}^{N_{classes}} N_{droplet,k}\dot{m}_{d,k}(b_{f,evap,k} - b_{UBZ}) - \dot{m}_{comb}(b_{f,UBZ} - b_{UBZ}) - m_{UBZ}\frac{\mathrm{d}b_{UBZ}}{\mathrm{d}t} \\ &+ \dot{B}_{Q_{spray}} + \left(1 - \frac{T_0}{T_{wall}}\right)\dot{Q}_{UBZ,walls} \\ &- \left(\dot{W}_{spray} - P_0\sum_{k=1}^{N_{classes}} N_{droplet,k}\left(-\frac{\mathrm{d}V_{d,k}}{\mathrm{d}t}\right)\right) - (P - P_0)\frac{\mathrm{d}\rlap{--}V_{BZ}}{\mathrm{d}t}\end{aligned} \quad (3.69)$$

The flow terms are equivalent to the ones of 3.58, but in terms of exergy. Additionally, there is the destroyed exergy/irreversibility rate term $\dot{B}_{d,UBZ}$. The burned zone exergy balance is represented by Eq. 3.70:

$$\dot{B}_{d,BZ} = \dot{m}_{comb}(b_{f,UBZ} - b_{BZ}) - m_{BZ}\frac{\mathrm{d}b_{BZ}}{\mathrm{d}t} - (P - P_0)\frac{\mathrm{d}V_{BZ}}{\mathrm{d}t} + \left(1 - \frac{T_0}{T_{wall}}\right)\dot{Q}_{BZ,walls} \quad (3.70)$$

The open-phase exergy balance is presented by Eq. 3.71:

$$\dot{B}_{d,g} = \sum_{k=1}^{N_{classes}} N_{droplet,k}\dot{m}_{d,k}(b_{f,evap,k} - b_g) + \delta_{adm,i}\dot{m}_{adm}(b_{f,adm} - b_g) + \delta_{exh,i}\dot{m}_{exh}(b_{f,exh} - b_g)$$
$$+ \delta_{adm,o}\dot{m}_{adm}(b_g - b_{f,g}) + \delta_{exh,o}\dot{m}_{exh}(b_g - b_{f,g}) - m_g\frac{\mathrm{d}b_g}{\mathrm{d}t} + \dot{B}_{Q_{spray}} + \left(1 - \frac{T_0}{T_{wall}}\right)\dot{Q}_{g,walls}$$
$$- \left(\dot{W}_{spray} - P_0 \sum_{k=1}^{N_{classes}} N_{droplet,k}\left(-\frac{\mathrm{d}V_{d,k}}{\mathrm{d}t}\right)\right) - (P - P_0)\frac{\mathrm{d}V_g}{\mathrm{d}t} \quad (3.71)$$

These equations are solved in a subroutine after the simulator convergence for the engine cycle. The algorithm procedure is equivalent to the aforementioned models, but with the gases and liquid phases thermodynamic states already known, thus resulting in computer acceleration.

4 WET ETHANOL DROPLET EVAPORATION PROCESS IN A FINITE VARIABLE TEMPERATURE ENVIRONMENT

This chapter encompasses some analyses related to the Lagrangian modeling of a single droplet in terms of its injection and evaporation in a similar environment as of the gases in a compression stroke of a SI engine. The idea is to understand how the fuel evaporation occurs in such conditions, besides to present this phenomenon under the eyes of the second law of thermodynamics. First, the chapter addresses a parametric analysis of some droplet properties for a pure ethanol evaporation under two different conditions. Later, this phenomenology is analyzed in terms of the four different evaporation models presented in Section 3.1.5. At last, the study is extended to wet ethanol and how the water content in the fuel blend influences the evaporation process and the entropy generation.

4.1 Parametric analysis through the second law of thermodynamics of a pure ethanol droplet injection and evaporation processes in a variable temperature environment

4.1.1 Simulation cases for a parametric analysis of a droplet model evaporation

Initially, a base case simulation was performed to demonstrate the phenomenological behavior of an ethanol droplet evaporating. This case consists of a droplet composed by ethanol at $288.15K$ moving inside a cylinder at $500K$ and 1 atm. The droplet mass was calculated based on the knowledge of its diameter and the liquid density (i.e., correlations). Then, the mass of the surrounding gases was obtained from the relative air-fuel ratio λ. Next, a parametric investigation was performed to investigate the effects of different initial conditions on the droplet evaporation. The simulation assumed two different thermodynamic states to represent two different moments of the compression stroke (i.e., beginning and end) while some droplet properties were varied. The initial conditions for the compression beginning were $T_\infty = 500K$ and $P_g = 1atm$, while for the compression end were $T_\infty = 900K$ and $P_g = 18atm$.

The total number of simulated cases was 250 and all cases are expressed in Tab. 4.1. Relevant parameters for the engine such as cooling charge effect, droplet penetration and evaporation time were also evaluated.

Table 4.1 – Simulated conditions of the injected droplet and in-cylinder gases

Parameter	Droplet		In-cylinder gases	
	Range	Step	Range	Step
T(K)	300-340	10	500-900	400
D(μm)	20-100	20	-	-
u(m/s)	0-40	10	0	0
P(atm)	-	-	1-18	17

4.1.2 Base case phenomenological analysis

The main goal in an phenomenological analysis of a droplet evaporation dynamics is to evaluate how this particle's parameters evolve over time, i.e., mass, diameter, temperature and velocity in a surrounding environment which is also changing. Still, most droplet studies related to evaporation (Turns, 2012; Kuo, 2005) take into account an infinite gas environment involving the droplet, with specific conditions regarding this assumption. This section addresses this situation by considering a gas whose physical dimensions (mass and volume) are proportional to the surrounded droplet. It is expected that this change on the gases causes a different evaporation behavior (droplet and gas) which is more similar to the direct injection in the engine cylinder.

Therefore, based on the conditions presented in Section 4.1.1, the mass transfer Spalding number (left, Eq. 4.1) and evaporation mass flow rate (right, Eq. 4.2) profiles are presented by Fig. 4.1 for the base case of an ethanol droplet evaporating. It is noted that the Spalding number do not stay constant throughout the phenomenon, as both droplet and environment thermodynamic conditions are changing all the time. If the surrounding gas were considered infinitely greater than the droplet, then this Spalding number would reach an asymptotic value, as both gas temperature and pressure would be constant and after the heat-up process, the droplet temperature would also be constant (wet-bulb temperature). Figure 4.1 right also indicates that the droplet mass flow rate reaches a peak near the maximum droplet temperature (see Fig. 4.3, left), as it depends of the droplet conditions. Later, it decays softly until evaporation ends.

$$B_M = (y_{fs} - y_{fg})/(1 - y_{fg}) \tag{4.1}$$

$$\dot{m}_d = \pi D_d (\rho \mathcal{D})_v Sh \ln(1 + B_M) \tag{4.2}$$

The droplet squared diameter and its diameter rate over time are shown on the left of Fig. 4.2. The classic D-squared law (Williams, 1973) for droplet evaporation/combustion processes is not completely followed during the beginning of evaporation process, as the droplet

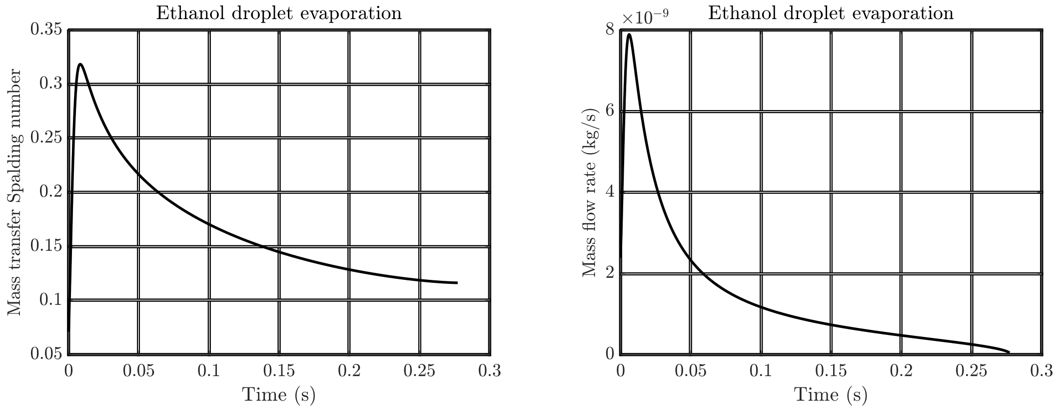

Figure 4.1 – Mass transfer Spalding number (left) and mass flow rate (right) versus evaporation time - Base Case ($T_{d,i} = 288.15K$,$D_{d,i} = 100\mu m$,$u_{d,i} = 10m/s$,$T_\infty = 500K$,$P_{g,i} = 1atm$).

temperature is variable during the evaporation process. Its slope reaches a constant value after 0.1s. Then it stays nearly constant until 0.2s, when it starts decreasing rapidly, indicating that the droplet almost disappeared. On the right in Fig. 4.2, it is presented the droplet dynamics over evaporation time. The droplet decelerates completely near 0.1s after its injection on the chamber due to the drag caused by the surrounding air. Hence, the droplet dynamics concentrates the convection effects (mass and heat transfer) during the initial evaporation period.

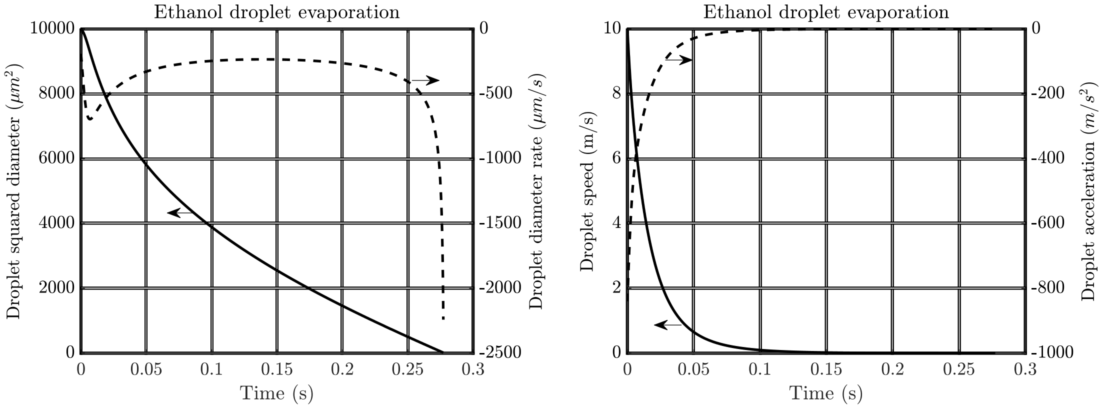

Figure 4.2 – Droplet squared diameter, diameter rate (left), speed and acceleration (right) versus evaporation time - Base Case ($T_{d,i} = 288.15K$,$D_{d,i} = 100\mu m$,$u_{d,i} = 10m/s$,$T_\infty = 500K$,$P_{g,i} = 1atm$).

The droplet temperature profile is presented in Fig. 4.3. The droplet heats up rapidly until 0.02s and then it starts cooling down after this peak. This behavior is completely different than presented in other analyses regarding droplet evaporation, as the amount of gases is finite here, thus its temperature and pressure vary constantly over time (as are indicated by Figs. 4.4 and 4.5). What justifies this cooling process is that the amount of energy related to vaporization overcomes the convective heat transfer from the surrounding gas to the droplet, as presented on the right of Fig. 4.3. After the peak, these energy sources balance each other, which justifies the asymptotic trend of the droplet temperature. Meanwhile, the kinetic energy presented no significant weight on droplet energy balance.

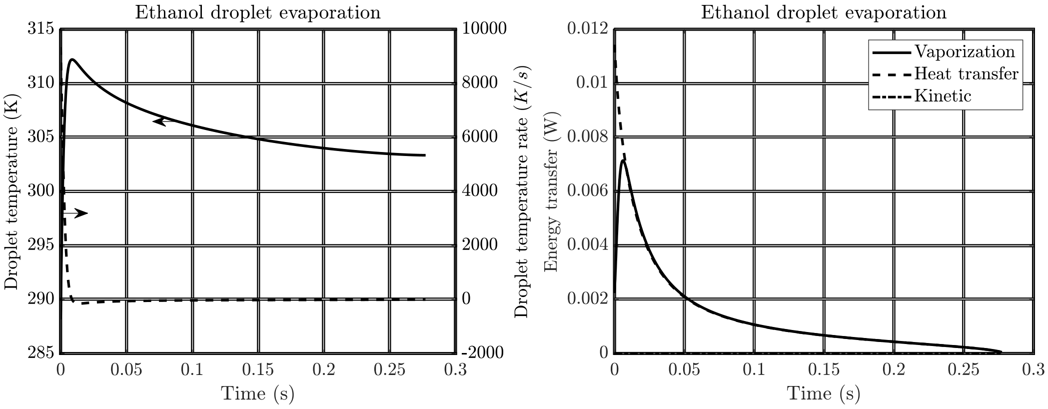

Figure 4.3 – Droplet temperature, temperature rate (left) and its energy sources (right) versus evaporation time - Base Case ($T_{d,i} = 288.15K$,$D_{d,i} = 100\mu m$,$u_{d,i} = 10m/s$,$T_\infty = 500K$,$P_{g,i} = 1atm$).

The surrounding gas behavior during evaporation is presented on Figs. 4.4 and 4.5. The former focus on the gas temperature and its rate over time and shows that the cooling process on the gas was evident, reducing from 500K to almost 360K during evaporation. This cooling process is commonly highlighted for ethanol as fuel, as it requires a considerably higher energy amount (i.e. heat of vaporization) than other commercial fuels for spark-ignition engines, such as gasoline. This temperature reduction is relatively high here as the air amount involving the ethanol droplet is following the stoichiometric air-fuel ratio ($A/F_{stoichiometric} \approxeq 9.0$). Additionally, the cooled gas affects directly the evaporation behavior, as it is visible on Figs 4.1 and 4.2. Lastly, a comparison between the evaporative cooling effect (i.e., the gas temperature reduction) obtained from this simulation and a simple estimation without taking into account the property variation over time indicates that the simple model was able to qualitatively predict the temperature reduction (139.9K *versus* 137.8K). Some questions may arise about this simple approach for more extreme cases, such as the low gas temperature variation and consequently its low property change. Still, the entropy generation will be somewhat overrated (5.3x$10^{-7}J/K$ *versus* 9.1$10^{-7}J/K$), which does emphasize the necessity for proper modeling and second law application in this phenomenon.

The gas pressure and its rate throughout evaporation are presented on the left in

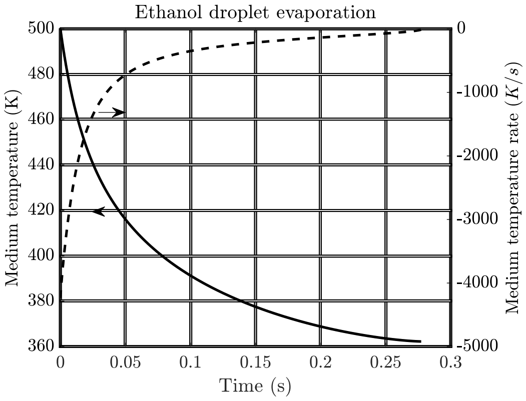

Figure 4.4 – Medium temperature and its rate versus evaporation time - Base Case ($T_{d,i} = 288.15K$,$D_{d,i} = 100\mu m$,$u_{d,i} = 10m/s$,$T_\infty = 500K$,$P_{g,i} = 1atm$).

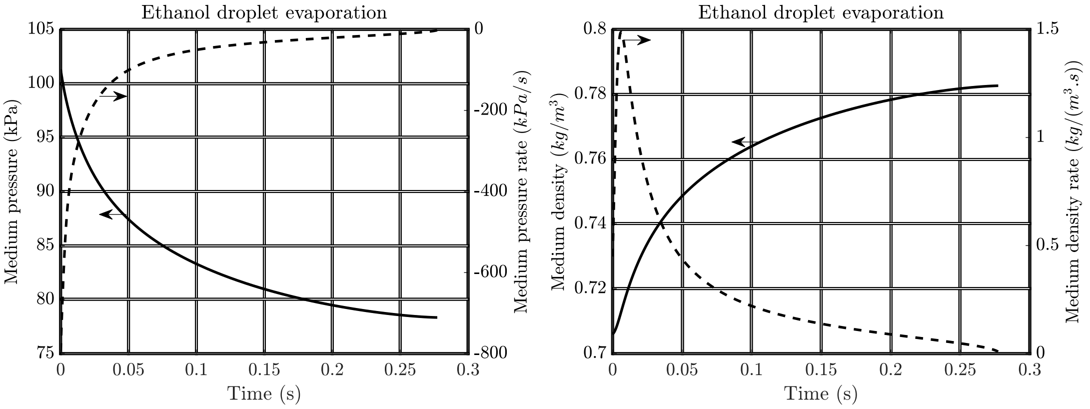

Figure 4.5 – Medium pressure, pressure rate (left), density and density rate (right) versus evaporation time - Base Case ($T_{d,i} = 288.15K$,$D_{d,i} = 100\mu m$,$u_{d,i} = 10m/s$,$T_\infty = 500K$,$P_{g,i} = 1atm$).

Fig. 4.5. The gas pressure reduces during evaporation owing to two different aspects: first, the volume occupied by the gas is growing during the process, as the droplet is reducing its own volume. Second, despite the additional ethanol mass entering the gas during evaporation, the temperature reduction clearly overcomes this effect, causing at the end a pressure reduction from 100 kPa to less than 80 kPa.

4.1.3 Parametric analysis

This parametric analysis aims to identify the behavior of relevant liquid fuel and in-cylinder gas properties on different initial conditions in DISI engines. The parameters of interest are droplet penetration, evaporation time, gas entropy generation and final gas temperature. All simulated conditions are described in Tab. 4.1.

First, the qualitative effect of the investigated properties at different initial droplet temperatures are illustrated by Figs. 4.6 and 4.7. Figure 4.6 indicates that the droplet penetration trends appears to change for one regime to another. At the beginning of compression, its trend accelerates at greater temperatures, while at the end of compression it is observed an almost linear profile. Meanwhile, the evaporation time maintains its qualitative tendencies for both regimes. However, the time necessary to evaporate the droplet is almost a order of magnitude smaller at the end of compression.

Both entropy generation and final medium temperature do not present any significant qualitative and quantitative variation for both regimes, as informed by Fig. 4.7. In fact, the charge cooling effect, estimated by the reduction of in-cylinder gas temperature, is almost the same (between 125 and 135K, depending on the compression case). This indicates that the cylinder pressure has almost no impact on the charge cooling effect under these conditions. As expected, the generated entropy decreases with the increase in droplet temperature as the temperature difference between droplet and medium reduce, besides the temperature difference between the initial and final (”wet bulb”) temperatures is reduced as higher degrees of droplet pre-heating occur.

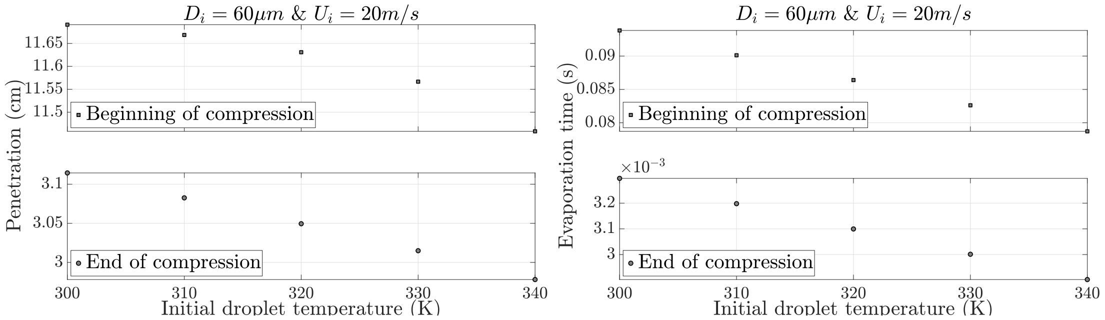

Figure 4.6 – Effects of initial droplet temperature on droplet penetration (left) and evaporation (right).

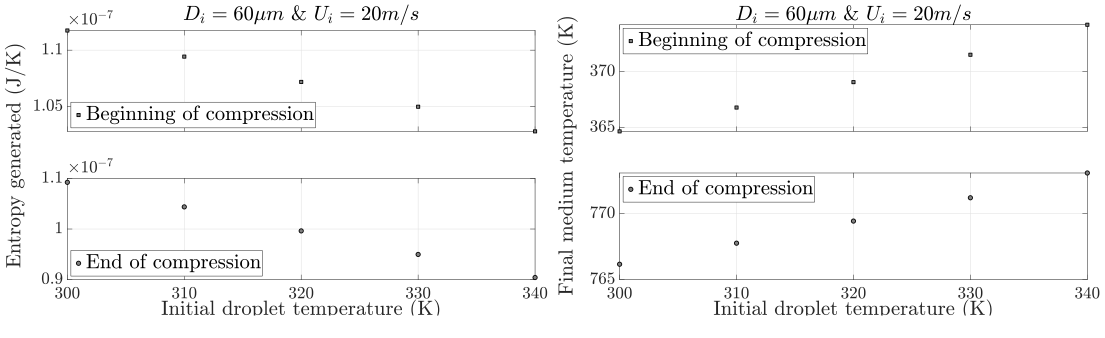

Figure 4.7 – Effects of initial droplet temperature on entropy generation (left) and final medium temperature (right).

The initial droplet velocity is a parameter that can be controlled by the pressure difference between the cylinder and the injector. The simulated influence of the velocity is shown by Figs. 4.8 and 4.9. Higher velocities barely change the tendencies for all four studied parameters, however, the droplet velocity has almost no influence on the final medium temperature with around one-degree difference (770 to 769K) for all simulated cases. Both droplet penetration and evaporation time reduce one order of magnitude between the beginning and the end of compression. Also, it is interesting to observe lower evaporation times from a stationary droplet to one with 10 m/s (convective heat transfer effect), however, the further increase in velocity only mildly influenced the evaporation time. Even though the entropy generated hardly alters for different in-cylinder regimes, it increases with initial droplet velocity.

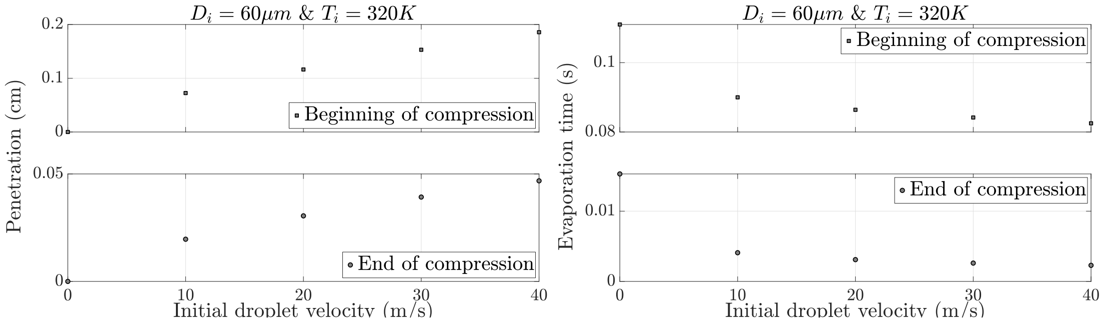

Figure 4.8 – Effects of initial droplet velocity on penetration (left) and evaporation (right).

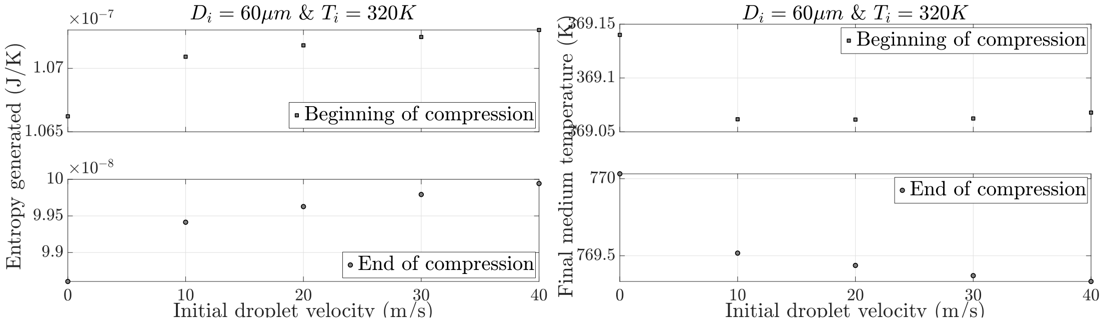

Figure 4.9 – Effects of initial droplet velocity on entropy generation (left) and final medium temperature (right).

Finally, the effects of initial droplet diameter are elucidated by Fig. 4.10 and 4.11. The droplet penetration and evaporation time exhibit a parabolic increase with the droplet initial diameter, which is expected as these parameters are proportional to the surface area of the droplet. Regarding the final medium temperature, the increase in droplet diameter slightly affects the temperature, although the profile changed with cylinder condition. At last, the rise in entropy generation is the highest among all initial properties. This is probably because more fuel has to evaporate owing to the increase of droplet's diameter.

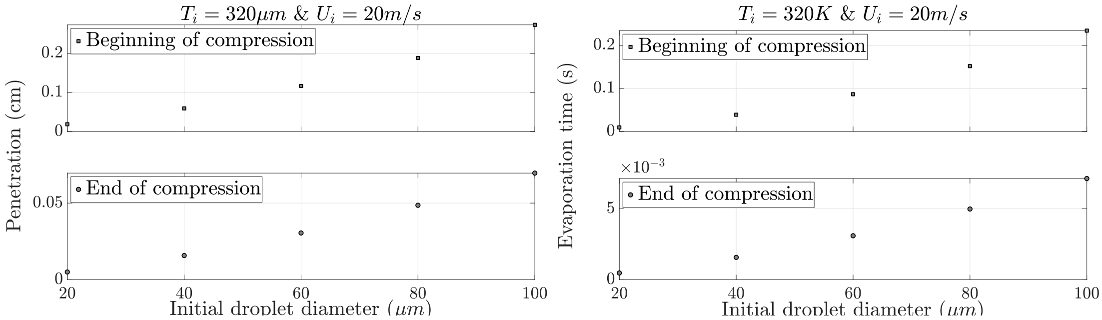

Figure 4.10 – Effects of initial droplet diameter on penetration (left) and evaporation (right).

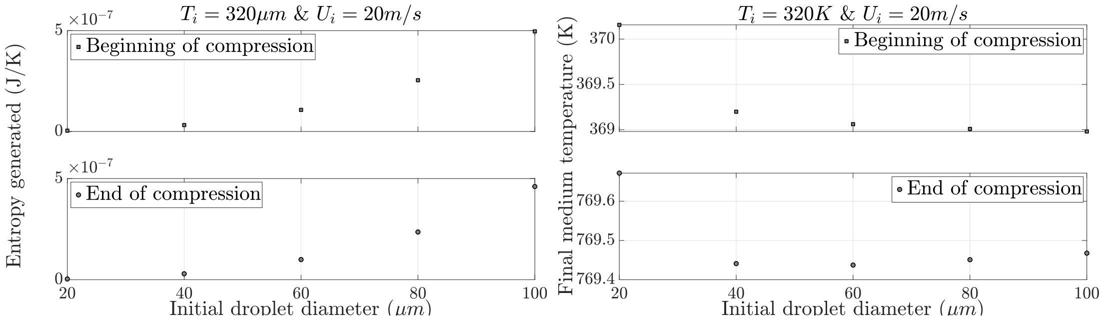

Figure 4.11 – Effects of initial droplet diameter on entropy generation (left) and final medium temperature (right).

Overall, this parametric study reveals some important characteristics regarding the evaporation of liquid ethanol. It is interesting to notice that greater droplet velocities increase penetration and reduces evaporation time, which are important parameters to investigate undesired events in a spark-ignition engine operation, such as fuel spray impingement and knock. These phenomena limit engine thermal efficiency improvement; besides, they affect pollutant gas emission. Moreover, the charge cooling effect appeared to be dominated by the temperature difference between the droplet and the in-cylinder gas, with medium pressure having little influence on this effect. In addition, the variation of droplet's velocity and diameter had only a slightly impact on the final medium temperature. As the initial droplet properties increased, temperature was the only studied property that decreased the generated entropy of the system. Additionally, entropy generation do not suffer a significant effect as the gas condition varies from the beginning to the end of compression.

4.2 Comparison of four different droplet evaporation models for a pure Ethanol droplet injection and evaporation

4.2.1 Base-case analysis

This study extended the droplet evaporation analysis presented previously by developing a comparison between four evaporation models presented in Section 3.1.5. This study was also based on similar conditions presented in Section 4.1.1. First, a base-case was defined to present some characteristics about the classical droplet evaporation model involved by a finite gas environment. The initial conditions are $D_d = 25\mu m$, $T_d = 288.15K$, $u_d = 10m/s$, $T_g = 900K$, $P_g = 1823.85kPa$ (18 atmospheres).

Figure 4.12 shows the droplet and surrounding gas temperatures over time. The classical approach was selected with a stoichiometric air-fuel ratio. The droplet temperature increases rapidly and near 0.3ms reaches a peak value. Additionally, the classical model predicts a slight cooling of droplet temperature after its peak. Moreover, the final temperature is near the wet-bulb temperature for ethanol under the final gas condition ($\approxeq 410K$). On the other hand, the gas temperature monotonically decreases during the process (almost 125K). Under conditions of a finite environment, the evaporation time increases when compared to an infinite environment, since the gas cooling over time affects negatively the convection phenomenon, hence it slows down the evaporation process on more realistic conditions.

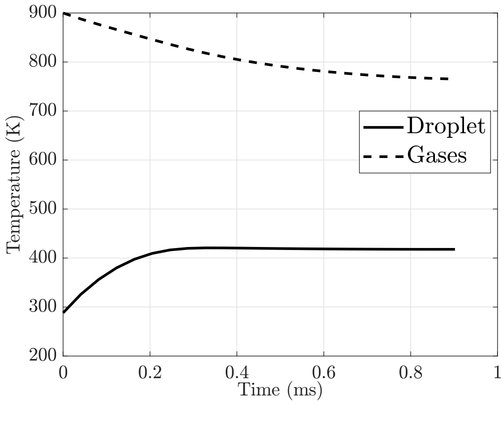

Figure 4.12 – Droplet and surrounding gas temperatures over time. (base-case + classical model)($D_d = 25\mu m$, $T_d = 288.15K$, $u_d = 10m/s$, $T_g = 900K$, $P_g = 1823.85kPa$)

Another result that corroborates the different behavior of this analysis is presented by Fig. 4.13, where the gas pressure profile is presented over time. The pressure notably reduces from 1800 to near 1600 kPa, therefore it interferes with the evaporation process by the vapor mass fractions over the droplet surface and the average mass fractions in the gas. Another piece of information available in the figure is the partial pressure of ethanol over time, in which its behavior is similar to the droplet temperature, but with a more intense reduction after its peak. In order to check the ideal gas validity near the final conditions of pressure and temperature found in this simulation, it was calculated the compressibility factor for ethanol, which provides $Z \approxeq 0.9$. Thus, the ideal gas model for ethanol is at its limit of validity at this point. Meanwhile, during earlier moments of evaporation, the gas pressure is higher and ethanol partial pressure is lower and both collaborate to a lower reduced pressure, therefore to an ideal gas condition ($Z \rightarrow 1.0$).

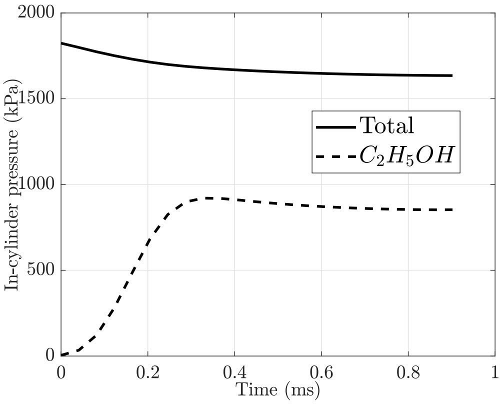

Figure 4.13 – Surrounding gas pressure over time. (base-case + classical model)($D_d = 25\mu m$, $T_d = 288.15K$, $u_d = 10m/s$, $T_g = 900K$, $P_g = 1823.85kPa$)

After understanding the temperature and pressure behaviors for the base-case condition, the author compared the previously mentioned four evaporation models in terms of the droplet and surrounding gas temperature profiles over time (Fig. 4.14). The time is normalized to compare the temperatures on the same basis. In the sub-figure 4.14 (a), it is evident that the classical model indicates the highest temperatures after the initial phase of evaporation. Moreover, it does not decelerate near 0.05, as it happens with the other three models. Therefore, the classical model overestimates the amount of energy transferred from the gases to the droplet. Another interesting characteristic of the left figure is that the temperatures of modified classical and non-equilibrium models do not tend asymptotically after the early moments of evaporation. These two models reach almost the same value during the whole simulation and reach the same value as the Abramzon model in the end. The latter model temperature profile presents an intermediate behavior, among the overestimated classical and the other two models. In the sub-figure 4.14 (b), the classical model underestimates the gas temperature cooling effect, although the difference among its result and the other three models is not significant (near 4K) at the end. Additionally, the other three models present the same profile for the gas temperature.

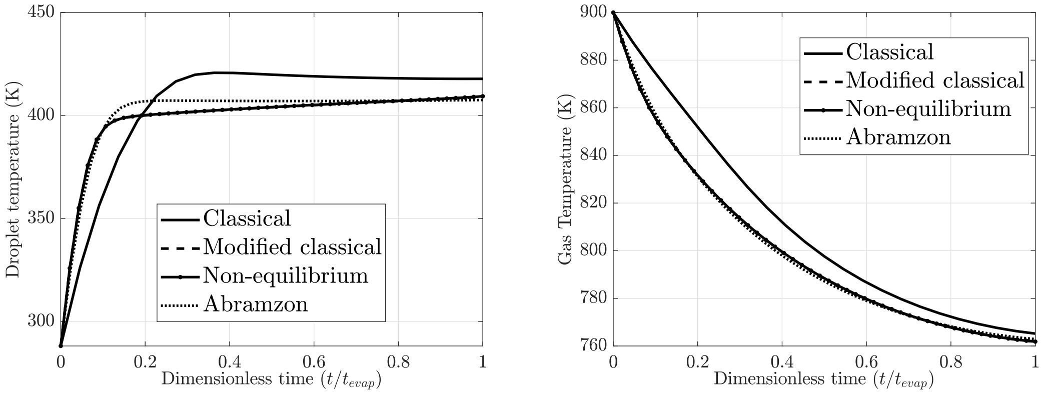

Figure 4.14 – Left (a): Droplet temperature profile; right (b): the surrounding gas temperature profile for different evaporation models - base-case ($D_d = 25\mu m$, $T_d = 288.15K$, $u_d = 10m/s$, $T_g = 900K$, $P_g = 1823.85kPa$).

The droplet diameter variation is shown by Fig. 4.15 for all droplet models. On the same time basis, the classical model overestimates the diameter during the whole process, instead of the other three models, which follow similar profiles. Moreover, the relative difference between the diameters may reach the maximum value of 10% in 0.35 dimensionless time, therefore they directly yield different results regarding the droplet surface for heat transfer, for instance.

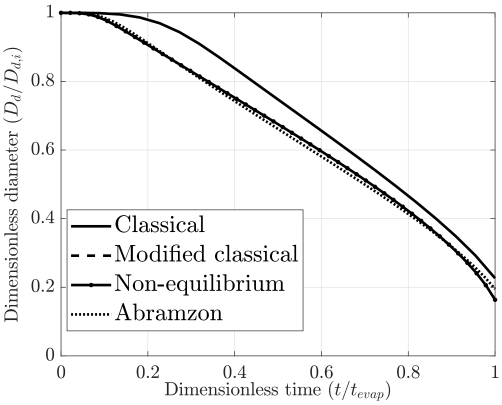

Figure 4.15 – Droplet diameter profiles for different evaporation models - base-case ($D_d = 25\mu m$, $T_d = 288.15K$, $u_d = 10m/s$, $T_g = 900K$, $P_g = 1823.85kPa$).

4.2.2 Relative air-fuel ratio effects on droplet evaporation

Now a comparison between the models is developed for different air-fuel ratios (A/F) on the evaporation process of a fuel droplet during the compression stroke of a SI engine. The results are presented in terms of droplet lifetime and penetration, as well as the evaporative cooling effect and the entropy generation for the gases. Additionally, these results highlight the main differences found for the four mentioned models in terms of these four variables.

First, droplet evaporation time and air-fuel ratio are shown in Fig. 4.16 during the final moments of compression. Evaporation time decreases as air-fuel ratio increases for all four models. The reduction is near 20% from the richest to the leanest mixture. The amount of surrounding gas over the droplet affects the evaporation process, since the higher the amount of mass the lower is the evaporative cooling effect over the gas temperature. Therefore, the time required to evaporate completely the droplet increases at richer air-fuel ratios. Furthermore, the classical evaporation model clearly underestimates the droplet lifetime, while the three others estimate higher times. The modified classical and non-equilibrium models predicted similar results in almost all cases presented here. Finally, the consolidated Abramzon model predicted an intermediate result, although more closely to the modified classical and non-equilibrium than to the classical.

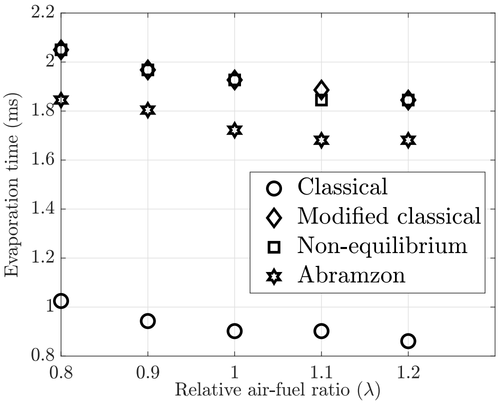

Figure 4.16 – Evaporation time versus ethanol air-fuel ratio for different evaporation models.

The droplet lifetime value indicates how long it would take for a droplet to evaporate inside the cylinder under these conditions. So, the aforementioned results show that independently of the chosen model, the order of magnitude of time shown for this condition is approximately $10°$ of crank angle (for an engine with 1000 RPM engine speed), which corresponds to a realistic condition for a droplet fuel in DISI engines.

Figure 4.17 presents the droplet penetration for all four models. The penetration is slightly reduced at higher relative air-fuel ratios since the droplet lifetime and pressure drop reduces on leaner mixtures. Moreover, the model which deviates clearly from all results is the classical model, underestimating the droplet displacement. This behavior is related to the underestimation of evaporation time. Meanwhile, the other three models agree well on all conditions.

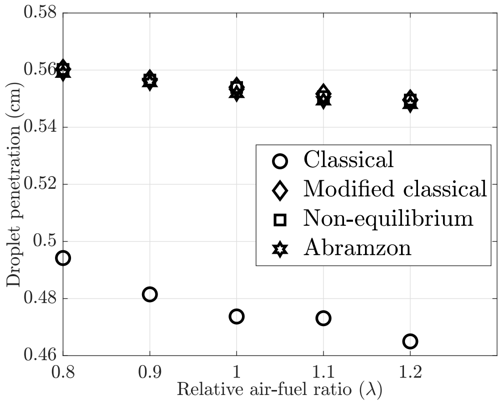

Figure 4.17 – Droplet penetration versus ethanol air-fuel ratio for different evaporation models.

The utility of droplet penetration is to identify a possible occurrence of fuel impingement on cylinder walls, which cause unburned fuel emissions in ICEs. Thus, based on the presented results, there is a possibility to occur such phenomenon on the conditions presented here, especially for fuel injections during the end of compression, when the distance between the piston head and the fuel injector is close to $5mm$.

The evaporative cooling effect caused by droplet evaporation in the surrounding gases is shown by Fig. 4.18. Richer relative air-fuel ratios cause higher temperature reductions in the surrounding gas, as the amount of air available to provide enough energy to cause evaporation is reduced. The difference between the extremes ($\lambda = 0.8$ and $\lambda = 1.2$) reaches almost 50K for all mentioned models. Furthermore, the four evaporation models did not present great differences in this result, although the classical model underestimates a little the gas cooling in all cases.

The benefit of evaporation cooling in DISI engines is to reduce the gas temperature before fuel combustion starts, which may avoid the occurrence of knock phenomenon under specific conditions in the engine. Therefore, this extra cooling effect obtained from fuel direct injection during the compression stroke offers a possible perspective of a compression ratio increase and extra power per engine cycle.

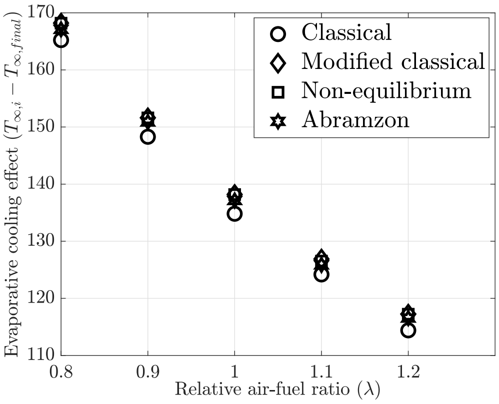

Figure 4.18 – Gas evaporative cooling versus ethanol air-fuel ratio for different evaporation models.

At last, Fig. 4.19 shows the entropy generation occurred in the surrounding gas control volume for all evaporation models. The classical evaporation model indicates the lowest entropy generation for all cases, independently of the air-fuel ratio. This result connects directly with underestimated droplet evaporation times and overestimated convection effects on the droplet surface. Therefore, the classical model reflects a more idealistic condition in which evaporation occurs. The other models present a higher entropy generation, which indicates more realistic calculations in terms of time evaporation and second law effects. The Abramzon model, which takes into account the film theory, yields an intermediate result both in terms of evaporation time and entropy generation among the four models. Another point to be considered is the main source of irreversibility on this process, which is the convective heat transfer, with minor contributions from the fuel-gas mixture. Furthermore, the leaner conditions showed the lowest specific entropy generation, followed by the stoichiometric and at last the richer conditions. This behavior is connected with lower gas temperature reduction and droplet lifetime found in leaner conditions, which suggests a more efficient evaporation process.

These results for entropy generation offer the possibility of a thermodynamic optimization together with the main common evaporation variables such as those presented in this study, i.e., droplet lifetime and penetration. A connection between these variables is evident. Thus, lower entropy generation presents a possibility to offer optimal conditions to fuel direct injection in engines during the compression phase.

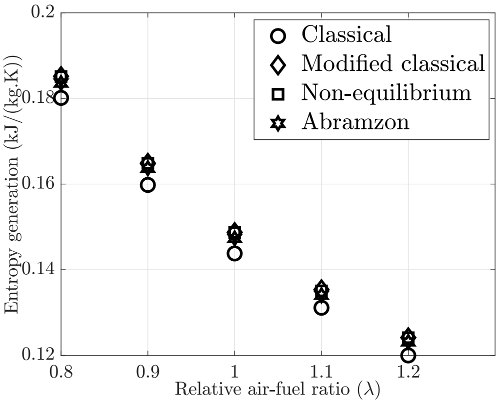

Figure 4.19 – Surrounding gas entropy generation versus ethanol air-fuel ratio for different evaporation models.

4.3 Second law analysis of wet ethanol droplet evaporation during a direct-injection spark-ignition engine compression stroke

4.3.1 Simulation cases

The simulation initiates at the bottom dead center (BDC) of the compression stroke ($\theta = 180°$) for all cases. The fuel is injected at different moments to verify the difference in the droplet evaporation process and on the gases entropy generation, in order to evaluate possible opportunities for a thermodynamic optimization. First, a base-case is presented to establish reference values for important droplet injection and evaporation parameters in our analysis, such as droplet lifetime, evaporative cooling and entropy generation on the gas control volume. The Abramzon-Sirignano model was selected to simulate the droplet evaporation. Thereafter, a parametric analysis is developed on droplet composition effects, as well as on initial conditions of the fuel injector, the droplet, and air-fuel ratio on the evaporation process in a piston-cylinder system. The initial ethanol-water liquid volumetric fraction is changed to identify possible effects of droplet composition on output model variables, such as droplet lifetime, evaporative cooling, and entropy generation on the gases. The obtained trends for all cases are presented as functions of the studied inputs described in Tab. 4.2. These inputs try to cover realistic values for these variables. For example, v_{H_2O} covers possible volumetric water contents in wet ethanol, whereas T_d, D_d, and θ_{inj} cover some conditions for the fuel injector operation. Finally, λ, r, N_{engine} act on different engine operation conditions and how they affect the fuel evaporation process.

Table 4.2 – Initial conditions.

	Base-case	Par. analysis
$v_{H_2O}\,(\%v.)$	10	$[0, 5, 10, ..., 40, 45, 50]$
λ	1.0	$[0.9, 1.0, 1.1, 1.2]$
$T_d\,(K)$	300	$[300, 330]$
$D_d\,(\mu m)$	45	$[15, 30, 45, 60]$
$\theta_{inj}\,(^\circ)$	270	$[240, 270, 300]$
$r\,(-)$	12	$[12, 14, 16, 18]$
$N_{engine}\,(RPM)$	1000	$[1000, 4000]$

4.3.2 Base-case analysis

A base-case analysis is presented in order to demonstrate the thermodynamic behavior of the studied system and how the droplet evaporation process influences in the gas evolution throughout the compression stroke. Figure 4.20 presents the droplet and gas temperatures, besides the gas pressure during compression. The wet ethanol droplet is injected in the in-cylinder gases and it is heated by the convection while it evaporates over time. The heat-up process is completely variable under these conditions, since the environment conditions (i.e. temperature, pressure, and ethanol/water mass fractions) change during the whole droplet lifetime. Therefore, there is no asymptotic tendency for the droplet temperature.

Meanwhile, the gas temperature increases until fuel injection takes place. This injection causes an evaporative cooling effect on the gases, as noticed by the sudden reduction on the gas temperature, in spite of the presence of some additive energy sources (e.g., cylinder heat transfer and compression work). Later, the temperature rises back until the end of compression, where the evaporation effects overcomes the aforementioned gas energy sources. The gas pressure follows a similar trend as in SI engines, with a little ”bump” right next to fuel injection in the system.

The gas composition over time (Fig. 4.21 a) changes as the droplet evaporates. The higher ethanol volatility dominates the evaporation over water, thus causing a predominance on the gas mass fraction during evaporation. Also, the ethanol rapid increase in the gas composition during the early stage contains its subsequent evaporation (due to Raoult law and $B_{M,i}$ expression), as noticed by its fractional evaporation rate in Fig. 4.21. Meanwhile, water evaporation rate reaches an almost constant value near 270° until the end of the droplet lifetime, because of its relative increase on liquid mass fraction over ethanol and its low gas mass fraction during the process. Moreover, the droplet diameter profile does not follow the widespread

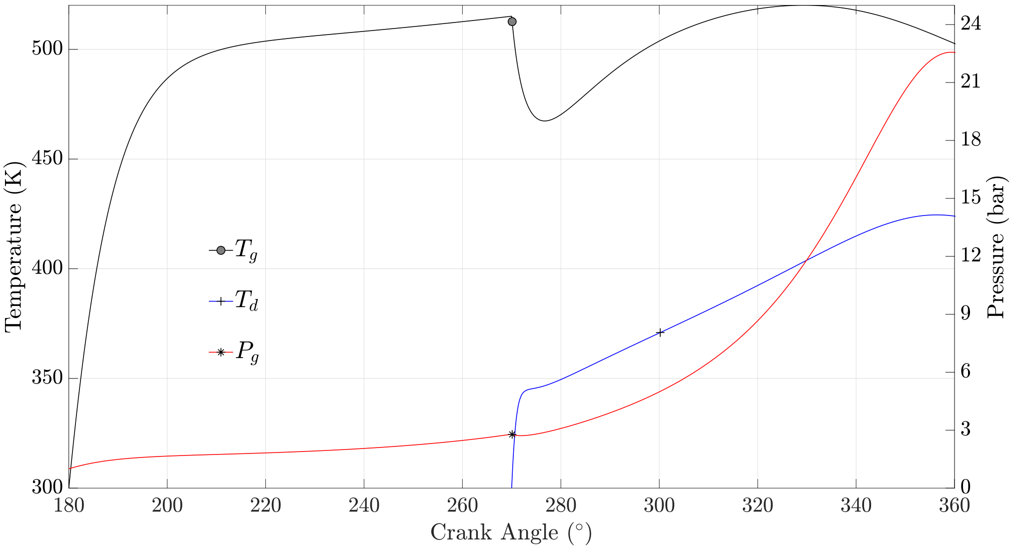

Figure 4.20 – Droplet and gas behaviors (left: temperature, right: pressure) versus crank angle - base case.

D^2 law due to the commented evaporation profile. Also, the droplet swelling effect is clearly noticeable during the first crank angle degrees, as highlighted by the box in Fig. 4.21 a.

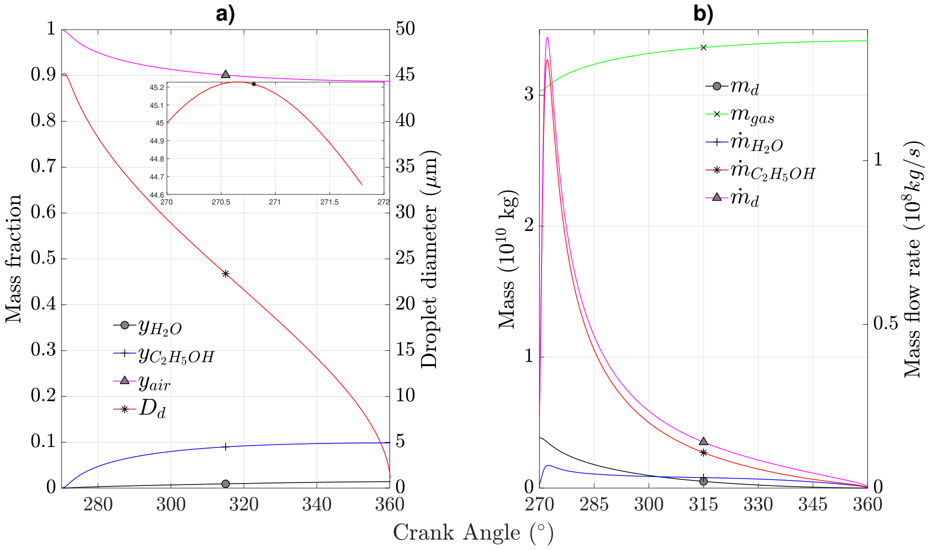

Figure 4.21 – a) Droplet size and gas composition versus crank angle; b) droplet, gas mass, and fractional evaporation rates versus crank angle - base case.

After understanding the main effects of evaporation on the studied system, the focus was presenting these effects under the view of the second law of thermodynamics. As Fig. 4.22 shows, there are two moments where the entropy generation increases: first, before fuel injection takes place and later, when the fuel is injected and the gases starts providing energy to the droplet for its heating and evaporation. This gas-droplet convection process is the main positive entropy transfer on the system, overcoming the final gas entropy reduction. Moreover, the cylinder wall heat transfer collaborates positively at the end of the process, although its influence varies throughout the simulation, mainly because of the evaporative cooling process in the middle of compression. On the other hand, the chemical mixture entropy component does not contribute as much as the other components to the entropy generation.

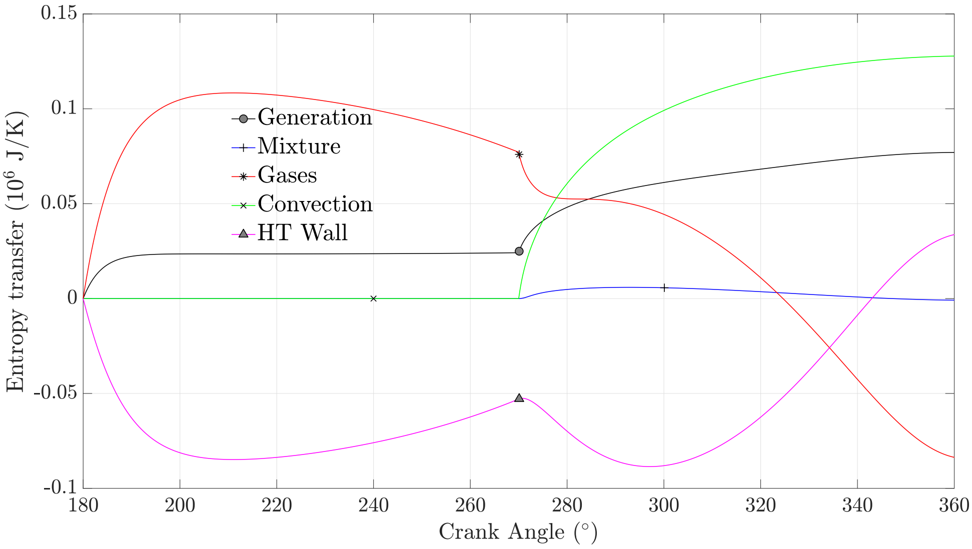

Figure 4.22 – Entropy transfer sources and entropy generation versus crank angle - base case.

In order to highlight the influence of the droplet evaporation process on our studied system, Fig. 4.23 indicates the suggested first (left) and second law (right) efficiencies for this process and their energy/exergy sources. Both first and second law efficiencies grows rapidly as convection predominates both droplet heating (sensible energy) and evaporation (latent energy). Additionally, they reach out almost asymptotic values after most of the cumulative droplet sensible energy stabilizes, which indicates that almost 100% of convection causes the fuel evaporation. An interesting point is that the exergetic efficiency is always higher than its first law equivalent, reaching out a cumulative value of 90% exergy conversion in the end.

4.3.3 Parametric analysis

A parametric analysis is developed for this study for different water contents of wet ethanol (up to 50% v/v) and air-fuel ratios (from rich to lean conditions). The purpose is to evaluate the main tendencies of certain observed parameters (i.e., droplet evaporation efficiencies, entropy generation, evaporative cooling effect, Top-dead center gas temperature, knock integral value, complete evaporation angle/time) as functions of the input parameters presented in Tab.

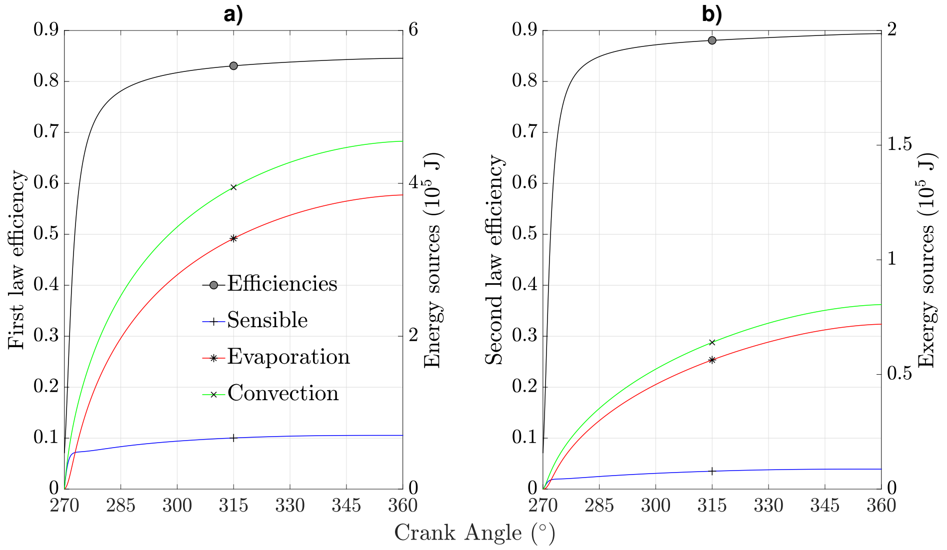

Figure 4.23 – Evaporation efficiencies and their respective energy/exergy sources (left: first law; right: second law) versus crank angle - base case.

4.2. These tendencies provide important information to find optimal conditions for the evaporation process in DISI engines. All results from this section are indicated in terms of contour curves. It was filtered the most interesting results for each input from this analysis to present in the text, in order to avoid an excessive amount of figures for all parameters.

4.3.3.1 Fuel pre-heating effects

The focus of this section is in showing how fuel pre-heating affects the droplet evaporation process. It was assumed that the flash boiling phenomenon is negligible under the conditions studied. Figures 4.24 and 4.25 indicate how pre-heating wet ethanol affects droplet evaporation first and second law efficiencies. These are the best result that features how fuel pre-heating affects droplet evaporation in our analysis. Higher efficiencies are obtained for leaner and less humid fuels. Moreover, increasing water content cause more intense reductions in both efficiencies for richer mixtures than for leaner ones. Another featured point is that droplet pre-heating increases both energetic and exergetic efficiencies, besides it reduces the difference between these two parameters. Basically, droplet pre-heating adds up sensible energy to the droplet, thus it collaborates to an easier evaporation inside the engine.

4.3.3.2 Droplet atomization level

The featured results for droplet atomization are presented by Figs. 4.26-4.27. which involve TDC temperature and knock integral value. Top-dead center gas temperature varies

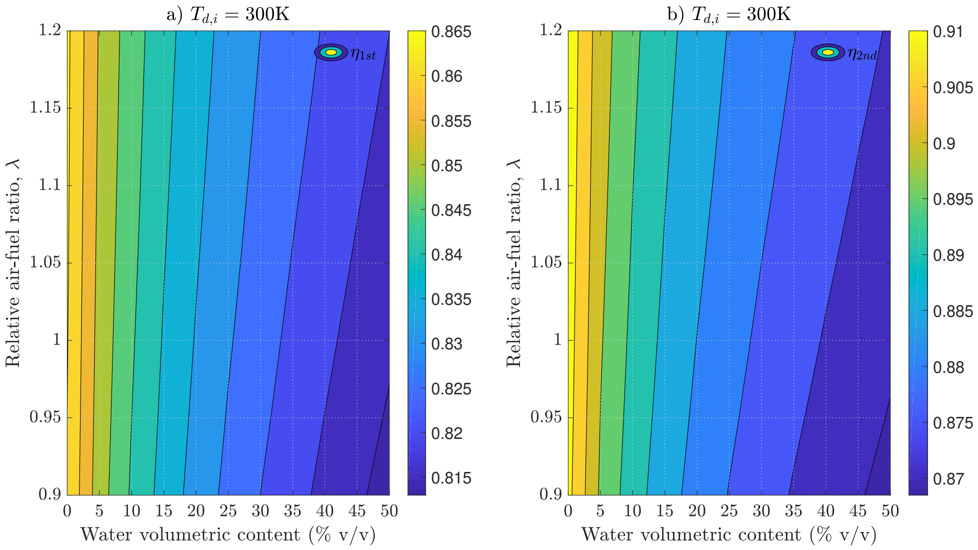

Figure 4.24 – First (a)) and second (b)) law efficiencies contour curves for wet ethanol droplet evaporation in terms of λ and v_{H_2O} at $T_{d,i} = 300$K.

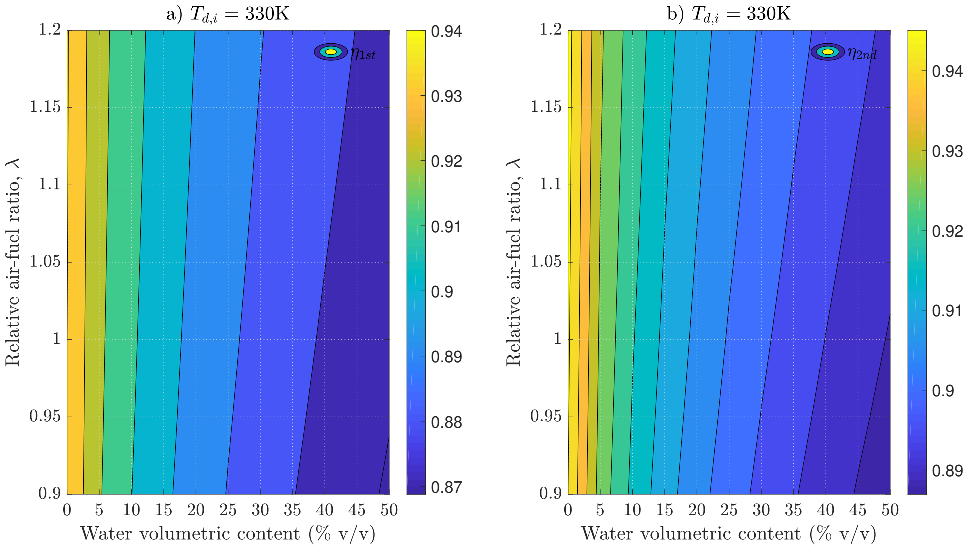

Figure 4.25 – First (a)) and second (b)) law efficiencies contour curves for wet ethanol droplet evaporation in terms of λ and v_{H_2O} at $T_{d,i} = 330$K.

significantly with initial droplet diameter, with a displacement to lower water content regions as the droplet gets bigger. The reason is the ratio between specific heats of vapor water and air, as the amount of both substances increases with droplet size. Also, higher water contents contains higher peak compression temperatures to be reached in our presented system. Then, there is a balance between these two parameters, especially for 15μ m. Following a similar trend, the knock integral value presents a clear gradient with water content for all cases.

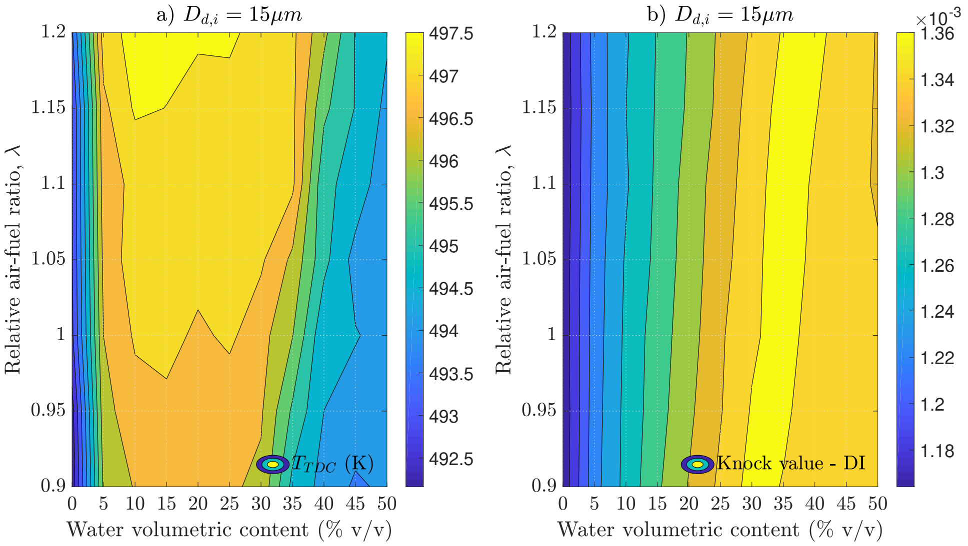

Figure 4.26 – Top-dead center gas temperature (a)) and knock integral value (b)) contour curves for wet ethanol droplet evaporation in terms of λ and v_{H_2O} at $D_{d,i} = 15\mu m$.

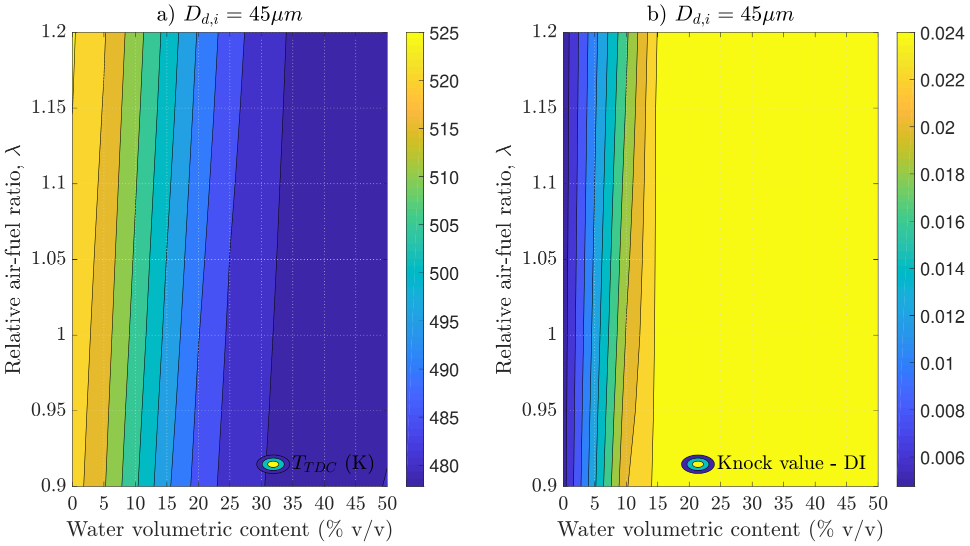

Figure 4.27 – Top-dead center gas temperature (a)) and knock integral value (b)) contour curves for wet ethanol droplet evaporation in terms of λ and v_{H_2O} at $D_{d,i} = 45\mu m$.

4.3.3.3 Injection timing

Fuel injection timing in DISI engines is essential for the desired combustion mode for the engine cycle, thus how start of injection (SoI) affects the observed variables is investigated sub-sequentially. Figures 4.28-4.29 show that late injection dislocated the final evaporation angle/time regions to after $440°$, which indicates that complete evaporation is not achieved for many cases of high water volumetric contents. It is worth remembering that the engine simulations represent motoring condition, i.e., there is no combustion stroke for this engine cycle.

Since complete evaporation takes a certain amount of time, the fuel injection angle must be anticipated to guarantee either a more homogeneous combustion mode or an efficient combustion during the engine cycle.

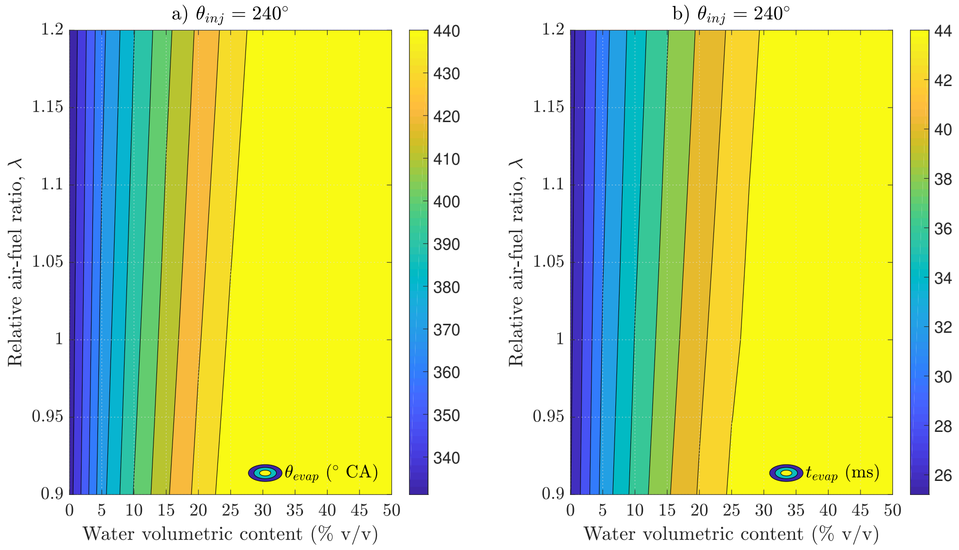

Figure 4.28 – Final evaporation angle (a)) and time (b)) contour curves for wet ethanol droplet evaporation in terms of λ and v_{H_2O} at $\theta_{inj} = 240°$ ATDCi.

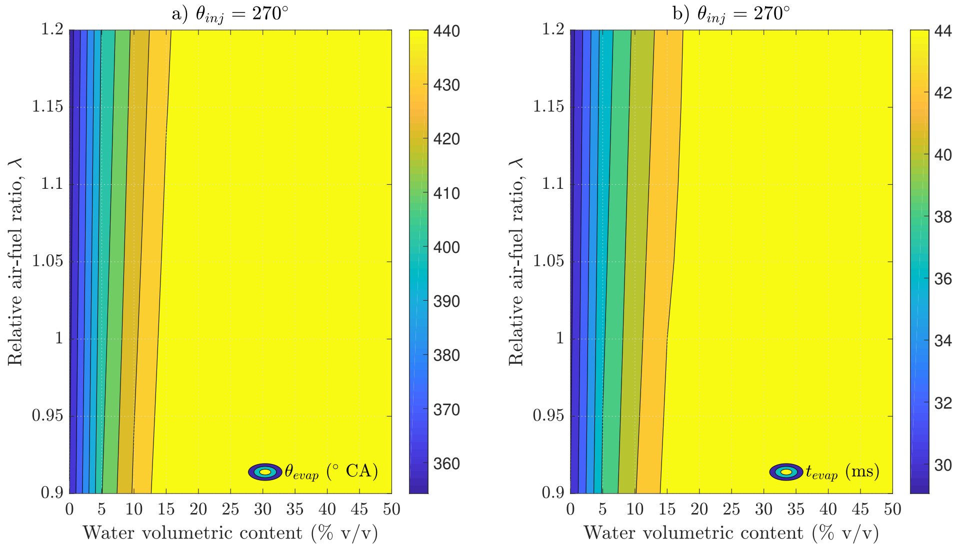

Figure 4.29 – Final evaporation angle (a)) and time (b)) contour curves for wet ethanol droplet evaporation in terms of λ and v_{H_2O} at $\theta_{inj} = 270°$ ATDCi.

4.3.3.4 Compression ratio and Engine speed

After presenting parametric analyses about variables associated to fuel injection, focus is given now to some engine parameters such as compression ratio and engine speed.

The presented model was not able to perceive any effects of compression ratio neither on the evaporation process nor on the knock index number, even though there is a clear relationship between these features. One possible reason for this is the environment dimension variation for each case, since the surrounding gases mass and its volume are obtained from the relative air-fuel ratio and the fuel droplet diameter and composition, which therefore modifies the amount of heat that directs from the cylinder walls to heat up the gases. A realistic dimension of the engine cylinder would cover this misperception obtained from the presented model.

On the other hand, the engine speed showed its importance for all the studied parameters. The droplet evaporation first and second law efficiencies reduced as the engine speed increased from 1000 to 4000 RPM, as indicate Figs. 4.30-4.31. Faster engine cycles do not give the droplet enough time to completely evaporate during the compression stroke. In addition, water only further complicates this process. Faster gas temperature and pressure variations at higher engine speeds cause rapid variations in the droplet's properties, collaborating to more energy being directed to sensible energy, rather than evaporation. Thus, only partial evaporation happens until the middle of expansion stroke for most cases. This behavior shows the direct dependency between droplet lifetime, engine speed and fuel injection timing for a proper engine operation with an adequate combustion. Contextualizing for real engines operation, complete evaporation would still happen due to extra heat transfer from the (less efficient) combustion process. Still, the combustion most probably yielded some undesired products such as unburned hydrocarbons and would not be as efficient as expected for a completely gaseous combustion, independently if it was homogeneous or stratified.

Another interesting point to highlight is the effect of higher turbulent kinetic energy and average gas velocity in the droplet evaporation. It is expected that evaporation accelerates at a higher engine speed due to the previously mentioned features.However, both turbulent kinetic energy and average gas velocity effects are (partially) included on the heat and mass transfer coefficients, since their correlations were experimentally obtained under several different conditions (laminar and turbulent). So, the author believes that these effects are already partially included in the results. In addition, the effects of average gas velocity affect more directly the calculations by its inclusion on the droplet Reynolds number, but this model assumed that the relative velocity between the droplet and the surrounding gases could be exclusively approximated by the droplet velocity (i.e., $|u_d - u_g| \approx u_d$).

The entropy generation peak region is displaced to lower water content regions

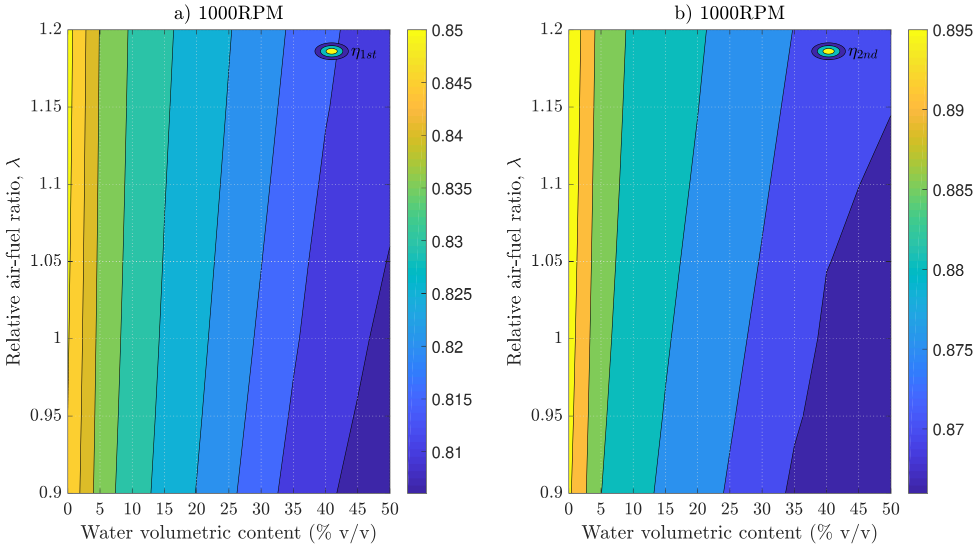

Figure 4.30 – First (a)) and second (b)) law efficiencies contour curves for wet ethanol droplet evaporation in terms of λ and v_{H_2O} at 1000RPM.

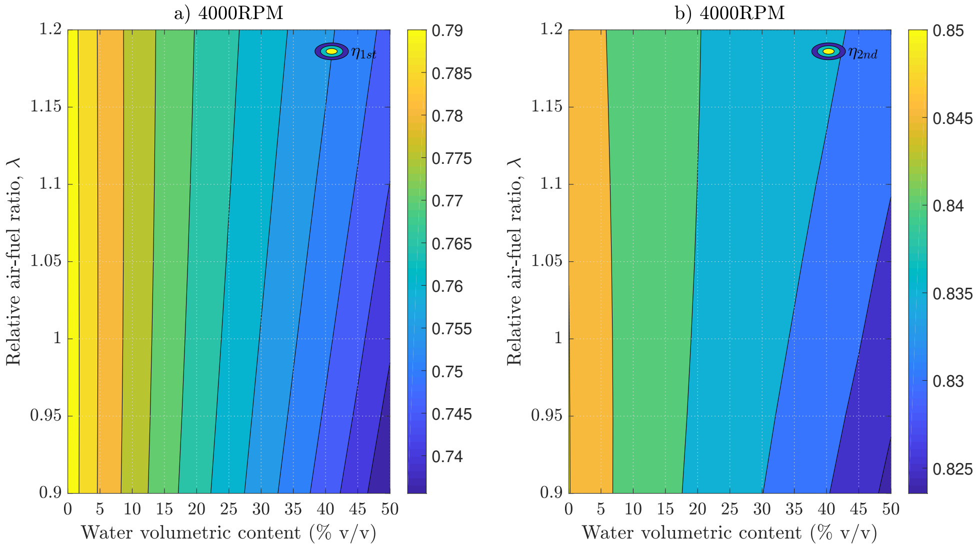

Figure 4.31 – First (a) and second (b) law efficiencies contour curves for wet ethanol droplet evaporation in terms of λ and v_{H_2O} at 4000RPM.

at a higher speed, as presented by Figs. 4.32-4.33. Engine speed also increase the entropy production by 15%, as faster engine cycles enhance the heat transfer coefficients, therefore the entropy production rate. Meanwhile, the charge cooling effect is also displaced from the southeast region to the northwest at higher speeds. Moreover, the 4-fold reduction in engine cycle period collaborates to double the evaporative cooling obtained.

The Top-dead center gas temperature is considerably reduced at higher engine speeds, as the peak values reduce from 515K to 416K in Figs. 4.34-4.35. Additionally, the temperature gradient is more clear at 4000 than at 1000 RPM. Meanwhile, the cumulative knock integral

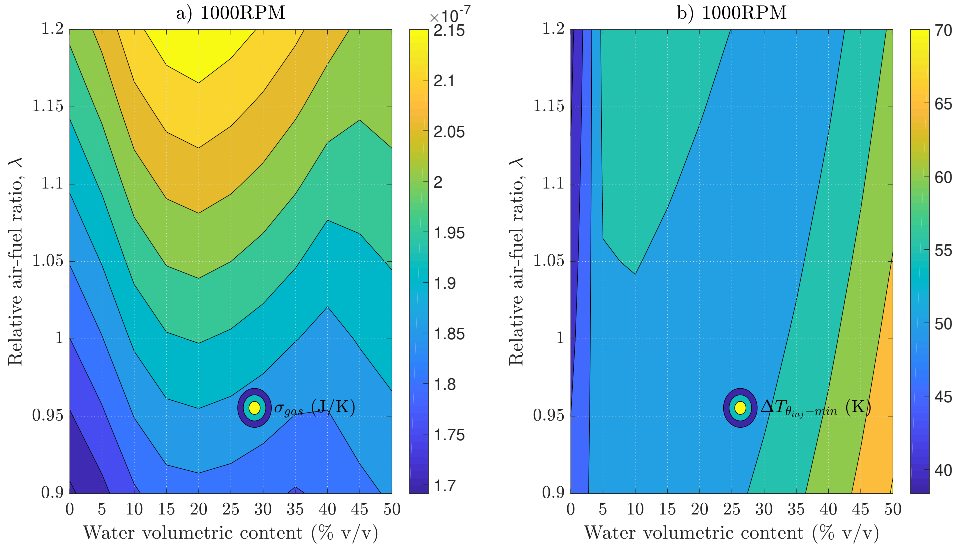

Figure 4.32 – Entropy generation (a)) and evaporative cooling effect (b)) contour curves for wet ethanol droplet evaporation in terms of λ and at 1000 RPM.

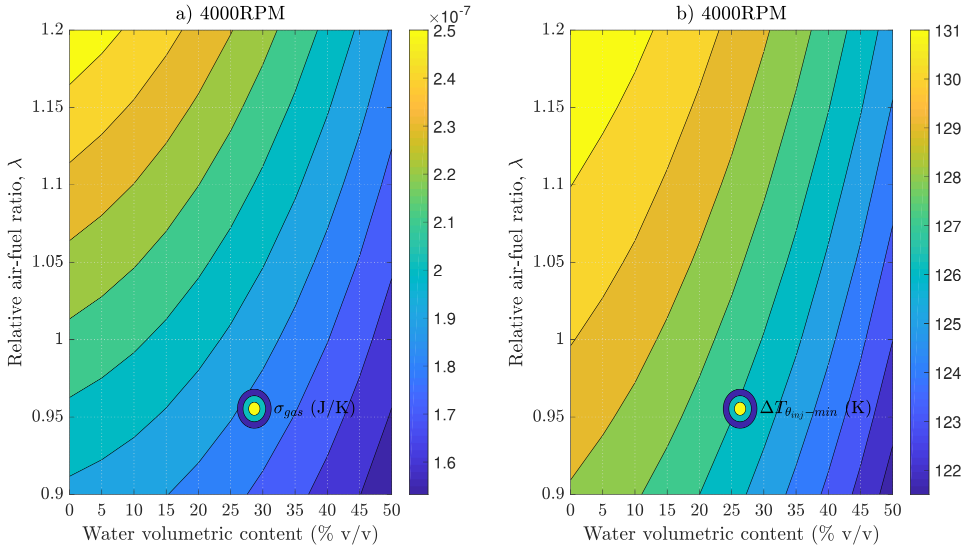

Figure 4.33 – Entropy generation (a)) and evaporative cooling effect (b)) contour curves for wet ethanol droplet evaporation in terms of λ and at 4000 RPM.

value is strongly reduced at 4000 RPM (more than 2-fold reduction at peak conditions), since a faster engine cycle does not give enough time to auto-ignition to occur.

One observation is that the 4000 RPM simulations did not provide any case where complete evaporation occurs until 450° CA. Since the simulations did not take into account energy from combustion, so the available energy sources were not capable of completely evaporate the fuel droplet under presented conditions. Hence, the authors decided not to present the results for final evaporation angle/complete evaporation time for 4000 RPM.

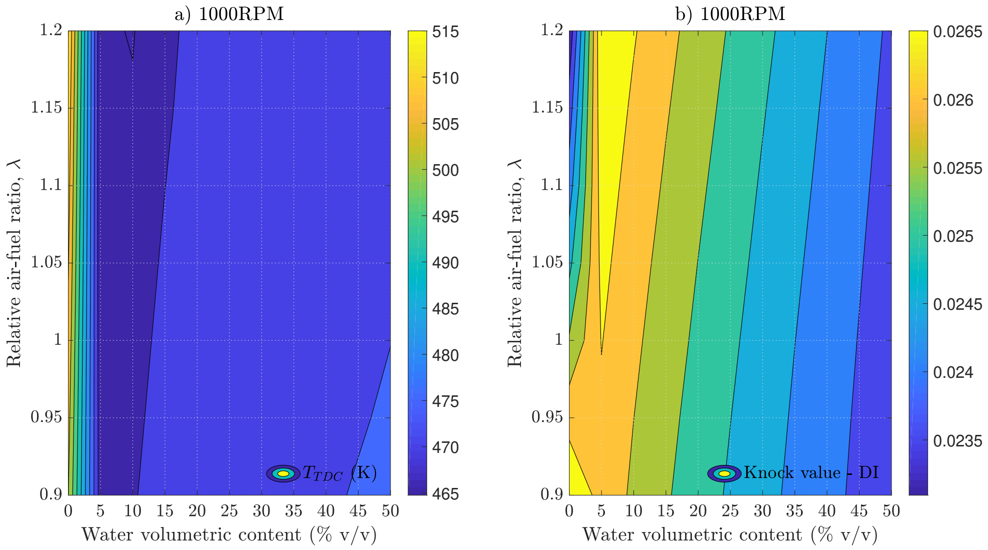

Figure 4.34 – Top-dead center gas temperature (a)) and knock integral value (b)) contour curves for wet ethanol droplet evaporation in terms of λ and v_{H_2O} at 1000 RPM.

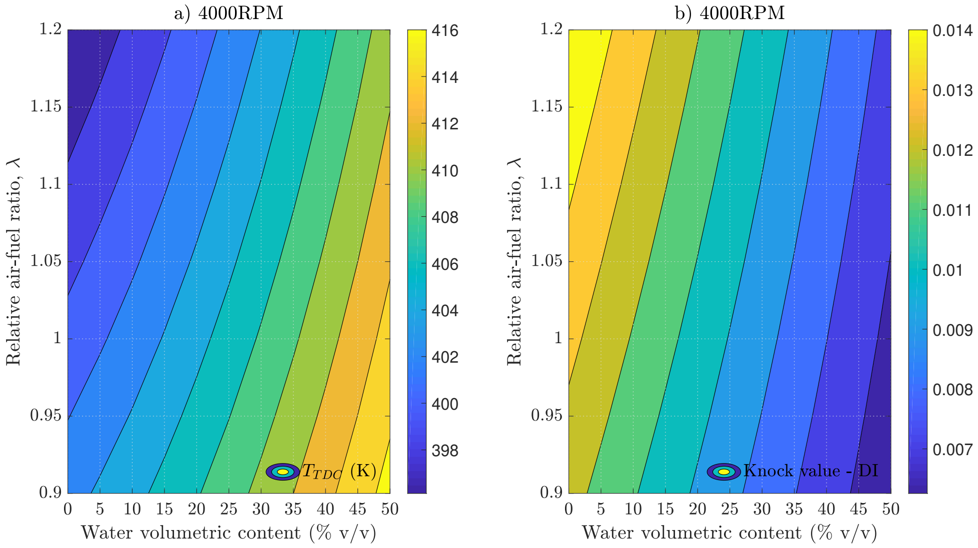

Figure 4.35 – Top-dead center gas temperature (a)) and knock integral value (b)) contour curves for wet ethanol droplet evaporation in terms of λ and v_{H_2O} at 4000 RPM.

4.3.3.5 Remaining results and discussion

This section compiles all minor results that the parametric analysis provided, yet they were not highlighted in previous sections. All tendencies presented in this section are secondary effects when compared to the ones presented in previous section, however they can still be applied to optimize the droplet evaporation process for the system in study. Thereafter, Tab. 4.3 overviews the qualitative tendencies of each observed parameter for each studied input.

Increasing the droplet size lowered the efficiencies for all cases. This size increase enhanced the energy directed towards the liquid phase sensible energy/exergy instead of latent energy/exergy. Meanwhile, delaying fuel injection reduced energetic and exergetic efficiencies for all conditions and avoided complete evaporation to occur before $450°$ CA (during expansion).

Pre-heating the fuel caused a reduction on entropy production for all lambda/water combinations. Meanwhile, the entropy generation increased as bigger droplets were injected and evaporated. There was a balance between the entropy sources mentioned in Eq. 3.35 (e.g., fuel-air mixture, droplet and wall heat transfer, and gas state variation) which collaborated to such change of entropy generation peak between droplet sizes. Additionally, neither delayed fuel injection nor higher compression ratios contributed to any significant entropy changes in the studied conditions.

In the case of evaporative cooling effect, pre-heating reduced this parameter and the highest values are encountered in the richest and high-water fraction regions (i.e., less air and higher latent heat of evaporation). In addition, the evaporative cooling reduced as droplet size increased, due to the environment dimension variation, as explained for the compression ratio case. Additionally, higher charge cooling values were obtained for late injections. Only slightly increases were found for both entropy generation and evaporative cooling effect at higher compression ratios.

The connection between top-dead center gas temperature and knock is clear, still only very mild differences were obtained with fuel pre-heating, which indicates that this level of pre-heating does not significantly affect both temperature and cumulative knock integral value. On the other hand, higher water contents decreased the gas temperature at TDC and increased knock occurrence (due to a higher in-cylinder mass prior to combustion), whereas leaning the mixture did not affect significantly both variables under simulated conditions. Also, gas TDC temperatures drastically reduced as fuel injection delayed from 240 to $300°$.

Finally, final evaporation angle and total evaporation time associated directly with homogeneous combustion for DISI homogeneous mode, but only slight reductions (approximately $10°$) were obtained for a hotter droplet. Moreover, their maximum were found for high water mixtures, with leaner mixtures only collaborating softly in reducing both the final evaporation angle and time. Additionally, these two variables have a clear dependency on droplet atomization, with results showing that the bigger the droplet size, the slower is the evaporation process. The main reason is the decrease of droplet surface area-volume ratio, thus there are more fuel to be evaporated even though the heat transfer rates also increase. This result connects directly with the evaporation efficiencies, as previously commented. Finally, no response was found of higher compression ratios on the final evaporation angle.

A table which encompasses all qualitative tendencies of the simulation input and output parameters is presented by Tab. 4.3. This table also presents the directions of some figures which were not presented in the text, whose tendencies are not significantly interesting. Some dependencies are not completely clear, as commented earlier, still this table gives a qualitative direction of how each one of these variables influence on droplet evaporation, compression stroke and on the engine cycle.

Table 4.3 – Parametric analysis overview.

	η_{1st}	η_{2nd}	σ_g	$\Delta T_{\theta_{inj}-\theta_{T_{min}}}$	T_{TDC}	$K_{In,TDC}$	θ_{evap}	t_{evap}
v_{H_2O} (↑)	↓	↓	↑	↑	↓	↑	↑	↑
λ (↑)	↑	↑	↑	↓	↑	-	↓	↓
T_d (↑)	↑	↑	↓	↓	-	-	↓	↓
D_d (↑)	↓	↓	↑	↓	↑↓	↑	↑	↑
θ_{inj} (↑)	↓	↓	↓	↑	↓	↓	-	-
r (↑)	-	-	-	-	-	↑	-	-
N_{engine} (↑)	↓	↓	↑	↑	↓	↓	-	-

5 WET ETHANOL SPRAY INJECTION DURING THE COMPRESSION STROKE OF A DISI ENGINE

This chapter extended the wet ethanol direct injection study by taking into account the fuel spray injection and evaporation processes in a compression stroke of a DISI engine. The main objective was to evaluate how droplet size distribution in a spray affects the gas thermodynamic behavior at this engine moment. Then, it was developed a thermodynamic parametric analysis of the wet ethanol direct injection during the compression stroke of an DISI engine. The authors tested several volumetric compositions of wet ethanol with the objective of obtaining the best proportion for the compression stroke in terms of evaporative cooling and knock suppression. The droplet spray classes introduced in Chapter 3 were applied to represent the fuel spray behavior in terms of droplet size, with $N_{classes} = 11$ for each spray layer. Results were presented in terms of suggested spray evaporation efficiencies (first and second law). The output parameters represented these two efficiencies, besides the in-cylinder gases entropy generation.

5.1 Simulation cases

The selected inputs of our optimization were the initial volumetric fraction of water in wet ethanol v (from 0 to 0.2 with steps of 0.05), the relative air-fuel ratio λ (from 0.9 to 1.2 with steps of 0.05) (Tab. 5.1). These variables varied within certain spectra with the objective of searching for optimum operational states in terms of the objective functions, which was previously unknown for this case of study.

Table 5.1 – Initial conditions.

	Base-case	Par. analysis
v_{H_2O} $(\%v.)$	10	$[0, 5, 10, 15, 20]$
λ	1.0	$[0.9, 0.95, 1.0, 1.05, 1.10, 1.15, 1.2]$
T_d (K)	300	300
θ_{inj}	270°	270°
N_{engine} (RPM)	1000	1000

The investigated candidates for the best objective function of this process were the in-cylinder gas entropy generation, the first and the second law spray evaporation efficiencies. The engine was simulated at 1000 RPM. The engine specifications are presented by Table 5.2:

Table 5.2 – Engine specifications

Parameter	Value
Bore x Stroke	(80 x 80) mm
Connecting rod	128.0 mm
Compression ratio	12.0
Cylinder volume	400 cm^3
Engine speed	1000 RPM
Nozzle diameter	0.5 mm
Number of injection nozzle holes	10
Nozzle injection pressure	200 MPa

5.2 Analyzing the thermodynamic behavior

This section initiates the analysis of direct injection of wet ethanol during the compression stroke of an engine by analyzing the main effects on the temperature and pressure curves when compared to a port-fuel injection (PFI) case. The engine operated in motoring operation. Figure 5.1 (a) shows these differences for a full load case, 10% water v/v, $\theta_{inj} = 270°$ and 1000 RPM. The first interesting point to highlight is the temperature profile change due to the evaporative cooling effect, with a reduction of almost 190K in the peak cylinder temperature ($360°CA$), thereby suppressing the chance of auto-ignition (knock) by the air-fuel mixture. Moreover, the cycle peak temperature during combustion would be lower than the PFI case, which also collaborates to less pollutant gases production through the combustion process (e.g, NO_x). The pressure peak reduces approximately 6 bar, enhancing previously described tendencies. Therefore, the direct fuel injection would allow the application of higher compression ratios without compromising the engine structure (with knock damage), improve the engine cycle thermal efficiency and reduce the pollutant gases production.

Figure 5.1 (b) presents the entropy transfer sources for the direct fuel injection process during the compression stroke. The main entropy transfer source was the heat transfer from the hot gases to the liquid droplets. On the other hand, the gas entropy reduced after the fuel injection, due to the evaporative cooling effect. The entropy transfers associated to the mass flows (i.e., mixture) and wall heat transfer contributed in a minor way to the DI entropy generation. Another highlight was the higher entropy production from the DI case when compared to the PFI one, since the evaporation and vapor mixing processes happen outside the engine cylinder. Also, the irreversible droplet heat transfer required to evaporate the fuel spray are present inside the cylinder. Hence, this model indicates that there is a number of benefits from the fuel direct

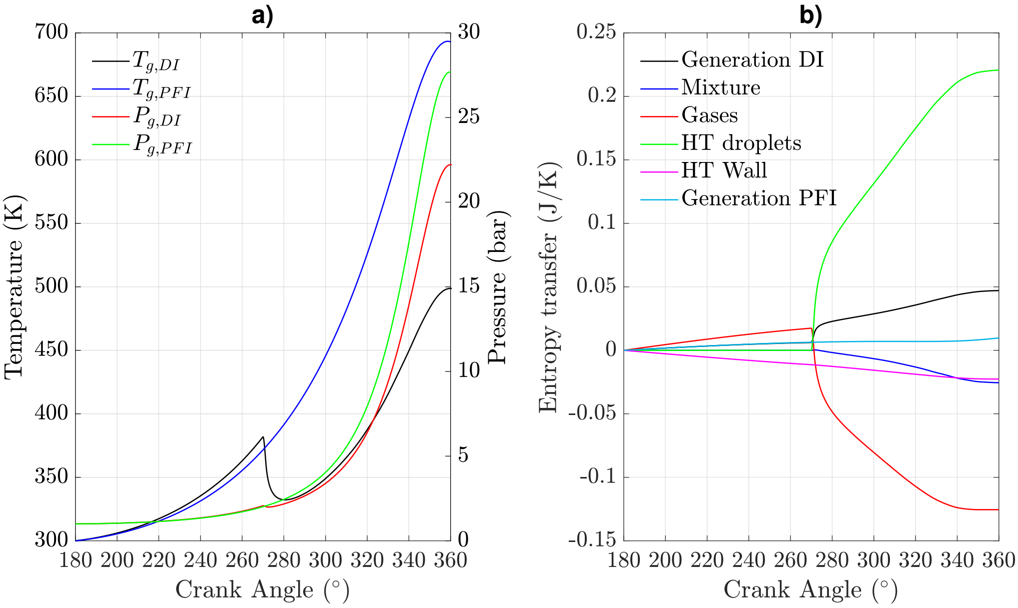

Figure 5.1 – Comparison between PFI and DI of wet ethanol: a) temperature and pressure profiles, b) entropy transfer sources ($v = 10\%$ v/v, 1000 RPM and $\theta_{inj,i} = 270°$).

injection, but these may come with an increase in the process irreversibility. Thus, there is a need to proper compare the irreversibilities for evaporation and mixing for PFI and DI cases, in order to confirm this higher irreversibility tendency.

The suggested first and second law efficiencies for the droplet spray evaporation process are presented by Fig. 5.2. Both efficiencies increased rapidly after the beginning of the injection and subsequently evaporation. Later, the efficiencies stabilized near 90% when most droplets from different classes (i.e., the droplets with different sizes generated from jet spray breakup and indicated by the PDF distribution) reached a near steady-state surface temperature. The slightly decrease in its value occurred due to an increase on a major part of the convection heat transfer being directed to cause sensible heating on the droplet classes, rather than causing direct evaporation. Also, the second law efficiency was higher than the first during the whole evaporation process. In terms of energy and exergy sources, there is a considerable difference between them, because of the low droplet surface temperatures during convection, which affect directly the Carnot efficiency of the evaporation process.

5.3 Investigation of the output candidates

The authors then decided to investigate the behavior of the first and second law efficiencies, besides the entropy generation to present three objective output candidates for the

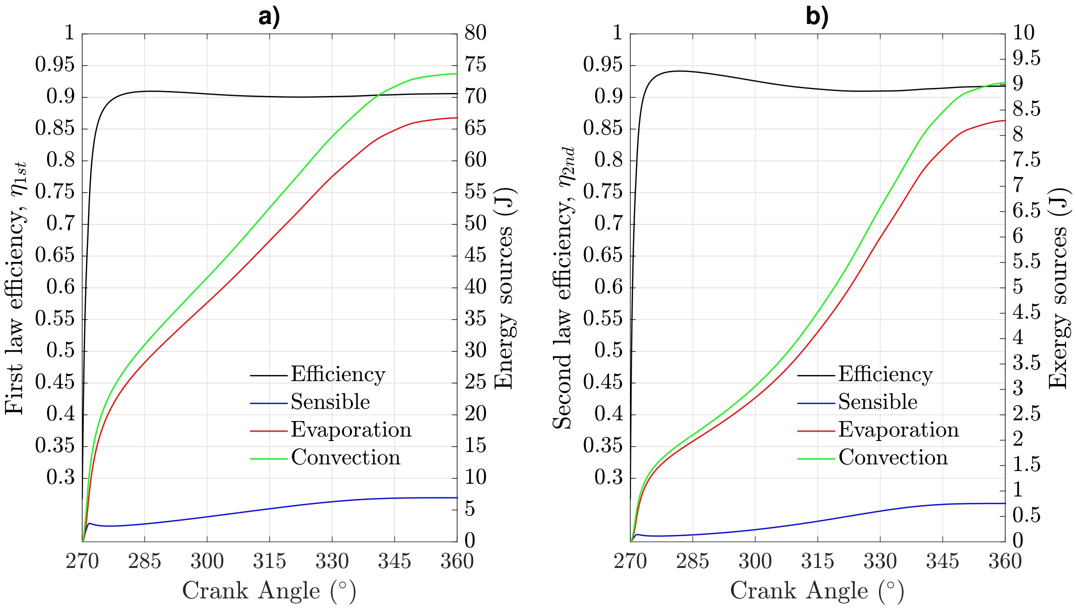

Figure 5.2 – Spray evaporation efficiencies and their sources for wet ethanol direct injection: a) first law, b) second law ($\upsilon = 10\%$ v/v, 1000 RPM and $\theta_{inj} = 270°$).

optimal spray evaporation process in the cycle. Thus, contour curves for these candidates are presented for different actual air-fuel ratios and water contents in wet ethanol for 1000 RPM, $\theta_{inj} = 240°$ and $T_d = 300K$. Figure 5.3 (a) and (b) show the behavior of the spray efficiencies and highlights the similarity between the two graphs. The evaporation process became less efficient at higher water contents, whereas higher efficiencies were found under leaner conditions. This behavior was expected because water is less volatile than ethanol, thus its addition to the liquid phase causes an increase on the amount of sensible energy/exergy required from the spray droplets to evaporate, therefore reducing the phenomenon efficiency. Moreover, the values of both efficiencies were very similar, due to the low Carnot efficiency associated with the exergy flows.

On the other hand, the contour curves of entropy generation in Fig. 5.4 (a) indicate a peak rather than a valley at higher water contents and richer mixtures. Thus, more water on wet ethanol caused an increase in the irreversibility during the compression stroke. Also, leaner mixtures yielded less irreversibility in the in-cylinder gases. In resume, the three chosen variables presented a similar behavior when it comes to an optimal operation condition for the spray evaporation process. In order to connect wet ethanol with the main effect of a DISI engine, contour curves of the evaporative cooling effect are presented on Fig. 5.4 (b). There was an inverse association between the evaporative cooling effect and the efficiencies, since higher values of charge cooling are found on the lowest efficiency points.

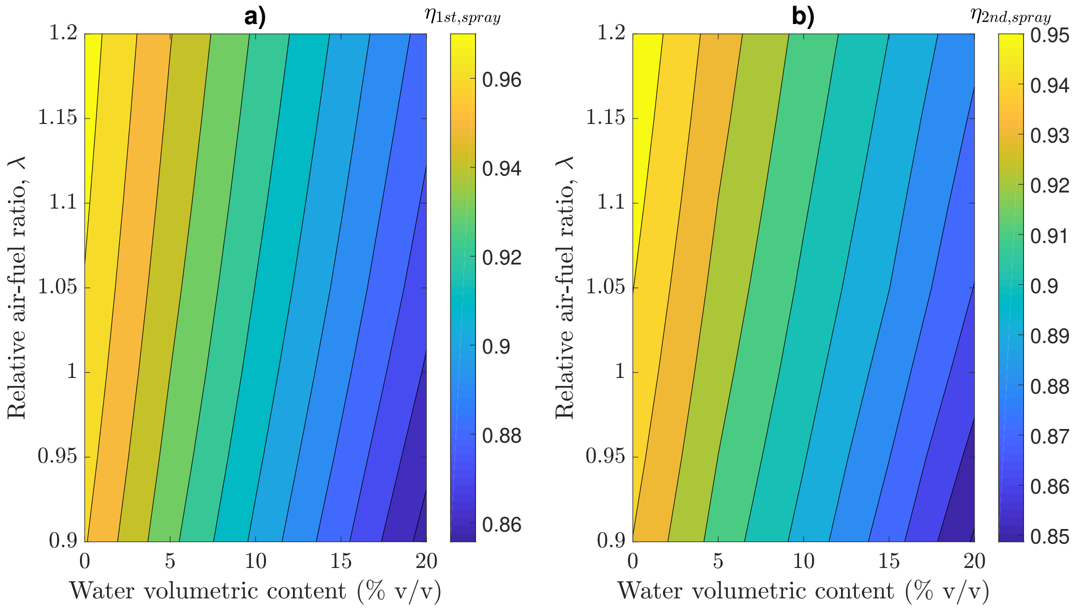

Figure 5.3 – Wet ethanol direct injection contour curves: a) first law efficiency b) second law efficiency (1000 RPM and $\theta_{inj} = 240°$).

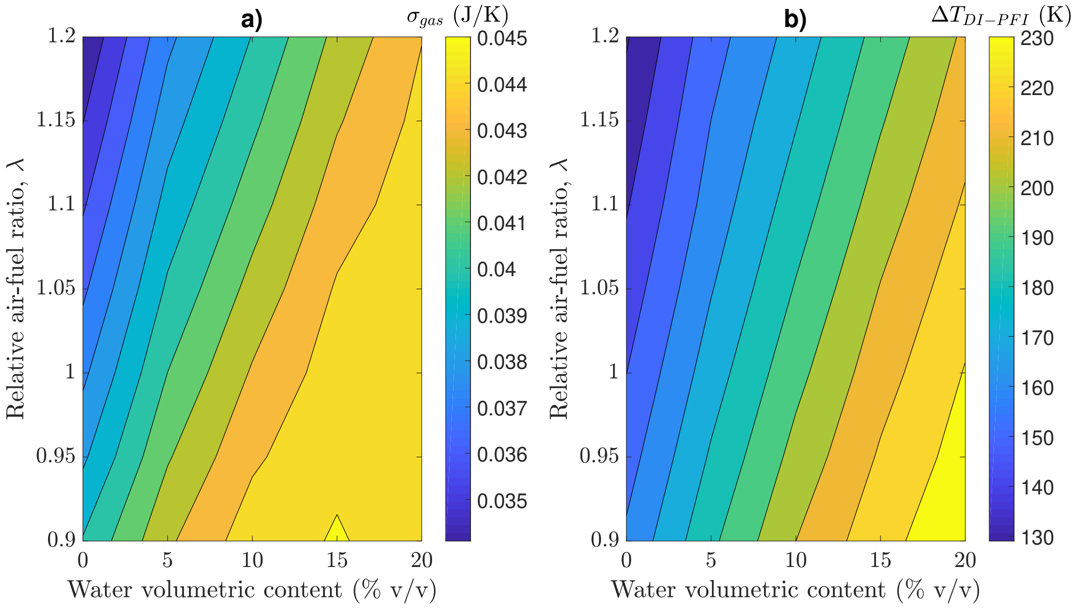

Figure 5.4 – Wet ethanol direct injection contour curves: a) entropy generation b) evaporative cooling (1000 RPM and $\theta_{inj} = 240°$).

Although these results indicate that the use of wet ethanol reduces the spray evaporation efficiency when compared to anhydrous ethanol, which already causes an acceptable evaporative cooling effect, three aspects need to be highlighted in order to see the whole figure of the problem. The additional mass of water in wet ethanol enhanced the gas mass, thus enhanced the work rate on the expansion process, such as it occurs through water injection systems in some engines. Also, the evaporative cooling effect is amplified in almost 50% on mixtures of 20% v/v water, therefore improving the knock suppression and allow the use of even higher compression ratios by the engine cycle. Lastly, the application of wet ethanol with higher contents of water (i.e., higher than 20% v/v) would avoid the exponential growth of energy required by the ethanol production process (Martins *et al.*, 2015), therefore turning the ethanol life cycle more efficient. But, in order to take into account these aspects in a more in-depth/optimization analysis, a multiobjective optimization in a DISI engine cycle would be more adequate, since the knock suppression would only appear with the participation of the combustion process.

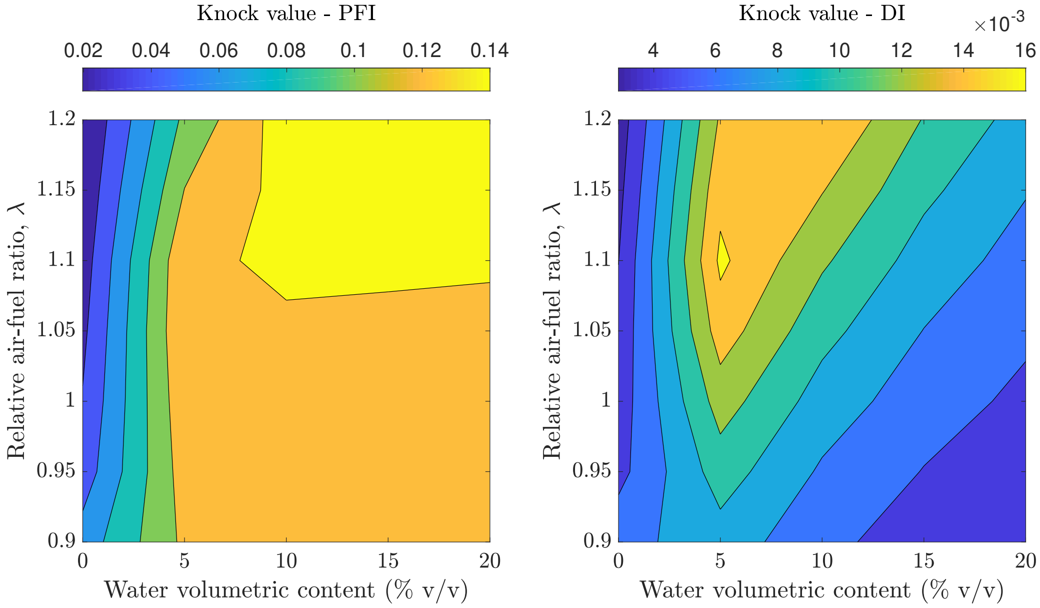

Figure 5.5 – Contour curve of the knock integral value for PFI of wet ethanol at the end of the compression stroke ($\theta = 360°$) compared to DI conditions (1000 RPM and $\theta_{inj,i} = 240°$).

In order to corroborate the previous argument about wet ethanol application, Fig. 5.5 presents the values of the cumulative knock integral value (M.; P., 1978) for PFI and DI engine motoring simulations. There was a 10-fold reduction on the values of the knock variable from the DI value to the PFI one, where the ethanol/water mixture needs to be vaporized in the former, while it is completely in vapor form for the latter. Therefore, the higher amount of vapor increased the gas pressure and temperature, thus the knock integral value. An interesting point is that there is a peak region for the DI knock integral value on leaner mixtures between 5 and 10 $\%$ v/v, which is clearly different than the maximum of entropy generation/minimum of both evaporation efficiencies. Nevertheless, the knock suppression caused by the fuel direct injection is quite valuable, since it corroborates the potential for higher compression ratio applications, thus increasing the engine cycle first and second law efficiencies.

6 VALIDATION OF THE DEVELOPED DISI ENGINE MODEL

This chapter utilized the mathematical modeling and knowledge previously presented in this thesis to show the results of the direct injection of wet ethanol in a spark-ignition engine simulation. These results were suitable to validate the developed DISI engine model by comparing them with experimental results found in literature. The objective was to show that the developed model is consistent with reality and robust enough to be able to accomplish the main objective of this thesis: the thermodynamic optimization of a DISI engine fueled with wet ethanol with the application of diverse technologies to improve the engine efficiency, such as turbocharging and downsizing, all combined with higher compression ratios and adequate knock suppression, in order to achieve a near state-of-the-art engine operating condition.

In order to corroborate the validity of the presented model, some comparisons with experimental measurements from Lanzanova *et al.* (2016) and Brewster *et al.* (2007) were developed and properly detailed in the next sections.

6.1 Model validation *versus* experimental data from Lanzanova *et al.* (2016)

A validation of the DISI engine simulator was necessary in order to check the its capacities of predicting engine outputs adequately. The experimental data and results available in Lanzanova *et al.* (2016) contained information related to wet ethanol in DISI engines, which were used on this validation to compare the simulation outputs with them. For example, the water volumetric content in wet ethanol was varied from zero to $20\%v/v$, therefore these data provided the development of a more trustworthy simulator which offers more details about wet ethanol usage in engines.

Unfortunately, some experimental data was not available, such as the cylinder wall temperature, admission and exhaust pressures. Thus it was necessary to develop a look-up (or iterative) method on the simulations in order to reach the same fuel mass flow rate as obtained in each case of the experiment. A series of simulations guessed some initial values for P_{adm}, P_{exh}, and T_{wall} for this validation. After a series of tests, the best compromise between simulation and experiments was found for $P_{exh} \approxeq 1.2bar$, and $T_{wall} = 373K$. The engine load (i.e., P_{adm} for this study) is the input variable iterated to guarantee the same fuel mass rate between experiment and simulation. Another important detail to the model validation was the modification from a classical/near-parabolic valve opening/closure profiles to a trapezoidal one. This modification was necessary since the experimental procedure occurred based on such a valve profile.

6.1.1 Engine specifications

The engine specifications provided by this paper encompasses the cylinder geometry, the valve command, as well as the direct fuel injection system (without the injector diameter). The net indicated mean effective pressure (NIMEP) was always adjusted to 3.1 or 6.1 bar, while the engine speed was set to 1500 RPM. One interesting set of data provided by Lanzanova *et al.* (2016) is the efficiencies related to the engine cycle; the net thermal, the gas exchange and combustion efficiencies are available for each case and all of them assisted on the simulation-experiment comparison. In addition, in-cylinder pressure profiles are plotted for 3.1 bar NIMEP during the closed-phase. Finally, the pressure and temperature maximum values/peaks are also used for the validation. Information regarding the fuel injector is also provided, although the nozzle diameter is not, thus some investigation was necessary to discover usual nozzle diameters based on the injector type. Based on this search, the inner diameter of spray G 28 (Duke *et al.*, 2017) ($D_{inj} \approx 0.173$ mm) was adopted as a reference for the value of $D_{inj} = 0.18$mm used in this validation. In short, Tab. 6.1.1 compiles all input data available in the paper about the engine.

6.1.2 Look-up method description

In order to make a proper comparison between the engine simulation and the experimental results from Lanzanova *et al.* (2016), some information about the thermodynamic conditions on the admission and the exhaust systems are necessary. Unfortunately, the paper does not provide all required data so that this validation can simply simulate under the same conditions as the engine experimental procedure. For example, there is no information on the paper about inlet and exhaust temperatures and pressures, as well as about the cylinder wall temperatures. Therefore, in order to overcome these difficulties, a look-up method was applied to make some proper estimates about these information gaps. The method basically consists of a series of simulations with all available information about the engine and some initial guesses about the values of T_{adm}, P_{adm} (related to the engine partial load), T_{exh}, P_{exh}, and T_{wall}. Realistic values for the admission and exhaust temperatures T_{adm}, T_{exh}, as well as the exhaust pressure P_{exh} are assumed in order to simplify the comparison. Next, the variables which af-

Table 6.1 – Engine specifications (Lanzanova *et al.*, 2016)

Parameter	Value
Displaced volume	350 cm^3
Stroke x Bore	(66.9 x 81.6) mm
Compression ratio	11.8:1
Number of valves	4 (2 inlet and 2 exhaust)
Inlet valve diameter	28.0 mm
Exhaust valve diameter	30.0 mm
Valve lift	2mm (3.1 bar NIMEP) and 6mm (6.1 bar NIMEP)
Cam duration (Exhaust, intake)	220° CA
IVO (intake valve opening)	7° BTDC$_{intake}$
IVC (intake valve closure)	189° ATDC$_{intake}$
EVO (exhaust valve opening)	179° BTDC$_{intake}$
EVC (exhaust valve closure)	3° ATDC$_{intake}$
Injection timing	90° CA BTDC$_{intake}$
Engine coolant temperature	$90°C$
NIMEP	3.1 and 6.1 bar
Engine speed	1500 RPM
Connecting rod	144.5 mm
Nozzle diameter	0.18 mm
Number of injection nozzle holes	6
Nozzle injection pressure	145 bar
Nozzle injection temperature	293 K
Spark advance timing (SAT)	max. indicated efficiency -40 to $-16°$ BTDC
Internal EGR ($\%$)	$10 - 20\%$

fect directly the cylinder mass and pressure profile (P_{adm} and T_{wall}) are investigated in order to discover which set of values provide a similar cylinder pressure curve with the same amount of air flow rate and air-fuel ratio provided by the paper. Also, the 3.1 bar NIMEP was taken into consideration as when simulating the cases. The obtained values were previously presented in Sec. 6.1.1.

6.1.3 Combustion phasing

The combustion phasing is obtained through experimental data for DISI engines with wet ethanol (up to $6\%v/v$ water). The Wiebe function presented in Eq. 3.63 is used to represent numerically the combustion process and it is adjusted by the usage of the instants where 10, 50, and 90% (θ_{10}, θ_{50}, and θ_{90}) of the mass fraction burned (MFB) are calculated for the experimental procedure. Equations 6.1-6.4 represent the system of equations that must be solved to obtain the parameters θ_0, n, and $\Delta\theta_b$ (Yeliana *et al.*, 2008; Rufino, 2020):

$$L = \frac{\ln\left(\frac{\ln 0.9}{\ln 0.1}\right)}{\ln\left(\frac{\ln 0.5}{\ln 0.1}\right)} \tag{6.1}$$

$$\frac{\theta_{10} - \theta_0}{\theta_{90} - \theta_0} = \left(\frac{\theta_{50} - \theta_0}{\theta_{90} - \theta_0}\right)^L \tag{6.2}$$

$$n = \frac{\ln\left(\frac{\ln 0.9}{\ln 0.1}\right)}{\ln\left(\frac{\theta_{10}-\theta_0}{\theta_{90}-\theta_0}\right)} - 1 \tag{6.3}$$

$$\Delta\theta_b = \frac{\theta_{50-\theta_0}}{\left(\frac{\ln 0.5}{-a}\right)^{\frac{1}{n+1}}} \tag{6.4}$$

The combustion phasing data is completely available (i.e., flame development phase, spark timing, combustion duration, etc.) with all the combustion efficiency values for each experiment presented by Lanzanova *et al.* (2016).

6.1.4 Simulated cases

The data from Lanzanova *et al.* (2016) involved only fuel injection during the admission stroke, thus only the homogeneous case simulation is presented here. Table 6.2 compiles all cases analyzed on this section. The idea was to cover different engine conditions based on the wet fuel composition for both stoichiometric and very lean combustion conditions, as well as two different engine loads. Thus, 7 cases were evaluated by the engine simulator in order to validate it with the experiments. Case 1 acted like a base-case reference, whereas the other six basically change the other variables.

Table 6.2 – Studied engine operation cases with data from Lanzanova *et al.* (2016)

Case	Conditions
1	E100W0, 1500 RPM, $\lambda = 1.0$, 3.1 NIMEP
2	E100W0, 1500 RPM, $\lambda = 1.0$, 6.1 NIMEP
3	E100W0, 1500 RPM, $\lambda = 1.3$, 3.1 NIMEP
4	E95W5, 1500 RPM, $\lambda = 1.0$, 3.1 NIMEP
5	E90W10, 1500 RPM, $\lambda = 1.0$, 3.1 NIMEP
6	E80W20, 1500 RPM, $\lambda = 1.0$, 3.1 NIMEP
7	E80W20, 1500 RPM, $\lambda = 1.3$, 3.1 NIMEP

6.1.5 Engine in-cylinder pressure

Some experimental in-cylinder gas pressure profiles were adopted to validate the DISI engine simulator. This comparison involved cases 1, 4, 5, and 6 (the ones with pressure curves available) and showed the effect of increasing water content on wet ethanol on the engine cycle under stoichiometric conditions and 3.1 bar NIMEP. A chemical kinetic model was coupled on the simulator for these comparisons, so that the engine performance was more related to reality (i.e., the experiments).

Figures 6.1-6.4 present how accurate the DISI engine simulator is capable of reproducing the closed-phase pressure profiles of Lanzanova *et al.* (2016). By comparing the figures, it is noticeable that the simulation was able to predict the pressure profiles for cases 1, 4, and 5. In addition, both the pressure peak and its value were also predicted coherently. Thus, the simulator is clearly capable of predicting realistic DISI engine performance and therefore it can be adopted to perform a thermodynamic optimization of a DISI engine fueled with wet ethanol, such as proposed by this research. It must be clarified, however, that there was a clear difference between the simulated and experimental curves for E80W20, with a peak difference of 2 bar. This difference was attributed to the requirement of adjusting the Hohenberg's heat transfer coefficient h_{conv} to conditions where higher water contents on the fuel composition exists. Nevertheless, this discrepancy did not affect significantly the other output variables, as it will be commented in the next section, so does not invalidate the simulator on its main goal of optimization.

6.1.6 Comparison of remaining engine outputs

This section shows the comparison between the remaining outputs available in Lanzanova *et al.* (2016) with the ones obtained by the simulations. The comparison involved the following outputs: NIMEP, SFC, net thermal engine efficiency, gas exchange efficiency, maximum cycle pressure and angle, besides maximum cycle temperature. These seven variables provide information regarding the engine cycle during both closed and open phases, which allow a proper analysis about the engine performance as well as the direct injection effect of wet ethanol. All results involving the previously described cases were studied, so that the engine simulator capacity could be evaluated in terms of water content and specific characteristics related to DISI engines operation (e.g., engine load and relative air-fuel ratio λ).

Table 6.3 presents the comparison for the case 1. The specific fuel consumption

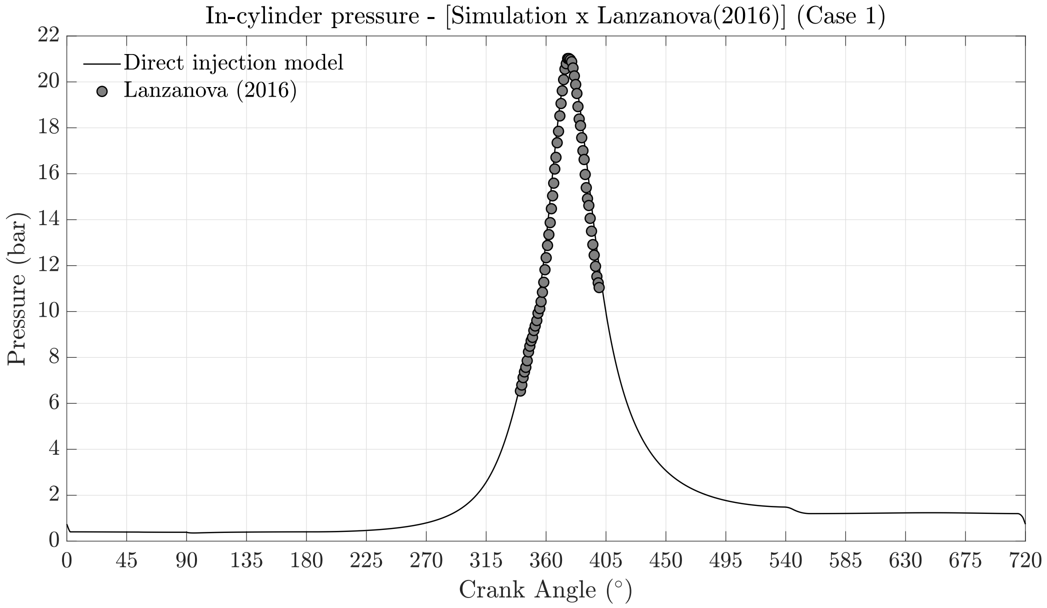

Figure 6.1 – In-cylinder gas pressure profile (simulation *versus* experimental data from Lanzanova *et al.* (2016)) - E100W0, 1500 RPM, $\lambda = 1.0$, 3.1 NIMEP.

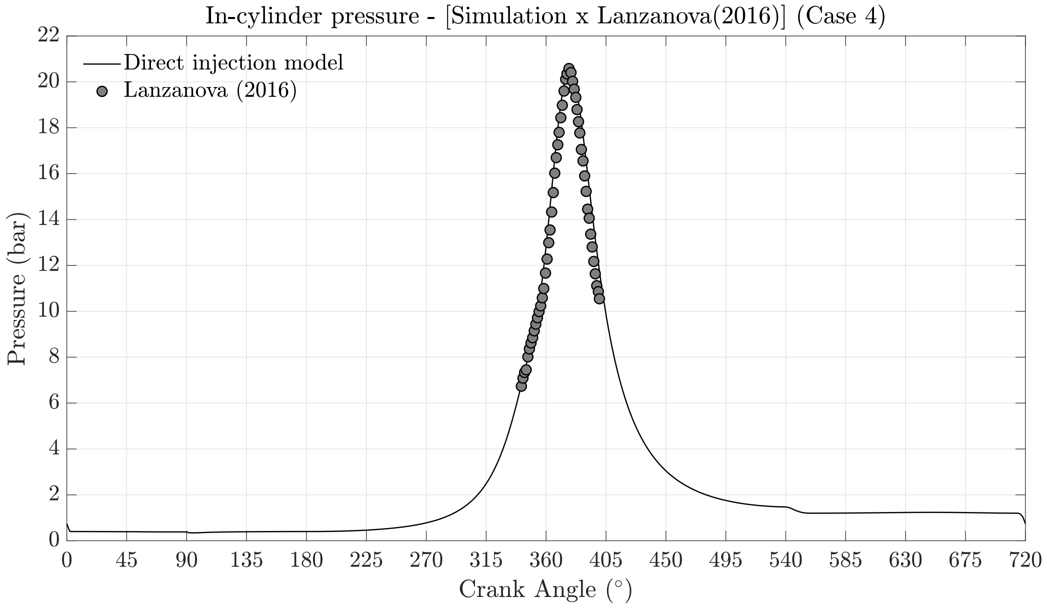

Figure 6.2 – In-cylinder gas pressure profile (simulation *versus* experimental data from Lanzanova *et al.* (2016)) - E95W5, 1500 RPM, $\lambda = 1.0$, 3.1 NIMEP.

and engine thermal efficiency are quite similar in values for both experiment and simulation, with relative differences of 0.91 and 0.39%, respectively. The obtained NIMEP related to the simulation is superior to the experiment (6.49%), but nevertheless it is realistically representative and its differences can be attributed to the engine open-phase calculation, since the already commented Fig. 6.1 showed very similar pressure curves during the closed-phase. In addition, the absence of information regarding the admission and exhaust manifold pressures, and the

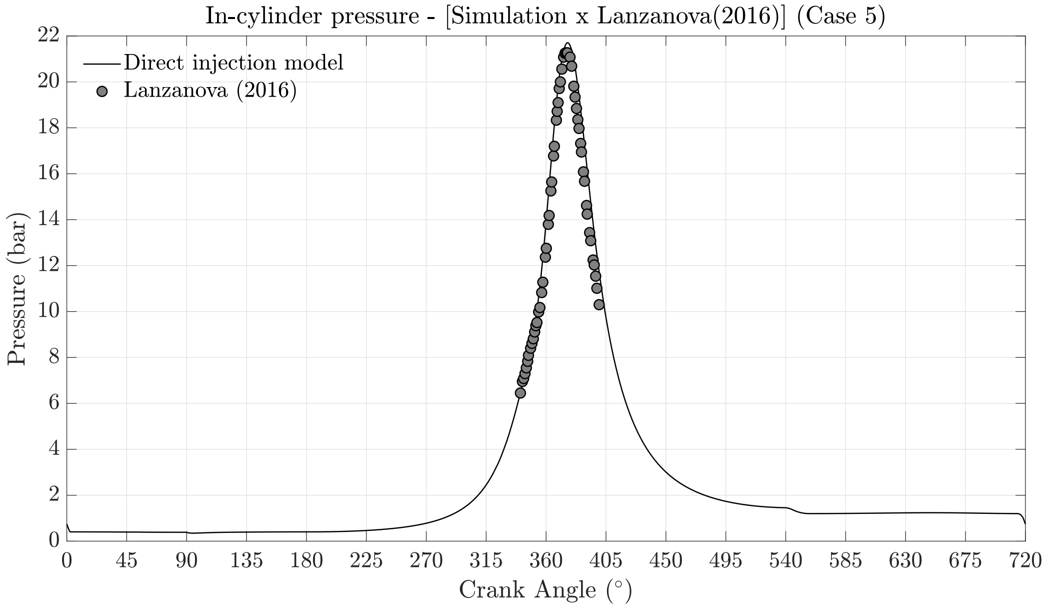

Figure 6.3 – In-cylinder gas pressure profile (simulation *versus* experimental data from Lanzanova *et al.* (2016)) - E90W10, 1500 RPM, $\lambda = 1.0$, 3.1 NIMEP.

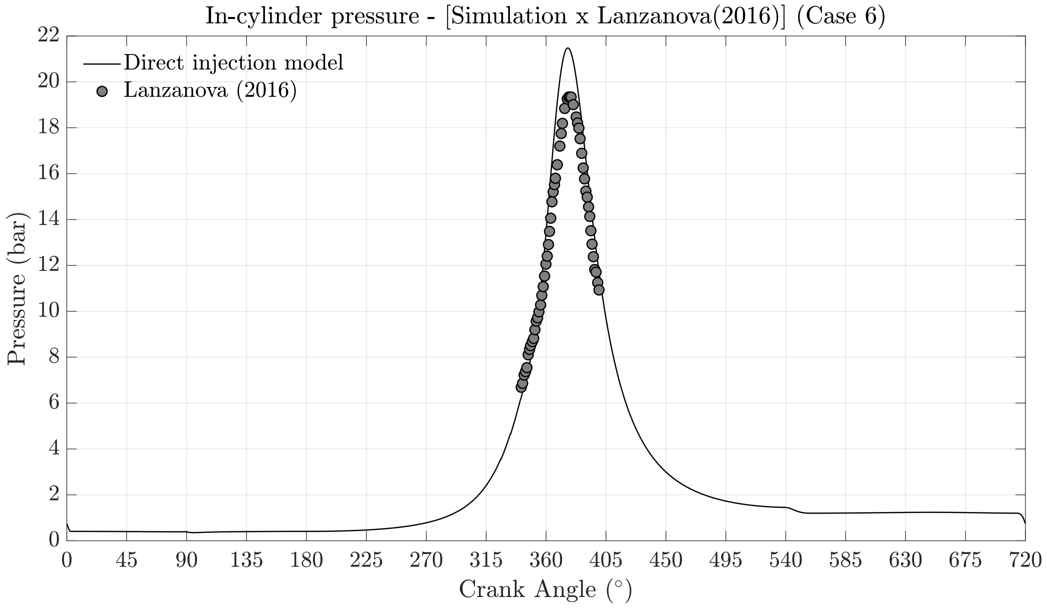

Figure 6.4 – In-cylinder gas pressure profile (simulation *versus* experimental data from Lanzanova *et al.* (2016)) - E80W20, 1500 RPM, $\lambda = 1.0$, 3.1 NIMEP.

cylinder wall temperature most likely contributed to this difference between the simulation and the experiment case, and thus affected the gas exchange efficiency (4.87%). Finally, the simulated maximum pressure and temperature values are similar to the experimental ones (3.72 and 3.87%, respectively). Thus, these results indicate that the engine combustion phasing operated by a Wiebe function coupled with experimental data from the paper was capable of reproducing the combustion behavior throughout the engine cycle, as it is noticed by the maximum pressure angle (0.06%).

Table 6.3 – Engine simulation outputs for case 1 *versus* Lanzanova *et al.* (2016)

Parameter	Simulation	Exp.	Rel. Diff.
NIMEP (bar)	3.293	3.10	6.49 %
SFC (g_{fuel}/kWh)	454.6	458.7	0.91 %
Thermal efficiency (%)	29.29	29.17	0.39 %
Gas exchange efficiency (%)	79.83	83.92	4.87 %
Max. P (bar)	20.71	21.51	3.72 %
Max. P angle (deg)	377.6	377.4	0.06 %
Max. T (K)	1853	1784	3.87 %

Table 6.4 presents the comparison between simulation and experiment in order to evaluate the main differences of increasing the engine load (from 3.1 to 6.1 bar NIMEP) on the engine outputs. The simulation was capable of predicting correctly the changes of all outputs. The highest relative difference was found for the NIMEP (7.28%), whereas most other variables stayed near 4 and 5%. These results corroborate the model ability of predicting changes on the engine load, which is a very important characteristic to be taken into account, since the optimization process adopts the engine load as an input for its calculations.

Table 6.4 – Engine simulation outputs for case 2 *versus* Lanzanova *et al.* (2016)

Parameter	Simulation	Exp.	Rel. Diff.
NIMEP (bar)	6.544	6.1	7.28 %
SFC (g_{fuel}/kWh)	393.3	413.3	4.85 %
Thermal efficiency (%)	33.97	32.38	4.92 %
Gas exchange efficiency (%)	91.53	95.63	4.29 %
Max. P (bar)	34.98	36.62	4.47 %
Max. P angle (deg)	377.8	374.7	0.82 %
Max. T (K)	1898	1805	5.15 %

Case 6 covers the comparison related to a change of fuel blends from E100W0 to E80W20 (Tab. 6.5). The increase in water content on the ethanol-water mixture increased the average relative differences between the simulation and the experiment. For example, most values increased to up than 6%. In addition, the maximum pressure and temperature were the highest differences on this comparison (15.26 and 12.89%, respectively). This behavior is justified based on the combination of a higher coefficient of variability (COV) on combustion on the experiments (Lanzanova *et al.*, 2016) with the simulator somewhat underestimating the water on the combustion process. The aforementioned requirement to adjust the Hohenberg's heat transfer coefficient is also valid here. Nevertheless, the simulation was capable of accurately predict two important outputs for the optimization process, such as SFC and thermal efficiency.

Table 6.5 – Engine simulation outputs for case 6 *versus* Lanzanova *et al.* (2016)

Parameter	Simulation	Exp.	Rel. Diff.
NIMEP (bar)	3.33	3.1	7.37 $\%$
SFC (g_{fuel}/kWh)	601.5	640.2	6.05 $\%$
Thermal efficiency ($\%$)	29.2	27.5	6.20 $\%$
Gas exchange efficiency ($\%$)	80.04	83.13	3.73 $\%$
Max. P (bar)	21.48	18.63	15.26 $\%$
Max. P angle (deg)	376.4	377.5	0.29 $\%$
Max. T (K)	1755	1555	12.89 $\%$

The final comparison involves the usage of E80W20 in a very lean mixture ($\lambda = 1.3$), whose results are presented by Tab. 6.6. The simulator presented very interesting results almost all outputs; the exceptions involve the maximum pressure and temperature. The most probable reason for this behavior is similar to the one presented for case 6, i.e., higher water content + higher COV. An interesting highlight is that leaning the mixture did not restrict the simulation in terms of the remaining variables. Actually, it has approximated them further quantitatively. Thus, this comparison corroborates the validity of the engine simulator for the proposed optimization process of this work, which is presented in the next chapter.

Table 6.6 – Engine simulation outputs for case 7 *versus* Lanzanova *et al.* (2016)

Parameter	Simulation	Exp.	Rel. Diff.
NIMEP (bar)	3.136	3.1	1.16 $\%$
SFC (g_{fuel}/kWh)	583.3	597.8	2.44 $\%$
Thermal efficiency ($\%$)	29.95	29.44	1.74 $\%$
Gas exchange efficiency ($\%$)	80.23	84.58	5.15 $\%$
Max. P (bar)	29.00	22.37	29.62 $\%$
Max. P angle (deg)	369.3	372.4	0.83 $\%$
Max. T (K)	1684	1417	18.81 $\%$

6.2 Model validation *versus* experimental data from Brewster *et al.* (2007)

A second validation of the DISI engine simulator was applied to check the simulator capacity to predict the engine behavior under more intense engine load conditions. The results from (Lanzanova *et al.*, 2016) only covered partial load cases. Also, the optimization process requires the application of a turbocharging system, so the simulator must be able to indicate (in a certain degree) the engine outputs (e.g., torque, MEP, efficiencies, emissions, etc.) under higher in-cylinder pressure profiles obtained for such a system. Thus, experimental data and results available in Brewster (2007), Brewster *et al.* (2007) contained information related to wet ethanol in turbocharged DISI engines and therefore were used to validate the engine for these operation conditions.

Some experimental data was not available either, such as the admission and exhaust valve diameters, as well as the cylinder wall temperature, and the exhaust manifold pressure. Thus, it was necessary to develop a similar look-up/iterative method as the one previously described in Sec. 6.1.2) on the simulations in order to reach the same air mass flow rate as obtained in each case of the experiment. A series of simulations guessed some initial values for D_{adm}, D_{exh} and T_{wall} for this validation. After a series of tests, the best compromise between simulation and experiments provided $D_{adm} = 32.0mm$, $D_{exh} = 30.0mm$ and $T_{wall} = 450K$. These features are highlighted with asterisks on Tab. 6.7. The exhaust pressure was the input variable iterated to guarantee the same air mass rate between the experiment and the simulation.

6.2.1 Engine specifications

The engine specifications provided by this paper encompasses the cylinder geometry, the valve command angles, as well as the direct fuel injection system (without the injector diameter). The injector diameter was previously unknown, but (Brewster, 2007) indicated that the SMD diameter was equivalent to 10 μm and from this it is estimated an injector diameter of $D_{inj} = 0.25$mm. The engine speed was 2000 RPM. The combustion efficiency was assumed as 0.99, which is an realistic value to a stoichiometric homogeneous combustion, which is the case of this comparison. In addition, in-cylinder pressure profiles are plotted for MBT conditions for each ethanol-water mixture at stoichiometric conditions. The brake torque, thermal efficiency and mean effective pressure are also available in the papers. Finally, the pressure maximum values/peaks are also used for the validation. In short, Table 6.7 compiles all input data available in the paper about the engine.

6.2.2 Look-up method

The look-up method for the unavailable engine features involving this validation was similar to the one presented previously on this chapter. However, the object of focus here was the exhaust manifold pressure (P_{exh}), since any direct information about this feature was

Table 6.7 – Engine specifications (Brewster, 2007; Brewster *et al.*, 2007)

Parameter	Value
Displaced volume	500 cm^3
Stroke x Bore	(86.0 x 86.0) mm
Compression ratio	10.4:1
Number of valves	4 (2 inlet and 2 exhaust)
Inlet valve diameter*	32.0 mm
Exhaust valve diameter*	30.0 mm
Valve lift/diameter ratio	0.3
IVO (intake valve opening)	9° BTDC$_{intake}$
IVC (intake valve closure)	222° ATDC$_{intake}$
EVO (exhaust valve opening)	221° BTDC$_{intake}$
EVC (exhaust valve closure)	15° ATDC$_{intake}$
Injection timing	40° CA BTDC$_{intake}$
Engine wall temperature*	137°C
Engine speed	2000 RPM
Connecting rod	144 mm
Nozzle diameter	0.25 mm (based on $D_{SMD} \approx$ 10 mm)
Number of injection nozzle holes	8
Nozzle injection pressure	140 bar
Nozzle injection temperature	293 K

available on the papers. On the other hand, the admission manifold pressure (P_{adm}) was clearly expressed due to its relationship with engine load, thus the iterative method did not need to focus on its search. Therefore, P_{exh} was iterated to guarantee the same amount of air mass flow rate between the experiment and the simulation.

6.2.3 Combustion phasing data

The procedure of obtaining the combustion phasing data to fit the Wiebe curve was also very similar to the one adopted to the validation based on data of (Lanzanova *et al.*, 2016). Fortunately, the paper provided the complete mass fraction burned (MFB) curve therefore it was simpler to obtain and confirm the combustion behavior on the simulations.

6.2.4 Simulated cases

Brewster *et al.* (2007) provided four cases where the pressure curves were readily highlighted. The cases differ on the amount of water content on the fuel. This paper adopted the acronym E100 to refer to an ethanol-water fuel mixture in a mass basis, while this thesis adopted the symbol E100W0 to represent the same fuel, although in a volumetric basis. Tab. 6.8

shows the values between mass and volume-basis for these ethanol-water mixtures, as well as the engine conditions of each experiment. Like on the first validation, the pressure information was only available for the closed-phase scenario during combustion, so the comparison occurred only on this period.

Table 6.8 – Studied engine operation cases with data from Brewster *et al.* (2007)

Case	Conditions
1	E100 <=> E100W0, MBT, 2000 RPM, $\lambda = 1.0$, $P_{adm} = 100$kPa, $P_{exh} = 222$kPa.
2	E93 <=> E94.3W5.7, MBT, 2000 RPM, $\lambda = 1.0$, $P_{adm} = 100$kPa, $P_{exh} = 220$kPa.
3	E87 <=> E89.4W10.6, MBT, 2000 RPM, $\lambda = 1.0$, $P_{adm} = 100$kPa, $P_{exh} = 222$kPa.
4	E80 <=> E83.5W16.5, MBT, 2000 RPM, $\lambda = 1.0$, $P_{adm} = 100$kPa, $P_{exh} = 261$kPa.

The exhaust manifold pressure value converged after applying a numerical secant method (look-up method) on the available data from each of the cases above. The air mass flow rate was the variable adopted to converge with the experimental data in order to guarantee the simulations are representative of the experiments.

6.2.5 Engine in-cylinder pressure

Figures 6.5-6.8 present the in-cylinder pressure profiles obtained from the simulations and from the experimental results of Brewster *et al.* (2007). It is clear that similar pressure curves exist on all four presented figures. The simulation predicted not only the pressure peak but also the angle where it occurred on the experiments. This validation shows therefore that the simulator was capable of reproducing the average in-cylinder pressure obtained on the experiments, regardless of the water content. Also, this validation indicated that the DISI engine simulator can handle the optimization process involving turbocharging and higher admission pressures as the ones presented on Lanzanova *et al.* (2016) in a way that is coherent with realistic engine operations.

6.2.6 Comparison of remaining engine outputs

Tables 6.9-6.12 show the remaining results obtained from the simulator that were compared with the experiments. It was noticeable the similarity of all values for all cases. The evaluated gross torque, thermal efficiency and mean effective pressure were very close to the experimental brake torque, thermal efficiency and mean effective pressure. The simulated net values are lower, yet very close as well. As Heywood (2018) mentioned, the mechanical

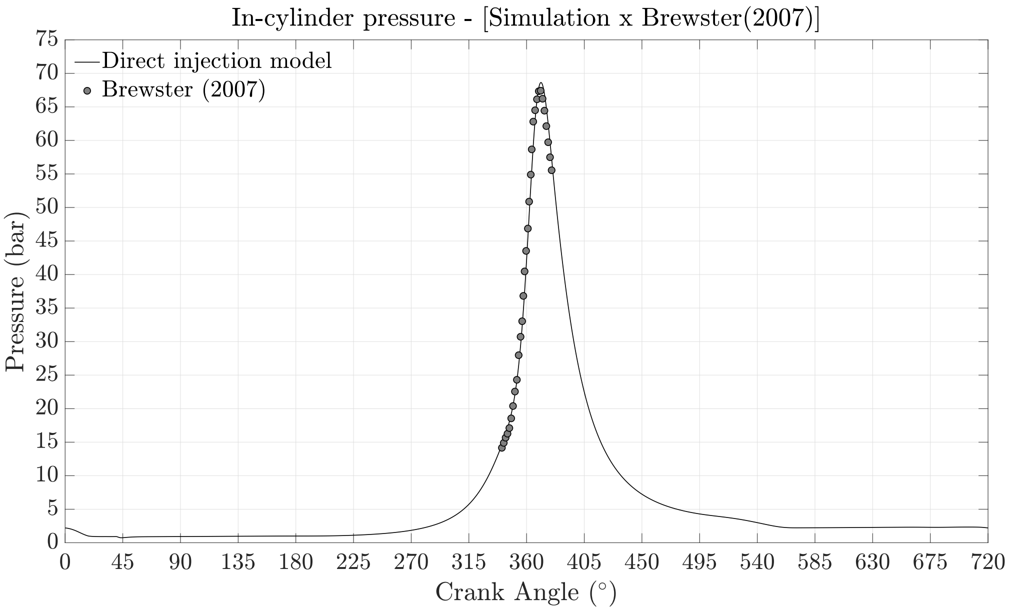

Figure 6.5 – In-cylinder gas pressure profile (simulation *versus* experimental data from Brewster *et al.* (2007)) - E100W0, MBT, 2000 RPM, $\lambda = 1.0$, $P_{adm} = 100$kPa.

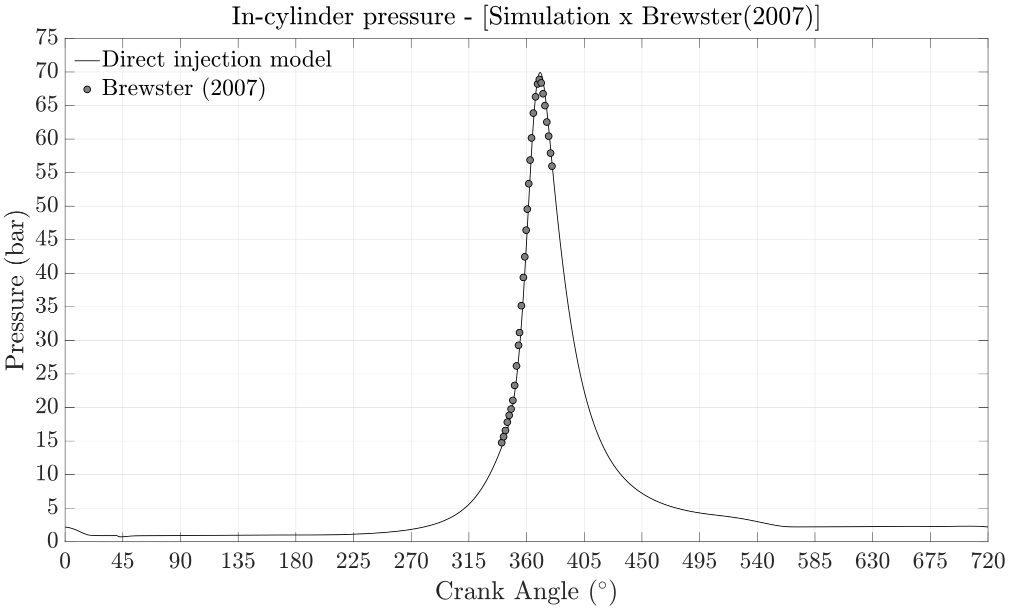

Figure 6.6 – In-cylinder gas pressure profile (simulation *versus* experimental data from Brewster *et al.* (2007)) - E94.3W5.7, MBT, 2000 RPM, $\lambda = 1.0$, $P_{adm} = 100$kPa.

efficiency is usually near 90% for modern vehicles at speeds below 2400 RPM, so the evaluated features are close to the real experimental results even for brake conditions. In conclusion,

6.2.7 Summary

The validation procedure covered comparisons with two different engine sources under different engine load conditions. While (Lanzanova *et al.*, 2016) presented partial load

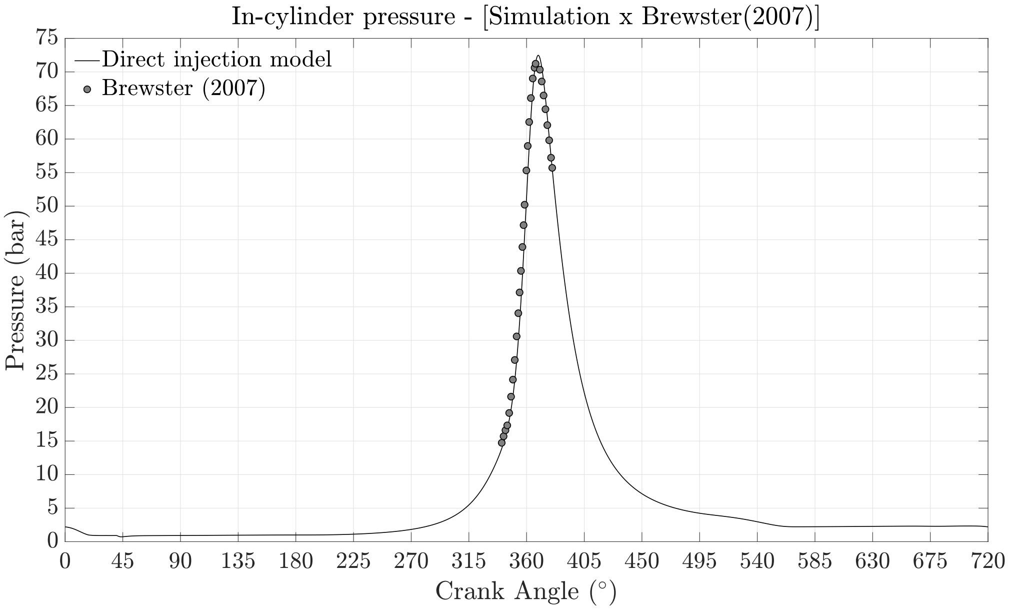

Figure 6.7 – In-cylinder gas pressure profile (simulation *versus* experimental data from Brewster *et al.* (2007)) - E89.4W10.6, MBT, 2000 RPM, $\lambda = 1.0$, $P_{adm} = 100$kPa.

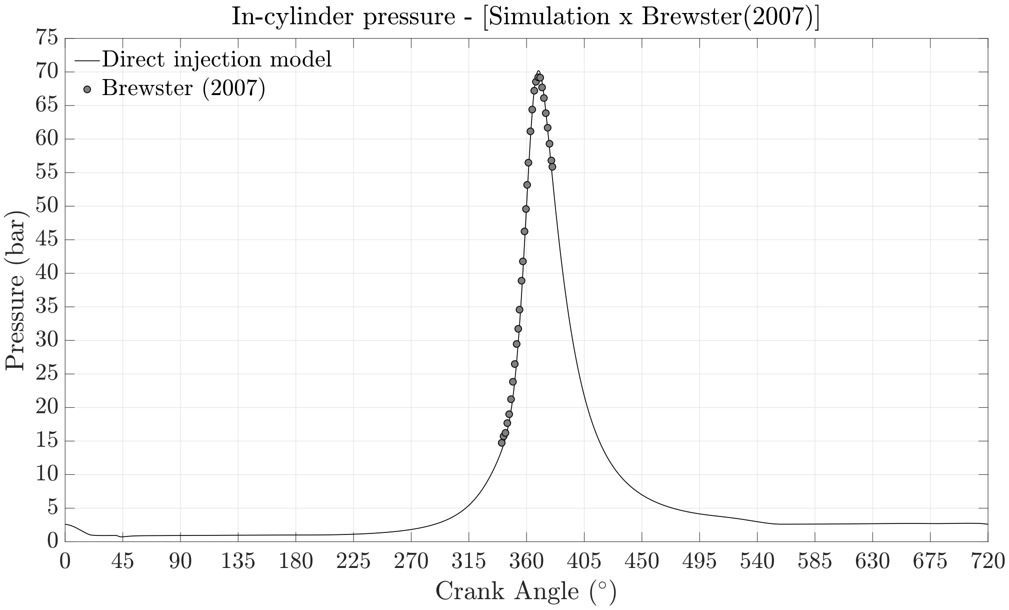

Figure 6.8 – In-cylinder gas pressure profile (simulation *versus* experimental data from Brewster *et al.* (2007)) - E83.5W16.5, MBT, 2000 RPM, $\lambda = 1.0$, $P_{adm} = 100$kPa.

Table 6.9 – Engine simulation outputs for case 1 *versus* Brewster *et al.* (2007)

	MEP (bar)	$\eta_{1st}(\%)$	T (N.m)	Airflow (g/s)	P_{peak} (bar)	$\theta_{P_{peak}}$
Simulation (Net)	9.392	31.85	37.37	8.300	68.64	371.3
Simulation (Gross)	10.49	35.58	41.75	8.300	68.64	371.3
Brewster *et al.* (2007) (Brake)	10.60	35.98	42.21	8.297	66.69	369.8

Table 6.10 – Engine simulation outputs for case 2 *versus* Brewster *et al.* (2007)

	MEP (bar)	$\eta_{1st}(\%)$	T (N.m)	Airflow (g/s)	P_{peak} (bar)	$\theta_{P_{peak}}$
Simulation (Net)	9.476	31.83	37.30	8.378	69.91	370.7
Simulation (Gross)	10.56	35.46	42.00	8.378	69.91	370.7
Brewster *et al.* (2007) (Brake)	10.51	35.13	41.73	8.380	68.76	370.1

Table 6.11 – Engine simulation outputs for case 3 *versus* Brewster *et al.* (2007)

	MEP (bar)	$\eta_{1st}(\%)$	T (N.m)	Airflow (g/s)	P_{peak} (bar)	$\theta_{P_{peak}}$
Simulation (Net)	9.390	31.50	37.36	8.384	72.48	369.2
Simulation (Gross)	10.49	35.21	41.75	8.384	72.48	369.2
Brewster *et al.* (2007) (Brake)	10.34	34.88	41.15	8.385	72.01	367.9

Table 6.12 – Engine simulation outputs for case 4 *versus* Brewster *et al.* (2007)

	MEP (bar)	$\eta_{1st}(\%)$	T (N.m)	Airflow (g/s)	P_{peak} (bar)	$\theta_{P_{peak}}$
Simulation (Net)	8.719	30.02	34.69	8.168	70.19	369.4
Simulation (Gross)	10.22	35.18	40.66	8.168	70.19	369.4
Brewster *et al.* (2007) (Brake)	10.13	35.18	40.36	8.167	69.35	368.9

results (Brewster *et al.*, 2007) used a turbocharger, thus conditions more closely related to an engine full load operation. The simulation outputs were compared with the experiments and good agreement was found for both validations. Next chapter will focus on the thermodynamic optimization of a DISI engine fueled with wet ethanol.

7 THERMODYNAMIC OPTIMIZATION TOWARDS A STATE-OF-THE-ART DISI ENGINE FUELED WITH WET ETHANOL

The final chapter of this thesis involves a mathematical optimization of a steady-state direct-injection spark-ignition engine fueled with wet ethanol. This optimization was developed as a function of the threshold knock index number, which represent the limit condition the engine operates without detonation/knock phenomenon. The engine operation conditions must represent some current requirements of a real engine operation (e.g., pollutant formation). Based on these requirements, the optimization process must take into account the knock index number ($K_{In} \approxeq 0.99$) on its algorithm, so that an optimal engine efficiency can be found under conditions which avoid considerable engine wear. In addition, pollutant emissions must be controlled in order to operate the optimized engine in a real sustainable mode. Therefore, it is not only the requirement of achieving the highest possible efficiency, but also obtaining an optimal state coherent with human society needs, that is, sustainability, usage of renewable fuels, CO_2 mitigation, etc.

7.1 Optimization conditions

The engine parameters (inputs) taken into account in this optimization process are the ones usually associated with recent engine performance, for example compression ratio (r), engine speed (N_{engine}), supercharging/turbocharging ($P_{adm} > P_{atm}$), downsizing (i.e., cylinder volume reduction), and relative air-fuel ratio (λ). In addition, water volumetric content is also assumed as variable and it respects its limitations, that is, how much water content wet ethanol can hold in order to be used as a fuel in DISI engines. This information is obtained based on previous analyses available on the literature (Lanzanova *et al.*, 2016; Brewster *et al.*, 2007). Thus, Tab. 7.1 presents the inferior and superior threshold values of the previously mentioned inputs which are modified on the optimization process. Other variables related to the studied DISI engine are assumed as constants on this study. The crank angle reference value (i.e, $0°$ CA) is the top-dead center (TDC) occurred during the open-phase (i.e., involving the admission/exhaust strokes).

The admission pressure is set free on its maximum value so that the optimum engine operation state can be as close as possible to the knock threshold condition, and therefore be

Table 7.1 – Engine parameter inputs to the optimization process

Parameter	Values
P_{adm} (bar)	[0.5, ∞)
V_{cyl} ($10^{-6}m^3$)	[300, 400]
r	[12,15,18]
N_{engine} (RPM)	[1000, 1250, 1500, 1750, 2000]
λ	[1.0, 1,3]
v_{H_2O}	[0.0, 0.05, 0.1, 0.2]
P_{atm} (bar)	1
T_{atm} (K)	300
P_{exh} (bar)	1.2
T_{exh} (K)	950
Number of valves	2 admission and 2 exhaust
Inlet valve diameter	30.94 mm
Exhaust valve diameter	28.27 mm
Valve lift/diameter ratio	0.3
IVO (intake valve opening) (° BTDC$_{intake}$)	0
IVC (intake valve closure) (° ATDC$_{intake}$)	180
EVO (exhaust valve opening) (° BTDC$_{intake}$)	180
EVC (exhaust valve closure) (° ATDC$_{intake}$)	0
Injection timing (° CA ATDC$_{intake}$)	90
T_{wall} (K)	$500K$
D/L ratio	1
Connecting rod	128 mm
Nozzle diameter	0.50 mm
Number of injection nozzle holes	10
Nozzle injection pressure	200 bar
Nozzle injection temperature	293 K
Internal EGR ($\%$)	$\approxeq 5\%$

near to optimal efficiencies (in terms of first and second laws of thermodynamics). So, each of these input variables was combined to find an engine optimal operation condition for four different fuel blends of wet ethanol (E100W0, E95W5, E90W10, E80W20). The combination of these input variables provide 144 different optimal states which are analyzed in terms of the outputs presented in Tab. 7.2. Each of this optimal states is presented as a case in Tabs. E.1-E.5. Besides the previously mentioned knock index value, other outputs are also analyzed on the discovered optimal states found by the algorithm, for example the engine efficiencies (η_{1st} and η_{2nd}), the nitric oxide emission (ppm_{NO_x}), and the exergy available on the engine exhaust ($\dot{B}_{exhaust}$).

The direct proportionality of η_{1st} with K_{In} is adopted to simplify the problem in this optimization process. Instead of solving this problem by searching for optimal values of

Table 7.2 – Optimization function objectives or outputs

Parameter	Values
K_{In}	< 1.0
η_{1st} and η_{2nd}	-
ppm_{NO_x}	-
ppm_{CO_2}	-
$\dot{B}_{exhaust}$	-
$SFC\ (g_{fuel}/kW.h)$	-

two (or more) objective functions, the algorithm focuses on finding the state where $K_{In} \approxeq 0.99$, therefore guaranteeing an optimal and secure engine operation without detonation. Thus, Eq. 7.1 represents the function objective for the case in study:

$$f = f(P_{adm}) = KIn(P_{adm}) \tag{7.1}$$

The *fgoalattain* function on MATLAB® was adopted to develop this optimization process. The details of this algorithm are presented in Matlab (2018). Some modifications were required on the function configuration in order to accelerate the algorithm search process, and these are presented by Tab. 7.3.

Table 7.3 – MATLAB fgoalattain function configuration

Parameter	Value
Constraint tolerance	0.001
Finite difference step-size	0.01
Finite difference type	central-difference second-order
Function tolerance	0.1
Maximum number of iterations	5
Maximum number of function evaluations	20
Step tolerance	0.001

7.2 Machine learning for wet ethanol combustion phasing

In order to apply realistic values of wet ethanol combustion phasing in the planned optimization process, a multivariate polynomial regression algorithm was adopted on the experimental data presented on Lanzanova *et al.* (2016). The multivariate polynomial regression is a supervised machine learning algorithm in which experimental data is provided to a computer code and based on previous knowledge about the output behavior (in this case, combustion phasing parameters), an analytical expression is obtained which best represents the experimental data. It is a least-squared method in which the cost function (i.e., the total sum of the mean of the squares of the differences between the predicted value by the method and its actual value) is minimized. Depending on the adopted hypothesis function (e.g., linear, parabolic, mixed polynomial regressions, etc.), a series of parameters/coefficients is obtained that provide a curve that best fits this experimental data. The cost function has the following form:

$$J(\Theta) = \frac{1}{2m}\sum_{i=1}^{m}(h_{\Theta}(X) - y_i)^2 \tag{7.2}$$

where J is the cost function, m is number of training examples, $h(\Theta)$ is the hypothesis function based on the parameters in the Θ vector, and y_i is the ith actual/original value. A standard feature scaling as well as a mean normalization were applied to the inputs in order to adjust all these variables into the same range (usually between -1 and 1), thus speeding up the process without oscillations. The normalized input vector X therefore has the following form:

$$X = \frac{x - \mu}{\sigma} \tag{7.3}$$

where x is the original input, $\mu = [1.23, 0.08, 4.43]$ is the average of each input, whereas $\sigma = [0.167, 0.073, 1.507]$ represents each input standard deviation. The values presented here are valid for the experimental data obtained from Lanzanova *et al.* (2016). In the current problem, the inputs adopted to the regression algorithm are λ, v_{H_2O} and IMEP, thus the original input vector:

$$x = [\lambda, v_{H_2O}, IMEP] \tag{7.4}$$

The hypothesis function adopted to this problem is cubic for each of these inputs, thus the normalized input vector X are:

$$X = [1, \lambda, v_{H_2O}, IMEP, \lambda^2, v_{H_2O}^2, IMEP^2, \lambda^3, v_{H_2O}^3, IMEP^3] \tag{7.5}$$

After applying both feature scaling and normalization to the vector X, the hypothesis function has the following form:

$$h(\Theta) = X\Theta^t \tag{7.6}$$

where $\Theta = [\theta_0, \theta_{1,1}, \theta_{1,2}, \theta_{1,3}, \theta_{2,1}, \theta_{2,2}, \theta_{2,3}, \theta_{3,1}, \theta_{3,2}, \theta_{3,3}]$. The first index indicates the order of the polynomial associated with theta whereas the second index indicates the original input associated with θ. The minimization procedure applied a gradient descent algorithm to find the best set of Θ to represent each output of interest (in this case, η_{comb}, $\Delta\theta_{0-10}$, $\Delta\theta_{10-90}$, and spark timing θ_0). Table 7.4 presents all optimized theta parameters obtained for all four output variables:

Table 7.4 – Multivariate polynomial parameters for the combustion phasing based on Lanzanova *et al.* (2016)

Parameter	θ_0	$\theta_{1,1}$	$\theta_{1,2}$	$\theta_{1,3}$	$\theta_{2,1}$	$\theta_{2,2}$	$\theta_{2,3}$	$\theta_{3,1}$	$\theta_{3,2}$	$\theta_{3,3}$
η_{comb}	49.476	-1.404	-1.019	-10.499	-1.471	0.225	46.055	0.382	-0.120	-0.083
$\Delta\theta_{0-10}$	14.219	3.058	0.541	-2.083	-0.268	0.047	13.442	-0.158	0.336	0.935
$\Delta\theta_{10-90}$	9.766	4.005	0.556	-1.923	0.941	-0.275	9.124	-0.145	0.413	0.137
θ_0	-11.970	-7.062	-4.417	1.527	-1.502	-0.487	-11.366	0.193	1.172	-1.020

After applying this algorithm, Figs. 7.1-7.4 present comparisons between the regression and experimental values for each one of the combustion phasing parameters. As can be noticed on all four figures, the predicted values were capable of mostly reproducing the original values with average relative differences lower than 5%. Thus, these expressions were adopted to simulate the combustion phasing during the optimization on the engine simulator.

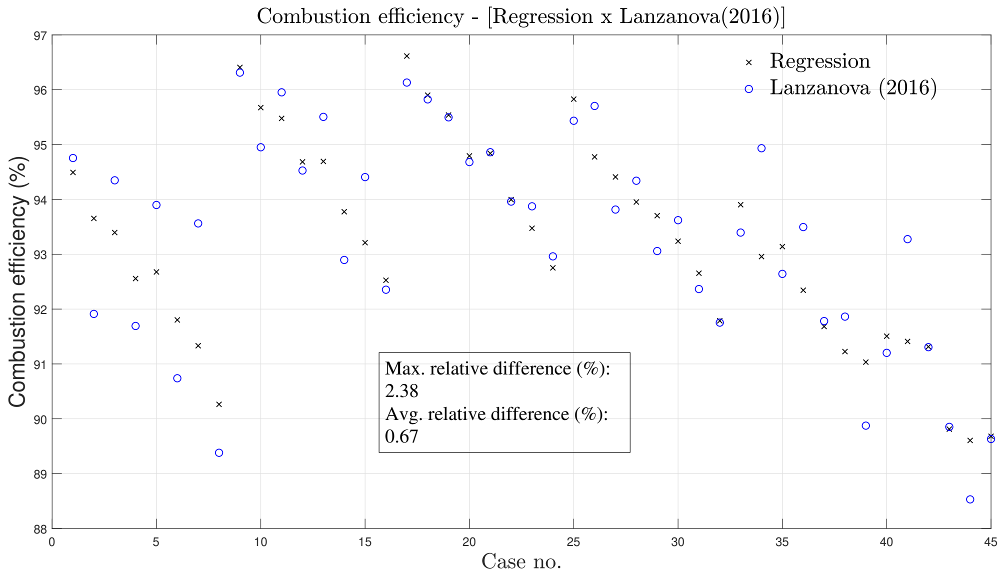

Figure 7.1 – Combustion efficiency multivariate nonlinear regression (based on experimental data from Lanzanova *et al.* (2016)

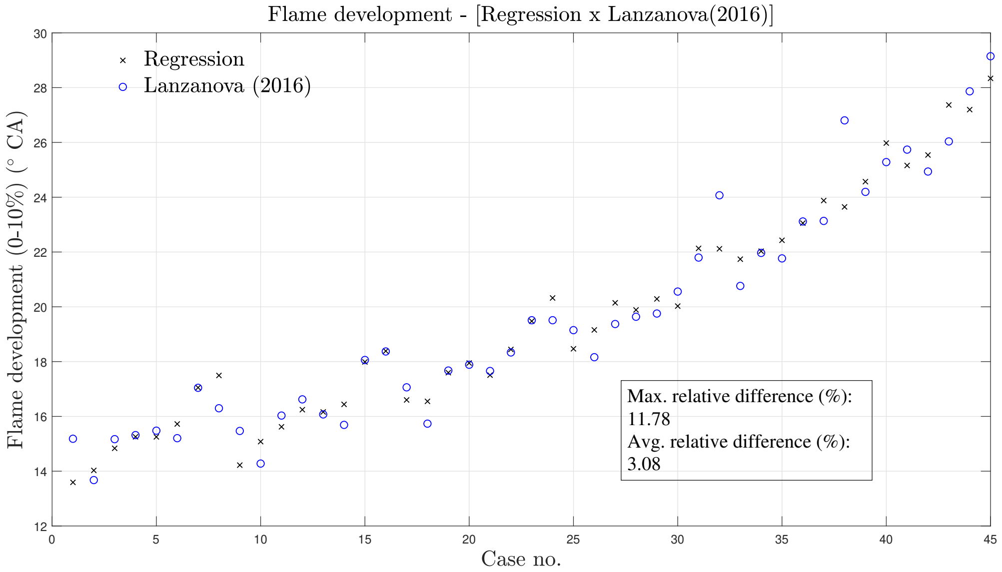

Figure 7.2 – Flame development angle ($\Delta\theta_{comb,0-10}$) multivariate nonlinear regression (based on experimental data from Lanzanova *et al.* (2016)

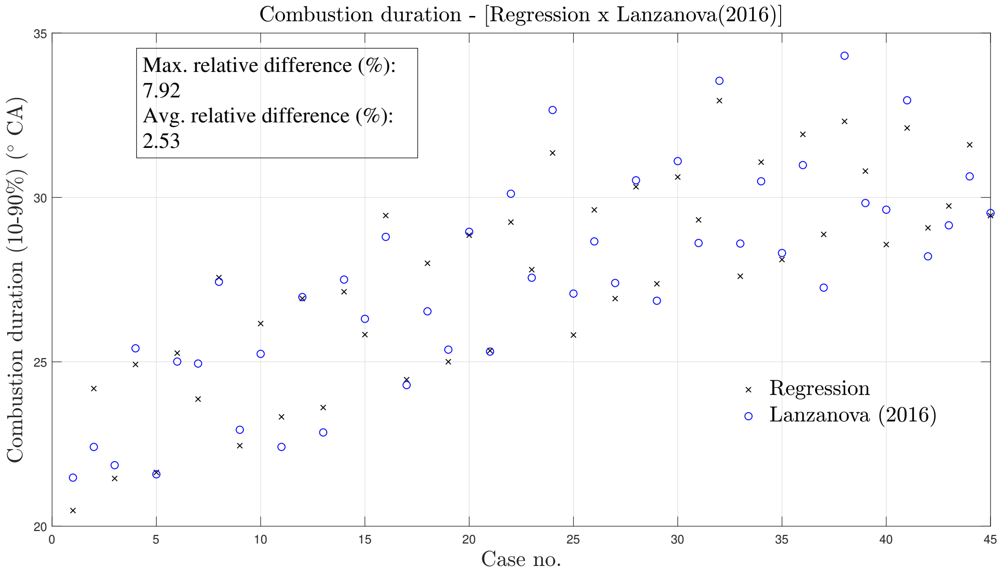

Figure 7.3 – Combustion duration ($\Delta\theta_{comb,10-90}$) multivariate nonlinear regression (based on experimental data from Lanzanova *et al.* (2016)

7.3 Super/turbocharging & intercooler effects

The thermodynamic optimization process of the described DISI engine adopted the supercharging and/or turbocharging techniques in order to increase the admission pressure, thus elevating the volumetric efficiency and the mass inside the engine cycle, consequently increas-

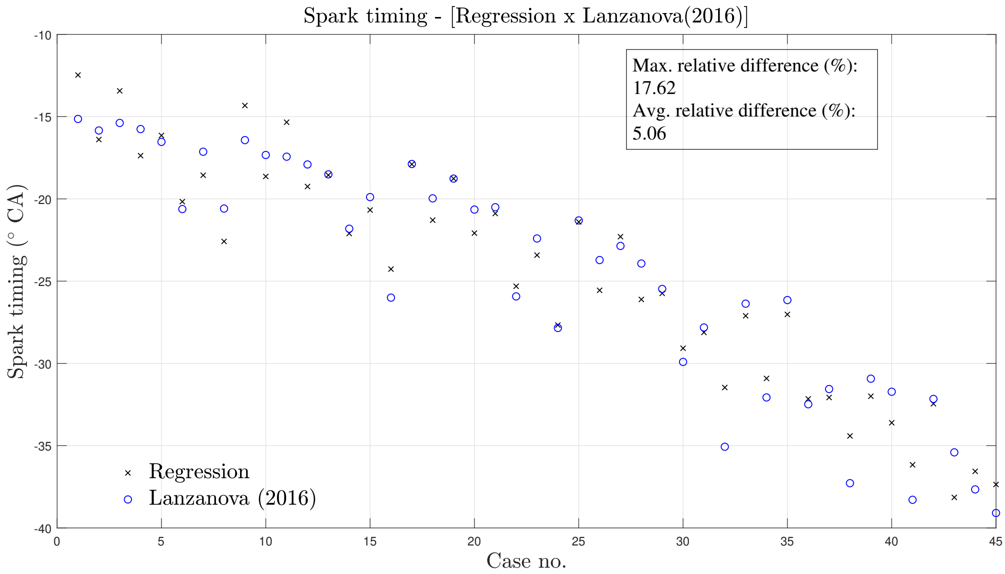

Figure 7.4 – Spark timing ($\theta_{comb,0}$) multivariate nonlinear regression (based on experimental data from Lanzanova *et al.* (2016)

ing the engine power and possibly the engine efficiencies as well.

In order to evaluate the intercooler demand for the super/turbocharging process, a comparison between two optimal engine states for two different admission temperatures is presented here. First, an optimization process was evaluated assuming the admission air temperature (just before the engine cycle) is 300K. Next, another optimization was developed, however it assumed the temperature as 373K. Since the air admission conditions depend directly on the intercooler cooling capacity ($\dot{Q}_{intercooler}$) and indirectly on the vehicle cooling water temperature (which ranges from 90 to 95 ° C)), it is prudent to analyze how this capacity affect the optimization process. Therefore, this comparison involves the cases 1 and 13 indicated at Tab. E.5 to illustrate the intercooler requirements and cases conditions are presented by Tab. 7.5.

Table 7.5 – Comparison cases to evaluate the intercooler demand effect on the optimization process

Parameter	Value
Engine speed	2000 RPM
Compression ratio	12 (both cases)
υ_{H_2O}	0 and 0.2
λ	1.0
υ_{cyl}	300 cm^3 (both cases)

Tables 7.6-7.7 present the engine performance for $T_{adm} = 300K$ and $T_{adm} = 373K$

for the cooler and hotter admission states, respectively. The first noticeable point in Tab. 7.6 is that the higher air temperatures reduced the engine load (19.5$\%$ reduction), and therefore its power (clearly) and efficiencies (slightly). The super/turbocharger was not applicable for the hotter case, since the pressure associated with the threshold knock index was below the adopted environment pressure. On the other hand, the cooler case could operate the turbocharger, thus slightly increasing the final engine power from 8.47 to 8.60 kW. When wet ethanol is used (Tab. 7.7), the engine load reduced 23.2%, but both efficiencies were equivalent. In addition, the obtained engine power values were quite different (11.8 *versus* 7.80 kW). This behavior is justified based on the drastic admission pressure reduction, thus reducing the cylinder mass and increasing the pumping work during the open-cycle. Lastly, there is room for improvement in the turbocharger operation, where adjustments on the admission/exhaust valve commands and consequently on the exhaust pressure (i.e., higher values with earlier EVO) and residual gases of the engine cycle may improve the turbocharger efficiency and net power, and therefore the overall engine efficiencies.

Table 7.6 – Optimized results for $v_{H_2O} = 0.0$ (anhydrous ethanol).

Parameter	$T_{adm} = 300$K	$T_{adm} = 373$K
$P_{post-comp}$ (kPa)	122.7	98.8
η_{1st}	0.4185	0.4039
η_{2nd}	0.3811	0.3678
$\dot{W}_{engine}$ (kW)	8.6	5.7

Table 7.7 – Optimized results for $v_{H_2O} = 0.2$ (wet ethanol).

Parameter	$T_{adm} = 300K$	$T_{adm} = 373K$
$P_{post-comp}$ (kPa)	174.1	133.7
η_{1st}	0.3994	0.3999
η_{2nd}	0.3637	0.3642
$\dot{W}_{engine}$ (kW)	11.8	7.8

In conclusion, a high intercooler capacity is very interesting towards an optimal engine state operation, and therefore it is assumed as true for the following results.

7.4 Optimization results

After contextualizing the conditions of the optimization, this section is dedicated to the main results related with this thesis. Most of them are presented based on the cases of Tabs.

E.1-E.5, where the case number identifies the combination of each input variables evaluated in the search process. The following figures have their x-axis representing the case number indicated on the tables of Appendix E, while their y-axis show the studied parameter (engine power, efficiency, etc.). This approach was chosen since it yields more compact graphs with several parameter effects possible to be analyzed in the same figure. For example, cases 1 and 2 present the differences between two cylinder volumes while the remaining inputs are constant. Other sets of comparisons involve cases 1 and 3, which evaluate relative air-fuel ratio effects, whereas cases 1, 5, 9, and 13 relate different water-in-ethanol volumetric fractions, 1, 17, and 33 different compression ratios, and so on.

7.4.1 Engine load

Figure 7.5 presents the optimal engine loads on threshold knock conditions encountered for the inputs indicated by Tab. 7.1. Cases 1 to 4 refer to E100W0, cases 5 to 8 to E95W05, cases 9 to 13 to E90W10, etc. This same pattern repeats for the remaining compression ratios. The engine load is assumed in this work as a function of the atmospheric pressure ($P_{atm} = 1$ bar). The horizontal dashed line indicates the transition between partial load ($P_{adm} < P_{atm}$) and turbocharging operation/overload ($P_{adm} > P_{atm}$). Also, the figure is divided into three rectangles by two vertical dashed lines, whose regions indicate the respective compression ratios for the cases involved in each of these areas.

Some characteristics about the engine optimization process involving engine load are worth mentioning. First, higher degrees of water in wet ethanol increased the optimal loads, as noticed for example by comparing cases 1, 5, 9, and 13, where a transition between partial load (case 1) to turbocharging operation (case 13) occurs for most speeds. Second, leaning the air-fuel mixture (cases 1 and 3) decreased the maximum engine load for all speeds. Third, increasing the compression ratio (cases 1, 17 and 33) reduced the engine load on all cases. Also, another interesting point is the reduction on the engine load amplitude for different engine speeds at higher compression ratios. These two characteristics are due to the existence of an upper limit unburned gas pressure the air-fuel-residual gas mixture reaches without detonating. Thus, it is reasonable to expect that higher compression ratios accept lower levels of turbocharging (and therefore engine load) in order to avoid detonation. Another point to highlight is the reduction of maximum work the compressor can develop at higher compression ratios, which is a characteristic that can be further explored in a future optimization such as this one. At last, an

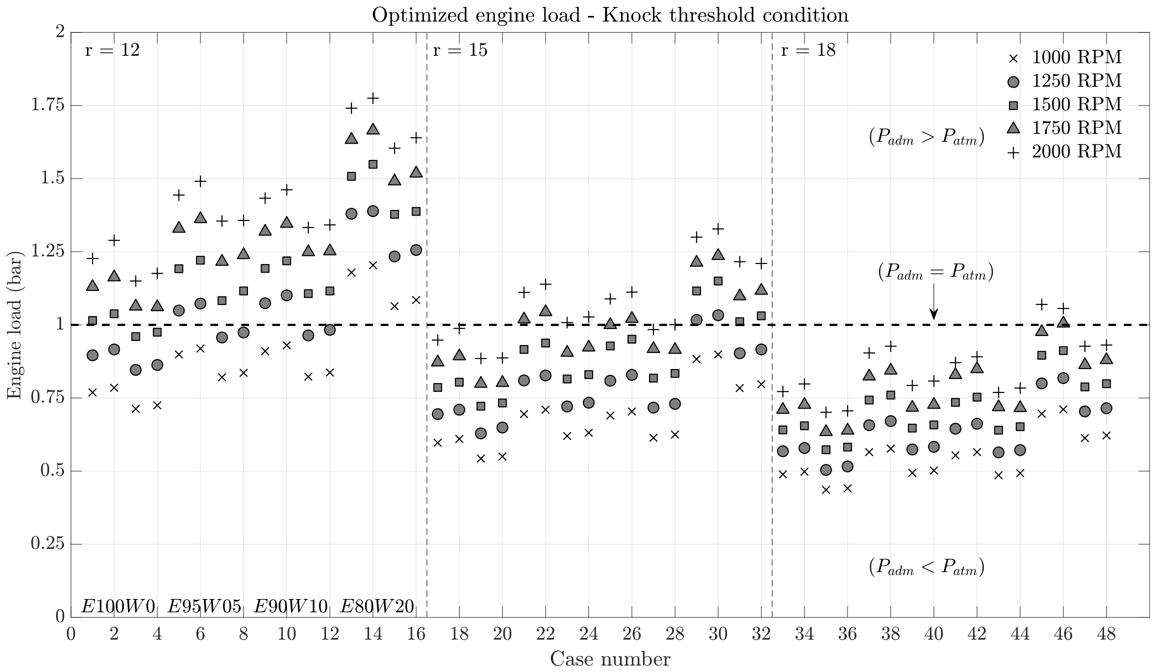

Figure 7.5 – Optimal engine loads at knock threshold conditions. The horizontal dashed line indicates the transition between partial load ($P_{adm} < P_{atm}$) and turbocharging operation/overload ($P_{adm} > P_{atm}$), while the vertical dashed lines separate the regions of different compression ratios.

important detail is that the results did not identify clear benefits on downsizing for the engine load; this is justified by the combustion phasing correlations that do not take into account the engine size as one of their parameters, thus they do not consider the cylinder volume effect on the variation of spark timing ($\theta_{comb,0}$), flame development (θ_{0-10}), combustion duration (θ_{10-90}), and combustion efficiency (η_{comb}).

In order to complement this section, Fig. 7.6 presents the volumetric efficiency. As expected, this variable shows the same trends as the engine load, however there is an important detail about the wet ethanol evaporative cooling capacity that is evident from this figure. Independently if there is the compressor actuation on the system, the ethanol-water evaporative cooling effect collaborates to enhance the volumetric efficiency. For example, this efficiency reaches values near 1 from cases 1 to 4 at 1250 RPM without any help of the supercharger/turbocharger system, as noticed in Fig. 7.5. In addition, at r = 12, E80W20 allows all engine speeds to reach an efficiency over 1, thus allowing the engine to operate in a more intense and efficient way without knock occurrence.

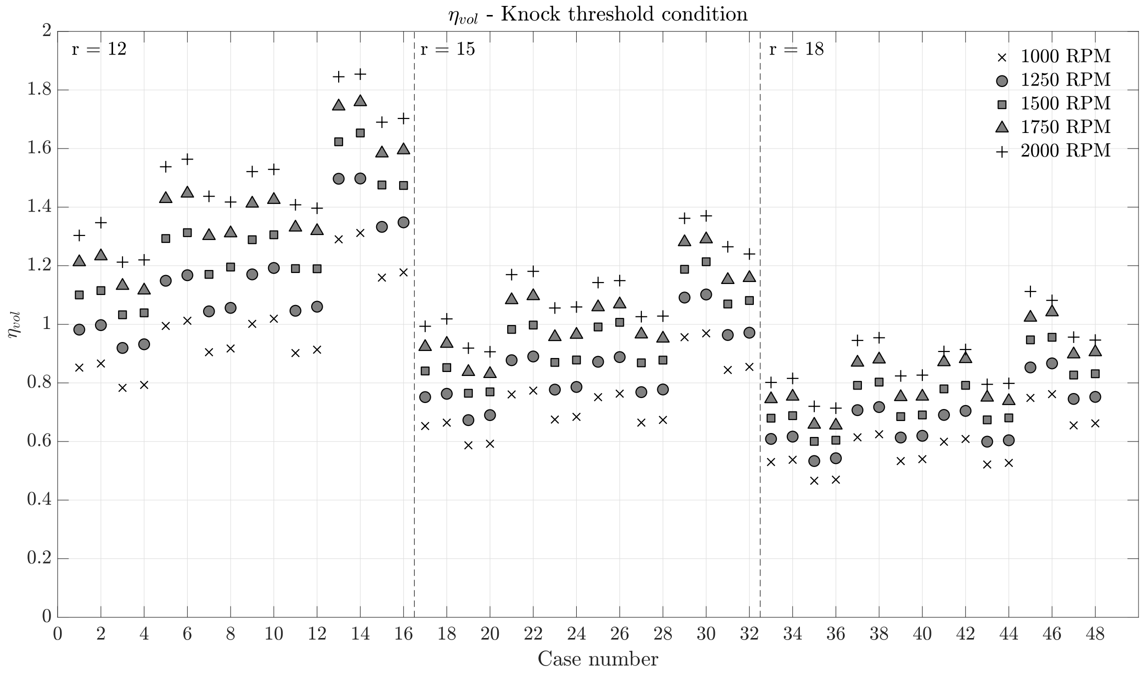

Figure 7.6 – Optimal engine volumetric efficiency at knock threshold conditions.

7.4.2 Engine power and NIMEP

Figure 7.7 presents the engine power characteristics for each optimized case. These values take into account the extra power that the turbocharger offers to the engine system when turbocharging is possible (Fig. 7.5); otherwise, the figure presents only the engine cycle output. Due to the higher engine loads, the cases 1 to 16, when compared to the ones at different compression ratios, but under the same conditions, offered higher values of engine power. These loads are directly associated with higher trapped in-cylinder masses, as Fig. 7.8 shows. Thus, it is expected higher power outputs for lower compression ratios. However, it is worth mentioning that this behavior does not indicate that cases 1 to 16 are more efficient than the others, since the total mass affects directly the total energy output the engine system develops.

Another point to highlight in Fig. 7.7 is the peak engine power obtained from $E80W20$ (cases 13 to 16 for $r = 12$, cases 29 to 32 for $r = 15$, and cases 45 to 48 for $r = 18$). For example, case 14 reached a value of almost 15.5 kW (20.8 HP or 75 N.m/cylinder of torque) at 2000 RPM without an optimal valve configuration. At last, the combination of leaner mixtures, higher compression ratios and water content can replace the engine operation for current ICE conditions of operation in Brazil (i.e., E95W05 rich/stoichiometric at $r = 12$) without losing power. For example, cases 32 and 48 yield the same 4 kW obtained from case 6 at 1000 RPM by operating at 1250 and 1500 RPM, respectively. So, the usage of wet ethanol can provide enough power if its characteristics as a fuel are properly taken into account and therefore optimized to the engine operation.

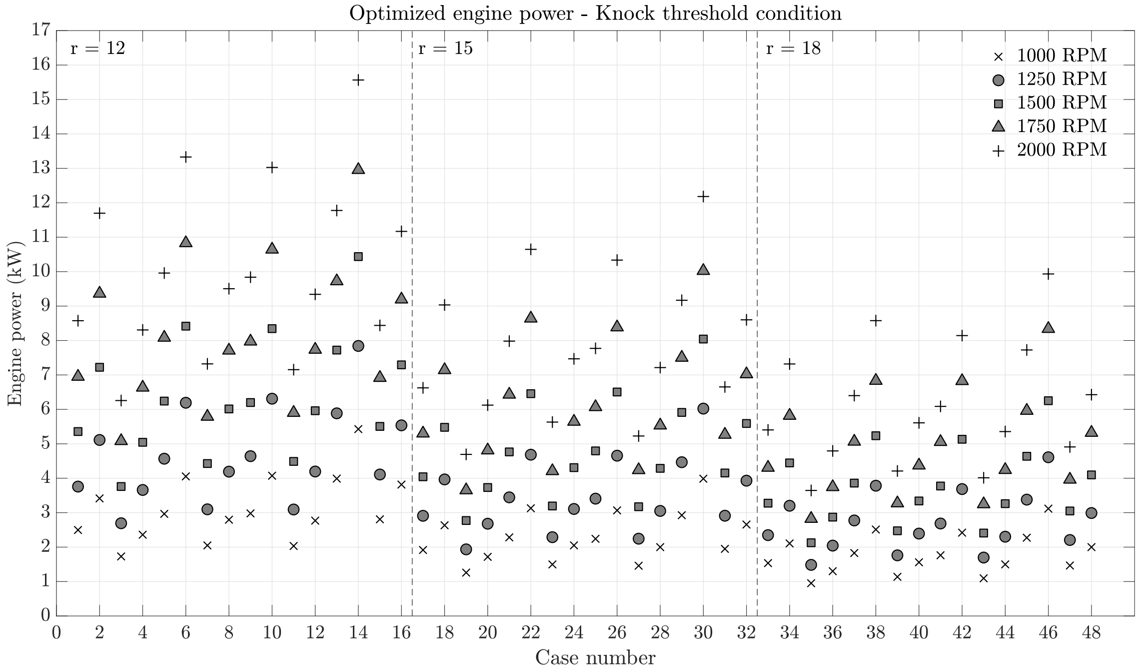

Figure 7.7 – Optimal engine power at knock threshold conditions. For cases where the engine load is greater than 1 bar, the power takes into account the turbocharger contribution; otherwise, it is only the DISI engine output.

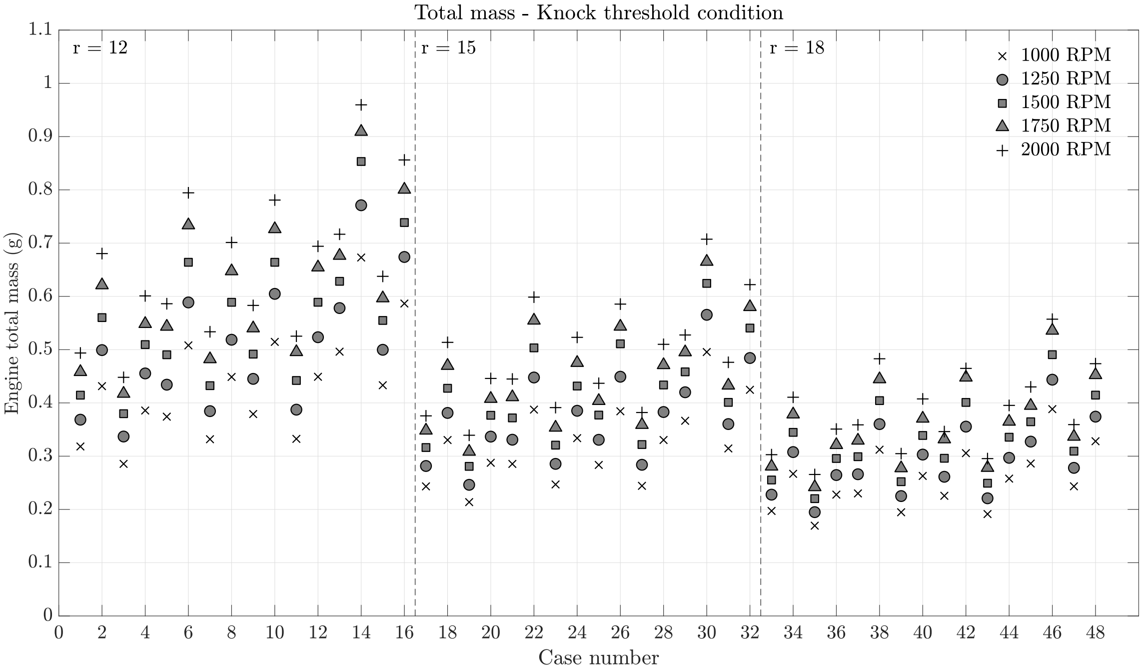

Figure 7.8 – Total trapped in-cylinder masses for the optimal states.

The net indicated mean effective pressure (NIMEP) is a characteristic parameter of

ICEs that represents their capacity to develop work for different engine volume values. Figure 7.9 shows the NIMEP values for all optimized cases. As noticed by the engine power in Fig. 7.7, higher water volumetric fractions indicate higher values of NIMEP, especially with the combination of evaporative cooling, turbocharging, higher in-cylinder mass, and knock suppression. On the other hand, the downsizing effect is not noticeable, for the reason previously explained in Sec. 7.4.1. Thus, for a raw capacity analysis, cases 13 and 14 are very interesting options, whereas to obtain the lowest NIMEP fluctuation with engine speed maybe the most valid cases are 47 and 48.

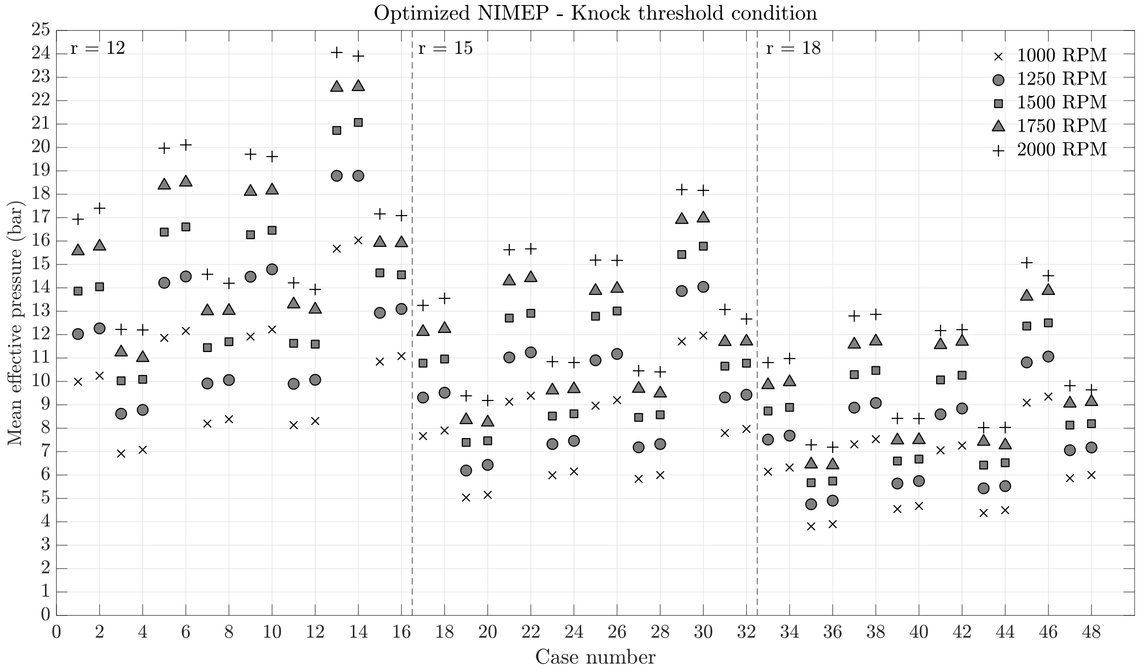

Figure 7.9 – Optimal net indicated engine mean effective pressures (NIMEP) at knock threshold conditions.

7.4.3 Engine efficiencies

After contextualizing the engine operation, Figs. 7.10-7.11 show how efficient the engine operates in terms of the first (energy) and second (exergy) laws of thermodynamics. The engine operation is simulated near the threshold knock condition, where the secure engine load is at its maximum and thus is the engine efficiency, since they are directly proportional.

First, the engine energetic (or thermal) efficiency is discussed, where the left sub-figure refers to the standalone engine efficiency or with supercharger when knock suppression allows it, whereas the right sub-figure refers to turbocharged-engine efficiencies. Figure 7.10 indicates that all calculated efficiencies are above 35%, even for 1000 RPM. Also, most engine speeds present efficiencies higher than 40%, with exception of 1000 RPM. The maximum efficiencies for standalone or supercharged cases are found for 2000 RPM with $r = 18$, with values higher than 42.5% for most cases. Another point to highlight is the efficiency increment due to turbocharging operation, as noticed on the right sub-figure. For example, case 28 (at 2000 RPM) increased almost 2% with turbocharging when compared to supercharging conditions. The highest efficiencies are obtained on cases 23, 24 and 28 at 2000 RPM and $r = 15$, which is justified based on a balance between compression ratio and engine load. Still, cases 45 and 46 are good alternatives as well, presenting efficiencies near 43% for a non-optimized valve command and without adoption of special EGR techniques.

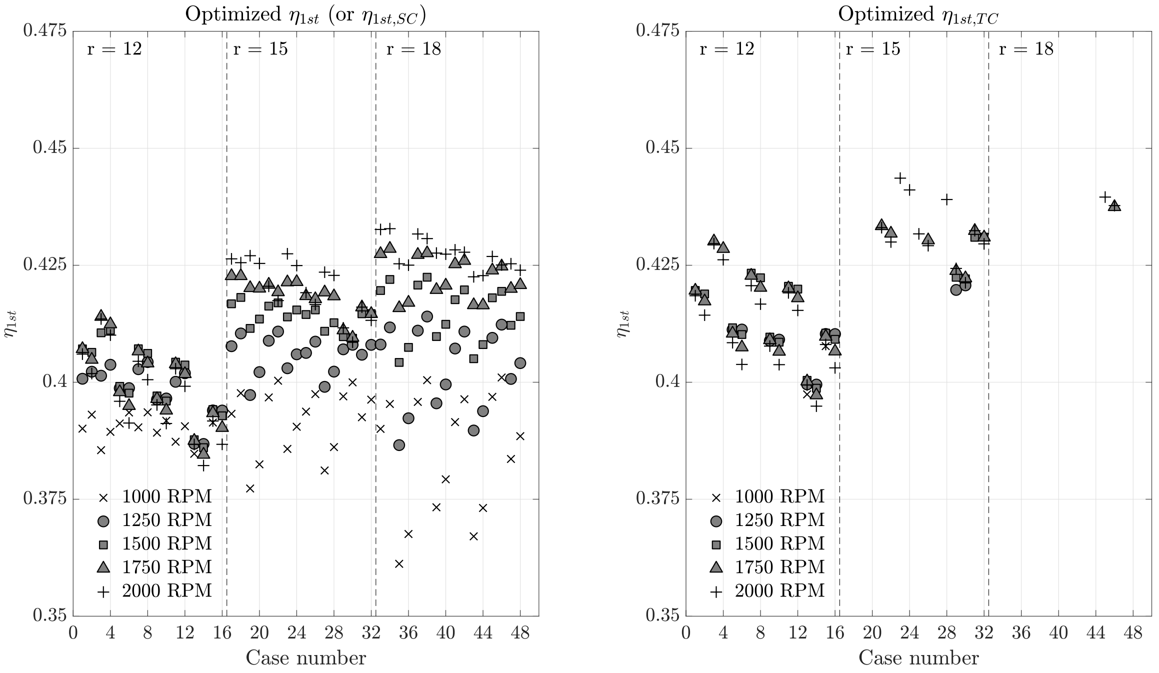

Figure 7.10 – Optimal first law engine efficiency at knock threshold conditions. The left sub-figure refers to the standalone engine efficiency or with supercharger when knock suppression allows it. The right sub-figure refers to turbocharged-engine efficiencies.

Speaking in terms of exergy, Fig. 7.11 indicates the second law efficiencies for the optimized cases. As expected, these efficiencies are always lower than its first-law parents, due to the ratio between the fuel chemical exergy and its lower heat value be always greater than one ($B_{ch,wet}/LHV_{wet} > 1$). Thus, the values for standalone or supercharged engine cases (left sub-figure) are below 40%, while the turbocharged ones are at maximum near 41%. The remaining exergy is transferred on the cylinder wall heat transfer, on the exhaust flow, or destroyed on internal irreversibilities (Gallo, 1990; Rufino *et al.*, 2019).

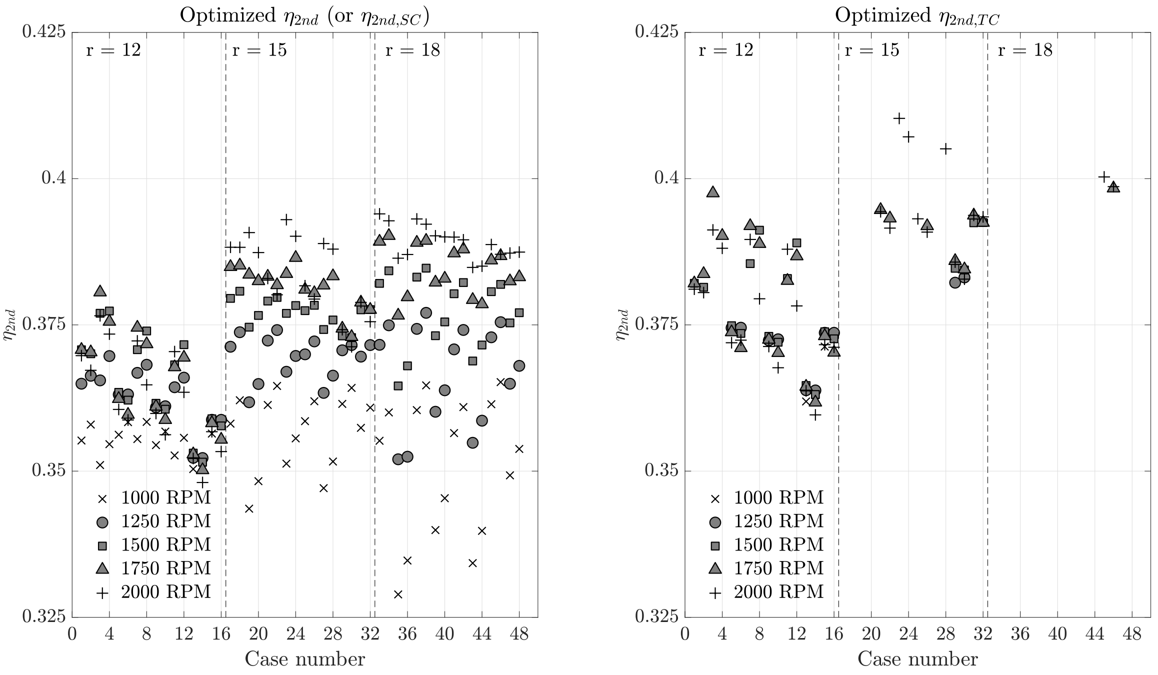

Figure 7.11 – Optimal second law engine efficiency at knock threshold conditions. The left sub-figure refers to the standalone engine efficiency or with supercharger when knock suppression allows it. The right sub-figure refers to turbocharged-engine efficiencies.

Even though the engine load presented a reduction on its variability at higher compression ratios as previously discussed, both efficiencies vary differently: they are more stable at lower compression ratios, whereas more dispersed under $r = 18$, for example. Thus, this behavior indicates that engine load affects more intensely the engine efficiency for higher compression ratios, and therefore it must be more carefully optimized in order to reach the optimal engine operation state. At last, the compression ratio also increases both efficiencies for higher water contents, such as visible for E80W20. Thus, a more efficient engine operation with higher v_{H_2O} require also higher r in order to explore properly the wet ethanol fuel characteristics.

7.4.4 Engine irreversibility

The total engine cycle irreversibility was also studied in this optimization process and Fig. 7.12 represents their values obtained on the knock threshold at all analyzed engine speeds. The values are presented in a specific/intensive form (i.e., per gram of in-cylinder gas) in order to properly compare the different engine operations. It is noticed that the engine speed slightly decreases the specific irreversibility for all cases. The amount of water increases the irreversibility of the engine cycle, mainly due to allow a more intense engine operation (i.e., higher admission pressure and in-cylinder mass). Other important point is that leaner mixtures decreased the irreversibility for most cases. On the other hand, the compression ratio appears to not affect significantly the specific irreversibility, as noticed by the same trends visible inside the three rectangular areas. In short, a final highlight is that the results of this figure may be better enriched by combining them with the ones from Figs. E.6-E.10, 7.8, and 7.11, in order to indicate how well each engine case operates in terms of exergy.

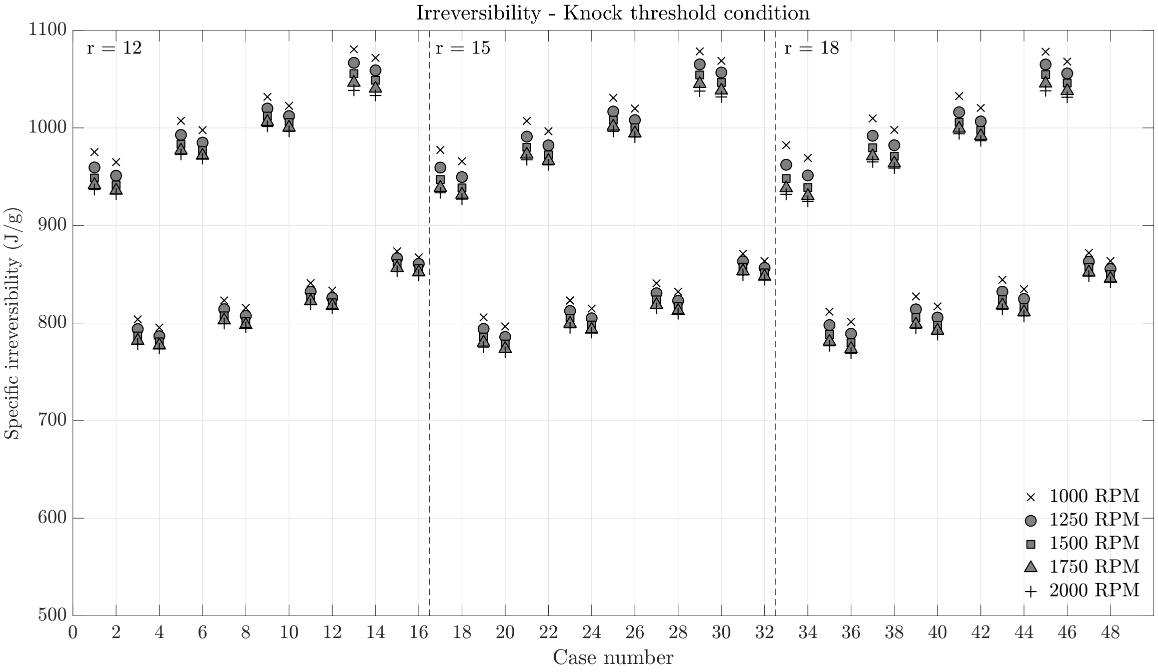

Figure 7.12 – Optimal engine cycle irreversibility at knock threshold conditions. All values are presented in a specific/intensive form in order to properly compare the different engine operations.

7.4.5 Pollutant emissions

This section focuses on presenting the emissions of nitric oxide and carbon dioxide of each case obtained from the optimization. The results for carbon monoxide and aldehydes obtained from the adopted chemical kinetics model (Marinov, 1999) were not proportionally significant, therefore their simulations require a rework. Thus, their analyses are not presented in this text.

Figure 7.13 shows the results for NO and Fig. 7.14 refers to CO_2. The results from NO_x indicate that the lowest values are found on cases 25, 26, 41 and 42 ($\upsilon_{H_2O} = 0.1$ with $\eta_{1st} \approx 0.4$ and $\eta_{2nd} \approx 0.36$) with approximately 9 $g_{NO}/(kW.h)$ at 1000 and 1250 RPM. On the other hand, the highest ones happen on cases 13 and 14 ($\upsilon_{H_2O} = 0.2$). The cases with the highest energetic and exergetic efficiencies (23 and 24) have emissions of near 14 $g_{NO}/(kW.h)$, a moderate value relative to the values presented on the figure. Additionally, in a case with turbocharger operation (cases 45 and 46), there is a combination of very high efficiencies (approximately 43.5 and 40.0%) at 1750 and 2000 RPM with moderate-to-high value of nitric oxide ($g_{NO}/(kW.h)$).

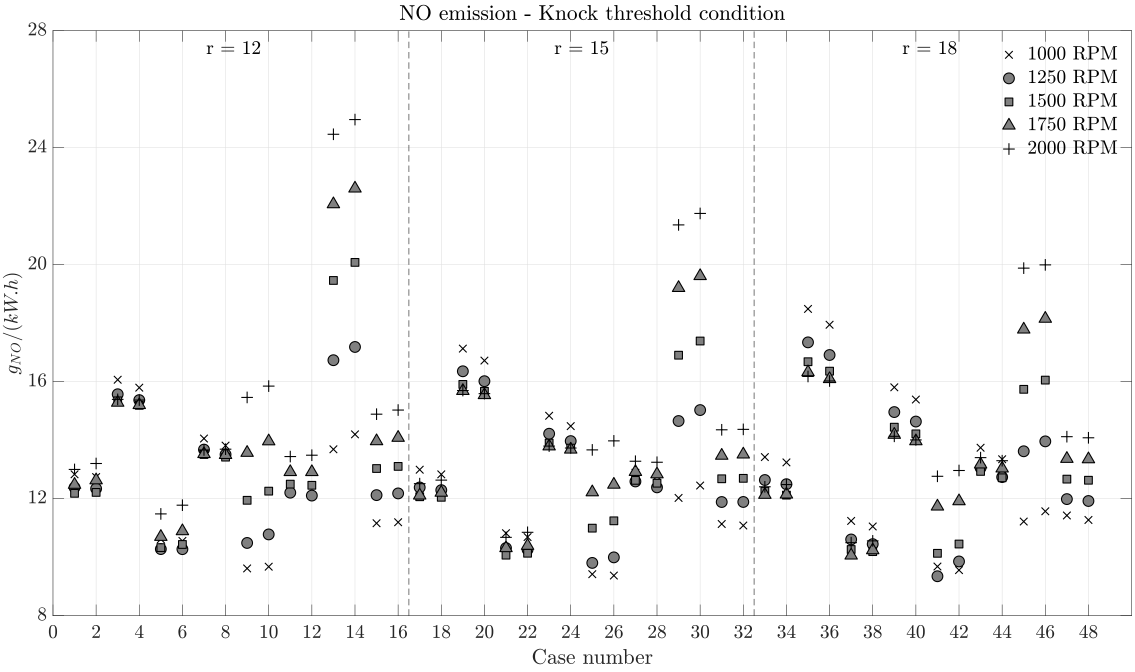

Figure 7.13 – NO_x emissions for the optimal states at knock threshold conditions.

In terms of carbon dioxide, it is clear that the influence of wet ethanol water volumetric fraction on the quantity of CO_2, as Fig. 7.14 shows. The lowest values are found for cases 45 and 46 at 2000 RPM (lower than 500 $g_{CO_2}/(kW.h)$), whereas the highest involves lower contents of water. Additionally, the results indicate no clear influence of compression ratio on the amount of carbon dioxide. Some of the highest efficiency cases (e.g., 24 and 45) involve two very different value ranges of CO_2, with the latter case providing lower productions, and therefore emissions of this gas.

7.4.6 Fuel consumption

Specific fuel consumption (SFC) deserves special attention on this text since it is a very usual parameter for engine performance as well as there are different fuel compositions under evaluation on the optimization process. An interesting characteristic involving this parameter is highlighted by Figs. 7.15-7.16, which involve the wet ethanol composition and its

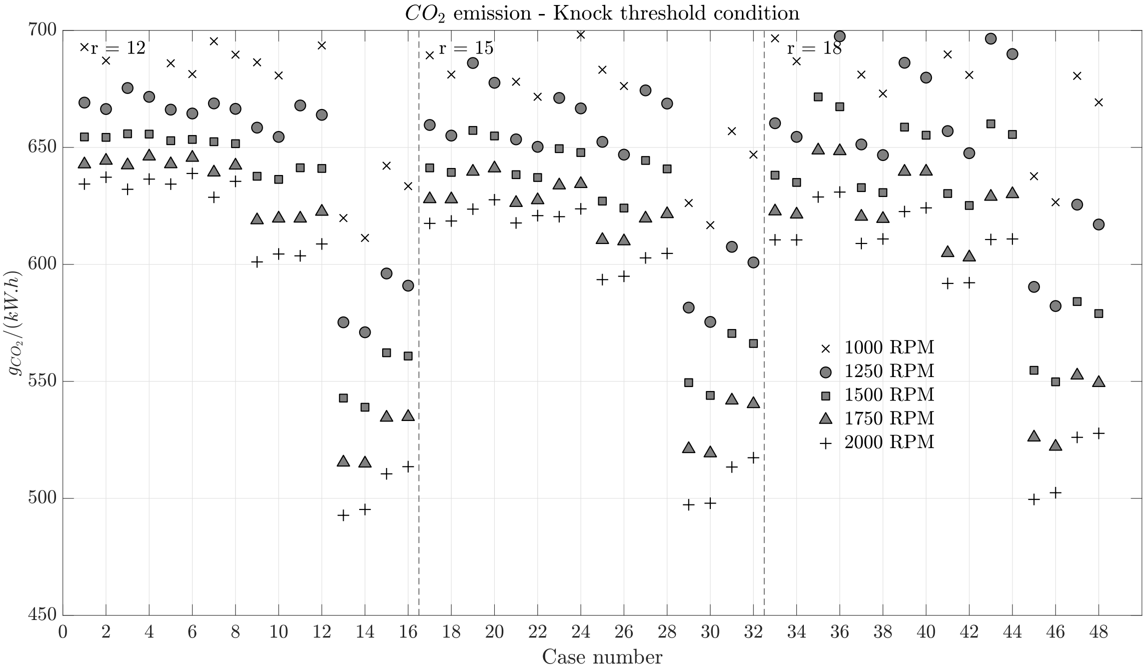

Figure 7.14 – CO_2 emissions for the optimal states at knock threshold conditions.

ethanol part on the calculations, respectively. A noticeable point is that these two different SFCs indicate different trends towards increasing water content on the fuel: although Fig. 7.15 indicates a significant increase on SFC (345 *versus* 445 $g_{fuel}/kW.h$ for cases 1 and 16 at 1000 RPM), Fig. 7.16 contrasts this result with different values (345 *versus* 335 $g_{EOH}/kW.h$) for the same cases. This behavior happens because the first result refers to the total amount of mass involved in the fuel (i.e., ethanol + water), even though the water part does not collaborate with chemical energy for the fuel combustion. Actually, water affects the amount of mass inserted in the engine cycle as well as on the evaporative cooling effect. Thus, the optimal results basically indicate that similar SFCs can be found for both anhydrous and wet ethanol on the proportions studied here and no negative effect was highlighted by the simulations.

Another point to be highlighted is the range variation between SFC at different engine speeds as the compression ratio increases. Both the lowest and the highest SFC values increases as well (Fig. 7.16). For example, cases 15 and 47 have ethanol SFCs of 323 and $315g/(kW.h)$, respectively. This behavior opens an opportunity to operate with lower fuel consumption values depending on the chosen engine speed.

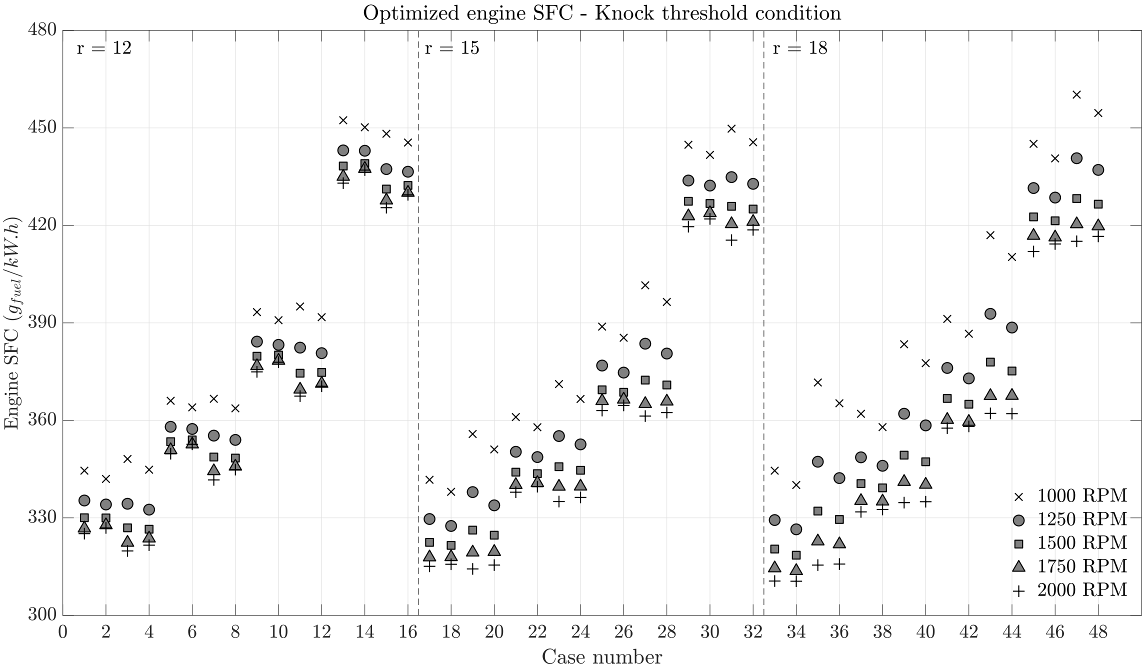

Figure 7.15 – Specific fuel consumption for the optimal states at knock threshold conditions.

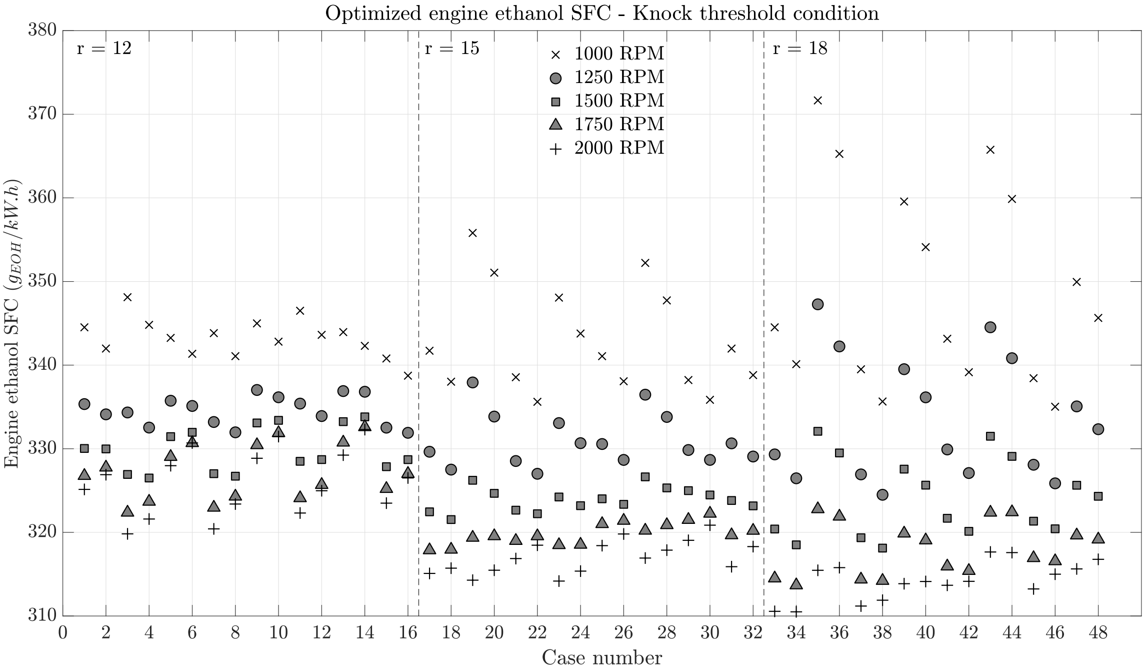

Figure 7.16 – Ethanol specific fuel consumption for the optimal states at knock threshold conditions.

7.4.7 Valve command & residual gases effects

This section presents a final analysis regarding the optimization process by applying a slightly different valve command on the engine operation system. The objective was to present a simple comparison between the adopted valve command (indicated in Tab. 7.1) and the negative valve opening (NVO) with values of Lanzanova *et al.* (2016) to check for possible alterations on the main outputs and on internal EGR. Both valve profiles were modeled as nearly parabolic (Rufino, 2020). Thus, Tab. 7.8 presents some optimization conditions as well as the valve command strategies. All other variables are equal to the ones of the first optimization.

Table 7.8 – Engine parameter inputs to the optimization process with a negative valve opening.

Parameter	Values
P_{adm} (bar)	[0.5, ∞)
V_{cyl} (cm^3)	400
r	[12,18]
N_{engine} (RPM)	[1000, 2000]
λ	[1.0, 1,3]
v_{H_2O}	[0.2]
IVO (intake valve opening) (° BTDC)	7
IVC (intake valve closure) (° ATDC)	189
EVO (exhaust valve opening) (° BTDC)	179
EVC (exhaust valve closure) (° ATDC)	3

A total of sixteen cases were analyzed for this section: eight from the first optimization and eight based on the new valve command. Cases A, B, C, D, E, F, G, and H are from the first optimization whereas cases I, J, K, L, M, N, O, and P are the new ones. For example, the input values refer to the cases 14, 16, 46, and 48 of the original optimization at 1000 (A, B, C, D) and 2000 RPM (E, F, G, H). Table 7.9 encompasses the comparison with the values of the main outputs studied on this text.

Cases G and O present the highest efficiencies among all cases for each valve command, with values near 43.0% and 42.0%, respectively. However in terms of emissions, the nitric oxide is significantly higher (5420 and 5220 ppm, respectively). The remaining variables stay under their expected ranges. The connection between total irreversibility and engine power is clear, especially due to the amount of fuel burned on each engine cycle. Thus, this table shows that the slight modification on the valve command did not improve some output parameters of the engine; it is necessary a further analysis on the valve angles towards increasing internal EGR as well as fresh new air to reduce the amount of fuel, and therefore increase the efficiency.

7.4.8 Discussion

This section focuses on discussing the results of the output parameters obtained from the optimization process. This process highlighted the main conditions on which the DISI

Table 7.9 – Comparison between two different valve command angles - optimization

Case	η_{1st}	η_{2nd}	$I(J)$	$\dot{W}(kW)$	$SFC(g/kW.h)$	$y_{Int,EGR}\,(\%)$	ppm_{NO}	ppm_{CO_2}
A	0.399	0.363	721.3	5.4	450.2	7.16	3500	10300
B	0.409	0.373	508.7	3.8	445.5	7.88	2200	8500
C	0.401	0.365	414.7	3.1	440.6	8.20	2880	10600
D	0.389	0.354	283.3	2.0	454.6	9.07	2150	8690
E	0.395	0.360	991.5	15.6	437.0	5.63	6490	8780
F	0.403	0.367	726.8	11.2	429.4	6.15	3140	7320
G	0.438	0.399	574.7	9.9	414.3	6.48	5420	9290
H	0.424	0.386	398.9	6.4	416.6	7.21	3000	7660
I	0.398	0.362	704.6	5.3	453.3	7.15	3430	10300
J	0.409	0.372	499.1	3.7	448.9	7.79	2210	8530
K	0.399	0.364	407.7	3.0	443.1	8.04	2890	10600
L	0.387	0.352	279.8	2.0	457.7	8.80	2180	8680
M	0.394	0.358	953.1	14.9	442.5	5.77	6040	9010
N	0.402	0.366	695.5	10.6	435.5	6.24	3040	7530
O	0.423	0.385	557.1	9.3	418.7	6.44	5220	9440
P	0.420	0.382	390.6	6.2	421.3	7.00	2980	7780

engine can operate near the threshold knock conditions, so that the efficiencies may be at their sustainable maximum values (i.e., without engine deterioration). However, it is also necessary to check the modifications occurred on other output parameters besides the efficiencies. The following points require special attention:

- The adoption of wet ethanol required higher compression ratios to explore properly its characteristics as a fuel in the DISI engine. The volumetric efficiency was greatly enhanced by wet ethanol evaporative cooling effect. This allowed more in-cylinder mass and it increased the power output;

- The optimal results basically indicated that similar ethanol SFCs can be found between anhydrous and wet ethanol mixture cases while reducing CO_2 emissions. Therefore, no negative effects were highlighted by the simulations. The engine load capacity to affect the engine efficiency at higher compression ratios requires careful optimization to avoid efficiency losses, instead of gains;

- The inverse relation between compression ratio and turbocharging affected directly the threshold engine load on all conditions. The possibility to contain the compression ratio increase to allow for higher levels of engine load and therefore turbocharging may be beneficial for the engine efficiency as a whole. On the other hand, higher compression ratios allow the reduction of work required by the compressor on supercharger/turbocharger systems. Thus, future optimizations may cover more directly this relationship in order to find the best conditions to operate the engine-compressor-turbine integrated system in terms of energetic and exergetic global efficiencies;

- The combination of lean combustion, higher compression ratios and water content allowed the DISI engine to operate more efficiently than more conventional engine states (i.e., E95W05 rich/stoichiometric at $r = 12$). For example, case 48 at 2000 RPM is more efficient than all cases at $r = 12$ and it yields a sufficient power and lower irreversibility to overcome most of the remaining cases. Also, the NIMEP trends also corroborate for this affirmation;

- Case 14 presented the highest engine power value found in the optimization (near 15.7 kW/cylinder at 2000 RPM). In spite of that, it presented the lowest efficiencies among the ones operating with the same compression ratio (39 and 35% for energy and exergy, respectively). Another curiosity is the pollutant emission profile: the highest nitric oxide emissions ($25g/(kW.h)$) and the lowest CO_2 ($495g/(kW.h)$);

- Even though they are not the best efficiency scenarios, cases 45 and 46 demonstrated to be interesting alternatives due to its combination of high energetic and exergetic efficiencies (approximately 43% and 40%), engine power (7.8 and $10.0kW$, respectively), and low CO_2 production (approximately $490g/(kW.h)$). This result may be further enhanced with a optimized valve command (with a Miller/Atkinson cycle) and additional EGR techniques;

- The engine speed may be lowered in some cases (4 and 16 from 1500 to 1250 RPM) without significant power loss;

- The E80W20 cases at $r = 18$ (cases 45 to 48) presented the lowest NIMEP variation among different engine speeds;

- Even though the irreversibility increased with high-water fuel mixtures, lean air-fuel mixtures can overcome this problem when compared to stoichiometric cases;

- The downsizing effect was not capable of affecting directly the simulations, as explained in Sec. 7.4.1;

In short, cases 14, 24, 25, besides 45 to 48 presented interesting combinations of input parameters, thus offering optimal efficiencies or optimal engine power outputs. The cases with E80W20 offered the lowest CO_2 emissions while usually moderate NO_x values were found for them. The possibility of downspeeding was highlighted for some specific cases by increasing water content. Also, a balance between compression ratio and engine load seems to offer an optimal condition for efficiency, depending on the turbocharger configuration. At last, further improvements towards a state-of-the-art DISI engine are available, such as internal and external EGR technology implementations, optimal valve control through Miller cycle, and turbocompounding, which all collaborate into a more sustainable and efficient engine operation, with applications both standalone as a pure ICE or in a hybrid engine operating in one specific engine speed at optimal conditions for wet ethanol.

8 CONCLUSION

This thesis had the objective of developing a thermodynamic optimization of a direct-injection spark-ignition engine fueled with different wet ethanol compositions. This engine concept was developed to specific regions in the world and utilizes some of the most recent technologies adopted to enhance direct fuel injection, such as turbocharging and higher compression ratios, and combine them with a renewable fuel mixture with great thermodynamic and environmental potentials, therefore enhancing ethanol life cycle efficiency. The idea is to operate this specific engine by taking into consideration the full potential of different wet ethanol mixtures in terms of optimal engine operation parameters related to thermal and exergetic efficiencies.

In order to develop this engine concept, a proper contextualization of the current energetic and environmental issues related to vehicle transportation via ICEs was developed, that together with the literature review, highlighted the gaps that this thesis contributed in their solution. The development of mathematical models from micro- (Lagrangian single droplet), intermediate- (spray droplet evaporation), and macro-scales (DISI engine simulation) was necessary to analyze how the fuel evaporation phenomenon would behave and affect the engine performance.

The micro-scale study involved first a parametric analysis based on second law of thermodynamics to evaluate how some fuel injector parameters affect the ethanol droplet evaporation inside a closed variable temperature environment. Then, a second analysis highlighted the main differences between four droplet evaporation models that are presented for an ethanol droplet with different air-fuel ratios. The second analysis indicates a higher specific entropy generation in the surrounding gas for richer air-fuel ratio conditions, which shows that droplet evaporation is better on lean conditions for specific injection moments. Furthermore, the analysis was expanded to a wet ethanol (bi-component) droplet evaporation injected in a piston-cylinder system during the compression stroke of a DISI engine. The main entropy transfers and the suggested droplet evaporation efficiencies provide interesting information about the set of phenomena occurring in the engine cylinder. The parametric contour curves indicated qualitative optimal conditions for several fuel injector parameters, such as fuel pre-heating, droplet size and injection timing.

The intermediate-scale model applied a study of a fuel spray injection and evaporation in a piston-cylinder system during the compression stroke of a DISI engine. Some equations for the droplet spray evaporation efficiencies were presented and suggested. The influence of the water volumetric content in wet ethanol and relative air-fuel ratio in the objective functions emphasize how direct injection can benefit the engine cycle and its efficiency. The knock integral index values obtained from the search analysis highlights the possibility of a compression ratio increase for wet ethanol without causing any significant harm to the engine and therefore obtaining higher thermal efficiencies from the engine cycle.

The engine model validation involved a comparison of some engine simulations with experimental data available in the literature (Lanzanova *et al.*, 2016; Brewster *et al.*, 2007). The simulated engine pressure curves representative of partial and full load conditions showed similarities with the experimental ones, thus indicating the code potentiality and limitations. Comparisons involving several engine outputs, such as engine fuel conversion efficiency and indicated specific fuel consumption, were also developed with good agreement found for most conditions.

The final work of this thesis involved the thermodynamic optimization of a direct-injection spark-ignition engine fueled with different wet ethanol mixtures for several different conditions. The threshold knock condition was adopted to find the highest efficiency possible under sustainable operation. The fuel mixture E80W20 was capable of overcoming the performance of both anhydrous ethanol (E100W0) and commercial ethanol (E95W5) on many conditions. The highest engine power was obtained for E80W20 on stoichiometric conditions at $r = 12$ and 2000 RPM, whereas the highest energetic and exergetic efficiencies were obtained for E95W05 at lean conditions, $r = 15$ and 2000 RPM. Still, E80W20 was also capable of reaching very similar values at both stoichiometric and lean conditions at $r = 18$. Additionally, the simulations showed that the ethanol specific fuel consumption of high water-in-ethanol mixtures is very similar to the ones of more conventional ethanol mixtures. Actually, at higher compression ratios, it can even be reduced if operated under the best conditions (i.e., engine speed, relative air-fuel ratio, etc.).

In conclusion, this research showed that wet ethanol is a very interesting alternative fuel for DISI engines if their characteristics as a fuel are respected and put into consideration on the engine concept design. This type of engine can be adopted either to operate alone as a steady-state engine in industries or especially in hybrid vehicles under configurations where the

ICE operates at an optimal engine speed while the electric engine usage is adjusted depending on the vehicle necessity.

8.1 Suggestions for future work

Future works related to this topic may cover the construction of a spray evaporation efficiency or an engine exergetic efficiency map for different engine speeds. Also, the expansion of the optimization analysis seeking for the compression rate limit value for DISI engines based on the evaporative cooling effect and the spray efficiencies presented here would be interesting. The application of such an engine integrated with a hybrid system would highlight its potential towards a sustainable engine operation especially for vehicles in countries where the electric ones are not currently feasible throughout all their regions (e.g., Brazil).

In terms of modeling, turbulence and droplet break-up models can be coupled with the engine simulator in order to approximate further the developed code from an actual engine. Adjustments on the chemical kinetic/combustion model are also interesting, in order to better predict some pollutants formation and the temperature/pressure profiles. In addition, an improvement in the knock index number correlation for wet ethanol would greatly benefit the simulator on discovering the threshold knock condition and thus optimizing the engine operation. Finally, internal and external EGR technology implementations, optimal valve control through Miller cycle, and turbocompounding enable the engine concept to go towards a state-of-the-art sustainable engine.

Novel results can be obtained if a real-gas equation of state would be used to represent the gas model, instead of the adopted ideal gas model. Finally, other ideas would possibly involve multi-injection strategies, proper downsizing and downspeeding, wet ethanol effects on engine corrosion/wear, and an exergoenvironmental analysis of the vehicle transport process (engine component and wet ethanol production, emissions, etc.), which can also evolve even further the developed work by providing more information with quality to comprehend the impact and importance of ICEs from 2022 ahead in this century.

BIBLIOGRAPHY

Abianeh, O. S.; Chen, C. P. A discrete multicomponent fuel evaporation model with liquid turbulence effects. **International Journal of Heat and Mass Transfer**, 2012.

Abramzon, B.; Sirignano, W. A. Droplet vaporization model for spray combustion calculations. **International Journal of Heat and Mass Transfer**, v. 32, n. 9, p. 1605–1618, sep 1989.

Abudour, A. M.; Mohammad, S. A.; Robinson, R. L.; Gasem, K. A. Generalized binary interaction parameters for the Peng-Robinson equation of state. **Fluid Phase Equilibria**, 2014.

Agarwal, A. K. Biofuels (alcohols and biodiesel) applications as fuels for internal combustion engines. **Progress in Energy and Combustion Science**, v. 33, n. 3, p. 233–271, jun 2007.

Agarwal, A. K.; Singh, A. P.; Maurya, R. K. Evolution, challenges and path forward for low temperature combustion engines. **Progress in Energy and Combustion Science**, v. 61, p. 1–56, jul 2017.

Aggarwal, S. A review of spray ignition phenomena: Present status and future research. **Progress in Energy and Combustion Science**, v. 24, n. 6, p. 565–600, jan 1998.

Aggarwal, S. K. Single droplet ignition: Theoretical analyses and experimental findings. **Progress in Energy and Combustion Science**, v. 45, p. 79–107, dec 2014.

Aggarwal, S. K.; Sirignano, W. A.; Tong, A. Y. A comparison of vaporization models in spray calculations. **AIAA Journal**, v. 22, n. 10, p. 1448–1457, oct 1984.

Ahmadi, L.; Yip, A.; Fowler, M.; Young, S. B.; Fraser, R. A. Environmental feasibility of re-use of electric vehicle batteries. **Sustainable Energy Technologies and Assessments**, v. 6, p. 64–74, 2014.

Al Qubeissi, M.; Al-Esawi, N.; Sazhin, S. S.; Ghaleeh, M. Ethanol/Gasoline Droplet Heating and Evaporation: Effects of Fuel Blends and Ambient Conditions. **Energy and Fuels**, v. 32, n. 6, p. 6498–6506, jun 2018.

Alderliesten, M. Mean Particle Diameters. Part I: Evaluation of Definition Systems. **Part. Part. Syst. Charact**, v. 7, p. 233–241, 1990.

Alderliesten, M. Mean Particle Diameters Part II: Standardization of Nomenclature. **Part. Part. Syst. Charact**, v. 8, p. 237–241, 1991.

Alderliesten, M. Mean Particle Diameters. Part III: An Empirical Evaluation of Integration and Summation Methods for Estimating Mean Particle Diameters from Histogram Data. **Part. Part. Syst. Charact.**, v. 19, p. 373–386, 2002.

Alderliesten, M. Mean particle diameters. Part IV: Empirical selection of the proper type of mean particle diameter describing a product or material property. **Particle & Particle Systems Characterization**, v. 21, n. 3, p. 179–196, oct 2004.

Alderliesten, M. Mean particle diameters. Part V: Theoretical derivation of the proper type of mean particle diameter describing a product or process property. **Particle & Particle Systems Characterization**, v. 22, n. 4, p. 233–245, jan 2006.

Alderliesten, M. Mean particle diameters. Part VI: Fundamental distinction between statistics based (ISO/DIN) and physics based (Moment-Ratio)definition systems. **Particle & Particle Systems Characterization**, v. 27, n. 1-2, p. 7–20, dec 2010.

Alderliesten, M. Mean Particle Diameters. Part VII. The Rosin-Rammler Size Distribution: Physical and Mathematical Properties and Relationships to Moment-Ratio Defined Mean Particle Diameters. **Particle & Particle Systems Characterization**, v. 30, n. 3, p. 244–257, mar 2013.

Arpaci, V. S.; Selamet, A. Entropic efficiency of energy systems. **Progress in Energy and Combustion Science**, v. 18, n. 5, p. 429–445, jan 1992.

Augoye, A.; Aleiferis, P. Characterization of Flame Development with Hydrous and Anhydrous Ethanol Fuels in a Spark-Ignition Engine with Direct Injection and Port Injection Systems. In: **SAE paper**. [s.n.], 2014. Disponível em: <https://www.sae.org/content/2014-01-2623/>.

Bae, C.; Kim, J. Alternative fuels for internal combustion engines. **Proceedings of the Combustion Institute**, v. 36, n. 3, p. 3389–3413, 2017.

Baêta, J. G. C.; Pontoppidan, M.; Silva, T. R. Exploring the limits of a down-sized ethanol direct injection spark ignited engine in different configurations in order to replace high-displacement gasoline engines. **Energy Conversion and Management**, v. 105, p. 858–871, nov 2015.

Baeyens, J.; Kang, Q.; Appels, L.; Dewil, R.; Lv, Y.; Tan, T. Challenges and opportunities in improving the production of bio-ethanol. **Progress in Energy and Combustion Science**, v. 47, p. 60–88, apr 2015.

Bank, D. D. **Heat of Vaporization of Ethanol**. 2022. 1 p. Disponível em: <http://www.ddbst.com/en/EED/PCP/HVP_C11.php>.

Baumgarten, C. **Mixture Formation in Internal Combustion Engines**. 1st. ed. [S.l.]: Springer Berlin Heidelberg, 2006. (Heat, Mass Transfer). ISBN 978-3-540-30835-5.

Bejan, A. A Study of Entropy Generation in Fundamental Convective Heat Transfer. **Journal of Heat Transfer**, v. 101, n. 4, p. 718–725, nov 1979.

Bejan, A. **Advanced Engineering Thermodynamics**. 3rd. ed. [S.l.]: John Wiley and Sons, 2006. ISBN 9780471677635.

Bejan, A. **Advanced engineering thermodynamics**. [S.l.]: Wiley, 2016. 789 p. ISBN 9781119052098.

Bernal, J. L. L. **Study of the operation of an internal combustion engine, fueled by indirect injection of ethanol and direct injection of water into the combustion chamber**. 233 p. Tese (Doutorado) — UNICAMP, 2019.

Boretti, A. Analysis of Design of Pure Ethanol Engines. In: **SAE Technical Paper**. [s.n.], 2010. p. 2010–01–1453. Disponível em: <http://papers.sae.org/2010-01-1453/>.

Borisov, A. A.; Gel'fand, B. E.; Natanzon, M. S.; Kossov, O. M. Droplet Breakup Regimes and Criteria for Their Existence. **Journal of Engineering Physics**, v. 40, n. 1, p. 44–49, 1981.

Borman, G. L.; Johnson, J. H. Unsteady Vaporization Histories and Trajectories of Fuel Drops Injected into Swirling Air. In: **SAE paper**. [s.n.], 1962. Disponível em: <https://www.sae.org/content/620271/>.

Brasil, E. d. P. E. **Balanço Energético Nacional**. Rio de Janeiro, 2020. 264 p. Disponível em: <https://www.epe.gov.br/pt/publicacoes-dados-abertos/publicacoes/balanco-energetico-nacional-2020>.

Brazil. **Resolução Nº 492**. Diário Oficial da União, 2018. 12 p. Disponível em: <https://www.in.gov.br/materia/-/asset_publisher/Kujrw0TZC2Mb/content/id/56643907>.

Breaux, B. **The Effect of Elevated Water Content on Ethanol Combustion**. Tese (Doutorado) — Louisiana State University, 2012.

Brenn, G.; Deviprasath, L. J.; Durst, F. Computations and Experiments on the Evaporation of Multi-Component Droplets. In: **Proc. 9th Int. Conf. Liquid Atomiz. Spray Syst.(ICLASS)**. Sorrento, Italy: ., 2003. p. 1–16.

Brenn, G.; Wiedemann, T.; Rensink, D.; Kastner, O.; Yarin, A. L. Modeling and Experimental Investigation of the Morphology of Spray Dryed Particles. **Chemical Engineering and Technology**, v. 24, n. 11, p. 1113–1116, nov 2001.

Brewster, S. Initial Development of a Turbo-charged Direct Injection E100 Combustion System. In: **SAE Paper**. [s.n.], 2007. Disponível em: <https://www.sae.org/content/2007-01-3625/>.

Brewster, S.; Railton, D.; Maisey, M.; Frew, R. The Effect of E100 Water Content on High Load Performance of a Spray Guide Direct Injection Boosted Engine. In: **SAE Paper**. [s.n.], 2007. Disponível em: <https://www.sae.org/content/2007-01-2648/>.

Brinkman, N. D. Ethanol Fuel-A Single-Cylinder Engine Study of Efficiency and Exhaust Emissions. In: **SAE Transactions**. [S.l.: s.n.], 1981. v. 90, n. 9, p. 1410–1424. ISSN 0148-7191.

Bromberg, L.; Cohn, D. R. Effective octane and efficiency advantages of direct injection alcohol engines. **MIT Plasma Science & Fusion Center**, p. 1–21, 2008.

Bromberg, L.; Cohn, D. R.; Heywood, J. B. Calculations of knock suppression in highly turbocharged gasoline/ethanol engines using direct ethanol injection. **MIT Plasma Science and Fusion Center**, p. 1–17, 2006.

Brusstar, M.; Bakenhus, M. **Economical, High-efficiency Engine Technologies for Alcohol fuels**. [S.l.], 2008. 10 p. Disponível em: <https://archive.epa.gov/otaq/technology/web/pdf/epa-fev-isaf-no55.pdf>.

Bureshaid, K.; Feng, D.; Zhao, H.; Bunce, M. Combustion and emissions of gasoline, anhydrous ethanol, and wet ethanol in an optical engine with a turbulent jet ignition system. **Proceedings of the Institution of Mechanical Engineers, Part D: Journal of Automobile Engineering**, v. 233, n. 13, p. 3528–3537, nov 2019.

Burger, M.; Schmehl, R.; Prommersberger, K.; Schäfer, O.; Koch, R.; Wittig, S. Droplet evaporation modeling by the distillation curve model: Accounting for kerosene fuel and elevated pressures. **International Journal of Heat and Mass Transfer**, 2003.

Calvo, G.; Mudd, G.; Valero, A.; Valero, A. Decreasing ore grades in global metallic mining: A theoretical issue or a global reality? **Resources**, v. 5, n. 4, dec 2016.

Capilla, A. V.; Delgado, A. V. **Thanatia: The Destiny of the Earth's Mineral Resources**. WORLD SCIENTIFIC, 2014. ISBN 978-981-4273-93-0.

Caspeta, L.; Buijs, N. A. A.; Nielsen, J. The role of biofuels in the future energy supply. **Energy and Environmental Science**, v. 6, n. 4, p. 1077, 2013.

Caton, J. A. On the importance of specific heats as regards efficiency increases for highly dilute IC engines. **Energy Conversion and Management**, v. 79, p. 146–160, mar 2014.

Chase Jr., M. W. NIST-JANAF Thermochemical Tables. **American Chemical Society; American Institute of Physics for the National Institute of Standards and Technology**, Washington, DC, 1998.

Chiang, C. H.; Raju, M. S.; Sirignano, W. A. Numerical analysis of convecting, vaporizing fuel droplet with variable properties. **International Journal of Heat and Mass Transfer**, Reston, Virigina, v. 35, n. 5, p. 1307–1324, may 1992.

CONAB. **Acompanhamento da safra brasileira de cana-de-açúcar**. [S.l.], 2021. Disponível em: <https://www.conab.gov.br/info-agro/safras/cana>.

Continillo, G.; Sirignano, W. A. Unsteady, Spherically-Symmetric Flame Propagation Through Multicomponent Fuel Spray Clouds. In: **Modern Research Topics in Aerospace Propulsion**. New York, NY: Springer New York, 1991. p. 173–198. Disponível em: <http://link.springer.com/10.1007/978-1-4612-0945-4_10>.

Corsetti, S.; Miles, R. E. H.; McDonald, C.; Belotti, Y.; Reid, J. P.; Kiefer, J.; McGloin, D. Probing the Evaporation Dynamics of Ethanol/Gasoline Biofuel Blends Using Single Droplet Manipulation Techniques. **The Journal of Physical Chemistry A**, v. 119, n. 51, p. 12797–12804, dec 2015.

Costa, C.; Barbosa, J.; Castro, H.; Gonçalves, R.; Lanceros-Méndez, S. Electric vehicles: To what extent are environmentally friendly and cost effective? – Comparative study by european countries. **Renewable and Sustainable Energy Reviews**, v. 151, p. 111548, nov 2021.

Costa, R. B. R. da; Rodrigues Filho, F. A.; Coronado, C. J.; Teixeira, A. F.; Netto, N. A. D. Research on hydrous ethanol stratified lean burn combustion in a DI spark-ignition engine. **Applied Thermal Engineering**, v. 139, p. 317–324, jul 2018.

Crowe, C. T. **Vapor-Droplet Flow Equations**. Livermore, 1975. 35 p.

Crowe, C. T. **Conservation Equations for Vapor-droplet Flows Including Boundary-Droplet Effects**. [S.l.], 1976. 40 p.

Crowe, C. T.; Schwarzkopf, J. D.; Sommerfeld, M.; Tsuji, Y. **Multiphase Flows with Droplets and Particles**. 2nd. ed. Boca Raton: CRC Press, 2012. 505 p. ISBN 978-1-4398-4051-1.

Curtis, E. W.; Uludogan, A.; Reitz, R. D. A New High Pressure Droplet Vaporization Model for Diesel Engine Modeling. In: **SAE paper**. [s.n.], 1995. Disponível em: <https://www.sae.org/content/952431/>.

Daif, A.; Bouaziz, M.; Chesneau, X.; Ali Chérif, A. Comparison of multicomponent fuel droplet vaporization experiments in forced convection with the Sirignano model. **Experimental Thermal and Fluid Science**, v. 18, n. 4, p. 282–290, dec 1998.

Dane, A.; Wright, D.; Montmasson-Clair, G. **Exploring the Policy Impacts of a Transition to Electric Vehicles in South Africa**. [S.l.], 2019. Disponível em: <www.tips.org.za>.

Daniel, R.; Wang, C.; Xu, H.; Tian, G. Split-injection strategies under full-load using DMF, a new biofuel candidate, compared to ethanol in a GDI engine. In: **SAE Technical Papers**. [S.l.]: SAE International, 2012. ISSN 26883627.

Dash, S. K.; Sengupta, S. P.; Som, S. K. Transport processes and associated irreversibilities in droplet evaporation. **Journal of Thermophysics and Heat Transfer**, v. 5, n. 3, p. 366–373, jul 1991.

Dash, S. K.; Som, S. K. Transport processes and associated irreversibilities in droplet combustion in a convective medium. **International Journal of Energy Research**, v. 15, n. 7, p. 603–619, sep 1991.

Datta, A.; Som, S. K. Thermodynamic irreversibilities and second law analysis in a spray combustion process. **Combustion science and technology**, v. 142, n. 1, p. 29–54, 1999.

Davidsson, S.; Höök, M. Material requirements and availability for multi-terawatt deployment of photovoltaics. **Energy Policy**, v. 108, p. 574–582, sep 2017.

de Lima, A. J. T. B.; Rufino, C. H.; Gomes, F. A. F.; Gallo, W. L. R. Parametric Analysis Through the Second Law of Thermodynamics of Ethanol Droplet Injection and Evaporation in a Variable Temperature Environment. In: **CERES 2020**. [S.l.: s.n.], 2020. p. 10.

Depredurand, V. **Approche Experimentale de L'evaporation de Sprays de Combustibles Multicomposant**. 226 p. Tese (Doutorado) — Nancy-Université, 2009.

Dombrovsky, L.; Sazhin, S. A simplified non-isothermal model for droplet heating and evaporation. **International Communications in Heat and Mass Transfer**, v. 30, n. 6, p. 787–796, aug 2003.

Dombrovsky, L. A.; Sazhin, S. S. A Parabolic Temperature Profile Model for Heating of Droplets. **Journal of Heat Transfer**, v. 125, n. 3, p. 535–537, jun 2003.

Drake, M. C.; Haworth, D. C. Advanced gasoline engine development using optical diagnostics and numerical modeling. **Proceedings of the Combustion Institute**, v. 31 I, n. 1, p. 99–124, 2007.

Duan, X.; Li, Y.; Liu, Y.; Liu, J.; Wang, S.; Guo, G. Quantitative investigation the influences of the injection timing under single and double injection strategies on performance, combustion and emissions characteristics of a GDI SI engine fueled with gasoline/ethanol blend. **Fuel**, v. 260, jan 2020.

Duke, D. J.; Kastengren, A. L.; Matusik, K. E.; Swantek, A. B.; Powell, C. F.; Payri, R.; Vaquerizo, D.; Itani, L.; Bruneaux, G.; Grover, R. O.; Parrish, S.; Markle, L.; Schmidt, D.; Manin, J.; Skeen, S. A.; Pickett, L. M. Internal and near nozzle measurements of Engine Combustion Network "Spray G" gasoline direct injectors. **Experimental Thermal and Fluid Science**, v. 88, p. 608–621, nov 2017.

Dukowicz, J. K. A particle-fluid numerical model for liquid sprays. **Journal of Computational Physics**, v. 35, n. 2, p. 229–253, apr 1980.

Egbue, O.; Long, S. Barriers to widespread adoption of electric vehicles: An analysis of consumer attitudes and perceptions. **Energy Policy**, v. 48, p. 717–729, sep 2012.

El-Faroug, M. O.; Yan, F.; Luo, M.; Turkson, R. F. Spark ignition engine combustion, performance and emission products from hydrous ethanol and its blends with gasoline. **Energies**, v. 9, n. 12, 2016.

Elkotb, M. Fuel atomization for spray modelling. **Progress in Energy and Combustion Science**, v. 8, n. 1, p. 61–91, jan 1982.

Eltoumi, F. M.; Becherif, M.; Djerdir, A.; Ramadan, H. S. The key issues of electric vehicle charging via hybrid power sources: Techno-economic viability, analysis, and recommendations. **Renewable and Sustainable Energy Reviews**, v. 138, mar 2021.

Elwardany, A. E.; Gusev, I. G.; Castanet, G.; Lemoine, F.; Sazhin, S. S. Mono-and Multi-component Droplet Cooling/Heating and Evaporation: Comparative Analysis of Numerical Models. **Atomization and Sprays**, v. 21, n. 11, p. 907–931, 2011.

Faeth, G. Current status of droplet and liquid combustion. **Progress in Energy and Combustion Science**, v. 3, n. 4, p. 191–224, jan 1977.

Faeth, G. Evaporation and combustion of sprays. **Progress in Energy and Combustion Science**, v. 9, n. 1-2, p. 1–76, jan 1983.

Faeth, G.; Lazar, R. S. Fuel droplet burning rates in a combustion gas environment. **AIAA Journal**, v. 9, n. 11, p. 2165–2171, nov 1971.

Fagundez, J. L.; Sari, R. L.; Mayer, F. D.; Martins, M. E.; Salau, N. P. Determination of optimal wet ethanol composition as a fuel in spark ignition engine. **Applied Thermal Engineering**, v. 112, p. 317–325, 2017.

Fajgenbaum, R.; Santos, R. G. Influence of fuel temperature on atomization parameters in a pressure-swirl atomizer from a port fuel injector by Shadowgraphy technique. **Journal of the Brazilian Society of Mechanical Sciences and Engineering**, v. 38, n. 7, p. 1877–1892, oct 2016.

Ford. **Ford Ecoboost Engine**. 2009. [online] p. Disponível em: <https://assets.pinterest.com/ext/embed.html?id=384143043223565964>.

Fournier, S.; Simon, G.; Seers, P. Evaluation of low concentrations of ethanol, butanol, BE, and ABE blended with gasoline in a direct-injection, spark-ignition engine. **Fuel**, v. 181, n. May, p. 396–407, 2016.

Gainey, B.; Gohn, J.; Hariharan, D.; Rahimi-Boldaji, M.; Lawler, B. Assessing the impact of injector included angle and piston geometry on thermally stratified compression ignition with wet ethanol. **Applied Energy**, v. 262, p. 114528, mar 2020.

Gainey, B.; Gohn, J.; Yan, Z.; Malik, K.; Rahimi Boldaji, M.; Lawler, B. HCCI with Wet Ethanol: Investigating the Charge Cooling Effect of a High Latent Heat of Vaporization Fuel in LTC. In: **SAE Technical Papers**. [S.l.]: SAE International, 2019. v. 2019-Septe, n. September. ISSN 01487191.

Gainey, B.; Hariharan, D.; Yan, Z.; Zilg, S.; Rahimi Boldaji, M.; Lawler, B. A split injection of wet ethanol to enable thermally stratified compression ignition. **International Journal of Engine Research**, v. 21, n. 8, p. 1441–1453, oct 2020.

Gainey, B.; Yan, Z.; Gohn, J.; Rahimi Boldaji, M.; Lawler, B. TSCI with Wet Ethanol: An investigation of the effects of injection strategy on a diesel engine architecture. In: **SAE Technical Papers**. [S.l.]: SAE International, 2019. v. 2019-April, n. April. ISSN 01487191.

Gainey, B.; Yan, Z.; Rahimi-Boldaji, M.; Lawler, B. On the Effects of Injection Strategy, Exhaust Gas Recirculation, and Intake Boost on TSCI With Wet Ethanol. **Journal of Engineering for Gas Turbines and Power**, v. 142, n. 9, sep 2020.

Gallo, W. L. R. **Análise Exergética de Motores a Gasolina e A Alcool**. 280 p. Tese (Doutorado) — UNICAMP, 1990.

Gavhane, S.; Pati, S.; Som, S. Evaporation of multicomponent liquid fuel droplets: Influences of component composition in droplet and vapor concentration in free stream ambience. **International Journal of Thermal Sciences**, v. 105, p. 83–95, jul 2016.

Ghoniem, A. F. Needs, resources and climate change: Clean and efficient conversion technologies. **Progress in Energy and Combustion Science**, v. 37, n. 1, p. 15–51, feb 2011.

Glassman, I. **Combustion**. 4th. ed. [S.l.]: Academic Press, 2008. v. 1. 770 p. ISBN 978-0-12-088573-2.

Godsave, G. Studies of the combustion of drops in a fuel spray—the burning of single drops of fuel. **Symposium (International) on Combustion**, v. 4, n. 1, p. 818–830, jan 1953.

Gohn, J.; Gainey, B.; Zainul, S.; Lawler, B. Wet ethanol in LTC: How water fraction and DTBP affect combustion and intake temperature at naturally aspirated and boosted conditions. **Fuel**, v. 267, p. 117094, may 2020.

Gonçalves, G. G. **Simulação Numérica de Injeção em Sistema Diesel**. Tese (Doutorado) — Universidade Federal de Santa Catarina, 2016.

Green, D. W.; Perry, R. H. **Perry's Chemical Engineers Handbook**. 8th. ed. [S.l.]: Mc-Graw Hill, 2008. 2728 p. ISBN 0-07-151124-5.

Group, S. . I. **Spray description**. 2022. 1 p. Disponível em: <https://spray-imaging.com/spray-description.html>.

Gu, X.; Basu, S.; Kumar, R. Dispersion and vaporization of biofuels and conventional fuels in a crossflow pre-mixer. **International Journal of Heat and Mass Transfer**, v. 55, n. 1-3, p. 336–346, jan 2012.

Hall, L. **Throwback Thursday: Henry Ford, alcohol-fuel visionary**. 2015. 1 p. Disponível em: <https://www.fuelfreedom.org/throwback-thursday-henry-ford-alcohol-fuel-visionary/>.

Heywood, J. B. **Internal Combustion Engine Fundamentals**. 2nd. ed. [S.l.]: McGraw-Hill, 2018. 1702 p.

Hiroyasu, H.; Kadota, T. Models for Combustion and Formation of Nitric Oxide and Soot in Direct Injection Diesel Engines. In: **SAE Transactions**. [s.n.], 1976. v. 85, p. 513–526. Disponível em: <https://www.sae.org/content/760129/>.

Hiroyasu, H.; Kadota, T.; Arai, M. Development and Use of a Spray Combustion Modeling to Predict Diesel Engine Efficiency and Pollutant Emissions : Part 1 Combustion Modeling. **Bulletin of JSME**, v. 26, n. 214, p. 569–575, 1983.

Hiwase, S. D.; Datta, A.; Som, S. K. Entropy balance and exergy analysis of the process of droplet combustion. **J. Phys. D: Appl. Phys**, v. 31, p. 1601–1610, 1998.

Hountalas, D. T.; Papagiannakis, R. G. Development of a Simulation Model for Direct Injection Dual Fuel Diesel-Natural Gas Engines. In: **SAE Transactions 2000-01-0286**. [S.l.: s.n.], 2000. v. 109, p. 373–383. ISBN 143.106.93.10.

Hsieh, K. C.; Shuen, J. S.; Yang, V. Droplet Vaporization In High-Pressure Environments I: Near Critical Conditions. **Combustion Science and Technology**, v. 76, n. 1-3, p. 111–132, mar 1991.

Hubbard, G.; Denny, V.; Mills, A. Droplet evaporation: Effects of transients and variable properties. **International Journal of Heat and Mass Transfer**, v. 18, n. 9, p. 1003–1008, sep 1975.

Imaoka, Y.; Shouji, K.; Inoue, T.; Noda, T. A Study of a Multistage Injection Mechanism for Improving the Combustion of Direct-Injection Gasoline Engines. **SAE International Journal of Engines**, v. 8, n. 3, p. 2015–01–0883, apr 2015.

Ismail, S.; Mehta, P. S. Second-law analysis of fuel-air mixing and combustion subprocesses in a heterogeneous charge engine. **Proceedings of the Institution of Mechanical Engineers, Part D: Journal of Automobile Engineering**, v. 226, n. 6, p. 815–827, jun 2012.

Ismail, S.; Mehta, P. S. A phenomenological model for predicting entropy generation during vaporization of droplets in engine fuel sprays. In: **Applied Mechanics and Materials**. [S.l.]: Trans Tech Publications Ltd, 2014. v. 592-594, p. 1403–1407. ISBN 9783038351634. ISSN 16627482.

Jadhav, P. D.; Mallikarjuna, J. M. Effect of fuel injector hole diameter and injection timing on the mixture formation in a GDI engine - A CFD study. **International Journal of Computational Methods and Experimental Measurements**, v. 6, n. 4, p. 737–748, 2018.

Jha, M. K.; Choubey, P. K.; Dinkar, O. S.; Panda, R.; Jyothi, R. K.; Yoo, K.; Park, I. Recovery of rare earth metals (Rems) from nickel metal hydride batteries of electric vehicles. **Minerals**, v. 12, n. 1, jan 2022.

Jin, D.; Choi, K.; Myung, C. L.; Lim, Y.; Lee, J.; Park, S. The impact of various ethanol-gasoline blends on particulates and unregulated gaseous emissions characteristics from a spark ignition direct injection (SIDI) passenger vehicle. **Fuel**, v. 209, n. January, p. 702–712, 2017.

Jin, J. D.; Borman, G. L. A Model for Multicomponent Droplet Vaporization at High Ambient Pressures. In: **SAE Technical Paper**. SAE International, 1985. p. 1–16. Disponível em: <https://www.sae.org/content/850264/>.

Johnson, T.; Joshi, A. Review of Vehicle Engine Efficiency and Emissions. In: **SAE Technical Paper**. [s.n.], 2017. ISSN 01487191. Disponível em: <http://papers.sae.org/2017-01-0907/>.

Kalghatgi, G. Is it really the end of internal combustion engines and petroleum in transport? **Applied Energy**, v. 225, p. 965–974, sep 2018.

Kalghatgi, G.; Levinsky, H.; Colket, M. Future transportation fuels. **Progress in Energy and Combustion Science**, v. 69, p. 103–105, nov 2018.

Kapus, P. E.; Fuerhapter, A.; Fuchs, H.; Fraidl, G. K. Ethanol Direct Injection on Turbocharged SI Engines - Potential and Challenges. In: **SAE Paper**. [s.n.], 2007. Disponível em: <https://www.sae.org/content/2007-01-1408/>.

Kazakov, A.; Conley, J.; Dryer, F. L. Detailed modeling of an isolated, ethanol droplet combustion under microgravity conditions. **Combustion and Flame**, v. 134, n. 4, p. 301–314, sep 2003.

Kent, J. C. Quasi-steady diffusion-controlled droplet evaporation and condensation. **Applied Scientific Research**, v. 28, n. 1, p. 315–360, jan 1973.

Khaliq, A.; Trivedi, S. K.; Dincer, I. Investigation of a wet ethanol operated HCCI engine based on first and second law analyses. **Applied Thermal Engineering**, v. 31, n. 10, p. 1621–1629, 2011.

Kim, H.; Sung, N. The effect of ambient pressure on the evaporation of a single droplet and a spray. **Combustion and Flame**, v. 135, n. 3, p. 261–270, 2003.

Koupaie, M. M.; Cairns, A.; Vafamehr, H.; Lanzanova, T. D. M. A study of hydrous ethanol combustion in an optical central direct injection spark ignition engine. **Applied Energy**, v. 237, p. 258–269, mar 2019.

Krisman, A.; Hawkes, E. R.; Kook, S.; Sjöberg, M.; Dec, J. E. On the potential of ethanol fuel stratification to extend the high load limit in stratified-charge compression-ignition engines. **Fuel**, v. 99, n. September, p. 45–54, sep 2012.

Kumagai, S.; Isoda, H. Combustion of fuel droplets in a falling chamber. **Symposium (International) on Combustion**, v. 6, n. 1, p. 726–731, jan 1957.

Kuo, K. K. **Recent Advances in Spray Combustion: Spray Combustion Measurements and Model Simulation**. Washington DC: American Institute of Aeronautics and Astronautics, 1996. v. 171. 468 p. ISBN 978-1-56347-181-0.

Kuo, K. K. **Principles of Combustion**. 2nd. ed. [S.l.]: John Wiley and Sons, 2005. 760 p.

Landis, R. B.; Mills, A. F. Effect of Internal Diffusional Resistance on Binary Products. In: **Proceeding of International Heat Transfer Conference 5**. Connecticut: Begellhouse, 1974. p. 345–349. Disponível em: <http://ihtcdigitallibrary.com/conferences/3ea7b3cd5b654406,56c7c9ac3f5a5a22,38d5cd5905e200c5.html>.

Lanzanova, T. D. M. **Experimental Investigations of Anhydrous and Wet Ethanol Combustion in a Spark Ignition Engine**. Tese (Doutorado), 2017.

Lanzanova, T. D. M.; Dalla Nora, M.; Zhao, H. Performance and economic analysis of a direct injection spark ignition engine fueled with wet ethanol. **Applied Energy**, v. 169, p. 230–239, may 2016.

Lanzanova, T. D. M.; Vielmo, H. A.; Sari, R. L.; Dornelles, H. M.; Tatsch, G. A.; Martins, M. E. S.; Michels, L. Performance Analysis of a Spark Ignited Engine Running on Different Water-in-Ethanol Mixtures. In: **SAE paper**. SAE, 2013. Disponível em: <https://www.sae.org/content/2013-36-0202/>.

Lapple, C.; Henry, J.; Blake, D. **Atomization - A survey and Critique of the Literature**. [S.l.], 1967. 267 p.

Law, C. K. Multicomponent droplet combustion with rapid internal mixing. **Combustion and Flame**, v. 26, n. C, p. 219–233, 1976.

Law, C. K. Recent advances in droplet vaporization and combustion. **Progress in Energy and Combustion Science**, v. 8, n. 3, p. 171–201, jan 1982.

Law, C. K. **Combustion Physics**. 1st. ed. Cambridge: Cambridge University Press, 2006. v. 9780521870. 1–722 p. ISSN 00319120. ISBN 9780511754517.

Law, C. K.; Law, H. K. Quasi-Steady Diffusion Flame Theory with Variable Specific Heats and Transport Coefficients. **Combustion Science and Technology**, v. 12, n. 4-6, p. 207–216, apr 1976.

Law, C. K.; Law, H. K. Theory of quasi-steady one-dimensional diffusional combustion with variable properties including distinct binary diffusion coefficients. **Combustion and Flame**, v. 29, n. C, p. 269–275, 1977.

Law, C. K.; Sirignano, W. A. Unsteady droplet combustion with droplet heating—II: Conduction limit. **Combustion and Flame**, v. 28, p. 175–186, jan 1977.

Law, C. K.; Williams, F. A. Kinetics and convection in the combustion of alkane droplets. **Combustion and Flame**, v. 19, n. 3, p. 393–405, dec 1972.

Lawler, B.; Splitter, D.; Szybist, J.; Kaul, B. Thermally Stratified Compression Ignition: A new advanced low temperature combustion mode with load flexibility. **Applied Energy**, v. 189, p. 122–132, 2017.

Lefebvre, A. H. **Atomization and Sprays**. 2nd. ed. CRC Press, 2017. 301 p. ISBN 9781498736268.

Li, X.; Li, M.; Fu, H. Modeling the Initial Droplet Size Distribution in Sprays Based on the Maximization of Entropy Generation. **Atomization and Sprays**, v. 15, n. 3, p. 295–322, 2005.

Lima, A. J. T. B. de; Gallo, W. L. R. Thermodynamic analysis of the fuel spray evaporation process for wet ethanol during the compression stroke of a direct-injection spark-ignition engine. In: **ECOS 2021**. Taormina, Italy: [s.n.], 2021. p. 12.

Lima, A. J. T. B. de; Rufino, C. H.; Gomes, F. A. F.; Gallo, W. L. R. A Second Law Approach for a Pure Ethanol Droplet Injection and Evaporation in a Variable Temperature Environment - Effects of Different Evaporation Models. In: **ENCIT 2020**. [S.l.: s.n.], 2020. p. 9.

Lior, N.; Sarmiento-Darkin, W.; Al-Sharqawi, H. S. The exergy fields in transport processes: Their calculation and use. **Energy**, v. 31, n. 5, p. 553–578, apr 2006.

Looney, B. **BP Statistical Review of World Energy 2020**. [S.l.], 2020. 68 p. Disponível em: <www.bp.com/statisticalreview.>

Lopes, M. L.; Paulillo, S. C. d. L.; Godoy, A.; Cherubin, R. A.; Lorenzi, M. S.; Giometti, F. H. C.; Bernardino, C. D.; Amorim Neto, H. B. de; Amorim, H. V. de. Ethanol production in Brazil: a bridge between science and industry. **Brazilian Journal of Microbiology**, v. 47, p. 64–76, dec 2016.

López-Plaza, E. L.; Hernández, S.; Barroso-Muñoz, F. O.; Segovia-Hernández, J. G.; Aceves, S. M.; Martínez-Frías, J.; Saxena, S.; Dibble, R. Experimental and Theoretical Study of the Energy Savings from Wet Ethanol Production and Utilization. **Energy Technology**, v. 2, n. 5, p. 440–445, may 2014.

M., D. A.; P., E. Four-octane-number method for predicting the anti-knock behavior of fuels and engines. **SAE Transactions**, p. 294–308, 1978.

Macedo, I.; Verde Leal, M.; Silva, J. da. **Assessment of greenhouse gas emissions in the production and use of fuel ethanol in Brazil Government of the State of São Paulo Secretariat of the Environment**. São Paulo, 2004. 32 p.

Macedo, I. C.; Seabra, J. E.; Silva, J. E. Green house gases emissions in the production and use of ethanol from sugarcane in Brazil: The 2005/2006 averages and a prediction for 2020. **Biomass and Bioenergy**, v. 32, n. 7, p. 582–595, jul 2008.

Mack, J. H.; Aceves, S. M.; Dibble, R. W. Demonstrating direct use of wet ethanol in a homogeneous charge compression ignition (HCCI) engine. **Energy**, v. 34, n. 6, p. 782–787, jun 2009.

Madson, P. W.; Monceaux, D. A. **Fuel ethanol production**. Cincinnati, 1995. 1–12 p. Disponível em: <https://www.researchgate.net/profile/Dale-Monceaux/publication/268441349_Fuel_ethanol_production_1_Fuel_ethanol_production/links/560957b508ae4d86bb11cca2/Fuel-ethanol-production-1-Fuel-ethanol-production.pdf>.

Malaquias, A. C. T.; Netto, N. A. D.; Filho, F. A. R.; Costa, R. B. R. da; Langeani, M.; Baêta, J. G. C. The misleading total replacement of internal combustion engines by electric motors and a study of the Brazilian ethanol importance for the sustainable future of mobility: a review. **Journal of the Brazilian Society of Mechanical Sciences and Engineering**, v. 41, n. 12, p. 567, dec 2019.

Marinov, N. M. A detailed chemical kinetic model for high temperature ethanol oxidation. **International Journal of Chemical Kinetics**, v. 31, n. 3, p. 183–220, 1999.

Martinez-Frias, J.; Aceves, S. M.; Flowers, D. L. Improving Ethanol Life Cycle Energy Efficiency by Direct Utilization of Wet Ethanol in HCCI Engines. **Journal of Energy Resources Technology**, v. 129, n. 4, p. 332–337, dec 2007.

Martins, M.; Lanzanova, T.; Sari, R. Low Cost Wet Ethanol for Spark-Ignited Engines: Further Investigations. **SAE International Journal of Fuels and Lubricants**, v. 8, n. 2, p. 367–373, apr 2015.

Martins, M. E.; Lanzanova, T. D. Full-load Miller cycle with ethanol and EGR: Potential benefits and challenges. **Applied Thermal Engineering**, v. 90, p. 274–285, nov 2015.

Matlab. Optimization Toolbox™ User's Guide R2018a. **Matlab**, p. 1172, 2018.

Megaridis, C. M.; Sirignano, W. A. Numerical modeling of a vaporizing multicomponent droplet. **Symposium (International) on Combustion**, v. 23, n. 1, p. 1413–1421, jan 1991.

Melo, T. C. C. D.; Machado, G. B.; Belchior, C. R.; Colaço, M. J.; Barros, J. E.; Oliveira, E. J. de; Oliveira, D. G. de. Hydrous ethanol–gasoline blends – Combustion and emission investigations on a Flex-Fuel engine. **Fuel**, v. 97, p. 796–804, jul 2012.

Mohammadzadeh, A. **Stochastic Combustion Modeling of a Direct Injection Diesel Engine**. 216 p. Tese (Doutorado) — University of Michigan, 1984.

Moran, M. J.; Shapiro, H. N.; Boettner, D. D.; Bailey, M. B. **Fundamentals of Engineering Thermodynamics**. 7th. ed. [S.l.]: John Wiley & Sons, 2011. 1026 p. ISBN 9780470495902.

Mugele, R. A.; Evans, H. D. Droplet Size Distribution in Sprays. **Industrial and Engineering Chemistry**, v. 43, n. 6, p. 1317–1324, jun 1951.

Munsin, R.; Laoonual, Y.; Jugjai, S.; Imai, Y. An experimental study on performance and emissions of a small SI engine generator set fuelled by hydrous ethanol with high water contents up to 40**Fuel**, v. 106, p. 586–592, apr 2013.

Narins, T. P. The battery business: Lithium availability and the growth of the global electric car industry. **Extractive Industries and Society**, v. 4, n. 2, p. 321–328, apr 2017.

Newbold, F. R.; Amundson, N. R. A model for evaporation of a multicomponent droplet. **AIChE Journal**, v. 19, n. 1, p. 22–30, jan 1973.

Nigra Júnior, E.; Fukumasu, N.; Berti, R.; Alegre, G.; Krieger Filho, G.; Santos, R. Effect of n-heptane temperature on atomization parameters from a single-hole port fuel injector. In: **Anais do XXIV Simpósio Internacional de Engenharia Automotiva**. São Paulo: Editora Edgard Blücher, 2016. p. 212–220.

Nigro, F.; Szwarc, A. **Ethanol as a Fuel**. 1st. ed. [S.l.], 2011. 35 p.

Nishiwaki, N. Kinetics of liquid combustion processes: Evaporation and ignition lag of fuel droplets. **Symposium (International) on Combustion**, v. 5, n. 1, p. 148–158, jan 1955.

NIST. **Ethanol condensed properties**. 2021. 1 p. Disponível em: <https://webbook.nist.gov/cgi/cbook.cgi?ID=C64175&Units=SI&Mask=2#Thermo-Condensed>.

O'Donnell, P. C.; Rahimi Boldaji, M.; Gainey, B.; Lawler, B. Varying Intake Stroke Injection Timing of Wet Ethanol in LTC. In: **SAE Technical Papers**. [S.l.]: SAE International, 2020. v. 2020-April, n. April. ISSN 01487191.

Olguin, H.; Gutheil, E. Influence of evaporation on spray flamelet structures. **Combustion and Flame**, v. 161, n. 4, p. 987–996, apr 2014.

Oliveira, A. V. S.; Alegre, G. H. M.; Santos, R. G. Gasoline surrogates in nucleate boiling heat transfer. **Journal of the Brazilian Society of Mechanical Sciences and Engineering**, v. 41, n. 3, p. 128, mar 2019.

Onat, N. C.; Kucukvar, M.; Tatari, O. Conventional, hybrid, plug-in hybrid or electric vehicles? State-based comparative carbon and energy footprint analysis in the United States. **Applied Energy**, v. 150, p. 36–49, 2015.

Payri, F.; Olmeda, P.; Martín, J.; García, A. A complete 0D thermodynamic predictive model for direct injection diesel engines. **Applied Energy**, v. 88, n. 12, p. 4632–4641, dec 2011.

Pinheiro, A. P. **Lagrangian modeling of droplet evaporation**. 123 p. Tese (Doutorado) — Universidade Federal de Uberlândia, Uberlândia, aug 2018. Disponível em: <https://repositorio.ufu.br/handle/123456789/22510>.

Pinheiro, A. P.; Vedovoto, J. M. Evaluation of Droplet Evaporation Models and the Incorporation of Natural Convection Effects. **Flow, Turbulence and Combustion**, v. 102, n. 3, p. 537–558, mar 2018.

Pope, D. N.; Raghavan, V.; Gogos, G. Gas-phase entropy generation during transient methanol droplet combustion. **International Journal of Thermal Sciences**, v. 49, n. 7, p. 1288–1302, jul 2010.

Poullikkas, A. **Sustainable options for electric vehicle technologies**. [S.l.]: Elsevier Ltd, 2015. 1277–1287 p.

Puri, I. K. Second law analysis of convective droplet burning. **International Journal of Heat and Mass Transfer**, v. 35, n. 10, p. 2571–2578, oct 1992.

Puri lng, T. N.; Soni lng, L. R.; Deshpande, S. Combined Effects of Injection Timing and Fuel Injection Pressure on Performance, Combustion and Emission Characteristics of a Direct Injection Diesel Engine Numerically Using CONVERGE CFD Tool. **SAE paper**, 2017.

Qiu, L.; Wang, Y.; Jiao, Q.; Wang, H.; Reitz, R. D. Development of a thermodynamically consistent, robust and efficient phase equilibrium solver and its validations. **Fuel**, v. 115, p. 1–16, jan 2014.

Ra, Y.; Reitz, R. D. The application of a multicomponent droplet vaporization model to gasoline direct injection engines. **International Journal of Engine Research**, v. 4, n. 3, p. 193–218, jun 2003.

Ra, Y.; Reitz, R. D. A vaporization model for discrete multi-component fuel sprays. **International Journal of Multiphase Flow**, 2009.

Rahimi Boldaji, M.; Gainey, B.; Lawler, B. Thermally stratified compression ignition enabled by wet ethanol with a split injection strategy: A CFD simulation study. **Applied Energy**, v. 235, p. 813–826, feb 2019.

Rakopoulos, C.; Antonopoulos, K.; Rakopoulos, D.; Hountalas, D. Multi-zone modeling of combustion and emissions formation in DI diesel engine operating on ethanol–diesel fuel blends. **Energy Conversion and Management**, v. 49, n. 4, p. 625–643, apr 2008.

Rakopoulos, C. D.; Antonopoulos, K. A.; Rakopoulos, D. C. Multi-zone modeling of Diesel engine fuel spray development with vegetable oil, bio-diesel or Diesel fuels. **Energy Conversion and Management**, v. 47, n. 11-12, p. 1550–1573, jul 2006.

Rakopoulos, C. D.; Giakoumis, E. G. Second-law analyses applied to internal combustion engines operation. **Progress in Energy and Combustion Science**, v. 32, n. 1, p. 2–47, 2006.

Ranz, W. E.; Marshall Jr., W. R. Evaporation from Drops. **Chemical Engineering Process**, v. 48, n. 3, p. 141–146, 1952.

Reitz, R. D.; Diwakar, R. Effect of Drop Breakup on Fuel Sprays. In: **SAE Transactions**. [s.n.], 1986. v. 95, p. 218–227. Disponível em: <https://www.jstor.org/stable/44725372https://www.sae.org/content/860469/>.

Reitz, R. D.; Diwakar, R. Structure of High-Pressure Fuel Sprays. In: **SAE Transactions**. [s.n.], 1987. v. 96, p. 492–509. Disponível em: <https://about.jstor.org/termshttps://www.sae.org/content/870598/>.

Reitz, R. D.; Ogawa, H.; Payri, R.; Fansler, T.; Kokjohn, S.; Moriyoshi, Y.; Agarwal, A.; Arcoumanis, D.; Assanis, D.; Bae, C.; Boulouchos, K.; Canakci, M.; Curran, S.; Denbratt, I.; Gavaises, M.; Guenthner, M.; Hasse, C.; Huang, Z.; Ishiyama, T.; Johansson, B.; Johnson, T.; Kalghatgi, G.; Koike, M.; Kong, S.; Leipertz, A.; Miles, P.; Novella, R.; Onorati, A.; Richter, M.; Shuai, S.; Siebers, D.; Su, W.; Trujillo, M.; Uchida, N.; Vaglieco, B. M.; Wagner, R.; Zhao, H. IJER editorial: The future of the internal combustion engine. **International Journal of Engine Research**, v. 21, n. 1, p. 3–10, jan 2020.

Renewable Fuels Association. **Annual Fuel Ethanol Production**. 2020. 1 p. Disponível em: <https://ethanolrfa.org/statistics/annual-ethanol-production/>.

Renksizbulut, M.; Yuen, M. C. Numerical Study of Droplet Evaporation in a High-Temperature Stream. **Journal of Heat Transfer**, v. 105, n. 2, p. 389–397, may 1983.

Réveillon, J.; Vervisch, L. Spray vaporization in nonpremixed turbulent combustion modeling: a single droplet model. **Combustion and Flame**, v. 121, n. 1-2, p. 75–90, apr 2000.

Rufino, C. H. **Conceptual study of an internal combustion engine with adjustable cubic capacity and compression ratio**. 228 p. Tese (Doutorado) — UNICAMP, 2020. Disponível em: <http://lattes.cnpq.br/8526204483675376>.

Rufino, C. H.; Lima, A. J. de; Mattos, A. P.; Allah, F. U.; Bernal, J. L.; Ferreira, J. V.; Gallo, W. L. Exergetic analysis of a spark ignition engine fuelled with ethanol. **Energy Conversion and Management**, v. 192, p. 20–29, jul 2019.

Santos, F. dos; Moyne, L. le. Spray atomization models in engine applications, from correlations to direct numerical simulations. **Oil and Gas Science and Technology**, v. 66, n. 5, p. 801–822, sep 2011.

Sari, R. L.; Golke, D.; Enzweiler, H. J.; Salau, N. P.; Pereira, F. M.; Martins, M. E. Exploring optimal operating conditions for wet ethanol use in spark ignition engines. **Applied Thermal Engineering**, v. 138, p. 523–533, jun 2018.

Sazhin, S. **Droplets and Sprays**. 1st. ed. London: Springer London, 2014. v. 9781447163. 1–345 p.

Sazhin, S.; Abdelghaffar, W.; Krutitskii, P.; Sazhina, E.; Heikal, M. New approaches to numerical modelling of droplet transient heating and evaporation. **International Journal of Heat and Mass Transfer**, v. 48, n. 19-20, p. 4215–4228, sep 2005.

Sazhin, S.; Castanet, G.; Sazhin, S. S.; Krutitskii, P. A.; Elwardany, A.; Castanet, G.; Lemoine, F.; Heikal, M. R. An analytical solution to the spherically symmetric species diffusion equation: application to modelling of heating and evaporation of bi-component droplets. In: **Conference on Liquid Atomization and Spray Systems**. [s.n.], 2010. Disponível em: <https://www.researchgate.net/publication/267562387>.

Sazhin, S.; Elwardany, A.; Krutitskii, P.; Deprédurand, V.; Castanet, G.; Lemoine, F.; Sazhina, E.; Heikal, M. Multi-component droplet heating and evaporation: Numerical simulation versus experimental data. **International Journal of Thermal Sciences**, v. 50, n. 7, p. 1164–1180, jul 2011.

Sazhin, S. S. Advanced models of fuel droplet heating and evaporation. **Progress in Energy and Combustion Science**, v. 32, n. 2, p. 162–214, jan 2006.

Sazhin, S. S. Modelling of fuel droplet heating and evaporation: Recent results and unsolved problems. **Fuel**, v. 196, p. 69–101, may 2017.

Sazhin, S. S.; Abdelghaffar, W. A.; Sazhina, E. M.; Heikal, M. R. Models for droplet transient heating: Effects on droplet evaporation, ignition, and break-up. **International Journal of Thermal Sciences**, 2005.

Sazhin, S. S.; Al Qubeissi, M.; Kolodnytska, R.; Elwardany, A. E.; Nasiri, R.; Heikal, M. R. Modelling of biodiesel fuel droplet heating and evaporation. **Fuel**, 2014.

Sazhin, S. S.; Krutitskii, P. A. A conduction model for transient heating of fuel droplets. In: **Progress in Analysis**. World Scientific Publishing Company, 2003. p. 1231–1239. ISBN 978-981-238-572-7. Disponível em: <www.worldscientific.comhttp://www.worldscientific.com/doi/abs/10.1142/9789812794253_0142>.

Sazhin, S. S.; Krutitskii, P. A.; Abdelghaffar, W. A.; Sazhina, E. M.; Mikhalovsky, S. V.; Meikle, S. T.; Heikal, M. R. Transient heating of diesel fuel droplets. **International Journal of Heat and Mass Transfer**, v. 47, n. 14-16, p. 3327–3340, jul 2004.

Sazhin, S. S.; Krutitskii, P. A.; Martynov, S. B.; Mason, D.; Heikal, M. R.; Sazhina, E. M. Transient heating of a semitransparent spherical body. **International Journal of Thermal Sciences**, v. 46, n. 5, p. 444–457, may 2007.

Sengupta, S. P. **Theorical studies on some aspects of droplet and spray evaporation**. [S.l.], 1987. 11 p.

Simmons, H. C. The Correlation of Drop-Size Distributions in Fuel Nozzle Sprays—Part I: The Drop-Size/Volume-Fraction Distribution. **Journal of Engineering for Power**, v. 99, n. 3, p. 309–314, jul 1977.

Simmons, H. C. The Correlation of Drop-Size Distributions in Fuel Nozzle Sprays—Part II: The Drop-Size/Number Distribution. **Journal of Engineering for Power**, v. 99, n. 3, p. 315–319, jul 1977.

Sirignano, W. A. Fuel droplet vaporization and spray combustion theory. **Progress in Energy and Combustion Science**, v. 9, n. 4, p. 291–322, jan 1983.

Sirignano, W. A. Fluid Dynamics of Sprays—1992 Freeman Scholar Lecture. **Journal of Fluids Engineering**, v. 115, n. 3, p. 34, 1993.

Sirignano, W. A. **Fluid Dynamics and Transport of Droplets and Sprays**. 2nd. ed. [S.l.]: Cambridge University Press, 2010. 482 p. ISBN 978-0-511-67564-5.

Sirignano, W. A. Advances in droplet array combustion theory and modeling. **Progress in Energy and Combustion Science**, v. 42, p. 54–86, jun 2014.

Sirignano, W. A.; Law, C. K. Transient Heating and Liquid-Phase Mass Diffusion in Fuel Droplet Vaporization. **Combustion and Flame**, v. 12, p. 3–26, jun 1978.

Snegirev, A. Y. Transient temperature gradient in a single-component vaporizing droplet. **International Journal of Heat and Mass Transfer**, 2013.

Som, S.; Datta, A. Thermodynamic irreversibilities and exergy balance in combustion processes. **Progress in Energy and Combustion Science**, v. 34, n. 3, p. 351–376, jun 2008.

Som, S. K.; Dash, S. K. Thermodynamics of spray evaporation. **J. Phys. D. Appl. Phys**, v. 26, n. 1SS3, p. 57–84, 1993.

Som, S. K.; Mitra, A. K.; Sengupta, S. P. Second Law Analysis of Spray Evaporation. **Journal of Energy Resources Technology**, v. 112, n. 2, p. 130–135, jun 1990.

Som, S. K.; Sharma, N. Y. Energy and exergy balance in the process of spray combustion in a gas turbine combustor. **Journal of Heat Transfer**, v. 124, n. 5, p. 828–836, oct 2002.

Spalding, D. B. The combustion of liquid fuels. **Symposium (International) on Combustion**, v. 4, n. 1, p. 847–864, jan 1953.

Spiegel, L.; Spicher, U. Mixture Formation and Combustion in a Spark Ignition Engine with Direct Fuel Injection. In: **SAE Technical Paper 920521**. [S.l.: s.n.], 1992. p. 11.

Stan, C.; Tröger, R.; Lensi, R.; Martoran, L.; Tarantino, C. Potentialities of Direct Injection in Spark Ignition Engines - from Gasoline to Ethanol. **SAE paper**, p. 11, 2000.

Stein, R. A.; Anderson, J. E.; Wallington, T. J. An Overview of the Effects of Ethanol-Gasoline Blends on SI Engine Performance, Fuel Efficiency, and Emissions. **SAE International Journal of Engines**, v. 6, n. 1, p. 2013–01–1635, 2013.

Strutt, J. W.; Rayleigh, L. On the instability of jets. In: **Proceedings of the London mathematical society**. [S.l.: s.n.], 1878. v. 10, p. 4–13.

Tamim, J. **A Continuous Thermodynamics Model for Multicomponent Droplet Vaporization**. 150 p. Tese (Doutorado) — University of Ottawa, 1996.

Tamim, J.; Hallett, W. A continuous thermodynamics model for multicomponent droplet vaporization. **Chemical Engineering Science**, v. 50, n. 18, p. 2933–2942, sep 1995.

Távora, F. L. **História e Economia dos Biocombustíveis no Brasil**. [S.l.], 2011. 78 p.

Tokimatsu, K.; Wachtmeister, H.; McLellan, B.; Davidsson, S.; Murakami, S.; Höök, M.; Yasuoka, R.; Nishio, M. Energy modeling approach to the global energy-mineral nexus: A first look at metal requirements and the 2 °C target. **Applied Energy**, v. 207, p. 494–509, dec 2017.

Tong, A. Y.; Sirignano, W. A. Multicomponent Transient Droplet Vaporization with Internal Circulation: Integral Equation Formulation and Approximate Solution. **Numerical Heat Transfer**, v. 10, n. 3, p. 253–278, sep 1986.

Tong, Y.; Sirignano, W. A. SHORT COMMUNICATION Transient Thermal Boundary Layer in Heating of Droplet with Internal Circulation: Evaluation of Assumptions. **Combustion Science and Technology**, v. 29, n. 1-2, p. 87–94, oct 1982.

Turkcan, A.; Ozsezen, A. N.; Canakci, M. Effects of second injection timing on combustion characteristics of a two stage direct injection gasoline-alcohol HCCI engine. **Fuel**, v. 111, p. 30–39, 2013.

Turkcan, A.; Ozsezen, A. N.; Canakci, M. Experimental investigation of the effects of different injection parameters on a direct injection HCCI engine fueled with alcohol-gasoline fuel blends. **Fuel Processing Technology**, v. 126, p. 487–496, 2014.

Turns, S. R. **An Introduction to Combustion - Concepts and Applications**. 3rd. ed. [S.l.]: Mc-Graw Hill, 2012. 754 p.

Valero, A.; Valero, A.; Calvo, G.; Ortego, A. **Material bottlenecks in the future development of green technologies**. [S.l.]: Elsevier Ltd, 2018. 178–200 p.

Vane, L. M. Separation technologies for the recovery and dehydration of alcohols from fermentation broths. **Biofuels, Bioproducts and Biorefining**, v. 2, n. 6, p. 553–588, nov 2008.

Walter, A.; Dolzan, P.; Quilodrán, O.; De Oliveira, J. G.; Da Silva, C.; Piacente, F.; Segerstedt, A. Sustainability assessment of bio-ethanol production in Brazil considering land use change, GHG emissions and socio-economic aspects. **Energy Policy**, v. 39, n. 10, p. 5703–5716, oct 2011.

Wang, Z.; Liu, H.; Reitz, R. D. Knocking combustion in spark-ignition engines. **Progress in Energy and Combustion Science**, v. 61, p. 78–112, jul 2017.

Way, R. J. B. Methods for Determination of Composition and Thermodynamic Properties of Combustion Products for Internal Combustion Engine Calculations. **Proceedings of the Institution of Mechanical Engineers**, v. 190, n. 1, p. 687–697, jun 1976.

Wikipedia. **Timeline of alcohol fuel**. 2022. 1 p. Disponível em: <https://en.wikipedia.org/wiki/Timeline_of_alcohol_fuel>.

Williams, A. Combustion of droplets of liquid fuels: A review. **Combustion and Flame**, v. 21, n. 1, p. 1–31, 1973.

Wilms, J. **Evaporation of multicomponent droplets**. 177 p. Tese (Doutorado) — Universität Stuttgart, 2005.

Xianguo, L.; Tankin, R. Droplet Size Distribution: A Derivation of a Nukiyama-Tanasawa Type Distribution Function. **Combustion Science and Technology**, v. 56, n. 1, p. 65–76, sep 1987.

Xu, B.; Sharif, A.; Shahbaz, M.; Dong, K. Have electric vehicles effectively addressed CO2 emissions? Analysis of eight leading countries using quantile-on-quantile regression approach. **Sustainable Production and Consumption**, v. 27, p. 1205–1214, jul 2021.

Yang, J.; Anderson, R. W. Fuel Injection Strategies to Increase Full-Load Torque Output of a Direct-Injection SI Engine. In: **SAE paper 980495**. [S.l.: s.n.], 1998. p. SAE 980495.

Yeliana, C. C.; Worm, J.; Michalek, D.; Naber, J. Wiebe function parameter determination for mass fraction burn calculation in an ethanol-gasoline fuelled SI engine. **Journal of KONES Powertrain and Transport**, v. 15, n. 3, p. 567–574, 2008.

Yi, P.; Long, W.; Jia, M.; Feng, L.; Tian, J. Development of an improved hybrid multi-component vaporization model for realistic multi-component fuels. **International Journal of Heat and Mass Transfer**, 2014.

Yi, P.; Long, W.; Jia, M.; Tian, J.; Li, B. Development of a quasi-dimensional vaporization model for multi-component fuels focusing on forced convection and high temperature conditions. **International Journal of Heat and Mass Transfer**, v. 97, p. 130–145, jun 2016.

Yin, C. Transient heating and evaporation of moving mono-component liquid fuel droplets. **Applied Thermal Engineering**, v. 104, p. 497–503, jul 2016.

Young, J. The fundamental equations of gas-droplet multiphase flow. **International Journal of Multiphase Flow**, v. 21, n. 2, p. 175–191, apr 1995.

Yuen, M. C.; Chen, L. W. On Drag of Evaporating Liquid Droplets. **Combustion Science and Technology**, v. 14, n. 4-6, p. 147–154, oct 1976.

Zeng, Y.; Lee, C.-f. F. A preferential vaporization model for multicomponent droplets and sprays. **Atomization and Sprays**, v. 12, n. 1-3, p. 163–186, 2002.

Zhao, F.; Lai, M.-C.; Harrington, D. Automotive spark-ignited direct-injection gasoline engines. **Progress in Energy and Combustion Science**, v. 25, n. 5, p. 437–562, oct 1999.

Zhao, F.-Q.; Lai, M.-C.; Harrington, D. L. A Review of Mixture Preparation and Combustion Control Strategies for Spark-Ignited Direct-Injection Gasoline Engines. In: **SAE Technical Paper**. [s.n.], 1997. p. SAE 970627. Disponível em: <http://dx.doi.org/10.4271/970627http://papers.sae.org/970627/>.

Zhao, H. **Advanced direct injection combustion engine technologies and development**. 1st. ed. Woodhead Publishing Limited, 2010. 298 p. ISSN 1098-6596. ISBN 978-1-84569-744-0.

Zhao, J. Research and application of over-expansion cycle (Atkinson and Miller) engines – A review. **Applied Energy**, v. 185, p. 300–319, jan 2017.

Zhuang, Y.; Hong, G. Investigation to Leveraging Effect of Ethanol Direct Injection (EDI) in a Gasoline Port Injection (GPI) Engine. In: **SAE paper**. [s.n.], 2013. Disponível em: <http://papers.sae.org/2013-01-1322/>.

Zhuang, Y.; Hong, G. The Effect of Direct Injection Timing and Pressure on Engine Performance in an Ethanol Direct Injection Plus Gasoline Port Injection (EDI+GPI) SI Engine. In: **SAE paper**. [s.n.], 2013. p. SAE 2013–01–0892. Disponível em: <http://papers.sae.org/2013-01-0892/>.

Zhuang, Y.; Hong, G. Effects of direct injection timing of ethanol fuel on engine knock and lean burn in a port injection gasoline engine. **Fuel**, v. 135, n. June, p. 27–37, nov 2014.

Zhuang, Y.; Qian, Y.; Hong, G. The effect of ethanol direct injection on knock mitigation in a gasoline port injection engine. **Fuel**, v. 210, n. August, p. 187–197, 2017.

APPENDIX A – LAGRANGIAN DROPLET EQUATIONS

The conservation equations (i.e. mass, momentum, energy) and the entropy equation are applied in the Lagrangian form to each droplet present in the system. These equations are valid to all droplets included in the same spray layer, therefore reducing massively the number of ODEs to be solved. Meanwhile, with exception of the momentum, the same properties are solved to the unburned and burned gases, but in the Eulerian form.

The fuel droplets are assumed to be injected in the unburned gas zone, therefore not interacting with the burned zone. Hence, the differential equation deductions which are presented in this appendix are the following:

- Mass conservation - droplet;
- Species conservation - droplet;
- Momentum conservation - droplet;
- Energy conservation - droplet;
- Entropy equation - droplet;

A.1 Mass conservation - droplet

The main model takes into consideration that each fuel droplet present in the system is represented by a control volume on their own. This control volume is variable in volume (i.e. not rigid in its control surfaces) and follows the droplets based on their dynamics (i.e. Lagrangian approach). Also, each droplet control volume exists inside the main system (i.e. in-cylinder gases) as long as the droplet exists.

The deduction begins at the mass conservation of a droplet:

$$\left.\frac{\mathrm{d}m_d}{\mathrm{d}t}\right|_{Sist.} = 0$$

The Reynolds Transport Theorem (RTT) is applied to this expression, which gives:

$$\frac{\partial}{\partial t}\int_{CV} \rho_d \,\mathrm{d}\forall + \int_{CS} \rho_s (w_i n_i)\,\mathrm{d}A = 0$$

The mass conservation for a droplet is divided in the transient term and an outlet mass flow due to evaporation. The transient term is presented below:

$$\frac{\partial}{\partial t}\int_{VC}\rho_d\,\mathrm{d}\mathcal{V}=\frac{\mathrm{d}(\rho_d\,\mathcal{V})}{\mathrm{d}t}=\frac{\mathrm{d}m_d}{\mathrm{d}t}$$

where the liquid specific mass is homogeneous in space, although it changes over time due to temperature variation.

As said before, the outlet flow is associated with the evaporation process, therefore:

$$\int_{SC}\rho_s(w_i n_i)\,\mathrm{d}A=\pi D_d^2\rho_s V_{r,s}=\dot{m}_d$$

Grouping these two terms provides the mass conservation for a droplet:

$$\frac{\mathrm{d}m_d}{\mathrm{d}t}=-\dot{m}_d \tag{A.1}$$

Although the previous equation is correct, is more common to express it in terms of droplet diameter in literature. So, expanding the droplet mass term m_d in terms of its liquid specific mass and volume, we obtain:

$$\rho_d\frac{\pi}{2}D_d^2\frac{\mathrm{d}D_d}{\mathrm{d}t}+\frac{\pi}{6}D_d^3\frac{\mathrm{d}\rho_d}{\mathrm{d}t}=-\dot{m}_d$$

Isolating the diameter derivative provides the sought equation:

$$\frac{\mathrm{d}D_d}{\mathrm{d}t}=-\frac{2\dot{m}_d}{\pi\rho_d D_d^2}-\frac{\pi D_d}{3\rho_d}\frac{\mathrm{d}\rho_d}{\mathrm{d}t}, \tag{A.2}$$

where the first term represents the mass variation due to evaporation, whereas the second refers to liquid specific mass variation due to temperature variation, which is usually known as the droplet swelling effect.

A.2 Species conservation - droplet

The demonstration here follows similar steps as presented in (Kuo, 2005). Also, the species conservation for the liquid phase (i.e. droplet) is obtained through the application of the RTT as the approach presented in (Crowe *et al.*, 2012) and some additional assumptions:

$$\frac{D}{Dt}\int_{VC}\rho y_A\,\mathrm{d}\mathcal{V}=\frac{\partial}{\partial t}\int_{VC}\rho y_A\,\mathrm{d}\mathcal{V}+\int_{SC}\left[\left(\rho y_A\vec{w}_i-\rho\frac{W_A}{\overline{W}}\mathcal{D}'_{AB}\nabla x_A\right)\cdot\vec{n}\right]\mathrm{d}A=\int_{VC}r_A W_A\,\mathrm{d}\mathcal{V}$$

Noticing that there are no chemical reactions in this control volume ($r_A = 0$), we have:

$$\frac{\partial}{\partial t}\int_{VC}\rho y_A \,\mathrm{d}\rlap{-}V + \int_{SC}\rho y_A w_i n_i \,\mathrm{d}A = -\int_{SC}\vec{j_A}\cdot\vec{n}\,\mathrm{d}A$$

where $\vec{j_A} = -\rho\frac{W_A}{\bar{W}}\mathcal{D}'_{AB}\nabla x_A$. For the transient term, the control volume varies the mass of species A and the species is assumed homogeneous throughout the volume, then:

$$\frac{\partial}{\partial t}\int_{VC}\rho_d y_A \,\mathrm{d}\rlap{-}V = \frac{\mathrm{d}m_{d,A}}{\mathrm{d}t}$$

The second term represents the mass flow rate from species A through the control surface of the droplet, thus:

$$\int_{SC}\rho y_A w_i n_i \,\mathrm{d}A = 4\pi r_d^2 \rho_s y_A V_{r,s}$$

The third term is the diffusive term of A, therefore:

$$-\int_{SC}\vec{j_A}\cdot\vec{n}\,\mathrm{d}A = -\int_{SC}\left[-\rho\frac{W_A}{\bar{W}}\mathcal{D}'_{AB}\nabla x_A\right]\cdot\vec{n}\,\mathrm{d}A$$

Since $\frac{W_A}{\bar{W}}\nabla x_A = \nabla y_A$, this modification yields:

$$-\int_{SC}\vec{j_A}\cdot\vec{n}\,\mathrm{d}A = \int_{SC}\left[\rho_s\mathcal{D}'_{AB}\nabla y_A\right]\cdot\vec{n}\,\mathrm{d}A = \int_{SC}\left[\rho_s\mathcal{D}'_{AB}\frac{\partial y_A}{\partial r}\right]\mathrm{d}A = 4\pi r_d^2\rho_s\mathcal{D}'_{AB}\left.\frac{\mathrm{d}y_A}{\mathrm{d}r}\right|_{r=r_d}$$

Thus, the species conservation for A on the droplet is:

$$\frac{\mathrm{d}m_{d,A}}{\mathrm{d}t} + 4\pi r_d^2\rho_s y_A V_{r,s} = 4\pi r_d^2\rho_s\mathcal{D}'_{AB}\left.\frac{\mathrm{d}y_A}{\mathrm{d}r}\right|_s$$

For species B (i.e. gases involving the droplet), the insolubility assumption indicates that there is no gas components inside the droplet control volume, so:

$$\frac{\partial}{\partial t}\int_{VC}\rho_d y_B \,\mathrm{d}\rlap{-}V = \left.\frac{\mathrm{d}m_B}{\mathrm{d}t}\right|_{VC} = 0$$

Therefore the convective and diffusive terms equal each other:

$$4\pi r_d^2\rho_s y_B V_{r,s} = 4\pi r_d^2\rho_s\mathcal{D}'_{AB}\left.\frac{\mathrm{d}y_B}{\mathrm{d}r}\right|_s \text{ (Insolubility of } B \text{ in } A\text{)}$$

Summing up both equations, we have:

$$\frac{\mathrm{d}m_{d,A}}{\mathrm{d}t} + \rho_s y_A V_{r,s} + \frac{\mathrm{d}m_{d,B}}{\mathrm{d}t} + \rho_s y_A V_{r,s} = \rho_s \mathcal{D}^{'}_{AB} \left.\frac{\mathrm{d}y_A}{\mathrm{d}r}\right|_s + \rho_s \mathcal{D}^{'}_{AB} \left.\frac{\mathrm{d}y_B}{\mathrm{d}r}\right|_s$$

The insolubility of B causes that only diffusive and convective terms of A are present on the droplet surface. Thus substituting the mass conservation of the droplet on $\frac{\mathrm{d}m_{d,A}}{\mathrm{d}t}$:

$$4\pi r_d^2 \rho_s V_{r,s} = 4\pi r_d^2 \rho_s y_A V_{r,s} - 4\pi r_d^2 \rho_s \mathcal{D}^{'}_{AB} \frac{\mathrm{d}y_A}{\mathrm{d}r}$$

Hence we obtain:

$$\rho \left. V_r \right|_s = \rho y_A \left. V_r \right|_s - \rho \mathcal{D}^{'}_{AB} \left.\frac{\mathrm{d}y_A}{\mathrm{d}r}\right|_s$$

$$\left. V_r \right|_s = \frac{\mathcal{D}^{'}_{AB} \frac{\mathrm{d}y_A}{\mathrm{d}r}}{y_A - 1}$$

Applying the Spalding number $b = \frac{y_A}{\left. y_A \right|_s - 1}$:

$$\left. V_r \right|_s = \mathcal{D}^{'}_{AB} \left.\frac{\mathrm{d}b}{\mathrm{d}r}\right|_s$$

Estimating now that the fuel evaporation rate may be approximated by a quasi-steady approach (Kuo, 2005), it is obtained the classical mass flow rate for an evaporative droplet:

$$\dot{m}_A = 4\pi r_s \rho_s D_s ln(1 + B_{M,A}) \tag{A.3}$$

The Spalding transfer number B_M is:

$$B_{M,A} = b_{\infty,A} - b_{s,A} = \frac{y_{A,s} - y_{A,\infty}}{1 - y_{A,s}}$$

This equation was extended by (Abramzon; Sirignano, 1989) and applied to multi-component droplets by (Brenn *et al.*, 2003), obtaining its final form:

$$\dot{m}_d = \sum_{i=1}^{N_{species}} \dot{m}_i = \sum_{i=1}^{n} \pi D_{part,i} (\rho \mathcal{D})_{i,v} Sh_i \ln(1 + B_{M,i}) \tag{A.4}$$

A.3 Momentum conservation - droplet

The demonstration presented here follows the equations presented in (Crowe, 1975; Crowe, 1976; Crowe *et al.*, 2012). It is presented here just for the sake of completeness of the droplet model. The RTT for a droplet has the following form:

$$F_i = \frac{\partial}{\partial t}\int_{VC} \rho_d U_i \,\mathrm{d}\,\forall + \int_{CS} \rho_s U_{i,s}(w_i n_i)\,\mathrm{d}A$$

where F_i compiles body and surface forces and $U_{i,s}$ is the fluid velocity on the control surface referred to an inertial reference. Assuming that there are no internal movements and the droplet rotation occurs around an axis which passes through its center of mass, we know that the particle velocity is:

$$U_i = v_i + \epsilon_{ijk}\omega_j\xi_k$$

where v_i is the droplet center of mass velocity referred to an inertial reference, ω_j is the droplet rotation vector and ξ_k is the distance from the center of mass. Therefore, the transient term turns into:

$$\frac{\partial}{\partial t}\int_{VC} \rho_d U_i \,\mathrm{d}\,\forall = \frac{\partial}{\partial t}\int_{VC} \rho_d \left(v_i + \epsilon_{ijk}\omega_j\xi_k\right)\mathrm{d}\,\forall$$

Since v_i and ω_j are constants around the surface:

$$\frac{\partial}{\partial t}\int_{VC} \rho_d U_i \,\mathrm{d}\,\forall = \frac{\mathrm{d}(m_d v_i)}{\mathrm{d}t} + \frac{\partial}{\partial t}\epsilon_{ijk}\omega_j\int_{VC} \rho_d \xi_k \,\mathrm{d}\,\forall$$

The second integral is zero, because of the definition of center of mass, thus:

$$\frac{\partial}{\partial t}\int_{VC} \rho_d U_i \,\mathrm{d}\,\forall = \frac{\mathrm{d}(m_d v_i)}{\mathrm{d}t} = v_i\frac{\mathrm{d}m_d}{\mathrm{d}t} + m_d\frac{\mathrm{d}v_i}{\mathrm{d}t}$$

The velocity on the droplet surface with respect to its center is:

$$\frac{\mathrm{d}r_d}{\mathrm{d}t}n_i + \epsilon_{ijk}\omega_j r_k$$

Hence, the fluid velocity crossing the control surface becomes (for a inertial reference):

$$U_{i,s} = v_i + \epsilon_{ijk}\omega_j r_k + \left(\frac{\mathrm{d}r_d}{\mathrm{d}t} + w\right)n_i = v_i + \epsilon_{ijk}\omega_j r_k + w^{'} n_i$$

where w is the efflux velocity. So, the liquid momentum flux around the control surface is:

$$\int_{SC} \rho_s U_{i,s}(w_i n_i)\,\mathrm{d}A = \int_{SC} \rho_s (v_i + \epsilon_{ijk}\omega_j r_k + w^{'} n_i)(w_l n_l)\,\mathrm{d}A$$

Assuming that v_i is uniform in this surface, we have:

$$\int_{SC} \rho_s U_{i,s}(w_i n_i)\,\mathrm{d}A = v_i \int_{SC} \rho_s (w_l n_l)\,\mathrm{d}A + \int_{SC} \rho_s (\epsilon_{ijk}\omega_j r_k + w^{'} n_i)(w_l n_l)\,\mathrm{d}A$$

$$\int_{SC} \rho_s U_{i,s}(w_i n_i)\,\mathrm{d}A = -v_i \frac{\mathrm{d}m_d}{\mathrm{d}t} + \int_{SC} \rho_s (\epsilon_{ijk}\omega_j r_k + w^{'} n_i)(w_l n_l)\,\mathrm{d}A$$

Accomplishing the transient and flow terms generates the following equation:

$$F_i = \left[v_i \frac{\mathrm{d}m_d}{\mathrm{d}t} + m_d \frac{\mathrm{d}v_i}{\mathrm{d}t} \right] + \left[-v_i \frac{\mathrm{d}m_d}{\mathrm{d}t} + \int_{SC} \rho_s (\epsilon_{ijk}\omega_j r_k + w^{'} n_i)(w_l n_l)\,\mathrm{d}A \right]$$

Therefore, we obtain the momentum equation for a droplet:

$$F_i = m_d \frac{\mathrm{d}v_i}{\mathrm{d}t} + \epsilon_{ijk}\omega_j \int_{SC} \rho_s r_k (w_l n_l)\,\mathrm{d}A + \int_{SC} \rho_s w^{'} n_i (w_l n_l)\,\mathrm{d}A \tag{A.5}$$

For a evaporating droplet, the evaporation rate (i.e surface regression rate) and the efflux velocity are normal to its surface, then:

$$\int_{SC} \rho_s w^{'} n_i (w_l n_l)\,\mathrm{d}A = \int_{SC} \rho_s w^{'} (w_i n_i)\,\mathrm{d}A = -T_i$$

where T_i is the negative impulse on the droplet due to mass efflux from the control surface. For a spherical droplet evaporating throughout its surface, this phenomenon is uniform, with causes this integral to be symmetric, therefore equal to zero:

$$\int_{SC} \rho_s w^{'} n_i (w_l n_l)\,\mathrm{d}A = \int_{SC} \rho_s w^{'} (w_i n_i)\,\mathrm{d}A = \rho_s w^{'} w \int_{SC} n_i\,\mathrm{d}A = 0$$

Besides, the rotation integral is also zero for an uniform evaporating droplet:

$$\epsilon_{ijk}\omega_j \int_{SC} \rho_s r w n_k \,\mathrm{d}A = 0$$

Henceforth, the momentum equation for a spherical droplet with uniform evaporation over its surface is:

$$F_i = m_d \frac{\mathrm{d}v_i}{\mathrm{d}t} \tag{A.6}$$

The forces F_i are usually divided in body and surface forces:

$$F_i = F_{b,i} + F_{s,i}$$

The gravity force is used as a body force:

$$F_{i,g} = m g_i$$

while the surface forces involve usually pressure effects.

$$F_{i,p} = -\int_{SC} p_s n_i \,\mathrm{d}A$$

This force may consider the drag between the droplet and the fluid and lift. The shear force is also taken into account:

$$F_{i,\tau} = \int_{SC} \tau_{ij} n_j \,\mathrm{d}A$$

Summing these equations leads to:

$$F_i = \int_{SC} \left(p_s n_i - \tau_{ij} n_j\right) \mathrm{d}A$$

Therefore, the final form of the droplet momentum equation is:

$$m_d \frac{\mathrm{d}v_i}{\mathrm{d}t} = F_{drag} + F_{i,b} \tag{A.7}$$

where $F_{drag} = \frac{1}{2}\rho_l C_d A_{rep}|u_i - v_i|(u_i - v_i)$ is obtained for a steady-state drag condition, $A_{rep} = \frac{A_d}{4} = \frac{\pi}{4}D_d^2$ is the droplet representative area. This expression is obtained for a Stokes flow, but it is usually extrapolated for other regimes. Therefore, we obtain:

$$\frac{\mathrm{d}u_d}{\mathrm{d}t} = \frac{3}{4}\frac{C_d}{D_d}\frac{\rho_s}{\rho_d}|u_g - u_d|(u_g - u_d) \tag{A.8}$$

A.4 Energy conservation - droplet

The first law of thermodynamics for a system is (Crowe *et al.*, 2012):

$$\left.\frac{\mathrm{d}E}{\mathrm{d}t}\right|_{Sist.} = \dot{Q} - \dot{W}$$

where E includes the internal and kinetic energies, besides the energy associated with surface tension, $U = mu$, $KE = m\frac{U_iU_i}{2}$, $E_\sigma = A\sigma$. Hence, the total energy is:

$$E = m(u + \frac{U_iU_i}{2}) + A\sigma = me + A\sigma$$

Applying the Reynolds transport theorem shows that:

$$\left.\frac{\mathrm{d}(Me)}{\mathrm{d}t}\right|_{Sist.} = \frac{\partial}{\partial t}\int_{VC}\rho_d e\,\mathrm{d}\,\forall + \int_{CS}\rho_s e_s(w_in_i)\,\mathrm{d}A + \frac{\mathrm{d}}{\mathrm{d}t}(A\sigma)$$

Equaling both equations generate:

$$\dot{Q} - \dot{W} = \frac{\partial}{\partial t}\int_{VC}\rho_d e\,\mathrm{d}\,\forall + \int_{CS}\rho_s e_s(w_in_i)\,\mathrm{d}A + \frac{\mathrm{d}}{\mathrm{d}t}(A\sigma)$$

The energy associated with the contents inside the control volume (i.e. droplet) does not consider neither rotation nor internal movement, so its kinetic energy turns from U_i para v_i. Therefore, the transient term becomes:

$$\frac{\partial}{\partial t}\int_{VC}\rho_d e\,\mathrm{d}\,\forall + \frac{\mathrm{d}}{\mathrm{d}t}(A\sigma) = \frac{\partial}{\partial t}\int_{VC}\rho_d\left(u + \frac{v_iv_i}{2}\right)\mathrm{d}\,\forall + A_d\frac{\mathrm{d}\sigma}{\mathrm{d}t} + \sigma\frac{\mathrm{d}A_d}{\mathrm{d}t}$$

Assuming that u e v_i are uniform in the control volume, we obtain:

$$\frac{\partial}{\partial t}\int_{VC}\rho_d e\,\mathrm{d}\,\forall + \frac{\mathrm{d}}{\mathrm{d}t}(A\sigma) = \frac{\mathrm{d}(m_d\frac{v_iv_i}{2})}{\mathrm{d}t} + \frac{\mathrm{d}(m_du)}{\mathrm{d}t} + A_d\frac{\mathrm{d}\sigma}{\mathrm{d}t} + 8\pi r_d\sigma\frac{\mathrm{d}r_d}{\mathrm{d}t}$$

Also the surface tension is constant, thus:

$$\frac{\partial}{\partial t}\int_{VC}\rho_d e\,\mathrm{d}\,\forall + \frac{\mathrm{d}}{\mathrm{d}t}(A\sigma) = \frac{\mathrm{d}(m_d\frac{v_iv_i}{2})}{\mathrm{d}t} + \frac{\mathrm{d}(m_du)}{\mathrm{d}t} + \frac{2\sigma}{r_d}\frac{\mathrm{d}r_d}{\mathrm{d}t}A_d$$

Opening the derivatives of the kinetic energy term yield:

$$\frac{\mathrm{d}(m_d \frac{v_i v_i}{2})}{\mathrm{d}t} = m_d v_i \frac{\mathrm{d}v_i}{\mathrm{d}t} + \frac{v^2}{2}\frac{\mathrm{d}m_d}{\mathrm{d}t}$$

where v is the absolute value of v_i. Grouping all terms from the transient term leads to the following equation:

$$\frac{\partial}{\partial t}\int_{VC} \rho_d e \,\mathrm{d}\rlap{-}V + \frac{\mathrm{d}}{\mathrm{d}t}(A\sigma) = m_d v_i \frac{\mathrm{d}v_i}{\mathrm{d}t} + \frac{v^2}{2}\frac{\mathrm{d}m_d}{\mathrm{d}t} + \frac{\mathrm{d}(m_d u)}{\mathrm{d}t} + \frac{2\sigma}{r_d}\frac{\mathrm{d}r_d}{\mathrm{d}t}A$$

For the mass flow terms (inlet and outlet), the energy which crosses the control surface is:

$$e_s = u_s + \frac{U_{i,s}U_{i,s}}{2}$$

where $U_{i,s}$ is the fluid velocity referred to an inertial reference and it is equal to:

$$U_{i,s} = v_i + w_i + \frac{\mathrm{d}r_d}{\mathrm{d}t}n_i$$

Applying the variable $w_i^{'} = (w + \frac{\mathrm{d}r_d}{\mathrm{d}t})n_i$, the kinetic energy is:

$$\frac{U_{i,s}U_{i,s}}{2} = \frac{(v_i + w^{'}n_i)(v_i + w^{'}n_i)}{2} = \frac{v^2}{2} + \frac{w^{'2}}{2} + w^{'}n_i v_i$$

Substituting this expression on the flux integral:

$$\int_{CS} \rho_s e_s (w_j n_j)\,\mathrm{d}A = \int_{CS} \rho_s u_s w_j n_j \,\mathrm{d}A + \left(\frac{v^2}{2} + \frac{w^{'2}}{2}\right)\int_{CS} \rho_s w_j n_j \,\mathrm{d}A + v_i \int_{CS} \rho_s w^{'} w n_i \,\mathrm{d}A$$

$$\int_{CS} \rho_s e_s (w_j n_j)\,\mathrm{d}A = \int_{CS} \rho_s u_s w_j n_j \,\mathrm{d}A - \left(\frac{v^2}{2} + \frac{w^{'2}}{2}\right)\frac{\mathrm{d}m_d}{\mathrm{d}t} + v_i \int_{CS} \rho_s w^{'} w n_i \,\mathrm{d}A$$

Summing up this equation with the transient term, we obtain:

$$\frac{\partial}{\partial t}\int_{VC} \rho_d e \,\mathrm{d}\rlap{-}V + \int_{CS} \rho_s e_s (w_i n_i)\,\mathrm{d}A + \frac{\mathrm{d}}{\mathrm{d}t}(A\sigma) = \left[m_d v_i \frac{\mathrm{d}v_i}{\mathrm{d}t} + \frac{v^2}{2}\frac{\mathrm{d}m_d}{\mathrm{d}t} + \frac{\mathrm{d}(m_d u)}{\mathrm{d}t} + \frac{2\sigma}{r_d}\frac{\mathrm{d}r_d}{\mathrm{d}t}A\right]$$
$$+ \int_{CS} \rho_s u_s w_j n_j \,\mathrm{d}A - \left(\frac{v^2}{2} + \frac{w^{'2}}{2}\right)\frac{\mathrm{d}m_d}{\mathrm{d}t} + v_i \int_{CS} \rho_s w^{'} w n_i \,\mathrm{d}A$$

$$\frac{\partial}{\partial t}\int_{VC}\rho_d e\,\mathrm{d}\mathcal{V} + \int_{CS}\rho_s e_s(w_i n_i)\,\mathrm{d}A + \frac{\mathrm{d}}{\mathrm{d}t}(A\sigma) = m_d v_i\frac{\mathrm{d}v_i}{\mathrm{d}t} - \frac{w^{'2}}{2}\frac{\mathrm{d}m_d}{\mathrm{d}t} + \frac{\mathrm{d}(m_d u)}{\mathrm{d}t}$$
$$+\int_{CS}\rho_s u_s w_j n_j\,\mathrm{d}A + v_i\int_{CS}\rho_s w^{'} w n_i\,\mathrm{d}A + \frac{2\sigma}{r_d}\frac{\mathrm{d}r_d}{\mathrm{d}t}A$$

The heat transfer term $\dot{Q}$ considers both conduction and radiation transfer modes:

$$\dot{Q} = \dot{Q}_{rad} + \dot{Q}_{conv}$$

The radiation term represents the net energy due to absorption and emission. For a droplet with a ”gray” body:

$$\dot{Q}_{rad} = 4\pi r_d^2(\alpha J - \epsilon\sigma T_d^4)$$

The conduction term only takes into account the radial term, which is connected with convection heat transfer:

$$\dot{Q}_{conv} = -\int_{CS} q_{i,conv} n_i\,\mathrm{d}A = 4\pi r_d^2 k\left.\frac{\mathrm{d}T}{\mathrm{d}r}\right|_s = 4\pi r_d^2 h(T_\infty - T_d)$$

$$\dot{Q} = 4\pi r_d^2(\alpha J - \epsilon\sigma T_d^4) + 4\pi r_d^2 h(T_\infty - T_d) \tag{A.9}$$

The work rate term $\dot{W}$ is divided in terms of body and surface forces:

$$\dot{W} = \dot{W}_b + \dot{W}_s$$

For the body forces:

$$\dot{W}_b = -F_{i,b}v_i = -\rho_s g V_d v_i$$

The pressure term for the surface force yields:

$$\dot{W}_p = \int_{CS}(v_i + w_i^{'})n_i P_s\,\mathrm{d}A$$

The work rate associated with shear tension over the control surface is:

$$\dot{W}_s = -\int_{CS}(v_i + w_i^{'})n_j\tau_{ij}\,\mathrm{d}A$$

Summing up these integral generates:

$$\int_{CS} (v_i + w_i^{'})(n_i p_s - n_j \tau_{ij})\,\mathrm{d}A = v_i \int_{CS} (n_i P_s - n_j \tau_{ij})\,\mathrm{d}A + \int_{CS} w_i^{'} n_i P_s\,\mathrm{d}A + \int_{CS} w_i^{'} n_j \tau_{ij}\,\mathrm{d}A$$

The first integral represents the surface forces over the droplet. Based on the droplet momentum conservation $-F_i = v_i \int_{CS} (n_i P_s - n_j \tau_{ji})\,\mathrm{d}A$, we have:

$$v_i \int_{CS} (n_i P_s - n_j \tau_{ij})\,\mathrm{d}A = -v_i F_i$$

The second integral is:

$$\int_{CS} w_i^{'} n_i P_s\,\mathrm{d}A = \int_{CS} P_s \left(w_i + \frac{\mathrm{d}r_d}{\mathrm{d}t} n_i \right) n_i\,\mathrm{d}A = \int_{CS} \rho_s \frac{P_s}{\rho_s} w_i n_i\,\mathrm{d}A + \int_{CS} P_s \frac{\mathrm{d}r_d}{\mathrm{d}t}\,\mathrm{d}A$$

The third integral is zero, since τ_{ji} is on the tangent plane to the control surface:

$$\int_{CS} w_i^{'} \tau_{ij} n_i\,\mathrm{d}A = \int_{CS} w^{'} n_i \tau_{ij} n_j\,\mathrm{d}A = 0$$

Summing up all these terms related to the work rate generates:

$$\int_{CS} (v_i + w_i^{'})(n_i P_s - n_j \tau_{ij})\,\mathrm{d}A = -v_i F_i + \int_{CS} \rho_s \frac{P_s}{\rho_s} w_i n_i\,\mathrm{d}A + \int_{CS} P_s \frac{\mathrm{d}r_d}{\mathrm{d}t}\,\mathrm{d}A$$

$$\dot{W} = -F_{i,b} v_i - v_i F_i + \int_{CS} \rho_s \frac{P_s}{\rho_s} w_i n_i\,\mathrm{d}A + \int_{CS} P_s \frac{\mathrm{d}r_d}{\mathrm{d}t}\,\mathrm{d}A$$

Grouping all the terms in the energy conservation equation yields:

$$\left[4\pi r_d^2(\alpha J - \epsilon \sigma T_d^4) + 4\pi r_d^2 h (T_\infty - T_d)\right] - \left[-F_{i,b} v_i - v_i F_i + \int_{CS} \rho_s \frac{p_s}{\rho_s} w_i n_i\,\mathrm{d}A + \int_{CS} p_s \frac{\mathrm{d}r_d}{\mathrm{d}t}\,\mathrm{d}A \right] =$$

$$m_d v_i \frac{\mathrm{d}v_i}{\mathrm{d}t} - \frac{w^{'2}}{2} \frac{\mathrm{d}m_d}{\mathrm{d}t} + \frac{\mathrm{d}(m_d u)}{\mathrm{d}t} + \int_{CS} \rho_s u_s w_j n_j\,\mathrm{d}A + v_i \int_{CS} \rho_s w^{'} w n_i\,\mathrm{d}A + \frac{2\sigma}{r_d} \frac{\mathrm{d}r_d}{\mathrm{d}t} A_d$$

Reorganizing:

$$\frac{\mathrm{d}(m_d u)}{\mathrm{d}t} + v_i \left(m_d \frac{\mathrm{d}v_i}{\mathrm{d}t} + \int_{CS} \rho_s w^{'} w n_i\,\mathrm{d}A - F_{i,b} - F_i \right)$$

$$- \frac{w^{'2}}{2} \frac{\mathrm{d}m_d}{\mathrm{d}t} + \frac{2\sigma}{r_d} \frac{\mathrm{d}r_d}{\mathrm{d}t} A_d + \int_{CS} \left(u_s + \rho_s \frac{P_s}{\rho_s} \right) \rho_s w_i n_i\,\mathrm{d}A$$

$$= \left[4\pi r_d^2(\alpha J - \epsilon\sigma T_d^4) + 4\pi r_d^2 h(T_\infty - T_d)\right] - \int_{CS} P_s \frac{\mathrm{d}r_d}{\mathrm{d}t}\,\mathrm{d}A$$

Recognizing the momentum conservation equation (second term) present in this equation:

$$\frac{\mathrm{d}(m_d u)}{\mathrm{d}t} - \frac{w^{'2}}{2}\frac{\mathrm{d}m_d}{\mathrm{d}t} + \frac{2\sigma}{r_d}\frac{\mathrm{d}r_d}{\mathrm{d}t}A_d + \int_{CS}\left(u_s + \rho_s\frac{P_s}{\rho_s}\right)\rho_s w_i n_i\,\mathrm{d}A$$
$$= \left[4\pi r_d^2(\alpha J - \epsilon\sigma T_d^4) + 4\pi r_d^2 h(T_\infty - T_d)\right] - \int_{CS} P_s \frac{\mathrm{d}r_d}{\mathrm{d}t}\,\mathrm{d}A$$

Assuming now that the evaporation associated with the radius reduction rate $\frac{\mathrm{d}r_d}{\mathrm{d}t}$ and pressure P_s are uniform on the control surface:

$$\frac{\mathrm{d}(m_d u)}{\mathrm{d}t} - \frac{w^{'2}}{2}\frac{\mathrm{d}m_d}{\mathrm{d}t} + \int_{CS} h_s\rho_s w_i n_i\,\mathrm{d}A$$
$$= \left[4\pi r_d^2(\alpha J - \epsilon\sigma T_d^4) + 4\pi r_d^2 h(T_\infty - T_d)\right] - \frac{\mathrm{d}r_d}{\mathrm{d}t}A_d\left(\bar{p_s} + \frac{2\sigma}{r_d}\right)$$

Calling $\left(\bar{P}_s + \frac{2\sigma}{r_d}\right) = P_d$ to equal internal and external pressures:

$$m_d\frac{\mathrm{d}u}{\mathrm{d}t} + u\frac{\mathrm{d}m_d}{\mathrm{d}t} - \frac{w^{'2}}{2}\frac{\mathrm{d}m_d}{\mathrm{d}t} + \int_{CS} h_s\rho_s w_i n_i\,\mathrm{d}A$$
$$= \left[4\pi r_d^2(\alpha J - \epsilon\sigma T_d^4) + 4\pi r_d^2 h(T_\infty - T_d)\right] - \rho_d\frac{P_d}{\rho_d}\frac{\mathrm{d}r_d}{\mathrm{d}t}A_d$$

Realizing that $\rho_d\frac{\mathrm{d}r_d}{\mathrm{d}t}A_d = \frac{\mathrm{d}m_d}{\mathrm{d}t}$, so putting together similar terms yields:

$$m_d\frac{\mathrm{d}u_d}{\mathrm{d}t} = \left[4\pi r_d^2(\alpha J - \epsilon\sigma T_d^4) + 4\pi r_d^2 h(T_\infty - T_d)\right] + \left[h_s - \left(u_d + \frac{P_d}{\rho_d}\right) + \frac{w^{'2}}{2}\right]\frac{\mathrm{d}m_d}{\mathrm{d}t}$$

Finally:

$$m_d\frac{\mathrm{d}u_d}{\mathrm{d}t} = 4\pi r_d^2(\alpha J - \epsilon\sigma T_d^4) + 4\pi r_d^2 h(T_\infty - T_d) + \left(h_s - h_d + \frac{w^{'2}}{2}\right)\frac{\mathrm{d}m_d}{\mathrm{d}t}$$

$$m_d c_{v,d}\frac{\mathrm{d}T_d}{\mathrm{d}t} = 4\pi r_d^2(\alpha J - \epsilon\sigma T_d^4) + 4\pi r_d^2 h(T_\infty - T_d) - \dot{m}\left(\Delta h_v + \frac{w^{'2}}{2}\right)$$

$$\frac{\mathrm{d}T_d}{\mathrm{d}t} = \frac{4\pi r_d^2(\alpha J - \epsilon\sigma T_d^4) + 4\pi r_d^2 h(T_\infty - T_d) - \dot{m}\left(\Delta h_v + \frac{w^{'2}}{2}\right)}{m_d c_{v,d}}$$

Neglecting the relative kinetic energy between the droplet velocity and the mass content that leaves the control volume, we obtain the final version of the droplet energy conservation:

$$\frac{\mathrm{d}T_d}{\mathrm{d}t} = \frac{4\pi r_d^2(\alpha J - \epsilon\sigma T_d^4) + 4\pi r_d^2 h(T_\infty - T_d) - \dot{m}\Delta h_v}{m_d c_{v,d}}, \tag{A.10}$$

where $c_{v,d} \equiv c_d$, since the specific heat transfer is approximately equal for the liquid state ($c_{v,d} \approxeq c_{p,d} \approxeq c_d$).

A.5 Entropy balance - droplet

The droplet entropy equation is deduced here, although it is not used in the model, since based on the assumptions considered in this deduction, it is linearly dependent with the energy equation. Thus, the droplet entropy expression implies in an internally reversible process.

The Reynolds transport theorem for the property entropy stays that:

$$\frac{\partial}{\partial t}\int_{droplet} \rho s d\forall + \int_{SC} \rho s(w_i n_i) dA = \int_{SC} \left(\frac{k\nabla T}{T}\right) \cdot \vec{n} dA + \int_{droplet} \left(\frac{q'''}{T}\right) dA + \dot{\sigma_d}$$

The transient term indicates how entropy varies inside the control volume, thus:

$$\frac{\partial}{\partial t}\int_{droplet} \rho s d\forall = \rho\frac{\mathrm{d}(m_d s)}{\mathrm{d}t} = s\frac{\mathrm{d}m_d}{\mathrm{d}t} + m_d \left.\frac{\mathrm{d}s}{\mathrm{d}t}\right|_d = -\dot{m}s_{l,s} + m_d \left.\frac{\mathrm{d}s}{\mathrm{d}t}\right|_d$$

where the entropy variation inside the CV is (incompressible fluid):

$$\left.\frac{ds}{dt}\right|_d = \frac{c_{p,d}}{T_d}\frac{dT_d}{dt} \tag{A.11}$$

The mass flow integral accounts for the entropy passing through the control surface:

$$\int_{SC} \rho s(w_i n_i) dA = \dot{m}s_{v,s}$$

The third term takes into account the entropy transfer due to heat transfer (only convection assumed here):

$$\int_{SC} \left(\frac{k\nabla T}{T}\right) \cdot \vec{n} dA = 4\pi r_d^2 \frac{k}{T_D} \left.\frac{\mathrm{d}T}{\mathrm{d}r}\right|_s = 4\pi r_d^2 h\frac{(T_\infty - T_d)}{T_d}$$

Grouping all terms leads to:

$$-\dot{m}s_{l,s} + m_d \left.\frac{\mathrm{d}s}{\mathrm{d}t}\right|_d + \dot{m}s_{v,s} = 4\pi r_d^2 h \frac{(T_\infty - T_d)}{T_d} + \dot{\sigma_d}$$

Therefore, the entropy generation on the droplet control volume is:

$$\dot{\sigma_d} = m_d \left.\frac{\mathrm{d}s}{\mathrm{d}t}\right|_d + \dot{m}\Delta s_v - 4\pi r_d^2 h \frac{(T_\infty - T_d)}{T_d} \tag{A.12}$$

This equation is linearly dependent with Eq. A.10 as can be verified by multiplying Eq. A.10 for $(1/T_d)$ and noticing that $\Delta s_v = \Delta h_v / T_d$ for liquid-gas phase change, and $c_{v,d} \approxeq c_{p,d}$, leading to $\dot{sigma}_{droplet} = 0$.

APPENDIX B – DEVELOPMENT OF A MULTI-ZONE DIRECT INJECTION SPARK-IGNITION ENGINE MODEL

The conservation equations (i.e. mass, momentum, energy) and the entropy equation were applied in the Lagrangian form to each droplet present in the system. These equations are valid to all droplets included in the same spray layer, therefore reducing massively the number of ODEs to be solved. Meanwhile, with exception of the momentum, the same conservation variables are applied to the unburned and burned gases (closed phase), but in the Eulerian form. On the other hand, the open-phase considers only a single zone for the gases.

The fuel droplets are assumed to be injected either in the unburned gas zone (closed-phase) or in the gas-phase (open-phase), therefore they do not interact with the burned zone. Hence, the differential equation deductions which are presented in this appendix are the following:

- Mass conservation - Unburned zone (UBZ - closed-phase);
- Species conservation - Unburned zone (UBZ - closed-phase);
- Energy conservation - Unburned zone (UBZ - closed-phase);
- Entropy balance - Unburned zone (UBZ - closed-phase);
- Exergy balance - Unburned zone (UBZ - closed-phase);
- Mass conservation - Burned zone (BZ - closed-phase);
- Species conservation - Burned zone (BZ - closed-phase);
- Energy conservation - Burned zone (BZ - closed-phase);
- Entropy balance - Burned zone (BZ - closed-phase);
- Exergy balance - Burned zone (BZ - closed-phase);
- Mass conservation - Gas (open-phase);
- Species conservation - Gas (open-phase);
- Energy conservation - Gas (open-phase);

- Entropy balance - Gas (open-phase);
- Exergy balance - Gas (open-phase);

B.1 Closed phase

The closed phase involves the engine cycle period between the inlet valve closure (IVC) until the exhaust valve opening (EVO). During this period, there are the processes of compression, fuel injection and evaporation, combustion and expansion. All these process modeling are presented in the subsequent sections.

B.1.1 Mass balance - unburned zone

The Reynolds Transport Theorem (RTT) is applied for mass conservation in the unburned zone control volume (CV):

$$\frac{\partial}{\partial t}\int_{UBZ}\rho_{UBZ}\,\mathrm{d}\forall+\int_{CS}\rho_s(w_i n_i)\,\mathrm{d}A=0$$

There are inlet mass flows from the droplets evaporation to the unburned zone CV and outlet flows for the burned zone CV. We can detail each one of these terms in a separate form and then we regroup them to close the balance. Thus, detailing first the transient term, which is assumed as homogeneous, we have:

$$\frac{\partial}{\partial t}\int_{UBZ}\rho_{UBZ}\,\mathrm{d}\forall=\frac{\mathrm{d}(\rho_{UBZ}\forall_{BZ})}{\mathrm{d}t}=\frac{\mathrm{d}m_{UBZ}}{\mathrm{d}t}$$

To the inlet terms, it is necessary to take into account the sum of evaporation rates from each droplet interacting with UBZ and to encompass them by size group. Thus, we can refer to this term as:

$$\int_{CS,inlet}\rho_s(w_i n_i)\,\mathrm{d}A=-\sum_{k=1}^{N_{classes}}N_{droplet,k}\dot{m}_{d,k}$$

where $N_{droplet,k}$ represents the number of droplets of the kth droplet class. The outlet term represents the mass transfer from UBZ to BZ through a combustion process. Therefore, this term is presented as:

$$\int_{CS,outlet}\rho_s(w_i n_i)\,\mathrm{d}A=\dot{m}_{comb}$$

Regrouping the terms, we obtain the unburned zone mass balance:

$$\frac{\mathrm{d}m_{UBZ}}{\mathrm{d}t} = \sum_{k=1}^{N_{classes}} N_{droplet,k}\dot{m}_{d,k} - \dot{m}_{comb} \tag{B.1}$$

B.1.2 Species balance - unburned zone

The species conservation for the unburned zone follows the same initial steps as the mass conservation. The main differences lie on the inlet species, which are only related to the fuel components of each droplet evaporating, while the outlets are related to the combustion process, therefore it depends on the approach assumed for this phenomenon modeling. The general species conservation for UBZ has the following form:

$$\frac{\partial}{\partial t}\int_{UBZ} \rho y_j \,\mathrm{d}\,\forall + \int_{CS} \rho y_j (w_i n_i)\,\mathrm{d}A = -\int_{CS} \vec{J}_j n_i \,\mathrm{d}A + \int_{UBZ} \dot{R}_j M_j \,\mathrm{d}\,\forall$$

where the diffusive term $\int_{CS} \vec{J}_j n_i \,\mathrm{d}A$ and the chemical reaction term $\int_{UBZ} \dot{R}_j M_j \,\mathrm{d}\,\forall$ are neglected due to the hypotheses of homogeneity and absence of chemical reactions in UBZ, respectively. The transient term is, therefore:

$$\frac{\partial}{\partial t}\int_{UBZ} \rho y_j \,\mathrm{d}\,\forall = \frac{\mathrm{d}m_{UBZ,j}}{\mathrm{d}t}$$

The inlet term is:

$$\int_{CS,inlet} \rho_s y_j (w_i n_i)\,\mathrm{d}A = -\sum_{k=1}^{N_{classes}} N_{droplet,k} y_{j,k,evap}\dot{m}_{d,k}$$

where $y_{j,k,s}$ is the vapor mass fraction of the jth fuel component on the droplet surface of the kth droplet class. Lastly, the outlet is:

$$\int_{CS,outlet} \rho_s y_j (w_i n_i)\,\mathrm{d}A = y_{j,UBZ}\dot{m}_{comb}$$

where $y_{j,UBZ}$ is the mass fraction of the jth component based on the combustion chemical reaction. Therefore, the final form of the species conservation is:

$$\frac{\mathrm{d}m_{UBZ,j}}{\mathrm{d}t} = \sum_{k=1}^{N_{classes}} N_{droplet,k} y_{j,k,evap}\dot{m}_{d,k} - y_{j,UBZ}\dot{m}_{comb} \tag{B.2}$$

B.1.3 Energy balance - unburned zone

The RTT for the energy conservation has the following form:

$$\frac{\partial}{\partial t}\int_{UBZ}\rho\left(\frac{V_I^2}{2}+gz+u\right)\mathrm{d}\forall+\int_{CS}\rho\left(\frac{V_I^2}{2}+gz+u+\frac{p}{\rho}\right)(\vec{V_r}\cdot\vec{n})\,\mathrm{d}A=\int_{CS}k(\nabla T\cdot\vec{n})\,\mathrm{d}A$$

$$-\int_{CS}p\left[\left(\vec{V_b}+\frac{\mathrm{d}\vec{R}}{\mathrm{d}t}+\vec{x}\times\vec{r}\right)\vec{n}\right]\mathrm{d}A+\int_{CS}(\tau\cdot\vec{n})\cdot\vec{V_I}\,\mathrm{d}A-\dot{W}_{comp}+\int_{UBZ}q^{'''}\,\mathrm{d}\forall$$

In the unburned zone, it occurs the following energetic interactions: enthalpy inlet of the vapor fuel evaporated from the droplets, enthalpy outlet from the combustion process (transfer to the burned zone), work due to the droplets volume variation, work due to the compression/expansion caused by the engine volume variation, heat transfer from UBZ to the droplets and from the engine cylinder walls to the UBZ. The transient term is initially:

$$\frac{\partial}{\partial t}\int_{UBZ}\rho_{UBZ}u\,\mathrm{d}\forall=\frac{\mathrm{d}(\rho_{UBZ}u\forall_{UBZ})}{\mathrm{d}t}=\frac{\mathrm{d}U_{UBZ}}{\mathrm{d}t}$$

The inlet enthalpy in the UBZ is related to the mass flow rates from the droplets evaporation:

$$\int_{CS,inlet}\rho_{UBZ}\left(\frac{V_I^2}{2}+u+\frac{P}{\rho}\right)(\vec{V_r}\cdot\vec{n})\,\mathrm{d}A=-\sum_{k=1}^{N_{classes}}N_{droplet,k}\dot{m}_{d,k}h_{evap,k}$$

For the outlet enthalpy from the UBZ, we have the air-fuel mixture which is burned and transported to the BZ:

$$\int_{CS,outlet}\rho_{UBZ}\left(\frac{V_I^2}{2}+u+\frac{P}{\rho}\right)(\vec{V_r}\cdot\vec{n})\,\mathrm{d}A=\dot{m}_{comb}h_{UBZ}$$

The terms related to work of expansion/contraction are presented below:

$$-\int_{CS}P\vec{V_b}\cdot\vec{n}\,\mathrm{d}A=-\dot{W}_{spray}-P\frac{\mathrm{d}\forall_{BZ}}{\mathrm{d}t}$$

Where $\dot{W}_{spray}=P\sum_{k=1}^{N_{classes}}N_{droplet,k}\left(-\frac{\mathrm{d}V_{d,k}}{\mathrm{d}t}\right)$.

Now we convert the expansion work related to the gas control volume in order to change the energy conservation from the internal energy form to the enthalpy one, so:

$$
\begin{aligned}
-\int_{CS} P\vec{V}_b \cdot \vec{n}\,\mathrm{d}A &= -\dot{W}_{spray} - P\frac{\mathrm{d}\mathcal{V}_{BZ}}{\mathrm{d}t} + \frac{\mathrm{d}(P\mathcal{V}_{BZ})}{\mathrm{d}t} - \frac{\mathrm{d}(P\mathcal{V}_{BZ})}{\mathrm{d}t} \\
&= -\dot{W}_{spray} + \mathcal{V}_{BZ}\frac{\mathrm{d}P}{\mathrm{d}t} - \frac{\mathrm{d}(P\mathcal{V}_{BZ})}{\mathrm{d}t}
\end{aligned}
$$

By transferring the $-\frac{\mathrm{d}(P\mathcal{V}_{BZ})}{\mathrm{d}t}$ to the transient term, we obtain the enthalpy form:

$$
\frac{\partial}{\partial t}\int_{UBZ} \rho_{UBZ} h\,\mathrm{d}\mathcal{V} = \frac{\mathrm{d}(\rho_{UBZ} h\mathcal{V}_{UBZ})}{\mathrm{d}t} = \frac{\mathrm{d}H_{UBZ}}{\mathrm{d}t}
$$

In this model, the transient term takes into account that both temperature and mass are homogeneous in space and variable in time, thus:

$$
\frac{\partial}{\partial t}\int_{UBZ} \rho_{UBZ} h\,\mathrm{d}\mathcal{V} = m_{UBZ}\frac{\mathrm{d}h_{UBZ}}{\mathrm{d}t} + h_{UBZ}\frac{\mathrm{d}m_{UBZ}}{\mathrm{d}t}
$$

Opening the term $\frac{\mathrm{d}h_{UBZ}}{\mathrm{d}t}$:

$$
\frac{\mathrm{d}h_{UBZ}}{\mathrm{d}t} = \frac{\mathrm{d}\left(\frac{H_{UBZ}}{m_{UBZ}}\right)}{\mathrm{d}t} = \frac{\mathrm{d}\left(\frac{\sum_{j=1}^{N_{species}} m_{j,UBZ} h_{j,UBZ}}{m_{UBZ}}\right)}{\mathrm{d}t} = \frac{\mathrm{d}(\sum_{j=1}^{N_{species}} y_{j,UBZ} h_{j,UBZ})}{\mathrm{d}t} =
$$

$$
\sum_{j=1}^{N_{species}}\left(y_{j,UBZ}\frac{\mathrm{d}h_{j,UBZ}}{\mathrm{d}t}\right) + \sum_{j=1}^{N_{species}}\left(h_{j,UBZ}\frac{\mathrm{d}y_{j,UBZ}}{\mathrm{d}t}\right)
$$

The gases are considered ideal in this model, therefore:

$$
\frac{\mathrm{d}h_{UBZ}}{\mathrm{d}t} = \sum_{j=1}^{N_{species}}\left(y_{j,UBZ} c_{p,j,UBZ}\frac{\mathrm{d}T_{UBZ}}{\mathrm{d}t}\right) + \sum_{j=1}^{N_{species}}\left(h_{j,UBZ}\frac{\mathrm{d}y_{j,UBZ}}{\mathrm{d}t}\right)
$$

$$
\frac{\mathrm{d}h_{UBZ}}{\mathrm{d}t} = c_{p,UBZ}\frac{\mathrm{d}T_{UBZ}}{\mathrm{d}t} + \sum_{j=1}^{N_{species}}\left(h_{j,UBZ}\frac{\mathrm{d}y_{j,UBZ}}{\mathrm{d}t}\right)
$$

Substituting this expression on the transient term:

$$
\frac{\partial}{\partial t}\int_{UBZ} \rho_{UBZ} h\,\mathrm{d}\mathcal{V} = m_{UBZ} c_{p,UBZ}\frac{\mathrm{d}T_{UBZ}}{\mathrm{d}t} + m_{UBZ}\sum_{j=1}^{N_{species}}\left(h_{j,UBZ}\frac{\mathrm{d}y_{j,UBZ}}{\mathrm{d}t}\right) + \frac{\mathrm{d}m_{UBZ}}{\mathrm{d}t} h_{UBZ}
$$

The heat transfer terms take into account the thermal convection which causes the droplets evaporation and the thermal convection associated with the interaction between the cylinder walls and the UBZ:

$$\int_{CS} k(\nabla T \cdot \vec{n})\, \mathrm{d}A = \dot{Q}_{spray} + \dot{Q}_{UBZ,walls}$$

where $\dot{Q}_{spray} = -\sum_{k=1}^{N_{classes}} N_{droplet,k}\dot{Q}_{conv,k}$ and the negative sign is required since the known values of $\dot{Q}_{conv,k}$ were obtained for the droplet control volumes, not for the unburned gases. After grouping all these terms, we have:

$$m_{UBZ}c_{p,UBZ}\frac{\mathrm{d}T_{UBZ}}{\mathrm{d}t} + m_{UBZ}\sum_{j=1}^{N_{species}}\left(h_{j,UBZ}\frac{\mathrm{d}y_{j,UBZ}}{\mathrm{d}t}\right) + \frac{\mathrm{d}m_{UBZ}}{\mathrm{d}t}h_{UBZ} =$$
$$\sum_{k=1}^{N_{classes}} N_{droplet,k}\dot{m}_{d,k}h_{evap,k} - \dot{m}_{comb}h_{UBZ} - \dot{W}_{spray} +$$
$$\cancel{V}_{BZ}\frac{\mathrm{d}P}{\mathrm{d}t} + \dot{Q}_{spray} + \dot{Q}_{UBZ,walls}$$

Applying the mass conservation to substitute the term $\frac{\mathrm{d}m_{UBZ}}{\mathrm{d}t}$ provides:

$$m_{UBZ}c_{p,UBZ}\frac{\mathrm{d}T_{UBZ}}{\mathrm{d}t} + m_{UBZ}\sum_{j=1}^{N_{species}}\left(h_{j,UBZ}\frac{\mathrm{d}y_{j,UBZ}}{\mathrm{d}t}\right) + \left(\sum_{k=1}^{N_{classes}} N_{droplet,k}\dot{m}_{d,k} - \dot{m}_{comb}\right)h_{UBZ} =$$
$$\sum_{k=1}^{N_{classes}} N_{droplet,k}\dot{m}_{d,k}h_{evap,k} - \dot{m}_{comb}h_{UBZ} - \dot{W}_{spray} +$$
$$\cancel{V}_{BZ}\frac{\mathrm{d}P}{\mathrm{d}t} + \dot{Q}_{spray} + \dot{Q}_{UBZ,walls}$$

$$m_{UBZ}c_{p,UBZ}\frac{\mathrm{d}T_{UBZ}}{\mathrm{d}t} = \sum_{k=1}^{N_{classes}} N_{droplet,k}\dot{m}_{d,k}(h_{evap,k} - h_{UBZ}) - m_{UBZ}\sum_{j=1}^{N_{species}}\left(h_{j,UBZ}\frac{\mathrm{d}y_{j,UBZ}}{\mathrm{d}t}\right)$$
$$- \dot{W}_{spray} + \cancel{V}_{BZ}\frac{\mathrm{d}P}{\mathrm{d}t} + \dot{Q}_{spray} + \dot{Q}_{UBZ,walls}$$

Finally we obtain the unburned zone temperature differential equation:

$$\frac{\mathrm{d}T_{UBZ}}{\mathrm{d}t} = \frac{1}{m_{UBZ}c_{p,UBZ}}\left\{\sum_{k=1}^{N_{classes}} N_{droplet,k}\dot{m}_{d,k}(h_{evap,k} - h_{UBZ}) - m_{UBZ}\sum_{j=1}^{N_{species}}\left(h_{j,UBZ}\frac{\mathrm{d}y_{j,UBZ}}{\mathrm{d}t}\right)\right.$$
$$\left. + \dot{Q}_{spray} + \dot{Q}_{UBZ,walls} - \dot{W}_{spray} + \cancel{V}_{BZ}\frac{\mathrm{d}P}{\mathrm{d}t}\right\} \tag{B.3}$$

Before ignition, the model takes into account the internal energy form instead of the enthalpy one, in order to simplify the energy balance in terms of work rate (i.e., $-P\,\mathrm{d}V_u/\,\mathrm{d}t$).

Hence, the transient term takes into account that both temperature and mass are homogeneous in space and variable in time, thus:

$$\frac{\partial}{\partial t}\int_{UBZ}\rho_{UBZ}u\,\mathrm{d}\forall = m_{UBZ}\frac{\mathrm{d}u_{UBZ}}{\mathrm{d}t} + u_{UBZ}\frac{\mathrm{d}m_{UBZ}}{\mathrm{d}t}$$

Opening the term $\frac{\mathrm{d}u_{UBZ}}{\mathrm{d}t}$:

$$\frac{\mathrm{d}u_{UBZ}}{\mathrm{d}t} = \frac{\mathrm{d}\left(\frac{U_{UBZ}}{m_{UBZ}}\right)}{\mathrm{d}t} = \frac{\mathrm{d}\left(\frac{\sum_{j=1}^{N_{species}} m_{j,UBZ}u_{j,UBZ}}{m_{UBZ}}\right)}{\mathrm{d}t} = \frac{\mathrm{d}(\sum_{j=1}^{N_{species}} y_{j,UBZ}u_{j,UBZ})}{\mathrm{d}t} =$$

$$\sum_{j=1}^{N_{species}}\left(y_{j,UBZ}\frac{\mathrm{d}u_{j,UBZ}}{\mathrm{d}t}\right) + \sum_{j=1}^{N_{species}}\left(u_{j,UBZ}\frac{\mathrm{d}y_{j,UBZ}}{\mathrm{d}t}\right)$$

The gases are considered ideal in this model, therefore:

$$\frac{\mathrm{d}u_{UBZ}}{\mathrm{d}t} = \sum_{j=1}^{N_{species}}\left(y_{j,UBZ}c_{v,j,UBZ}\frac{\mathrm{d}T_{UBZ}}{\mathrm{d}t}\right) + \sum_{j=1}^{N_{species}}\left(u_{j,UBZ}\frac{\mathrm{d}y_{j,UBZ}}{\mathrm{d}t}\right)$$

$$\frac{\mathrm{d}u_{UBZ}}{\mathrm{d}t} = c_{v,UBZ}\frac{\mathrm{d}T_{UBZ}}{\mathrm{d}t} + \sum_{j=1}^{N_{species}}\left(u_{j,UBZ}\frac{\mathrm{d}y_{j,UBZ}}{\mathrm{d}t}\right)$$

Substituting this expression on the transient term:

$$\frac{\partial}{\partial t}\int_{UBZ}\rho_{UBZ}u\,\mathrm{d}\forall = m_{UBZ}c_{v,UBZ}\frac{\mathrm{d}T_{UBZ}}{\mathrm{d}t} + m_{UBZ}\sum_{j=1}^{N_{species}}\left(u_{j,UBZ}\frac{\mathrm{d}y_{j,UBZ}}{\mathrm{d}t}\right) + \frac{\mathrm{d}m_{UBZ}}{\mathrm{d}t}u_{UBZ}$$

The heat transfer terms take into account the thermal convection which causes the droplets evaporation and the thermal convection associated with the interaction between the cylinder walls and the UBZ:

$$\int_{CS} k(\nabla T\cdot\vec{n})\,\mathrm{d}A = \dot{Q}_{spray} + \dot{Q}_{UBZ,walls}$$

where $\dot{Q}_{spray} = -\sum_{k=1}^{N_{classes}} N_{droplet,k}\dot{Q}_{conv,k}$ and the negative sign is required since the known values of $\dot{Q}_{conv,k}$ were obtained for the droplet control volumes, not for the unburned gases. After grouping all these terms, we have:

$$m_{UBZ}c_{v,UBZ}\frac{\mathrm{d}T_{UBZ}}{\mathrm{d}t}+m_{UBZ}\sum_{j=1}^{N_{species}}\left(u_{j,UBZ}\frac{\mathrm{d}y_{j,UBZ}}{\mathrm{d}t}\right)+\frac{\mathrm{d}m_{UBZ}}{\mathrm{d}t}u_{UBZ}=$$
$$\sum_{k=1}^{N_{classes}}N_{droplet,k}\dot{m}_{d,k}h_{evap,k}-\dot{m}_{comb}h_{UBZ}-\dot{W}_{spray}-$$
$$P\frac{\mathrm{d}\,{\rlap{-}V}_{BZ}}{\mathrm{d}t}+\dot{Q}_{spray}+\dot{Q}_{UBZ,walls}$$

Applying the mass conservation to substitute the term $\frac{\mathrm{d}m_{UBZ}}{\mathrm{d}t}$ provides:

$$m_{UBZ}c_{v,UBZ}\frac{\mathrm{d}T_{UBZ}}{\mathrm{d}t}+m_{UBZ}\sum_{j=1}^{N_{species}}\left(u_{j,UBZ}\frac{\mathrm{d}y_{j,UBZ}}{\mathrm{d}t}\right)+\left(\sum_{k=1}^{N_{classes}}N_{droplet,k}\dot{m}_{d,k}-\dot{m}_{comb}\right)u_{UBZ}=$$
$$\sum_{k=1}^{N_{classes}}N_{droplet,k}\dot{m}_{d,k}h_{evap,k}-\dot{m}_{comb}h_{UBZ}-\dot{W}_{spray}-$$
$$P\frac{\mathrm{d}\,{\rlap{-}V}_{BZ}}{\mathrm{d}t}+\dot{Q}_{spray}+\dot{Q}_{UBZ,walls}$$

$$m_{UBZ}c_{v,UBZ}\frac{\mathrm{d}T_{UBZ}}{\mathrm{d}t}=\sum_{k=1}^{N_{classes}}N_{droplet,k}\dot{m}_{d,k}(h_{evap,k}-u_{UBZ})-m_{UBZ}\sum_{j=1}^{N_{species}}\left(u_{j,UBZ}\frac{\mathrm{d}y_{j,UBZ}}{\mathrm{d}t}\right)$$
$$-\dot{W}_{spray}-P\frac{\mathrm{d}\,{\rlap{-}V}_{BZ}}{\mathrm{d}t}+\dot{Q}_{spray}+\dot{Q}_{UBZ,walls}$$
$$+\dot{m}_{comb}(h_{UBZ}-u_{UBZ})$$

Finally we obtain the unburned zone temperature differential equation:

$$\frac{\mathrm{d}T_{UBZ}}{\mathrm{d}t}=\frac{1}{m_{UBZ}c_{v,UBZ}}\left\{\sum_{k=1}^{N_{classes}}N_{droplet,k}\dot{m}_{d,k}(h_{evap,k}-u_{UBZ})-m_{UBZ}\sum_{j=1}^{N_{species}}\left(u_{j,UBZ}\frac{\mathrm{d}y_{j,UBZ}}{\mathrm{d}t}\right)\right.$$
$$\left.-\dot{m}_{comb}(h_{UBZ}-u_{UBZ})+\dot{Q}_{spray}+\dot{Q}_{UBZ,walls}-\dot{W}_{spray}-P\frac{\mathrm{d}\,{\rlap{-}V}_{BZ}}{\mathrm{d}t}\right\} \quad \text{(B.4)}$$

B.1.4 Entropy balance - unburned zone

The RTT for entropy stays that:

$$\frac{\partial}{\partial t}\int_{VC}\rho s d{\rlap{-}V}+\int_{SC}\rho s(w_i n_i)dA=\int_{SC}\left(\frac{k\nabla T}{T}\right)\cdot\vec{n}dA+\int_{VC}\left(\frac{q^{'''}}{T}\right)dA+\dot{\sigma_{VC}}$$

The transient term accounts for entropy variation on the unburned gases, as showed by the following equation:

$$\frac{\partial}{\partial t}\int_{VC} \rho s d\forall = s_{UBZ}\frac{\mathrm{d}(m_{UBZ})}{\mathrm{d}t} + m_{UBZ}\frac{\mathrm{d}s_{UBZ}}{\mathrm{d}t}$$

The second term on RTT represents the entropy flow terms:

$$\int_{SC} \rho s(w_i n_i)dA = -\sum_{k=1}^{N_{classes}} N_{droplet,k}\dot{m}_{d,k}s_{evap,k} + \dot{m}_{comb}s_{UBZ}$$

Finally, the entropy transfer associated with heat transfer accounts for the convection between unburned gases and the droplet classes and also for the interaction between the gases and cylinder walls:

$$\int_{SC}\left(\frac{k\nabla T}{T}\right)\cdot \vec{n}dA = \frac{\dot{Q}_{spray}}{T_{d,avg}} + \frac{\dot{Q}_{UBZ,walls}}{T_{wall}}$$

where $\frac{\dot{Q}_{spray}}{T_{d,avg}} = -\sum_{k=1}^{N_{classes}} N_{droplet,k}\frac{\dot{Q}_{conv,k}}{T_{d,k}}$. Meanwhile, $\dot{\sigma}_{UBZ}$ is the entropy generation on the control volume. Then, grouping all terms leads to:

$$\frac{\mathrm{d}m_{UBZ}}{\mathrm{d}t}s_{UBZ} + m_{UBZ}\frac{\mathrm{d}s_{UBZ}}{\mathrm{d}t} - \sum_{k=1}^{N_{classes}} N_{droplet,k}\dot{m}_{d,k}s_{evap,k} + \dot{m}_{comb}s_{UBZ} = \frac{\dot{Q}_{spray}}{T_{d,avg}} + \frac{\dot{Q}_{UBZ,walls}}{T_{wall}} + \dot{\sigma}_{UBZ}$$

Opening $\frac{\mathrm{d}m_{UBZ}}{\mathrm{d}t}$ leads to:

$$\left(\sum_{k=1}^{N_{classes}} N_{droplet,k}\dot{m}_{d,k} - \dot{m}_{comb}\right)s_{UBZ} + m_{UBZ}\frac{\mathrm{d}s_{UBZ}}{\mathrm{d}t} - \sum_{k=1}^{N_{classes}} N_{droplet,k}\dot{m}_{d,k}s_{evap,k} + \dot{m}_{comb}s_{UBZ} = \frac{\dot{Q}_{spray}}{T_{d,avg}} + \frac{\dot{Q}_{UBZ,walls}}{T_{wall}} + \dot{\sigma}_{UBZ}$$

The final expression for the entropy generation on the unburned zone is:

$$\dot{\sigma}_{UBZ} = \sum_{k=1}^{N_{classes}} N_{droplet,k}\dot{m}_{d,k}(s_{UBZ} - s_{evap,k}) + m_{UBZ}\frac{\mathrm{d}s_{UBZ}}{\mathrm{d}t} - \frac{\dot{Q}_{spray}}{T_{d,avg}} - \frac{\dot{Q}_{UBZ,walls}}{T_{wall}} \tag{B.5}$$

B.1.5 Exergy balance - unburned zone

The exergy balance is obtained by combining the expressions for the first and second laws of thermodynamics and it is written as it follows:

$$\frac{\mathrm{d}B_{UBZ}}{\mathrm{d}t} - \sum_i \dot{m}_i b_{fi} + \sum_e \dot{m}_e b_{fe} = \sum_j \left(1 - \frac{T_0}{T_j}\right)\dot{Q}_j - \left(\dot{W} - P_0\frac{\mathrm{d}V}{\mathrm{d}t}\right) - \dot{B}_{d,UBZ}$$

The transient term accounts for entropy variation on the unburned gases, as showed by the following equation:

$$\frac{\mathrm{d}B_{UBZ}}{\mathrm{d}t} = b_{UBZ}\frac{\mathrm{d}m_{UBZ}}{\mathrm{d}t} + m_{UBZ}\frac{\mathrm{d}b_{UBZ}}{\mathrm{d}t}$$

The second term on RTT represents the exergy flow terms:

$$-\sum_i \dot{m}_i b_{fi} + \sum_e \dot{m}_e b_{fe} = -\sum_{k=1}^{N_{classes}} N_{droplet,k}\dot{m}_{d,k} b_{f,evap,k} + \dot{m}_{comb} b_{f,UBZ}$$

Finally, the exergy transfer associated with heat transfer accounts for the convection between unburned gases and the droplet classes and also for the interaction between the gases and cylinder walls:

$$\sum_j \left(1 - \frac{T_0}{T_j}\right)\dot{Q}_j = \dot{B}_{Q_{spray}} + \left(1 - \frac{T_0}{T_{wall}}\right)\dot{Q}_{UBZ,walls}$$

where $\dot{B}_{Q_{spray}} = -\sum_{k=1}^{N_{classes}} N_{droplet,k}\left(1 - \frac{T_0}{T_{d,k}}\right)\dot{Q}_{conv,k}$. The exergy terms related to work of expansion/contraction are presented below:

$$-\left(\dot{W} - P_0\frac{\mathrm{d}V}{\mathrm{d}t}\right) = -\left(\dot{W}_{spray} - P_0\sum_{k=1}^{N_{classes}} N_{droplet,k}\left(-\frac{\mathrm{d}V_{d,k}}{\mathrm{d}t}\right)\right) - P\frac{\mathrm{d}\,\text{Ꝟ}_{BZ}}{\mathrm{d}t} + P_0\frac{\mathrm{d}\,\text{Ꝟ}_{BZ}}{\mathrm{d}t}$$

while $\dot{B}_{d,UBZ}$ is the exergy destruction on the control volume. Then, returning to the main equation:

$$\begin{aligned}\frac{\mathrm{d}m_{UBZ}}{\mathrm{d}t}b_{UBZ} + m_{UBZ}\frac{\mathrm{d}b_{UBZ}}{\mathrm{d}t} - \sum_{k=1}^{N_{classes}} N_{droplet,k}\dot{m}_{d,k} b_{evap,k} + \dot{m}_{comb} b_{f,UBZ} = \\ \dot{B}_{Q_{spray}} + \left(1 - \frac{T_0}{T_{wall}}\right)\dot{Q}_{UBZ,walls} \\ - \left(\dot{W}_{spray} - P_0\sum_{k=1}^{N_{classes}} N_{droplet,k}\left(-\frac{\mathrm{d}V_{d,k}}{\mathrm{d}t}\right)\right) - (P - P_0)\frac{\mathrm{d}\,\text{Ꝟ}_{BZ}}{\mathrm{d}t} - \dot{B}_{d,UBZ}\end{aligned}$$

Opening $\frac{\mathrm{d}m_{UBZ}}{\mathrm{d}t}$ leads to:

$$\left(\sum_{k=1}^{N_{classes}} N_{droplet,k}\dot{m}_{d,k} - \dot{m}_{comb}\right) b_{UBZ} + m_{UBZ}\frac{\mathrm{d}b_{UBZ}}{\mathrm{d}t} - \sum_{k=1}^{N_{classes}} N_{droplet,k}\dot{m}_{d,k} b_{f,evap,k}$$
$$+ \dot{m}_{comb} b_{f,UBZ} = \dot{B}_{Q_{spray}} + \left(1 - \frac{T_0}{T_{wall}}\right)\dot{Q}_{UBZ,walls}$$
$$- \left(\dot{W}_{spray} - P_0 \sum_{k=1}^{N_{classes}} N_{droplet,k}\left(-\frac{\mathrm{d}V_{d,k}}{\mathrm{d}t}\right)\right) - (P - P_0)\frac{\mathrm{d}\cancel{V}_{BZ}}{\mathrm{d}t} - \dot{B}_{d,UBZ}$$

$$m_{UBZ}\frac{\mathrm{d}b_{UBZ}}{\mathrm{d}t} = \sum_{k=1}^{N_{classes}} N_{droplet,k}\dot{m}_{d,k}(b_{f,evap,k} - b_{UBZ}) - \dot{m}_{comb}(b_{f,UBZ} - b_{UBZ})$$
$$+ \dot{B}_{Q_{spray}} + \left(1 - \frac{T_0}{T_{wall}}\right)\dot{Q}_{UBZ,walls}$$
$$- \left(\dot{W}_{spray} - P_0 \sum_{k=1}^{N_{classes}} N_{droplet,k}\left(-\frac{\mathrm{d}V_{d,k}}{\mathrm{d}t}\right)\right) - (P - P_0)\frac{\mathrm{d}\cancel{V}_{BZ}}{\mathrm{d}t} - \dot{B}_{d,UBZ}$$

The final expression for the exergy destruction on the unburned zone is:

$$\dot{B}_{d,UBZ} = \sum_{k=1}^{N_{classes}} N_{droplet,k}\dot{m}_{d,k}(b_{f,evap,k} - b_{UBZ}) - \dot{m}_{comb}(b_{f,UBZ} - b_{UBZ}) - m_{UBZ}\frac{\mathrm{d}b_{UBZ}}{\mathrm{d}t}$$
$$+ \dot{B}_{Q_{spray}} + \left(1 - \frac{T_0}{T_{wall}}\right)\dot{Q}_{UBZ,walls}$$
$$- \left(\dot{W}_{spray} - P_0 \sum_{k=1}^{N_{classes}} N_{droplet,k}\left(-\frac{\mathrm{d}V_{d,k}}{\mathrm{d}t}\right)\right) - (P - P_0)\frac{\mathrm{d}\cancel{V}_{BZ}}{\mathrm{d}t} \tag{B.6}$$

B.1.6 Mass balance - burned zone

The RTT applied to the burned zone mass conservation is:

$$\frac{\partial}{\partial t}\int_{UBZ} \rho_{UBZ}\,\mathrm{d}\cancel{V} + \int_{CS} \rho_s(w_i n_i)\,\mathrm{d}A = 0$$

There is only a mass inlet due to mass transfer from the unburned zone to the burned zone from the combustion process, whereas no mass outlets exist in this model. The transient model considers that the content inside the control volume is homogeneous, thus:

$$\frac{\partial}{\partial t}\int_{UBZ} \rho_{BZ}\,\mathrm{d}\cancel{V} = \frac{\mathrm{d}(\rho_{BZ}V_{BZ})}{\mathrm{d}t} = \frac{\mathrm{d}m_{BZ}}{\mathrm{d}t}$$

For the mass inlet, we obtain:

$$\int_{CS,inlet} \rho_s (w_i n_i)\,\mathrm{d}A = -\dot{m}_{comb}$$

When these terms are put together in the main equation, the burned zone mass conservation is obtained:

$$\frac{\mathrm{d}m_{BZ}}{\mathrm{d}t} = \dot{m}_{comb} \tag{B.7}$$

B.1.7 Energy balance - burned zone

The full energy conservation equation based on the RTT is presented next:

$$\frac{\partial}{\partial t}\int_{BZ} \rho\left(\frac{V_I^2}{2} + gz + u\right)\mathrm{d}\forall + \int_{CS} \rho\left(\frac{V_I^2}{2} + gz + u + \frac{p}{\rho}\right)(\vec{V_r}\cdot\vec{n})\,\mathrm{d}A = \int_{CS} k(\nabla T\cdot\vec{n})\,\mathrm{d}A$$

$$-\int_{CS} p\left[\left(\vec{V_b} + \frac{\mathrm{d}\vec{R}}{\mathrm{d}t} + \vec{x}\times\vec{r}\right)\vec{n}\right]\mathrm{d}A + \int_{CS}(\tau\cdot\vec{n})\cdot\vec{V_I}\,\mathrm{d}A - \dot{W}_{eixo} + \int_{UBZ} q^{'''}\,\mathrm{d}\forall$$

For the burned zone, we need to take into account the following terms: the enthalpy inlet from UBZ to BZ (due to combustion mass transfer), the source term referred to enthalpy of combustion, the heat transfer from cylinder walls to BZ (or vice-versa) and the expansion work related to system volume variation. For the transient term, both temperature and mass are temporally variable and homogeneous in space, therefore:

$$\frac{\partial}{\partial t}\int_{BZ} \rho_{BZ} u\,\mathrm{d}\forall = \frac{\mathrm{d}(\rho_{BZ} u \forall_{BZ})}{\mathrm{d}t} = m_{BZ}\frac{\mathrm{d}u_{BZ}}{\mathrm{d}t} + u_{BZ}\frac{\mathrm{d}m_{BZ}}{\mathrm{d}t}$$

The enthalpy inlet expression is:

$$\int_{CS,inlet} \rho_{BZ}\left(\frac{V_I^2}{2} + u + \frac{p}{\rho}\right)(\vec{V_r}\cdot\vec{n})\,\mathrm{d}A = -\dot{m}_{comb} h_{UBZ}$$

while there is no enthalpy outlet in this CV. The term related to expansion work is then:

$$-\int_{CS} P\vec{V_b}\cdot\vec{n}\,\mathrm{d}A = -P\frac{\mathrm{d}V_{BZ}}{\mathrm{d}t}$$

The heat transfer term is connected to the interaction between the cylinder walls and the control volume gases:

$$\int_{CS} k(\nabla T \cdot \vec{n})\, \mathrm{d}A = \dot{Q}_{BZ,walls}$$

There are not source terms for this equation, thus:

$$\int_{UBZ} q^{'''}\, \mathrm{d}\forall = 0$$

Grouping all terms in the main equation yields the following expression:

$$m_{BZ}\frac{\mathrm{d}u_{BZ}}{\mathrm{d}t} + u_{BZ}\frac{\mathrm{d}m_{BZ}}{\mathrm{d}t} = \dot{m}_{comb}h_{UBZ} - P\frac{\mathrm{d}V_{BZ}}{\mathrm{d}t} + \dot{Q}_{BZ,walls}$$

while the transient term (i.e., $\frac{\mathrm{d}u_{BZ}}{\mathrm{d}t}$) is:

$$\frac{\mathrm{d}u_{BZ}}{\mathrm{d}t} = c_{v,BZ}\frac{\mathrm{d}T_{BZ}}{\mathrm{d}t} + \sum_{j=1}^{N_{species}} \left(u_{j,BZ}\frac{\mathrm{d}y_{j,BZ}}{\mathrm{d}t} \right)$$

with the second term representing the chemical energy variation due to combustion (similar to $\frac{\Delta H_{fuel}}{m_{fuel}}$). Opening the volume derivative in terms of the ideal gas differential equation produces:

$$m_{BZ}\frac{\mathrm{d}u_{BZ}}{\mathrm{d}t} + u_{BZ}\frac{\mathrm{d}m_{BZ}}{\mathrm{d}t} = \dot{m}_{comb}h_{UBZ} - \\ P\left\{ V_{BZ}\left[\frac{1}{m_{BZ}}\frac{\mathrm{d}m_{BZ}}{\mathrm{d}t} + \frac{1}{T_{BZ}}\frac{\mathrm{d}T_{BZ}}{\mathrm{d}t} - \frac{1}{P}\frac{\mathrm{d}P}{\mathrm{d}t} \right] \right\} + \dot{Q}_{BZ,walls}$$

Since the gases are considered ideal, reorganization of this equation yields:

$$m_{BZ}c_{p,BZ}\frac{\mathrm{d}T_{BZ}}{\mathrm{d}t} + m_{BZ}\sum_{j=1}^{N_{species}} \left(h_{j,BZ}\frac{\mathrm{d}y_{j,BZ}}{\mathrm{d}t} \right) = \dot{m}_{comb}(h_{UBZ} - h_{BZ}) + V_{BZ}\frac{\mathrm{d}P}{\mathrm{d}t} + \dot{Q}_{BZ,walls}$$

Isolating the temperature derivative, we obtain the burned zone temperature differential equation:

$$\frac{\mathrm{d}T_{BZ}}{\mathrm{d}t} = \frac{\dot{m}_{comb}(h_{UBZ} - h_{BZ}) + V_{BZ}\frac{\mathrm{d}P}{\mathrm{d}t} + \dot{Q}_{BZ,walls} - m_{BZ}\sum_{j=1}^{N_{species}} \left(h_{j,BZ}\frac{\mathrm{d}y_{j,BZ}}{\mathrm{d}t} \right)}{m_{BZ}c_{p,BZ}} \tag{B.8}$$

B.1.8 Entropy balance - burned zone

The RTT for entropy stays that:

$$\frac{\partial}{\partial t}\int_{VC}\rho s d\forall + \int_{SC}\rho s(w_i n_i)dA = \int_{SC}\left(\frac{k\nabla T}{T}\right)\cdot\vec{n}dA + \int_{VC}\left(\frac{q'''}{T}\right)dA + \dot{\sigma_{VC}}$$

For the burned zone, we need to take into account the following terms: the enthalpy inlet from UBZ to BZ (due to combustion mass transfer), the source term referred to enthalpy of combustion, the heat transfer from cylinder walls to BZ (or vice-versa).

$$\frac{\mathrm{d}S_{BZ}}{\mathrm{d}t} = m_{BZ}\frac{\mathrm{d}s_{BZ}}{\mathrm{d}t} + s_{BZ}\frac{\mathrm{d}m_{BZ}}{\mathrm{d}t}$$

The exergy inlet expression is:

$$-\sum_i \dot{m}_i s_{fi} + \sum_e \dot{m}_e s_{fe} = -\dot{m}_{comb} s_{UBZ}$$

while there is no entropy outlet in this CV. The heat transfer term is connected to the interaction between the cylinder walls and the control volume gases:

$$\int_{SC}\left(\frac{k\nabla T}{T}\right)\cdot\vec{n}dA = \frac{\dot{Q}_{BZ,walls}}{T_{wall}}$$

Grouping all terms in the main equation yields the following expression:

$$m_{BZ}\frac{\mathrm{d}s_{BZ}}{\mathrm{d}t} + s_{BZ}\frac{\mathrm{d}m_{BZ}}{\mathrm{d}t} = \dot{m}_{comb} s_{UBZ} + \frac{\dot{Q}_{BZ,walls}}{T_{wall}} + \dot{\sigma}_{BZ}$$

$$m_{BZ}\frac{\mathrm{d}s_{BZ}}{\mathrm{d}t} = \dot{m}_{comb}\left(s_{UBZ} - s_{BZ}\right) + \frac{\dot{Q}_{BZ,walls}}{T_{wall}} + \dot{\sigma}_{BZ}$$

We obtain the burned zone exergy destruction by isolating its term:

$$\dot{\sigma}_{BZ} = \dot{m}_{comb}(s_{BZ} - s_{UBZ}) + m_{BZ}\frac{\mathrm{d}s_{BZ}}{\mathrm{d}t} - \frac{\dot{Q}_{BZ,walls}}{T_{wall}} \tag{B.9}$$

B.1.9 Exergy balance - burned zone

The exergy balance is obtained by combining the expressions for the first and second laws of thermodynamics and it is written as it follows:

$$\frac{\mathrm{d}B_{UBZ}}{\mathrm{d}t} - \sum_i \dot{m}_i b_{fi} + \sum_e \dot{m}_e b_{fe} = \sum_j \left(1 - \frac{T_0}{T_j}\right)\dot{Q}_j - \sum_j \left(\dot{W}_j - P_0\frac{\mathrm{d}V_j}{\mathrm{d}t}\right) - \dot{B}_{d,UBZ}$$

For the burned zone, we need to take into account the following terms: the enthalpy inlet from UBZ to BZ (due to combustion mass transfer), the source term referred to enthalpy of combustion, the heat transfer from cylinder walls to BZ (or vice-versa) and the expansion work related to system volume variation.

$$\frac{\mathrm{d}B_{UBZ}}{\mathrm{d}t} = m_{BZ}\frac{\mathrm{d}b_{BZ}}{\mathrm{d}t} + b_{BZ}\frac{\mathrm{d}m_{BZ}}{\mathrm{d}t}$$

The exergy inlet expression is:

$$-\sum_i \dot{m}_i b_{fi} + \sum_e \dot{m}_e b_{fe} = -\dot{m}_{comb} b_{f,UBZ}$$

while there is no exergy outlet in this CV. The term related to expansion work is then:

$$-\int_{CS} P\vec{V}_b \cdot \vec{n}\,\mathrm{d}A = -\left(P - P_0\right)\frac{\mathrm{d}V_{BZ}}{\mathrm{d}t}$$

The heat transfer term is connected to the interaction between the cylinder walls and the control volume gases:

$$\sum_j \left(1 - \frac{T_0}{T_j}\right)\dot{Q}_j = \left(1 - \frac{T_0}{T_{wall}}\right)\dot{Q}_{BZ,walls}$$

Grouping all terms in the main equation yields the following expression:

$$m_{BZ}\frac{\mathrm{d}b_{BZ}}{\mathrm{d}t} + b_{BZ}\frac{\mathrm{d}m_{BZ}}{\mathrm{d}t} = \dot{m}_{comb} b_{f,UBZ} - P\frac{\mathrm{d}V_{BZ}}{\mathrm{d}t} + P_0\frac{\mathrm{d}V_{BZ}}{\mathrm{d}t} + \left(1 - \frac{T_0}{T_{wall}}\right)\dot{Q}_{BZ,walls} - \dot{B}_{d,BZ}$$

$$m_{BZ}\frac{\mathrm{d}b_{BZ}}{\mathrm{d}t} = \dot{m}_{comb}\left(b_{f,UBZ} - b_{BZ}\right) - \left(P - P_0\right)\frac{\mathrm{d}V_{BZ}}{\mathrm{d}t} + \left(1 - \frac{T_0}{T_{wall}}\right)\dot{Q}_{BZ,walls} - \dot{B}_{d,BZ}$$

We obtain the burned zone exergy destruction by isolating its term:

$$\dot{B}_{d,BZ} = \dot{m}_{comb}(b_{f,UBZ} - b_{BZ}) - m_{BZ}\frac{\mathrm{d}b_{BZ}}{\mathrm{d}t} - \left(P - P_0\right)\frac{\mathrm{d}V_{BZ}}{\mathrm{d}t} + \left(1 - \frac{T_0}{T_{wall}}\right)\dot{Q}_{BZ,walls} \quad \text{(B.10)}$$

B.1.10 Unburned and burned zone volume equations

The ideal gas equation in the mass form and its differential form are:

$$PV = mRT$$

$$\frac{1}{P}\frac{\mathrm{d}P}{\mathrm{d}t} + \frac{1}{V}\frac{\mathrm{d}V}{\mathrm{d}t} = \frac{1}{m}\frac{\mathrm{d}m}{\mathrm{d}t} + \frac{1}{R}\frac{\mathrm{d}R}{\mathrm{d}t} + \frac{1}{T}\frac{\mathrm{d}T}{\mathrm{d}t}$$

We apply the differential form for the unburned and burned zone with the hypothesis the cylinder pressure is the same between these zones, thus:

$$\frac{1}{P}\frac{\mathrm{d}P}{\mathrm{d}t} + \frac{1}{\cancel{V}_{BZ}}\frac{\mathrm{d}\cancel{V}_{BZ}}{\mathrm{d}t} = \frac{1}{m_{UBZ}}\frac{\mathrm{d}m_{UBZ}}{\mathrm{d}t} + \frac{1}{R_{UBZ}}\frac{\mathrm{d}R_{UBZ}}{\mathrm{d}t} + \frac{1}{T_{UBZ}}\frac{\mathrm{d}T_{UBZ}}{\mathrm{d}t}$$

$$\frac{1}{P}\frac{\mathrm{d}P}{\mathrm{d}t} + \frac{1}{V_{BZ}}\frac{\mathrm{d}V_{BZ}}{\mathrm{d}t} = \frac{1}{m_{BZ}}\frac{\mathrm{d}m_{BZ}}{\mathrm{d}t} + \frac{1}{R_{BZ}}\frac{\mathrm{d}R_{BZ}}{\mathrm{d}t} + \frac{1}{T_{BZ}}\frac{\mathrm{d}T_{BZ}}{\mathrm{d}t}$$

Neglecting the influence of composition on the ideal gas constant derivative yields:

$$\frac{1}{P}\frac{\mathrm{d}P}{\mathrm{d}t} + \frac{1}{\cancel{V}_{BZ}}\frac{\mathrm{d}\cancel{V}_{BZ}}{\mathrm{d}t} = \frac{1}{m_{UBZ}}\frac{\mathrm{d}m_{UBZ}}{\mathrm{d}t} + \frac{1}{T_{UBZ}}\frac{\mathrm{d}T_{UBZ}}{\mathrm{d}t}$$

$$\frac{1}{P}\frac{\mathrm{d}P}{\mathrm{d}t} + \frac{1}{V_{BZ}}\frac{\mathrm{d}V_{BZ}}{\mathrm{d}t} = \frac{1}{m_{BZ}}\frac{\mathrm{d}m_{BZ}}{\mathrm{d}t} + \frac{1}{T_{BZ}}\frac{\mathrm{d}T_{BZ}}{\mathrm{d}t}$$

Isolating the volumes, we obtain:

$$\frac{\mathrm{d}\cancel{V}_{BZ}}{\mathrm{d}t} = \cancel{V}_{BZ}\left[\frac{1}{m_{UBZ}}\frac{\mathrm{d}m_{UBZ}}{\mathrm{d}t} + \frac{1}{T_{UBZ}}\frac{\mathrm{d}T_{UBZ}}{\mathrm{d}t} - \frac{1}{P}\frac{\mathrm{d}P}{\mathrm{d}t}\right] \tag{B.11}$$

$$\frac{\mathrm{d}V_{BZ}}{\mathrm{d}t} = V_{BZ}\left[\frac{1}{m_{BZ}}\frac{\mathrm{d}m_{BZ}}{\mathrm{d}t} + \frac{1}{T_{BZ}}\frac{\mathrm{d}T_{BZ}}{\mathrm{d}t} - \frac{1}{P}\frac{\mathrm{d}P}{\mathrm{d}t}\right] \tag{B.12}$$

Isolating the pressure, we obtain:

$$\frac{\mathrm{d}P}{\mathrm{d}t} = P\left[-\frac{1}{\cancel{V}_{BZ}}\frac{\mathrm{d}\cancel{V}_{BZ}}{\mathrm{d}t} + \frac{1}{m_{UBZ}}\frac{\mathrm{d}m_{UBZ}}{\mathrm{d}t} + \frac{1}{T_{UBZ}}\frac{\mathrm{d}T_{UBZ}}{\mathrm{d}t}\right] \tag{B.13}$$

$$\frac{\mathrm{d}P}{\mathrm{d}t} = P\left[-\frac{1}{V_{BZ}}\frac{\mathrm{d}V_{BZ}}{\mathrm{d}t} + \frac{1}{m_{BZ}}\frac{\mathrm{d}m_{BZ}}{\mathrm{d}t} + \frac{1}{T_{BZ}}\frac{\mathrm{d}T_{BZ}}{\mathrm{d}t}\right] \tag{B.14}$$

Equaling the equations:

$$P\left[-\frac{1}{\cancel{V}_{BZ}}\frac{\mathrm{d}\cancel{V}_{BZ}}{\mathrm{d}t}+\frac{1}{m_{UBZ}}\frac{\mathrm{d}m_{UBZ}}{\mathrm{d}t}+\frac{1}{T_{UBZ}}\frac{\mathrm{d}T_{UBZ}}{\mathrm{d}t}\right]=P\left[-\frac{1}{V_{BZ}}\frac{\mathrm{d}V_{BZ}}{\mathrm{d}t}+\frac{1}{m_{BZ}}\frac{\mathrm{d}m_{BZ}}{\mathrm{d}t}+\frac{1}{T_{BZ}}\frac{\mathrm{d}T_{BZ}}{\mathrm{d}t}\right]$$

$$-\frac{1}{\cancel{V}_{BZ}}\frac{\mathrm{d}\cancel{V}_{BZ}}{\mathrm{d}t}+\frac{1}{m_{UBZ}}\frac{\mathrm{d}m_{UBZ}}{\mathrm{d}t}+\frac{1}{T_{UBZ}}\frac{\mathrm{d}T_{UBZ}}{\mathrm{d}t}=-\frac{1}{V_{BZ}}\frac{\mathrm{d}V_{BZ}}{\mathrm{d}t}+\frac{1}{m_{BZ}}\frac{\mathrm{d}m_{BZ}}{\mathrm{d}t}+\frac{1}{T_{BZ}}\frac{\mathrm{d}T_{BZ}}{\mathrm{d}t}$$

$$\begin{aligned}&\frac{1}{T_{UBZ}}\left[\frac{1}{m_{UBZ}c_{v,UBZ}}\left\{\sum_{k=1}^{N_{classes}}N_{droplet,k}\dot{m}_{d,k}(h_{evap,k}-u_{UBZ})-m_{UBZ}\sum_{j=1}^{N_{species}}\left(u_{j,UBZ}\frac{\mathrm{d}y_{j,UBZ}}{\mathrm{d}t}\right)\right.\right.\\&\qquad+\dot{m}_{comb}(h_{UBZ}-u_{UBZ})-\sum_{k=1}^{N_{classes}}N_{droplet,k}\dot{Q}_{conv,k}+\dot{Q}_{UBZ,walls}-\dot{W}_{spray}\\&\qquad\left.\left.-P\frac{\mathrm{d}\cancel{V}_{BZ}}{\mathrm{d}t}\right\}\right]-\frac{1}{\cancel{V}_{BZ}}\frac{\mathrm{d}\cancel{V}_{BZ}}{\mathrm{d}t}+\frac{1}{m_{UBZ}}\frac{\mathrm{d}m_{UBZ}}{\mathrm{d}t}=-\frac{1}{V_{BZ}}\frac{\mathrm{d}V_{BZ}}{\mathrm{d}t}+\frac{1}{m_{BZ}}\frac{\mathrm{d}m_{BZ}}{\mathrm{d}t}\\&\qquad\qquad+\frac{1}{T_{BZ}}\left[\frac{\dot{m}_{comb}(h_{UBZ}-u_{BZ})-P\frac{\mathrm{d}V_{BZ}}{\mathrm{d}t}+\dot{Q}_{BZ,walls}+\Delta H_{fuel}}{m_{BZ}c_{v,BZ}}\right]\end{aligned}$$

$$\begin{aligned}&\frac{1}{T_{UBZ}}\left[\frac{1}{m_{UBZ}c_{v,UBZ}}\left\{\sum_{k=1}^{N_{classes}}N_{droplet,k}\dot{m}_{d,k}(h_{evap,k}-u_{UBZ})-m_{UBZ}\sum_{j=1}^{N_{species}}\left(u_{j,UBZ}\frac{\mathrm{d}y_{j,UBZ}}{\mathrm{d}t}\right)\right.\right.\\&\qquad\left.\left.+\dot{m}_{comb}(h_{UBZ}-u_{UBZ})-\sum_{k=1}^{N_{classes}}N_{droplet,k}\dot{Q}_{conv,k}+\dot{Q}_{UBZ,walls}-\dot{W}_{spray}\right\}\right]\\&\qquad-\frac{P}{T_{UBZ}}\frac{\mathrm{d}\cancel{V}_{BZ}}{\mathrm{d}t}-\frac{1}{\cancel{V}_{BZ}}\frac{\mathrm{d}\cancel{V}_{BZ}}{\mathrm{d}t}+\frac{1}{m_{UBZ}}\frac{\mathrm{d}m_{UBZ}}{\mathrm{d}t}=-\frac{1}{V_{BZ}}\frac{\mathrm{d}V_{BZ}}{\mathrm{d}t}+\frac{1}{m_{BZ}}\frac{\mathrm{d}m_{BZ}}{\mathrm{d}t}\\&\qquad\qquad+\frac{1}{T_{BZ}}\left[\frac{\dot{m}_{comb}(h_{UBZ}-u_{BZ})+\dot{Q}_{BZ,walls}+\Delta H_{fuel}}{m_{BZ}c_{v,BZ}}\right]-\frac{P}{T_{BZ}}\frac{\mathrm{d}V_{BZ}}{\mathrm{d}t}\end{aligned}$$

$$\begin{aligned}&\left[\frac{1}{m_{UBZ}c_{v,UBZ}T_{UBZ}}\left\{\sum_{k=1}^{N_{classes}}N_{droplet,k}\dot{m}_{d,k}(h_{evap,k}-u_{UBZ})-m_{UBZ}\sum_{j=1}^{N_{species}}\left(u_{j,UBZ}\frac{\mathrm{d}y_{j,UBZ}}{\mathrm{d}t}\right)\right.\right.\\&\qquad\left.\left.+\dot{m}_{comb}(h_{UBZ}-u_{UBZ})-\sum_{k=1}^{N_{classes}}N_{droplet,k}\dot{Q}_{conv,k}+\dot{Q}_{UBZ,walls}-\dot{W}_{spray}\right\}\right]\\&-(m_{UBZ}R_{UBZ}+1)\frac{1}{\cancel{V}_{BZ}}\frac{\mathrm{d}\cancel{V}_{BZ}}{\mathrm{d}t}+\frac{1}{m_{UBZ}}\frac{\mathrm{d}m_{UBZ}}{\mathrm{d}t}=-\left(m_{BZ}R_{BZ}+1\right)\frac{1}{V_{BZ}}\frac{\mathrm{d}V_{BZ}}{\mathrm{d}t}+\frac{1}{m_{BZ}}\frac{\mathrm{d}m_{BZ}}{\mathrm{d}t}\\&\qquad\qquad+\left[\frac{\dot{m}_{comb}(h_{UBZ}-u_{BZ})+\dot{Q}_{BZ,walls}+\Delta H_{fuel}}{m_{BZ}c_{v,BZ}T_{BZ}}\right]\end{aligned}$$

$$\left(m_{BZ}R_{BZ}+1\right)\frac{1}{V_{BZ}}\frac{\mathrm{d}V_{BZ}}{\mathrm{d}t}-\left(m_{UBZ}R_{UBZ}+1\right)\frac{1}{\not{V}_{BZ}}\frac{\mathrm{d}\not{V}_{BZ}}{\mathrm{d}t}=-\frac{1}{m_{UBZ}}\frac{\mathrm{d}m_{UBZ}}{\mathrm{d}t}+\frac{1}{m_{BZ}}\frac{\mathrm{d}m_{BZ}}{\mathrm{d}t}$$

$$-\frac{1}{m_{UBZ}c_{v,UBZ}T_{UBZ}}\left\{\sum_{k=1}^{N_{classes}}N_{droplet,k}\dot{m}_{d,k}(h_{evap,k}-u_{UBZ})-m_{UBZ}\sum_{j=1}^{N_{species}}\left(u_{j,UBZ}\frac{\mathrm{d}y_{j,UBZ}}{\mathrm{d}t}\right)\right.$$

$$\left.+\dot{m}_{comb}(h_{UBZ}-u_{UBZ})-\sum_{k=1}^{N_{classes}}N_{droplet,k}\dot{Q}_{conv,k}+\dot{Q}_{UBZ,walls}-\dot{W}_{spray}\right\}$$

$$+\left[\frac{\dot{m}_{comb}(h_{UBZ}-u_{BZ})+\dot{Q}_{BZ,walls}+\Delta H_{fuel}}{m_{BZ}c_{v,BZ}T_{BZ}}\right]$$

Where the right-hand side (RHS) is known for each time-step. This equation together with the geometric relationship between the volumes provides a system of equations for $\frac{\mathrm{d}\not{V}_{BZ}}{\mathrm{d}t}$ and $\frac{\mathrm{d}V_{BZ}}{\mathrm{d}t}$:

$$\frac{\mathrm{d}\not{V}_{BZ}}{\mathrm{d}t}+\frac{\mathrm{d}V_{BZ}}{\mathrm{d}t}=\frac{\mathrm{d}V}{\mathrm{d}t}-\frac{\mathrm{d}V_{spray}}{\mathrm{d}t}$$

Isolating $\frac{\mathrm{d}V_{BZ}}{\mathrm{d}t}$ we have:

$$\frac{\mathrm{d}V_{BZ}}{\mathrm{d}t}=\left(\frac{\mathrm{d}V}{\mathrm{d}t}-\frac{\mathrm{d}V_{spray}}{\mathrm{d}t}\right)-\frac{\mathrm{d}\not{V}_{BZ}}{\mathrm{d}t}\tag{B.15}$$

Using this expression on the other equation:

$$\left(m_{BZ}R_{BZ}+1\right)\frac{1}{V_{BZ}}\left[\left(\frac{\mathrm{d}V}{\mathrm{d}t}-\frac{\mathrm{d}V_{spray}}{\mathrm{d}t}\right)-\frac{\mathrm{d}\not{V}_{BZ}}{\mathrm{d}t}\right]-\left(m_{UBZ}R_{UBZ}+1\right)\frac{1}{\not{V}_{BZ}}\frac{\mathrm{d}\not{V}_{BZ}}{\mathrm{d}t}=$$

$$-\frac{1}{m_{UBZ}}\frac{\mathrm{d}m_{UBZ}}{\mathrm{d}t}+\frac{1}{m_{BZ}}\frac{\mathrm{d}m_{BZ}}{\mathrm{d}t}+\left[\frac{\dot{m}_{comb}(h_{UBZ}-u_{BZ})+\dot{Q}_{BZ,walls}+\Delta H_{fuel}}{m_{BZ}c_{v,BZ}T_{BZ}}\right]$$

$$-\frac{1}{m_{UBZ}c_{v,UBZ}T_{UBZ}}\left\{\sum_{k=1}^{N_{classes}}N_{droplet,k}\dot{m}_{d,k}(h_{evap,k}-u_{UBZ})-m_{UBZ}\sum_{j=1}^{N_{species}}\left(u_{j,UBZ}\frac{\mathrm{d}y_{j,UBZ}}{\mathrm{d}t}\right)\right.$$

$$\left.+\dot{m}_{comb}(h_{UBZ}-u_{UBZ})-\sum_{k=1}^{N_{classes}}N_{droplet,k}\dot{Q}_{conv,k}+\dot{Q}_{UBZ,walls}-\dot{W}_{spray}\right\}$$

$$\frac{m_{BZ}R_{BZ}+1}{V_{BZ}}\left(\frac{\mathrm{d}V}{\mathrm{d}t}-\frac{\mathrm{d}V_{spray}}{\mathrm{d}t}\right)-\frac{m_{BZ}R_{BZ}+1}{V_{BZ}}\frac{\mathrm{d}\rlap{\,-}V_{BZ}}{\mathrm{d}t}-\frac{m_{UBZ}R_{UBZ}+1}{\rlap{\,-}V_{BZ}}\frac{\mathrm{d}\rlap{\,-}V_{BZ}}{\mathrm{d}t}=$$
$$-\frac{1}{m_{UBZ}}\frac{\mathrm{d}m_{UBZ}}{\mathrm{d}t}+\frac{1}{m_{BZ}}\frac{\mathrm{d}m_{BZ}}{\mathrm{d}t}+\left[\frac{\dot{m}_{comb}(h_{UBZ}-u_{BZ})+\dot{Q}_{BZ,walls}+\Delta H_{fuel}}{m_{BZ}c_{v,BZ}T_{BZ}}\right]$$
$$-\frac{1}{m_{UBZ}c_{v,UBZ}T_{UBZ}}\left\{\sum_{k=1}^{N_{classes}}N_{droplet,k}\dot{m}_{d,k}(h_{evap,k}-u_{UBZ})-m_{UBZ}\sum_{j=1}^{N_{species}}\left(u_{j,UBZ}\frac{\mathrm{d}y_{j,UBZ}}{\mathrm{d}t}\right)\right.$$
$$\left.+\dot{m}_{comb}(h_{UBZ}-u_{UBZ})-\sum_{k=1}^{N_{classes}}N_{droplet,k}\dot{Q}_{conv,k}+\dot{Q}_{UBZ,walls}-\dot{W}_{spray}\right\}$$

Thus we can directly obtain $\frac{\mathrm{d}\rlap{\,-}V_{BZ}}{\mathrm{d}t}$:

$$-\left(\frac{m_{BZ}R_{BZ}+1}{V_{BZ}}+\frac{m_{UBZ}R_{UBZ}+1}{\rlap{\,-}V_{BZ}}\right)\frac{\mathrm{d}\rlap{\,-}V_{BZ}}{\mathrm{d}t}=-\frac{m_{BZ}R_{BZ}+1}{V_{BZ}}\left(\frac{\mathrm{d}V}{\mathrm{d}t}-\frac{\mathrm{d}V_{spray}}{\mathrm{d}t}\right)$$
$$-\frac{1}{m_{UBZ}}\frac{\mathrm{d}m_{UBZ}}{\mathrm{d}t}+\frac{1}{m_{BZ}}\frac{\mathrm{d}m_{BZ}}{\mathrm{d}t}+\left[\frac{\dot{m}_{comb}(h_{UBZ}-u_{BZ})+\dot{Q}_{BZ,walls}+\Delta H_{fuel}}{m_{BZ}c_{v,BZ}T_{BZ}}\right]$$
$$-\frac{1}{m_{UBZ}c_{v,UBZ}T_{UBZ}}\left\{\sum_{k=1}^{N_{classes}}N_{droplet,k}\dot{m}_{d,k}(h_{evap,k}-u_{UBZ})-m_{UBZ}\sum_{j=1}^{N_{species}}\left(u_{j,UBZ}\frac{\mathrm{d}y_{j,UBZ}}{\mathrm{d}t}\right)\right.$$
$$\left.+\dot{m}_{comb}(h_{UBZ}-u_{UBZ})-\sum_{k=1}^{N_{classes}}N_{droplet,k}\dot{Q}_{conv,k}+\dot{Q}_{UBZ,walls}-\dot{W}_{spray}\right\}$$

$$\frac{\mathrm{d}\rlap{\,-}V_{BZ}}{\mathrm{d}t}=\left(\frac{m_{BZ}R_{BZ}+1}{V_{BZ}}+\frac{m_{UBZ}R_{UBZ}+1}{\rlap{\,-}V_{BZ}}\right)^{-1}\left\{\frac{m_{BZ}R_{BZ}+1}{V_{BZ}}\left(\frac{\mathrm{d}V}{\mathrm{d}t}-\frac{\mathrm{d}V_{spray}}{\mathrm{d}t}\right)\right.$$
$$+\frac{1}{m_{UBZ}}\frac{\mathrm{d}m_{UBZ}}{\mathrm{d}t}-\frac{1}{m_{BZ}}\frac{\mathrm{d}m_{BZ}}{\mathrm{d}t}-\left[\frac{\dot{m}_{comb}(h_{UBZ}-u_{BZ})+\dot{Q}_{BZ,walls}+\Delta H_{fuel}}{m_{BZ}c_{v,BZ}T_{BZ}}\right]$$
$$+\frac{1}{m_{UBZ}c_{v,UBZ}T_{UBZ}}\left\{\sum_{k=1}^{N_{classes}}N_{droplet,k}\dot{m}_{d,k}(h_{evap,k}-u_{UBZ})-m_{UBZ}\sum_{j=1}^{N_{species}}\left(u_{j,UBZ}\frac{\mathrm{d}y_{j,UBZ}}{\mathrm{d}t}\right)\right.$$
$$\left.\left.+\dot{m}_{comb}(h_{UBZ}-u_{UBZ})-\sum_{k=1}^{N_{classes}}N_{droplet,k}\dot{Q}_{conv,k}+\dot{Q}_{UBZ,walls}-\dot{W}_{spray}\right\}\right\}\tag{B.16}$$

And the pressure P is obtained by the ideal gas law for whichever preferably zone.

B.1.11 Volume balance and pressure rate

The total cylinder volume available in terms of crank angle is:

$$V(\theta) = \cancel{V}_{BZ} + V_{BZ} + V_{spray}$$

The spray volume is usually much less than the gases volumes ($V_{spray} \ll \cancel{V}_{BZ}$ (or V_{BZ})), still it is taken into account in this model development in order to evaluate its influence and therefore corroborate the aforementioned hypothesis. Getting the time derivative of the previous equation in time yields:

$$\frac{\mathrm{d}V}{\mathrm{d}t} = \frac{\mathrm{d}\cancel{V}_{BZ}}{\mathrm{d}t} + \frac{\mathrm{d}V_{BZ}}{\mathrm{d}t} + \frac{\mathrm{d}V_{spray}}{\mathrm{d}t}$$

Applying the ideal gas equation for both zones produces:

$$\frac{\mathrm{d}V}{\mathrm{d}t} = \cancel{V}_{BZ}\left[\frac{1}{m_{UBZ}}\frac{\mathrm{d}m_{UBZ}}{\mathrm{d}t} + \frac{1}{T_{UBZ}}\frac{\mathrm{d}T_{UBZ}}{\mathrm{d}t} - \frac{1}{P}\frac{\mathrm{d}P}{\mathrm{d}t}\right] + \\ + V_{BZ}\left[\frac{1}{m_{BZ}}\frac{\mathrm{d}m_{BZ}}{\mathrm{d}t} + \frac{1}{T_{BZ}}\frac{\mathrm{d}T_{BZ}}{\mathrm{d}t} - \frac{1}{P}\frac{\mathrm{d}P}{\mathrm{d}t}\right] + \frac{\mathrm{d}V_{spray}}{\mathrm{d}t}$$

Grouping similar terms provides the following equation:

$$\frac{\mathrm{d}V}{\mathrm{d}t} = \frac{\cancel{V}_{BZ}}{m_{UBZ}}\frac{\mathrm{d}m_{UBZ}}{\mathrm{d}t} + \frac{V_{BZ}}{m_{BZ}}\frac{\mathrm{d}m_{BZ}}{\mathrm{d}t} - \frac{\cancel{V}_{BZ} + V_{BZ}}{P}\frac{\mathrm{d}P}{\mathrm{d}t} + \\ \frac{\cancel{V}_{BZ}}{T_{UBZ}}\frac{\mathrm{d}T_{UBZ}}{\mathrm{d}t} + \frac{V_{BZ}}{T_{BZ}}\frac{\mathrm{d}T_{BZ}}{\mathrm{d}t} + \frac{\mathrm{d}V_{spray}}{\mathrm{d}t}$$

Isolating the pressure derivative yields:

$$\frac{\mathrm{d}P}{\mathrm{d}t} = \frac{P}{\cancel{V}_{BZ} + V_{BZ}}\left[\frac{\cancel{V}_{BZ}}{m_{UBZ}}\frac{\mathrm{d}m_{UBZ}}{\mathrm{d}t} + \frac{V_{BZ}}{m_{BZ}}\frac{\mathrm{d}m_{BZ}}{\mathrm{d}t} + \frac{\cancel{V}_{BZ}}{T_{UBZ}}\frac{\mathrm{d}T_{UBZ}}{\mathrm{d}t} + \frac{V_{BZ}}{T_{BZ}}\frac{\mathrm{d}T_{BZ}}{\mathrm{d}t} - \frac{\mathrm{d}V}{\mathrm{d}t} + \frac{\mathrm{d}V_{spray}}{\mathrm{d}t}\right]$$

Imposing the ideal gas equation for both zones produces:

$$\frac{\mathrm{d}P}{\mathrm{d}t} = \frac{P}{V - V_{spray}}\left[\frac{R_{UBZ}T_{UBZ}}{P}\frac{\mathrm{d}m_{UBZ}}{\mathrm{d}t} + \frac{R_{BZ}T_{BZ}}{P}\frac{\mathrm{d}m_{BZ}}{\mathrm{d}t} + \frac{m_{UBZ}R_{UBZ}}{P}\frac{\mathrm{d}T_{UBZ}}{\mathrm{d}t} \right. \\ \left. + \frac{m_{BZ}R_{BZ}}{P}\frac{\mathrm{d}T_{BZ}}{\mathrm{d}t} - \frac{\mathrm{d}V}{\mathrm{d}t} + \frac{\mathrm{d}V_{spray}}{\mathrm{d}t}\right]$$

$$\frac{\mathrm{d}P}{\mathrm{d}t} = \frac{1}{V - V_{spray}}\left[R_{UBZ}T_{UBZ}\frac{\mathrm{d}m_{UBZ}}{\mathrm{d}t} + R_{BZ}T_{BZ}\frac{\mathrm{d}m_{BZ}}{\mathrm{d}t} + m_{UBZ}R_{UBZ}\frac{\mathrm{d}T_{UBZ}}{\mathrm{d}t} \right. \\ \left. + m_{BZ}R_{BZ}\frac{\mathrm{d}T_{BZ}}{\mathrm{d}t} - P\left(\frac{\mathrm{d}V}{\mathrm{d}t} - \frac{\mathrm{d}V_{spray}}{\mathrm{d}t}\right)\right]$$

Expanding the temperature derivatives generates the following equation:

$$\frac{\mathrm{d}P}{\mathrm{d}t} = \frac{1}{V - V_{spray}} \left[R_{UBZ}T_{UBZ}\frac{\mathrm{d}m_{UBZ}}{\mathrm{d}t} + R_{BZ}T_{BZ}\frac{\mathrm{d}m_{BZ}}{\mathrm{d}t} \right.$$
$$+ m_{UBZ}R_{UBZ}\left\{ \frac{\sum_{k=1}^{N_{classes}} N_{droplet,k}\dot{m}_{d,k}(h_{evap,k} - h_{UBZ}) - m_{UBZ}\sum_{j=1}^{N_{species}}\left(h_{j,UBZ}\frac{\mathrm{d}y_{j,UBZ}}{\mathrm{d}t}\right)}{m_{UBZ}c_{p,UBZ}} \right.$$
$$\left. + \frac{P\sum_{k=1}^{N_{classes}} N_{droplet,k}\frac{\mathrm{d}V_{d,k}}{\mathrm{d}t} + \cancel{V}_{BZ}\frac{\mathrm{d}P}{\mathrm{d}t} - \sum_{k=1}^{N_{classes}} N_{droplet,k}\dot{Q}_{conv,k} + \dot{Q}_{UBZ,walls}}{m_{UBZ}c_{p,UBZ}} \right\}$$
$$\left. + m_{BZ}R_{BZ}\left\{ \frac{\dot{m}_{comb}(h_{UBZ} - h_{BZ}) + V_{BZ}\frac{\mathrm{d}P}{\mathrm{d}t} + \dot{Q}_{BZ,walls} + \Delta H_{fuel}}{m_{BZ}c_{p,BZ}} \right\} - P\left(\frac{\mathrm{d}V}{\mathrm{d}t} - \frac{\mathrm{d}V_{spray}}{\mathrm{d}t}\right) \right]$$

Grouping similar terms and isolating the pressure derivative yields the final equation:

$$\frac{\mathrm{d}P}{\mathrm{d}t} = \frac{1}{V - \frac{R_{BZ}V_{BZ}}{c_{p,BZ}} - \frac{R_{UBZ}\cancel{V}_{BZ}}{c_{p,UBZ}} - V_{spray}} \left\{ R_{UBZ}T_{UBZ}\frac{\mathrm{d}m_{UBZ}}{\mathrm{d}t} + R_{BZ}T_{BZ}\frac{\mathrm{d}m_{BZ}}{\mathrm{d}t} \right.$$
$$+ \frac{R_{UBZ}}{c_{p,UBZ}}\left[\sum_{k=1}^{N_{classes}} N_{droplet,k}\dot{m}_{d,k}(h_{evap,k} - h_{UBZ}) - m_{UBZ}\sum_{j=1}^{N_{species}}\left(h_{j,UBZ}\frac{\mathrm{d}y_{j,UBZ}}{\mathrm{d}t}\right) \right.$$
$$\left. + P\sum_{k=1}^{N_{classes}} N_{droplet,k}\frac{\mathrm{d}V_{d,k}}{\mathrm{d}t} - \sum_{k=1}^{N_{classes}} N_{droplet,k}\dot{Q}_{conv,k} + \dot{Q}_{UBZ,walls} \right]$$
$$\left. + \frac{R_{BZ}}{c_{p,BZ}}\left[\dot{m}_{comb}(h_{UBZ} - h_{BZ}) + \dot{Q}_{BZ,walls} + \Delta H_{fuel} \right] - P\left(\frac{\mathrm{d}V}{\mathrm{d}t} - \frac{\mathrm{d}V_{spray}}{\mathrm{d}t}\right) \right\} \quad \text{(B.17)}$$

B.2 Open phase

The open phase involves the engine cycle period between the exhaust valve opening (EVO) until the inlet valve closure (IVC). During this period, there are the processes of exhaust and admission of in-cylinder gases, besides fuel injection and evaporation. All these process modeling are presented in the subsequent sections.

B.2.1 Mass balance - gas

The Reynolds Transport Theorem (RTT) is applied for mass conservation for the gas-phase control volume:

$$\frac{\partial}{\partial t}\int_{g} \rho_g \, \mathrm{d}\cancel{V} + \int_{CS} \rho_s (w_i n_i) \, \mathrm{d}A = 0$$

There are inlet mass flows from the droplets evaporation to the gas-phase and outlet flows involving the gas-phase with the admission and exhaust valves. It is detailed each one of these terms in a separate form and then they are regrouped to close the balance. Thus, detailing first the transient term, which is assumed as homogeneous, we have:

$$\frac{\partial}{\partial t}\int_{g} \rho_g \,\mathrm{d}\,\cancel{V} = \frac{\mathrm{d}(\rho_g V_g)}{\mathrm{d}t} = \frac{\mathrm{d}m_g}{\mathrm{d}t}$$

To the inlet terms, it is necessary to take into account the sum of evaporation rates from each droplet interacting with the gas-phase and to encompass them by size group. Also, there are terms associated to the mass flow due to the admission and exhaust valves when they are open during the open-phase. Thus, we can refer to these terms as:

$$\int_{CS,inlet} \rho_s(w_i n_i)\,\mathrm{d}A = -\sum_{k=1}^{N_{classes}} N_{droplet,k}\dot{m}_{d,k} - \delta_{adm,i}\dot{m}_{adm} - \delta_{exh,i}\dot{m}_{exh}$$

where $N_{droplet,k}$ represents the number of droplets of the kth droplet class, while $\delta_{adm,i}$ and $\delta_{exh,i}$ are the Kronecker delta indicating the flow direction related to the admission and exhaust valves, respectively (0 or 1). The outlet term represents the mass flow terms representing the cylinder-valves interactions. Therefore, this term is presented as:

$$\int_{CS,outlet} \rho_s(w_i n_i)\,\mathrm{d}A = \delta_{adm,o}\dot{m}_{adm} + \delta_{exh,o}\dot{m}_{exh}$$

where $\delta_{adm,o}$ and $\delta_{exh,o}$ are defined as their similar terms previously presented. Regrouping the terms, we obtain the open-phase gas mass balance:

$$\frac{\mathrm{d}m_g}{\mathrm{d}t} = \sum_{k=1}^{N_{classes}} N_{droplet,k}\dot{m}_{d,k} + (\delta_{adm,i} - \delta_{adm,o})\dot{m}_{adm} + (\delta_{exh,i} - \delta_{exh,o})\dot{m}_{exh} \tag{B.18}$$

B.2.2 Species balance - gas

The species conservation for the gas-phase follows the same initial steps as the mass conservation. The main differences lie on the inlet species, which are only related to the fuel components of each droplet evaporating, while the outlets are related to the composition of the admission and exhaust states. The admission state is assumed to be composed by air, whereas the exhaust is composed by combustion products (EGR). The general species conservation for UBZ has the following form:

$$\frac{\partial}{\partial t}\int_{g}\rho y_j \,\mathrm{d}\cancel{V} + \int_{CS}\rho y_j (w_i n_i)\,\mathrm{d}A = -\int_{CS}\vec{J}_j n_i \,\mathrm{d}A + \int_{g}\dot{R}_j M_j \,\mathrm{d}\cancel{V}$$

where the diffusive term $\int_{CS}\vec{J}_j n_i \,\mathrm{d}A$ and the chemical reaction term $\int_{g}\dot{R}_j M_j \,\mathrm{d}\cancel{V}$ are neglected due to the hypotheses of homogeneity and absence of chemical reactions in this gas-phase, respectively. The transient term is, therefore:

$$\frac{\partial}{\partial t}\int_{g}\rho y_j \,\mathrm{d}\cancel{V} = \frac{\mathrm{d}m_{g,j}}{\mathrm{d}t}$$

The inlet terms are:

$$\int_{CS,inlet}\rho_s y_j (w_i n_i)\,\mathrm{d}A = -\sum_{k=1}^{N_{classes}} N_{droplet,k} y_{j,k,evap}\dot{m}_{d,k} - \delta_{adm,i} y_{j,air}\dot{m}_{adm} - \delta_{exh,i} y_{j,EGR}\dot{m}_{exh}$$

where $y_{j,k,s}$ is the vapor mass fraction of the jth fuel component on the droplet surface of the kth droplet class. Lastly, the outlet terms are:

$$\int_{CS,outlet}\rho_s y_j (w_i n_i)\,\mathrm{d}A = \delta_{adm,o} y_{j,g}\dot{m}_{adm} + \delta_{exh,o} y_{j,g}\dot{m}_{exh}$$

where $y_{j,g}$ is the mass fraction of the jth component in the gas-phase. Therefore, the final form of the species conservation is:

$$\begin{aligned}\frac{\mathrm{d}m_{gas,j}}{\mathrm{d}t} = \sum_{k=1}^{N_{classes}} N_{droplet,k} y_{j,k,evap}\dot{m}_{d,k} + (\delta_{adm,i} y_{j,air} - \delta_{adm,o} y_{j,g})\dot{m}_{adm} \\ + (\delta_{exh,i} y_{j,EGR} - \delta_{exh,o} y_{j,g})\dot{m}_{exh} \quad \text{(B.19)}\end{aligned}$$

B.2.3 Energy balance - gas

The RTT for the energy conservation has the following form:

$$\begin{aligned}\frac{\partial}{\partial t}\int_{g}\rho\left(\frac{V_I^2}{2} + gz + u\right)\mathrm{d}\cancel{V} + \int_{CS}\rho\left(\frac{V_I^2}{2} + gz + u + \frac{p}{\rho}\right)(\vec{V}_r \cdot \vec{n})\,\mathrm{d}A = \int_{CS} k(\nabla T \cdot \vec{n})\,\mathrm{d}A \\ -\int_{CS} p\left[\left(\vec{V}_b + \frac{\mathrm{d}\vec{R}}{\mathrm{d}t} + \vec{x}\times\vec{r}\right)\vec{n}\right]\mathrm{d}A + \int_{CS}(\tau\cdot\vec{n})\cdot\vec{V}_I\,\mathrm{d}A - \dot{W}_{comp} + \int_{g} q''' \,\mathrm{d}\cancel{V}\end{aligned}$$

In the open-phase gas CV, it occurs the following energetic interactions: enthalpy inlet of the vapor fuel evaporated from the droplets, enthalpy inlet from the admission and exhaust valves, enthalpy outlet to the admission and exhaust valves, work due to the droplets volume variation, work due to the compression/expansion caused by the engine volume variation, heat transfer from the gas to the droplets and from the engine cylinder walls to the gas.

The transient term is initially:

$$\frac{\partial}{\partial t}\int_g \rho_g u \, \mathrm{d}\forall = \frac{\mathrm{d}(\rho_g u \forall_g)}{\mathrm{d}t} = \frac{\mathrm{d}U_g}{\mathrm{d}t}$$

The inlet enthalpy in the gas-phase is related to the mass flow rates from the droplets evaporation, as well as to the mass flow from the admission and exhaust valves:

$$\int_{CS,inlet} \rho_g \left(\frac{V_I^2}{2} + u + \frac{P}{\rho}\right)(\vec{V_r}\cdot\vec{n})\,\mathrm{d}A = -\sum_{k=1}^{N_{classes}} N_{droplet,k}\dot{m}_{d,k}h_{evap,k} - \delta_{adm,i}\dot{m}_{adm}h_{adm} - \delta_{exh,i}\dot{m}_{exh}h_{exh}$$

For the outlet enthalpy from the gas-phase, we have:

$$\int_{CS,outlet} \rho_g \left(\frac{V_I^2}{2} + u + \frac{P}{\rho}\right)(\vec{V_r}\cdot\vec{n})\,\mathrm{d}A = \delta_{adm,o}\dot{m}_{adm}h_g + \delta_{exh,o}\dot{m}_{exh}h_g$$

The terms related to work of expansion/contraction are presented below:

$$-\int_{CS} P\vec{V_b}\cdot\vec{n}\,\mathrm{d}A = -\dot{W}_{spray} - P\frac{\mathrm{d}V_g}{\mathrm{d}t}$$

Where $\dot{W}_{spray} = P\sum_{k=1}^{N_{classes}} N_{droplet,k}\left(-\frac{\mathrm{d}V_{d,k}}{\mathrm{d}t}\right)$.

The internal energy transient term takes into account that both temperature and mass are homogeneous in space and variable in time, thus:

$$\frac{\partial}{\partial t}\int_g \rho_g u \, \mathrm{d}\forall = m_g\frac{\mathrm{d}u_g}{\mathrm{d}t} + u_g\frac{\mathrm{d}m_g}{\mathrm{d}t}$$

Repeating the previously presented mathematical development, it is obtained:

$$\frac{\partial}{\partial t}\int_g \rho_g u \, \mathrm{d}\forall = m_g c_{v,g}\frac{\mathrm{d}T_g}{\mathrm{d}t} + m_g\sum_{j=1}^{N_{species}}\left(u_{j,UBZ}\frac{\mathrm{d}y_{j,UBZ}}{\mathrm{d}t}\right) + \frac{\mathrm{d}m_g}{\mathrm{d}t}u_g$$

$$\int_{CS} k(\nabla T\cdot\vec{n})\,\mathrm{d}A = \dot{Q}_{spray} + \dot{Q}_{g,walls}$$

where $\dot{Q}_{spray} = -\sum_{k=1}^{N_{classes}} N_{droplet,k}\dot{Q}_{conv,k}$ and the negative sign is required since the known values of $\dot{Q}_{conv,k}$ were obtained for the droplet control volumes, not for the gas. After grouping all these terms, we have:

$$m_g c_{v,g}\frac{\mathrm{d}T_g}{\mathrm{d}t} + m_g\sum_{j=1}^{N_{species}}\left(h_{j,g}\frac{\mathrm{d}y_{j,g}}{\mathrm{d}t}\right) + \frac{\mathrm{d}m_g}{\mathrm{d}t}u_g = \sum_{k=1}^{N_{classes}} N_{droplet,k}\dot{m}_{d,k}h_{evap,k}$$
$$+\,\delta_{adm,i}\dot{m}_{adm}h_{adm} + \delta_{exh,i}\dot{m}_{exh}h_{exh} - \delta_{adm,o}\dot{m}_{adm}h_g - \delta_{exh,o}\dot{m}_{exh}h_g - \dot{W}_{spray} -$$
$$P\frac{\mathrm{d}V_g}{\mathrm{d}t} + \dot{Q}_{spray} + \dot{Q}_{g,walls}$$

Applying the mass conservation to substitute the term $\frac{\mathrm{d}m_g}{\mathrm{d}t}$ provides:

$$m_g c_{v,g}\frac{\mathrm{d}T_g}{\mathrm{d}t} + m_g\sum_{j=1}^{N_{species}}\left(h_{j,g}\frac{\mathrm{d}y_{j,g}}{\mathrm{d}t}\right)$$
$$+\left(\sum_{k=1}^{N_{classes}} N_{droplet,k}\dot{m}_{d,k} + (\delta_{adm,i}-\delta_{adm,o})\dot{m}_{adm} + (\delta_{exh,i}-\delta_{exh,o})\dot{m}_{exh}\right)u_g =$$
$$\sum_{k=1}^{N_{classes}} N_{droplet,k}\dot{m}_{d,k}h_{evap,k} + \dot{m}_{adm}(\delta_{adm,i}h_{adm} - \delta_{adm,o}h_g) + \dot{m}_{exh}(\delta_{exh,i}h_{exh} - \delta_{exh,o}h_g)$$
$$-\,\dot{W}_{spray} - P\frac{\mathrm{d}V_g}{\mathrm{d}t} + \dot{Q}_{spray} + \dot{Q}_{g,walls}$$

$$m_g c_{v,g}\frac{\mathrm{d}T_g}{\mathrm{d}t} = \sum_{k=1}^{N_{classes}} N_{droplet,k}\dot{m}_{d,k}(h_{evap,k} - u_g) - m_g\sum_{j=1}^{N_{species}}\left(h_{j,g}\frac{\mathrm{d}y_{j,g}}{\mathrm{d}t}\right)$$
$$+\,\delta_{adm,i}\dot{m}_{adm}(h_{adm} - u_g) + \delta_{exh,i}\dot{m}_{exh}(h_{exh} - u_g) + \delta_{adm,o}\dot{m}_{adm}(u_g - h_g)$$
$$+\,\delta_{exh,o}\dot{m}_{exh}(u_g - h_g) - \dot{W}_{spray} - P\frac{\mathrm{d}V_g}{\mathrm{d}t} + \dot{Q}_{spray} + \dot{Q}_{g,walls}$$

Finally we obtain the gas-phase temperature differential equation:

$$\frac{\mathrm{d}T_g}{\mathrm{d}t} = \frac{1}{m_g c_{v,g}}\left\{\sum_{k=1}^{N_{classes}} N_{droplet,k}\dot{m}_{d,k}(h_{evap,k} - u_g) - m_g\sum_{j=1}^{N_{species}}\left(h_{j,g}\frac{\mathrm{d}y_{j,g}}{\mathrm{d}t}\right)\right.$$
$$+\delta_{adm,i}\dot{m}_{adm}(h_{adm} - u_g) + \delta_{exh,i}\dot{m}_{exh}(h_{exh} - u_g) + \delta_{adm,o}\dot{m}_{adm}(u_g - h_g)$$
$$\left.+\delta_{exh,o}\dot{m}_{exh}(u_g - h_g) + \dot{Q}_{spray} + \dot{Q}_{g,walls} - \dot{W}_{spray} - P\frac{\mathrm{d}V_g}{\mathrm{d}t}\right\} \qquad \text{(B.20)}$$

B.2.4 Entropy balance - gas

The RTT for entropy stays that:

$$\frac{\partial}{\partial t}\int_{VC}\rho s d\not{V} + \int_{SC}\rho s(w_i n_i)dA = \int_{SC}\left(\frac{k\nabla T}{T}\right)\cdot\vec{n}dA + \int_{VC}\left(\frac{q'''}{T}\right)dA + \sigma\dot{_{VC}}$$

The transient term accounts for entropy variation on the unburned gases, as showed by the following equation:

$$\frac{\partial}{\partial t}\int_{VC}\rho s d\not{V} = s_g\frac{\mathrm{d}m_g}{\mathrm{d}t} + m_g\frac{\mathrm{d}s_g}{\mathrm{d}t}$$

The second term on RTT represents the entropy flow terms (inlet and outlet):

$$\int_{SC}\rho s(w_i n_i)dA = -\sum_{k=1}^{N_{classes}} N_{droplet,k}\dot{m}_{d,k}s_{evap,k} \\ - \dot{m}_{adm}(\delta_{adm,i}s_{adm} - \delta_{adm,o}s_g) - \dot{m}_{exh}(\delta_{exh,i}s_{exh} - \delta_{exh,o}s_g)$$

Finally, the entropy transfer associated with heat transfer accounts for the convection between the gases and the droplet classes and also for the interaction between the gases and cylinder walls:

$$\int_{SC}\left(\frac{k\nabla T}{T}\right)\cdot\vec{n}dA = \frac{\dot{Q}_{spray}}{T_{d,avg}} + \frac{\dot{Q}_{g,walls}}{T_{wall}}$$

where $\frac{\dot{Q}_{spray}}{T_{d,avg}} = -\sum_{k=1}^{N_{classes}} N_{droplet,k}\frac{\dot{Q}_{conv,k}}{T_{d,k}}$. Meanwhile, $\dot{\sigma}_g$ is the entropy generation on the control volume. Then, grouping all terms leads to:

$$\frac{\mathrm{d}m_g}{\mathrm{d}t}s_g + m_g\frac{\mathrm{d}s_g}{\mathrm{d}t} - \sum_{k=1}^{N_{classes}} N_{droplet,k}\dot{m}_{d,k}s_{evap,k} - \dot{m}_{adm}(\delta_{adm,i}s_{adm} - \delta_{adm,o}s_g) - \\ \dot{m}_{exh}(\delta_{exh,i}s_{exh} - \delta_{exh,o}s_g) = \frac{\dot{Q}_{spray}}{T_{d,avg}} + \frac{\dot{Q}_{g,walls}}{T_{wall}} + \dot{\sigma}_g$$

Opening $\frac{\mathrm{d}m_g}{\mathrm{d}t}$ leads to:

$$\left(\sum_{k=1}^{N_{classes}} N_{droplet,k}\dot{m}_{d,k} + (\delta_{adm,i} - \delta_{adm,o})\dot{m}_{adm} + (\delta_{exh,i} - \delta_{exh,o})\dot{m}_{exh}\right) s_g +$$
$$m_g\frac{\mathrm{d}s_g}{\mathrm{d}t} - \dot{m}_{adm}(\delta_{adm,i}s_{adm} - \delta_{adm,o}s_g) - \dot{m}_{exh}(\delta_{exh,i}s_{exh} - \delta_{exh,o}s_g) =$$
$$\frac{\dot{Q}_{spray}}{T_{d,avg}} + \frac{\dot{Q}_{g,walls}}{T_{wall}} + \dot{\sigma}_g$$

The final expression for the entropy generation on the unburned zone is:

$$\dot{\sigma}_g = \sum_{k=1}^{N_{classes}} N_{droplet,k}\dot{m}_{d,k}(s_g - s_{evap,k}) + \delta_{adm,i}\dot{m}_{adm}(s_g - s_{adm}) + \delta_{exh,i}\dot{m}_{exh}(s_g - s_{exh})$$
$$+ m_g\frac{\mathrm{d}s_g}{\mathrm{d}t} - \frac{\dot{Q}_{spray}}{T_{d,avg}} - \frac{\dot{Q}_{g,walls}}{T_{wall}} \quad \text{(B.21)}$$

B.2.5 Exergy balance - gas

The exergy balance is obtained by combining the expressions for the first and second laws of thermodynamics and it is written as it follows:

$$\frac{\mathrm{d}B_g}{\mathrm{d}t} - \sum_i \dot{m}_i b_{fi} + \sum_e \dot{m}_e b_{fe} = \sum_j \left(1 - \frac{T_0}{T_j}\right)\dot{Q}_j - \left(\dot{W} - P_0\frac{\mathrm{d}V}{\mathrm{d}t}\right) - \dot{B}_{d,g}$$

The transient term accounts for entropy variation on the unburned gases, as showed by the following equation:

$$\frac{\mathrm{d}B_g}{\mathrm{d}t} = b_g\frac{\mathrm{d}m_g}{\mathrm{d}t} + m_g\frac{\mathrm{d}b_g}{\mathrm{d}t}$$

The second term on RTT represents the exergy flow terms:

$$-\sum_i \dot{m}_i b_{fi} + \sum_e \dot{m}_e b_{fe} = -\sum_{k=1}^{N_{classes}} N_{droplet,k}\dot{m}_{d,k}b_{f,evap,k}$$
$$- \dot{m}_{adm}(\delta_{adm,i}b_{f,adm} - \delta_{adm,o}b_{f,g}) - \dot{m}_{exh}(\delta_{exh,i}b_{f,exh} - \delta_{exh,o}b_{f,g})$$

Finally, the exergy transfer associated with heat transfer accounts for the convection between unburned gases and the droplet classes and also for the interaction between the gases and cylinder walls:

$$\sum_j \left(1-\frac{T_0}{T_j}\right)\dot{Q}_j = \dot{B}_{Q_{spray}} + \left(1-\frac{T_0}{T_{wall}}\right)\dot{Q}_{g,walls}$$

where $\dot{B}_{Q_{spray}} = -\sum_{k=1}^{N_{classes}} N_{droplet,k}\left(1-\frac{T_0}{T_{d,k}}\right)\dot{Q}_{conv,k}$. The exergy terms related to work of expansion/contraction are presented below:

$$-\left(\dot{W} - P_0\frac{\mathrm{d}V}{\mathrm{d}t}\right) = -\left(\dot{W}_{spray} - P_0\sum_{k=1}^{N_{classes}} N_{droplet,k}\left(-\frac{\mathrm{d}V_{d,k}}{\mathrm{d}t}\right)\right) - P\frac{\mathrm{d}V_g}{\mathrm{d}t} + P_0\frac{\mathrm{d}V_g}{\mathrm{d}t}$$

while $\dot{B}_{d,g}$ is the exergy destruction on the control volume. Then, returning to the main equation:

$$\begin{aligned}\frac{\mathrm{d}m_g}{\mathrm{d}t}b_g + m_g\frac{\mathrm{d}b_g}{\mathrm{d}t} - \sum_{k=1}^{N_{classes}} N_{droplet,k}\dot{m}_{d,k}b_{f,evap,k} - \dot{m}_{adm}(\delta_{adm,i}b_{f,adm} - \delta_{adm,o}b_{f,g})\\ - \dot{m}_{exh}(\delta_{exh,i}b_{f,exh} - \delta_{exh,o}b_{f,g}) = \dot{B}_{Q_{spray}} + \left(1-\frac{T_0}{T_{wall}}\right)\dot{Q}_{g,walls}\\ - \left(\dot{W}_{spray} - P_0\sum_{k=1}^{N_{classes}} N_{droplet,k}\left(-\frac{\mathrm{d}V_{d,k}}{\mathrm{d}t}\right)\right) - (P-P_0)\frac{\mathrm{d}V_g}{\mathrm{d}t} - \dot{B}_{d,g}\end{aligned}$$

Opening $\frac{\mathrm{d}m_g}{\mathrm{d}t}$ leads to:

$$\begin{aligned}\left(\sum_{k=1}^{N_{classes}} N_{droplet,k}\dot{m}_{d,k} + (\delta_{adm,i}-\delta_{adm,o})\dot{m}_{adm} + (\delta_{exh,i}-\delta_{exh,o})\dot{m}_{exh}\right)b_g + m_g\frac{\mathrm{d}b_g}{\mathrm{d}t}\\ - \sum_{k=1}^{N_{classes}} N_{droplet,k}\dot{m}_{d,k}b_{f,evap,k} - \dot{m}_{adm}(\delta_{adm,i}b_{f,adm} - \delta_{adm,o}b_{f,g})\\ - \dot{m}_{exh}(\delta_{exh,i}b_{f,exh} - \delta_{exh,o}b_{f,g}) = \dot{B}_{Q_{spray}} + \left(1-\frac{T_0}{T_{wall}}\right)\dot{Q}_{g,walls}\\ - \left(\dot{W}_{spray} - P_0\sum_{k=1}^{N_{classes}} N_{droplet,k}\left(-\frac{\mathrm{d}V_{d,k}}{\mathrm{d}t}\right)\right) - (P-P_0)\frac{\mathrm{d}V_g}{\mathrm{d}t} - \dot{B}_{d,g}\end{aligned}$$

$$\begin{aligned}m_g\frac{\mathrm{d}b_g}{\mathrm{d}t} = \sum_{k=1}^{N_{classes}} N_{droplet,k}\dot{m}_{d,k}(b_{f,evap,k}-b_g) + \delta_{adm,i}\dot{m}_{adm}(b_{f,adm}-b_g) + \delta_{exh,i}\dot{m}_{exh}(b_{f,exh}-b_g)\\ + \delta_{adm,o}\dot{m}_{adm}(b_g - b_{f,g}) + \delta_{exh,o}\dot{m}_{exh}(b_g - b_{f,g}) + \dot{B}_{Q_{spray}} + \left(1-\frac{T_0}{T_{wall}}\right)\dot{Q}_{g,walls}\\ - \left(\dot{W}_{spray} - P_0\sum_{k=1}^{N_{classes}} N_{droplet,k}\left(-\frac{\mathrm{d}V_{d,k}}{\mathrm{d}t}\right)\right) - (P-P_0)\frac{\mathrm{d}V_g}{\mathrm{d}t} - \dot{B}_{d,g}\end{aligned}$$

The final expression for the exergy destruction on the unburned zone is:

$$\dot{B}_{d,g} = \sum_{k=1}^{N_{classes}} N_{droplet,k}\dot{m}_{d,k}(b_{f,evap,k} - b_g) + \delta_{adm,i}\dot{m}_{adm}(b_{f,adm} - b_g) + \delta_{exh,i}\dot{m}_{exh}(b_{f,exh} - b_g)$$

$$+ \delta_{adm,o}\dot{m}_{adm}(b_g - b_{f,g}) + \delta_{exh,o}\dot{m}_{exh}(b_g - b_{f,g}) - m_g\frac{\mathrm{d}b_g}{\mathrm{d}t} + \dot{B}_{Q_{spray}} + \left(1 - \frac{T_0}{T_{wall}}\right)\dot{Q}_{g,walls}$$

$$- \left(\dot{W}_{spray} - P_0\sum_{k=1}^{N_{classes}} N_{droplet,k}\left(-\frac{\mathrm{d}V_{d,k}}{\mathrm{d}t}\right)\right) - (P - P_0)\frac{\mathrm{d}V_g}{\mathrm{d}t} \tag{B.22}$$

B.2.6 Volume balance and pressure rate

The total cylinder volume available in terms of crank angle is:

$$V(\theta) = V_g + V_{spray}$$

The spray volume is usually much less than the gases volumes ($V_{spray} \ll V_g$), still it is taken into account in this model development in order to evaluate its influence and therefore corroborate the aforementioned hypothesis. Getting the time derivative of the previous equation in time yields:

$$\frac{\mathrm{d}V}{\mathrm{d}t} = \frac{\mathrm{d}V_g}{\mathrm{d}t} + \frac{\mathrm{d}V_{spray}}{\mathrm{d}t}$$

Applying the ideal gas derivative for the gas-phase produces:

$$\frac{\mathrm{d}V}{\mathrm{d}t} = V_g\left[\frac{1}{m_g}\frac{\mathrm{d}m_g}{\mathrm{d}t} + \frac{1}{T_g}\frac{\mathrm{d}T_g}{\mathrm{d}t} - \frac{1}{P}\frac{\mathrm{d}P}{\mathrm{d}t}\right] + \frac{\mathrm{d}V_{spray}}{\mathrm{d}t}$$

Grouping similar terms provides the following equation:

$$\frac{\mathrm{d}V}{\mathrm{d}t} = \frac{V_g}{m_g}\frac{\mathrm{d}m_g}{\mathrm{d}t} - \frac{V_g}{P}\frac{\mathrm{d}P}{\mathrm{d}t} + \frac{V_g}{T_g}\frac{\mathrm{d}T_g}{\mathrm{d}t} + \frac{\mathrm{d}V_{spray}}{\mathrm{d}t}$$

Isolating the pressure derivative yields:

$$\frac{\mathrm{d}P}{\mathrm{d}t} = \frac{P}{V_g}\left[\frac{V_g}{m_g}\frac{\mathrm{d}m_g}{\mathrm{d}t} + \frac{V_g}{T_g}\frac{\mathrm{d}T_g}{\mathrm{d}t} - \frac{\mathrm{d}V}{\mathrm{d}t} + \frac{\mathrm{d}V_{spray}}{\mathrm{d}t}\right]$$

Imposing the ideal gas equation produces:

$$\frac{\mathrm{d}P}{\mathrm{d}t} = \frac{P}{V - V_{spray}}\left[\frac{R_gT_g}{P}\frac{\mathrm{d}m_g}{\mathrm{d}t} + \frac{m_gR_g}{P}\frac{\mathrm{d}T_g}{\mathrm{d}t} - \frac{\mathrm{d}V}{\mathrm{d}t} + \frac{\mathrm{d}V_{spray}}{\mathrm{d}t}\right]$$

$$\frac{\mathrm{d}P}{\mathrm{d}t} = \frac{1}{V - V_{spray}} \left[R_g T_g \frac{\mathrm{d}m_g}{\mathrm{d}t} + m_g R_g \frac{\mathrm{d}T_g}{\mathrm{d}t} - P \left(\frac{\mathrm{d}V}{\mathrm{d}t} - \frac{\mathrm{d}V_{spray}}{\mathrm{d}t} \right) \right]$$

Expanding the temperature derivatives generates the following equation:

$$\begin{aligned}\frac{\mathrm{d}P}{\mathrm{d}t} = \frac{1}{V - V_{spray}} \Bigg[& R_g T_g \frac{\mathrm{d}m_g}{\mathrm{d}t} \\ & + m_g R_g \Bigg\{ \frac{\sum_{k=1}^{N_{classes}} N_{droplet,k} \dot{m}_{d,k} (h_{evap,k} - h_g) - m_g \sum_{j=1}^{N_{species}} \left(h_{j,g} \frac{\mathrm{d}y_{j,g}}{\mathrm{d}t} \right)}{m_g c_{p,g}} \\ & \quad + \delta_{adm,i} \dot{m}_{adm} (h_{adm} - h_g) + \delta_{exh,i} \dot{m}_{exh} (h_{exh} - h_g) \\ & + \frac{P \sum_{k=1}^{N_{classes}} N_{droplet,k} \frac{\mathrm{d}V_{d,k}}{\mathrm{d}t} + V_g \frac{\mathrm{d}P}{\mathrm{d}t} - \sum_{k=1}^{N_{classes}} N_{droplet,k} \dot{Q}_{conv,k} + \dot{Q}_{g,walls}}{m_g c_{p,g}} \Bigg\} \\ & - P \left(\frac{\mathrm{d}V}{\mathrm{d}t} - \frac{\mathrm{d}V_{spray}}{\mathrm{d}t} \right) \Bigg]\end{aligned}$$

Grouping similar terms and isolating the pressure derivative yields the final equation:

$$\begin{aligned}\frac{\mathrm{d}P}{\mathrm{d}t} = \frac{1}{V - \frac{R_g V_g}{c_{p,g}} - V_{spray}} \Bigg\{ & R_g T_g \frac{\mathrm{d}m_g}{\mathrm{d}t} \\ & + \frac{R_g}{c_{p,g}} \Bigg[\sum_{k=1}^{N_{classes}} N_{droplet,k} \dot{m}_{d,k} (h_{evap,k} - h_g) - m_g \sum_{j=1}^{N_{species}} \left(h_{j,g} \frac{\mathrm{d}y_{j,g}}{\mathrm{d}t} \right) \\ & \quad + \delta_{adm,i} \dot{m}_{adm} (h_{adm} - h_g) + \delta_{exh,i} \dot{m}_{exh} (h_{exh} - h_g) \\ & \quad + P \sum_{k=1}^{N_{classes}} N_{droplet,k} \frac{\mathrm{d}V_{d,k}}{\mathrm{d}t} - \sum_{k=1}^{N_{classes}} N_{droplet,k} \dot{Q}_{conv,k} + \dot{Q}_{g,walls} \Bigg] \\ & - P \left(\frac{\mathrm{d}V}{\mathrm{d}t} - \frac{\mathrm{d}V_{spray}}{\mathrm{d}t} \right) \Bigg\} \end{aligned} \tag{B.23}$$

APPENDIX C – ENERGETIC INTERNAL COMBUSTION ENGINE EFFICIENCIES

C.1 Efficiencies definition

- $\eta_{comb} = \frac{\dot{Q}_{combustion}}{\dot{Q}_{fuel}}$ (Combustion efficiency - How much energy is converted from the fuel combustion into ideal combustion products (e.g., CO_2, H_2O, etc.);
- $\eta_{thermodynamic} = \frac{\dot{W}_{Gross,Indicated}}{\dot{Q}_{combustion}}$ (Thermodynamic efficiency - How much energy is converted from combustion in real situations (i.e., from $\dot{Q}_{combustion}$) into mechanical power from the engine cycle (open and closed-phases);
- $\eta_{closed-phase} = \frac{\dot{W}_{Gross,Indicated}}{\dot{Q}_{fuel}} = \eta_{comb}\eta_{thermodynamic}$ (Closed-phase (gross) efficiency - How much energy is converted into work from the total fuel combustion energy (only compression and expansion phases);
- $\eta_{Gross,thermal} = \frac{\dot{W}_{Gross,Indicated}}{\dot{Q}_{fuel}}$ (Gross thermal/indicated efficiency - How much energy is converted into work from combustion in real situations (i.e., from $\dot{Q}_{combustion}$) into mechanical power from the engine cycle (closed-phase);
- $\eta_{Net,thermal} = \frac{\dot{W}_{Net,Indicated}}{\dot{Q}_{fuel}}$ (Net thermal/indicated efficiency - How much energy is converted from combustion in real situations (i.e., from $\dot{Q}_{combustion}$) into mechanical power from the engine cycle (open and closed-phases);
- $\eta_{Gas,exchange} = \frac{\dot{W}_{Net,Indicated}}{\dot{W}_{Gross,Indicated}}$ (Gas exchange efficiency - How much energy is converted into net indicated work from gross indicated work;
- $\eta_{open-phase} = \eta_{Gas,exchange}$ (Open-phase efficiency - How much energy is required to re-initiate the engine cycle (exhaust and admission processes);

Similarities:

$\eta_{thermal,conversion} \equiv \eta_{closed-phase} = \eta_{Gross,thermal}.$

APPENDIX D – REMAINING RESULTS FROM THE VALIDATION OF THE ADOPTED DISI ENGINE SIMULATOR

This appendix has the objective of presenting the remaining results related to the validation of the adopted DISI engine simulator of this thesis. All available results are related to the comparison with (Lanzanova *et al.*, 2016).

D.1 Engine outputs comparison

D.1.1 Case 3

Table D.1 – Engine simulation outputs for case 3 *versus* (Lanzanova *et al.*, 2016)

Parameter	Simulation	Exp.	Rel. Diff.
IMEP (bar)	3.093	3.1	0.21 $\%$
SFC (g_{fuel}/kWh)	438.9	419.2	4.69 $\%$
Thermal efficiency ($\%$)	30.98	31.92	4.84 $\%$
Gas exchange efficiency ($\%$)	79.94	85.25	6.24 $\%$
Max. P (bar)	25.27	21.51	17.48 $\%$
Max. P angle (deg)	372.6	375	0.65 $\%$
Max. T (K)	1706	1522	12.07 $\%$

D.1.2 Case 4

Table D.2 – Engine simulation outputs for case 4 *versus* (Lanzanova *et al.*, 2016)

Parameter	Simulation	Exp.	Rel. Diff.
IMEP (bar)	3.28	3.1	5.81 $\%$
SFC (g_{fuel}/kWh)	485.6	501.7	3.19 $\%$
Thermal efficiency ($\%$)	29.24	28.45	2.80 $\%$
Gas exchange efficiency ($\%$)	79.68	83.8	4.92 $\%$
Max. P (bar)	20.48	19.35	5.84 $\%$
Max. P angle (deg)	377.7	377.2	0.1427 $\%$
Max. T (K)	1821	1702	6.96 $\%$

D.1.3 Case 5

Table D.3 – Engine simulation outputs for case 5 *versus* (Lanzanova *et al.*, 2016)

Parameter	Simulation	Exp.	Rel. Diff.
IMEP (bar)	3.32	3.1	7.21 %
SFC (g_{fuel}/kWh)	517.1	553.4	6.57 %
Thermal efficiency (%)	29.42	27.57	6.71 %
Gas exchange efficiency (%)	79.95	82.69	3.31 %
Max. P (bar)	21.70	20.79	4.39 %
Max. P angle (deg)	376.3	375.5	0.21 %
Max. T (K)	1809	1681	7.65 %

APPENDIX E – DISI ENGINE OPTIMIZED IDENTIFICATION AND REMAINING RESULTS

This appendix has the objective of identifying the conditions of operation for each studied case of Chapter 7 as well as to present the remaining results that do not fit into the main text.

E.1 Table of cases

Tables E.1-E.5 describe the cases for each studied engine speed, as described in the main text.

Table E.1 – Optimized cases for 1000 RPM

Case no.	Engine load ($\%P_{atm}$)	Comp. ratio	v_{H_2O}	λ	$V_{cyl}(cm^3)$
1	0.769	12	0.00	1.0	300
2	0.785	12	0.00	1.0	400
3	0.713	12	0.00	1.3	300
4	0.725	12	0.00	1.3	400
5	0.889	12	0.05	1.0	300
6	0.919	12	0.05	1.0	400
7	0.821	12	0.05	1.3	300
8	0.836	12	0.05	1.3	400
9	0.910	12	0.10	1.0	300
10	0.930	12	0.10	1.0	400
11	0.823	12	0.10	1.3	300
12	0.837	12	0.10	1.3	400
13	1.179	12	0.20	1.0	300
14	1.204	12	0.20	1.0	400
15	1.064	12	0.20	1.3	300
16	1.085	12	0.20	1.3	400
17	0.597	15	0.00	1.0	300
18	0.610	15	0.00	1.0	400
19	0.543	15	0.00	1.3	300
20	0.550	15	0.00	1.3	400
21	0.695	15	0.05	1.0	300
22	0.710	15	0.05	1.0	400
23	0.620	15	0.05	1.3	300
24	0.631	15	0.05	1.3	400
25	0.690	15	0.10	1.0	300
26	0.704	15	0.10	1.0	400
27	0.614	15	0.10	1.3	300
28	0.625	15	0.10	1.3	400
29	0.883	15	0.20	1.0	300
30	0.899	15	0.20	1.0	400
31	0.784	15	0.20	1.3	300
32	0.797	15	0.20	1.3	400
33	0.489	18	0.00	1.0	300
34	0.498	18	0.00	1.0	400
35	0.436	18	0.00	1.3	300
36	0.441	18	0.00	1.3	400
37	0.565	18	0.05	1.0	300
38	0.577	18	0.05	1.0	400
39	0.494	18	0.05	1.3	300
40	0.502	18	0.05	1.3	400
41	0.554	18	0.10	1.0	300
42	0.565	18	0.10	1.0	400
43	0.486	18	0.10	1.3	300
44	0.493	18	0.10	1.3	400
45	0.696	18	0.20	1.0	300
46	0.711	18	0.20	1.0	400
47	0.613	18	0.20	1.3	300
48	0.622	18	0.20	1.3	400

Table E.2 – Optimized cases for 1250 RPM

Case no.	Engine load ($\%P_{atm}$)	Comp. ratio	v_{H_2O}	λ	$V_{cyl}(cm^3)$
1	0.896	12	0.00	1.0	300
2	0.916	12	0.00	1.0	400
3	0.846	12	0.00	1.3	300
4	0.863	12	0.00	1.3	400
5	1.049	12	0.05	1.0	300
6	1.073	12	0.05	1.0	400
7	0.957	12	0.05	1.3	300
8	0.974	12	0.05	1.3	400
9	1.074	12	0.10	1.0	300
10	1.101	12	0.10	1.0	400
11	0.964	12	0.10	1.3	300
12	0.964	12	0.10	1.3	400
13	1.380	12	0.20	1.0	300
14	1.389	12	0.20	1.0	400
15	1.234	12	0.20	1.3	300
16	1.256	12	0.20	1.3	400
17	0.695	15	0.00	1.0	300
18	0.710	15	0.00	1.0	400
19	0.629	15	0.00	1.3	300
20	0.649	15	0.00	1.3	400
21	0.810	15	0.05	1.0	300
22	0.827	15	0.05	1.0	400
23	0.721	15	0.05	1.3	300
24	0.734	15	0.05	1.3	400
25	0.809	15	0.10	1.0	300
26	0.829	15	0.10	1.0	400
27	0.717	15	0.10	1.3	300
28	0.730	15	0.10	1.3	400
29	1.017	15	0.20	1.0	300
30	1.033	15	0.20	1.0	400
31	0.903	15	0.20	1.3	300
32	0.916	15	0.20	1.3	400
33	0.568	18	0.00	1.0	300
34	0.579	18	0.00	1.0	400
35	0.504	18	0.00	1.3	300
36	0.516	18	0.00	1.3	400
37	0.657	18	0.05	1.0	300
38	0.671	18	0.05	1.0	400
39	0.574	18	0.05	1.3	300
40	0.583	18	0.05	1.3	400
41	0.645	18	0.10	1.0	300
42	0.662	18	0.10	1.0	400
43	0.564	18	0.10	1.3	300
44	0.572	18	0.10	1.3	400
45	0.800	18	0.20	1.0	300
46	0.818	18	0.20	1.0	400
47	0.704	18	0.20	1.3	300
48	0.715	18	0.20	1.3	400

Table E.3 – Optimized cases for 1500 RPM

Case no.	Engine load ($\%P_{atm}$)	Comp. ratio	v_{H_2O}	λ	$V_{cyl}(cm^3)$
1	1.015	12	0.00	1.0	300
2	1.038	12	0.00	1.0	400
3	0.960	12	0.00	1.3	300
4	0.975	12	0.00	1.3	400
5	1.192	12	0.05	1.0	300
6	1.221	12	0.05	1.0	400
7	1.083	12	0.05	1.3	300
8	1.116	12	0.05	1.3	400
9	1.193	12	0.10	1.0	300
10	1.219	12	0.10	1.0	400
11	1.107	12	0.10	1.3	300
12	1.116	12	0.10	1.3	400
13	1.508	12	0.20	1.0	300
14	1.549	12	0.20	1.0	400
15	1.378	12	0.20	1.3	300
16	1.388	12	0.20	1.3	400
17	0.786	15	0.00	1.0	300
18	0.804	15	0.00	1.0	400
19	0.722	15	0.00	1.3	300
20	0.733	15	0.00	1.3	400
21	0.916	15	0.05	1.0	300
22	0.938	15	0.05	1.0	400
23	0.815	15	0.05	1.3	300
24	0.830	15	0.05	1.3	400
25	0.928	15	0.10	1.0	300
26	0.951	15	0.10	1.0	400
27	0.818	15	0.10	1.3	300
28	0.834	15	0.10	1.3	400
29	1.116	15	0.20	1.0	300
30	1.150	15	0.20	1.0	400
31	1.011	15	0.20	1.3	300
32	1.031	15	0.20	1.3	400
33	0.641	18	0.00	1.0	300
34	0.655	18	0.00	1.0	400
35	0.573	18	0.00	1.3	300
36	0.582	18	0.00	1.3	400
37	0.743	18	0.05	1.0	300
38	0.760	18	0.05	1.0	400
39	0.647	18	0.05	1.3	300
40	0.658	18	0.05	1.3	400
41	0.735	18	0.10	1.0	300
42	0.753	18	0.10	1.0	400
43	0.640	18	0.10	1.3	300
44	0.652	18	0.10	1.3	400
45	0.896	18	0.20	1.0	300
46	0.912	18	0.20	1.0	400
47	0.788	18	0.20	1.3	300
48	0.799	18	0.20	1.3	400

Table E.4 – Optimized cases for 1750 RPM

Case no.	Engine load ($\%P_{atm}$)	Comp. ratio	v_{H_2O}	λ	$V_{cyl}(cm^3)$
1	1.130	12	0.00	1.0	300
2	1.163	12	0.00	1.0	400
3	1.063	12	0.00	1.3	300
4	1.061	12	0.00	1.3	400
5	1.329	12	0.05	1.0	300
6	1.362	12	0.05	1.0	400
7	1.216	12	0.05	1.3	300
8	1.239	12	0.05	1.3	400
9	1.319	12	0.10	1.0	300
10	1.346	12	0.10	1.0	400
11	1.249	12	0.10	1.3	300
12	1.252	12	0.10	1.3	400
13	1.633	12	0.20	1.0	300
14	1.665	12	0.20	1.0	400
15	1.491	12	0.20	1.3	300
16	1.518	12	0.20	1.3	400
17	0.872	15	0.00	1.0	300
18	0.893	15	0.00	1.0	400
19	0.799	15	0.00	1.3	300
20	0.802	15	0.00	1.3	400
21	1.019	15	0.05	1.0	300
22	1.044	15	0.05	1.0	400
23	0.905	15	0.05	1.3	300
24	0.923	15	0.05	1.3	400
25	1.000	15	0.10	1.0	300
26	1.021	15	0.10	1.0	400
27	0.918	15	0.10	1.3	300
28	0.915	15	0.10	1.3	400
29	1.213	15	0.20	1.0	300
30	1.236	15	0.20	1.0	400
31	1.098	15	0.20	1.3	300
32	1.117	15	0.20	1.3	400
33	0.710	18	0.00	1.0	300
34	0.727	18	0.00	1.0	400
35	0.634	18	0.00	1.3	300
36	0.639	18	0.00	1.3	400
37	0.824	18	0.05	1.0	300
38	0.844	18	0.05	1.0	400
39	0.717	18	0.05	1.3	300
40	0.727	18	0.05	1.3	400
41	0.829	18	0.10	1.0	300
42	0.849	18	0.10	1.0	400
43	0.719	18	0.10	1.3	300
44	0.716	18	0.10	1.3	400
45	0.976	18	0.20	1.0	300
46	1.005	18	0.20	1.0	400
47	0.863	18	0.20	1.3	300
48	0.880	18	0.20	1.3	400

Table E.5 – Optimized cases for 2000 RPM

Case no.	Engine load ($\%P_{atm}$)	Comp. ratio	v_{H_2O}	λ	$V_{cyl}(cm^3)$
1	1.227	12	0.00	1.0	300
2	1.289	12	0.00	1.0	400
3	1.150	12	0.00	1.3	300
4	1.176	12	0.00	1.3	400
5	1.444	12	0.05	1.0	300
6	1.491	12	0.05	1.0	400
7	1.355	12	0.05	1.3	300
8	1.357	12	0.05	1.3	400
9	1.433	12	0.10	1.0	300
10	1.462	12	0.10	1.0	400
11	1.333	12	0.10	1.3	300
12	1.342	12	0.10	1.3	400
13	1.741	12	0.20	1.0	300
14	1.775	12	0.20	1.0	400
15	1.604	12	0.20	1.3	300
16	1.640	12	0.20	1.3	400
17	0.948	15	0.00	1.0	300
18	0.988	15	0.00	1.0	400
19	0.885	15	0.00	1.3	300
20	0.887	15	0.00	1.3	400
21	1.111	15	0.05	1.0	300
22	1.139	15	0.05	1.0	400
23	1.008	15	0.05	1.3	300
24	1.027	15	0.05	1.3	400
25	1.089	15	0.10	1.0	300
26	1.112	15	0.10	1.0	400
27	0.984	15	0.10	1.3	300
28	1.001	15	0.10	1.3	400
29	1.300	15	0.20	1.0	300
30	1.328	15	0.20	1.0	400
31	1.216	15	0.20	1.3	300
32	1.210	15	0.20	1.3	400
33	0.772	18	0.00	1.0	300
34	0.798	18	0.00	1.0	400
35	0.701	18	0.00	1.3	300
36	0.706	18	0.00	1.3	400
37	0.904	18	0.05	1.0	300
38	0.927	18	0.05	1.0	400
39	0.793	18	0.05	1.3	300
40	0.808	18	0.05	1.3	400
41	0.871	18	0.10	1.0	300
42	0.891	18	0.10	1.0	400
43	0.769	18	0.10	1.3	300
44	0.784	18	0.10	1.3	400
45	1.070	18	0.20	1.0	300
46	1.056	18	0.20	1.0	400
47	0.927	18	0.20	1.3	300
48	0.931	18	0.20	1.3	400

E.2 Remaining results

E.2.1 Optimal mean effective pressure

This section presents the results for the optimal MEPs at 1250, 1500, 1750, and 2000 RPM. Figures E.2-E.5 present these results for all studied engine speeds.

To complement the previously described figure, an alternative way to analyze the engine behavior for all optimized cases is to adopt bar graphs to represent the mean effective pressures (MEP) associated with the fuel, closed-phase (compression, combustion and expansion), total engine cycle (closed-phase + exhaust and admission), and pumping (exhaust and admission) energies involved in the engine cycle (FuelIMEP, GIMEP, NIMEP, and PMEP, respectively). For example, Fig. E.1 represents the results for 1000 RPM adopted in the optimization. It is worth remembering that the trapped in-cylinder mass in indirectly taken into consideration in these results, as it seems clear by the different sizes of FuelIMEP bars on all cases. The total MEP for cases 13 and 14 (i.e., $\upsilon_{H_2O} = 0.2$) overcomes the others for $r = 12$. Another highlighted point is the reduction on IMEP on $\lambda = 1.3$ when compared to stoichiometric conditions (e.g., cases 1 and 2 *versus* 3 and 4) on all cases.

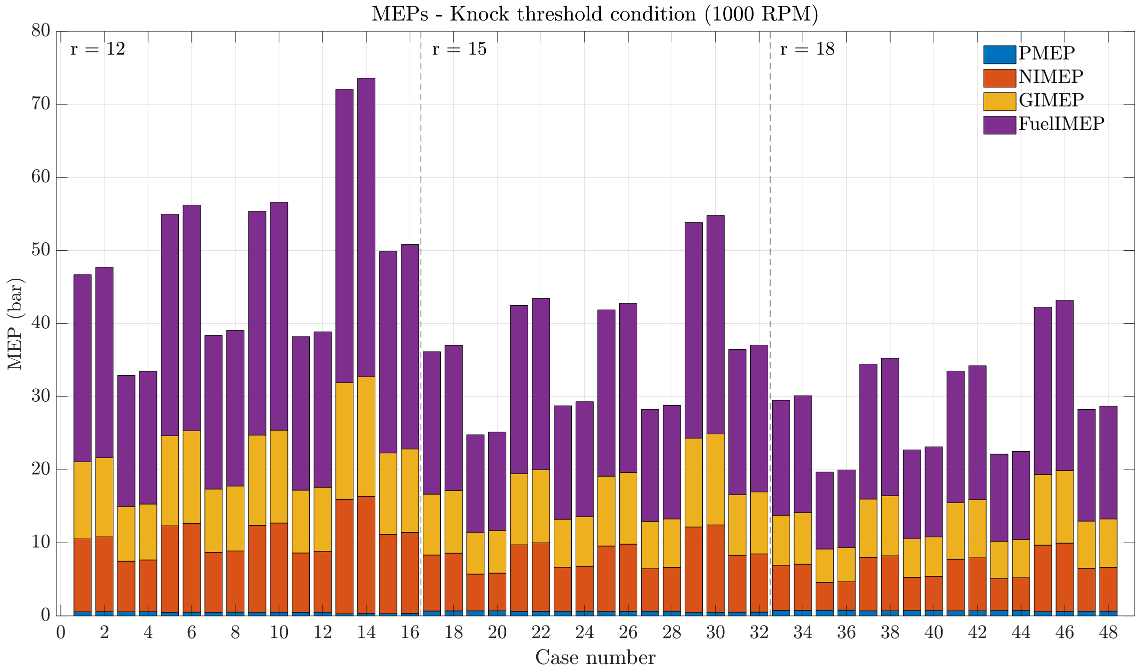

Figure E.1 – Optimal engine mean effective pressures at 1000 RPM at knock threshold conditions.

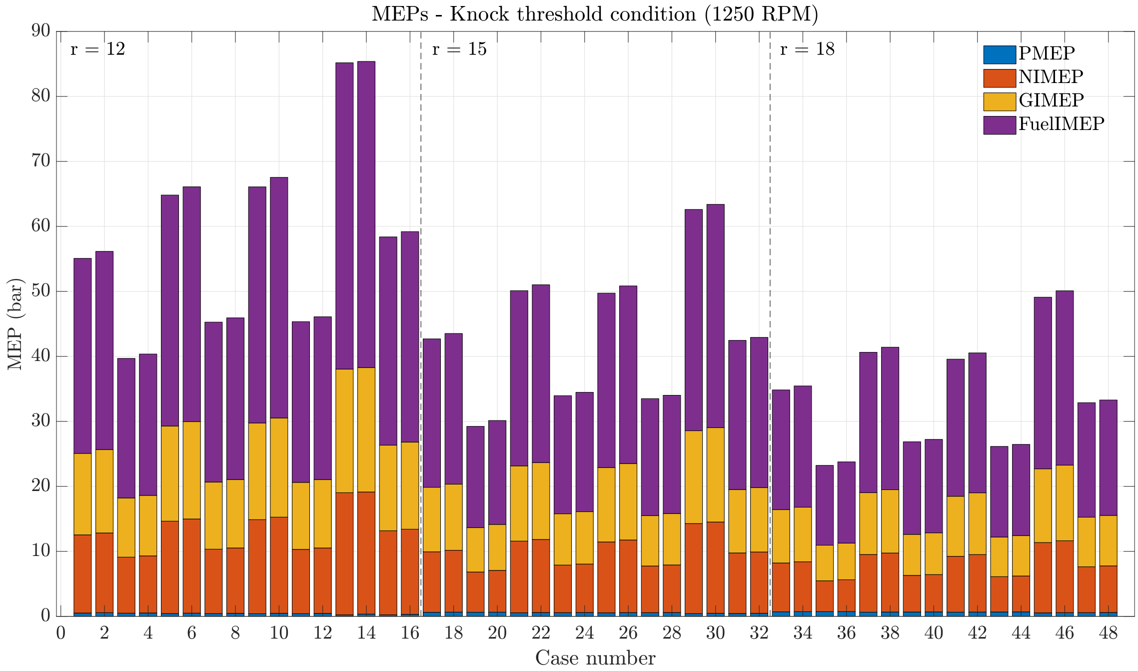

Figure E.2 – Optimal engine mean effective pressures at 1250 RPM at knock threshold conditions.

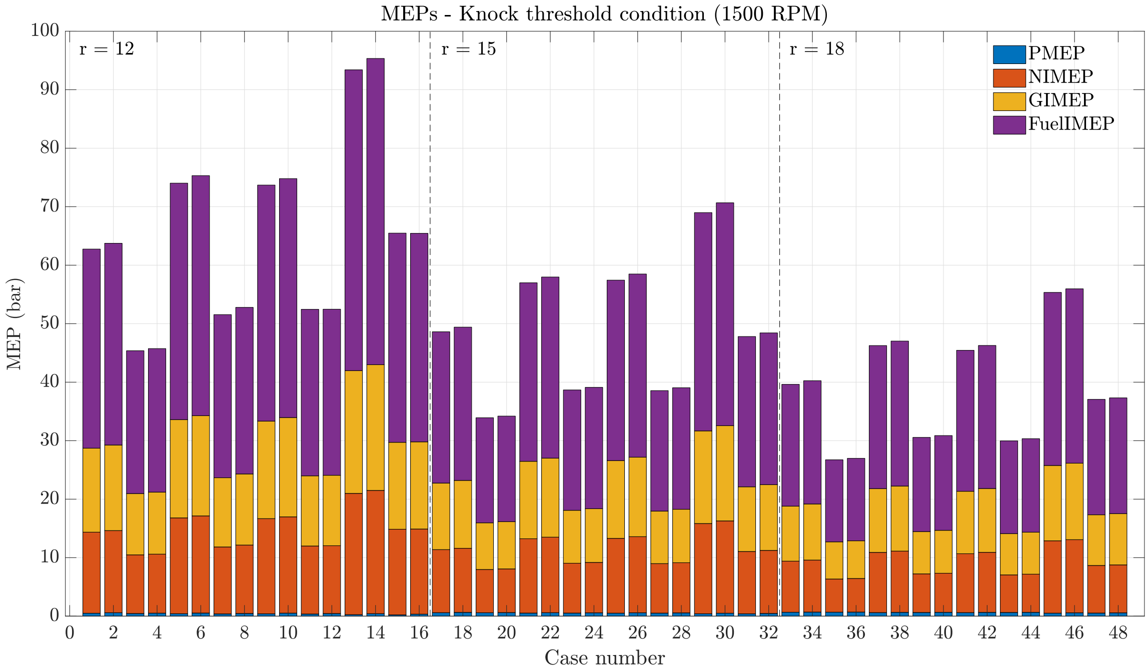

Figure E.3 – Optimal engine mean effective pressures at 1500 RPM at knock threshold conditions.

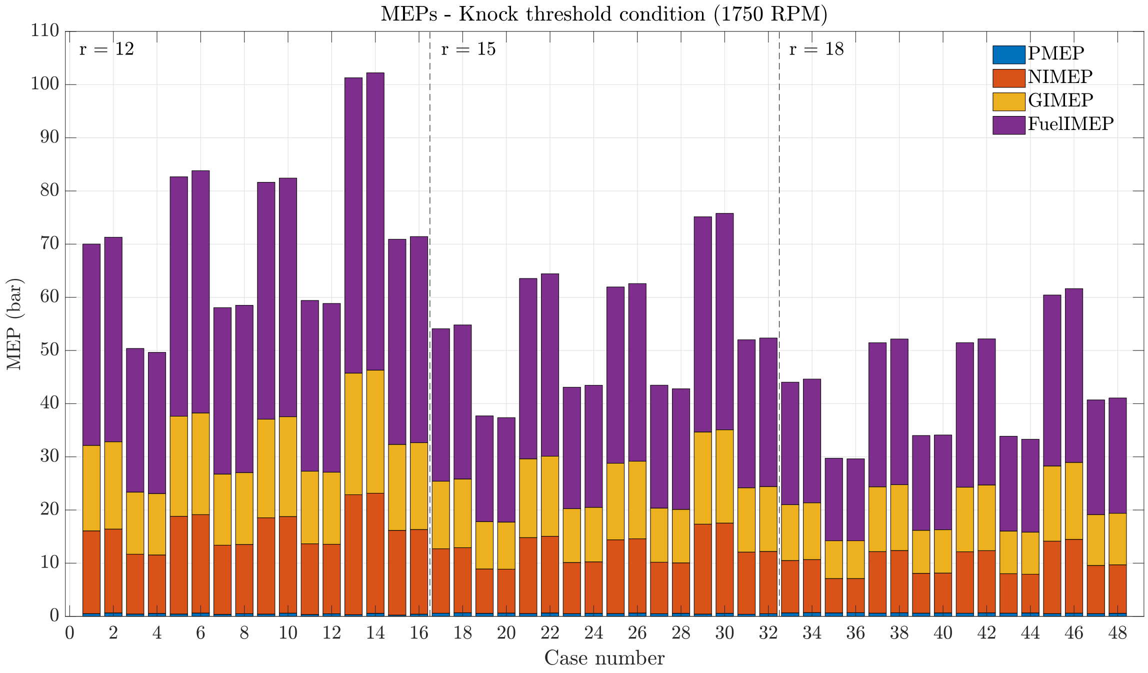

Figure E.4 – Optimal engine mean effective pressures at 1750 RPM at knock threshold conditions.

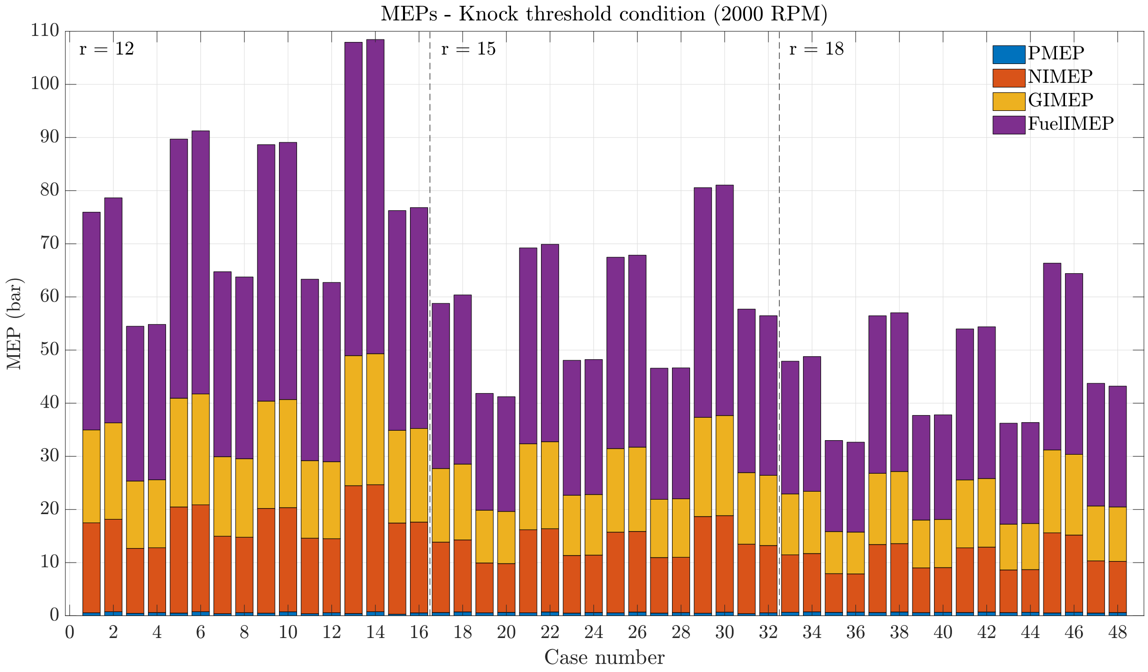

Figure E.5 – Optimal engine mean effective pressures at 2000 RPM at knock threshold conditions.

E.2.2 Optimal engine work

This section presents the results for the optimal engine work values at 1000, 1250, 1500, 1750, and 2000 RPM. Figures E.6-E.10 present these results for all studied engine speeds.

These figures indicate how much work was developed by the complete DISI engine system under the influence of the compressor and/or turbine. It is noticed that all cases at $r = 12$ operate under supercharging/turbocharging conditions. In addition, the compressor in these cases required a higher amount of energy than the turbine can offer. The limiting condition for the turbocharging operation is the low exhaust pressure (P_{exh}) assumed in the simulation process, which constraints the level of expansion on the turbine. Still, the turbine reduces the amount of power required by the compressor to allow the engine to operate on the desired conditions. Another detail worth mentioning is the case 46 (20% water and $r = 18$), which develops an equivalent amount of energy per cycle than case 2 (anhydrous ethanol and $r = 12$), besides allowing turbocharging operation to get an extra power to the engine system.

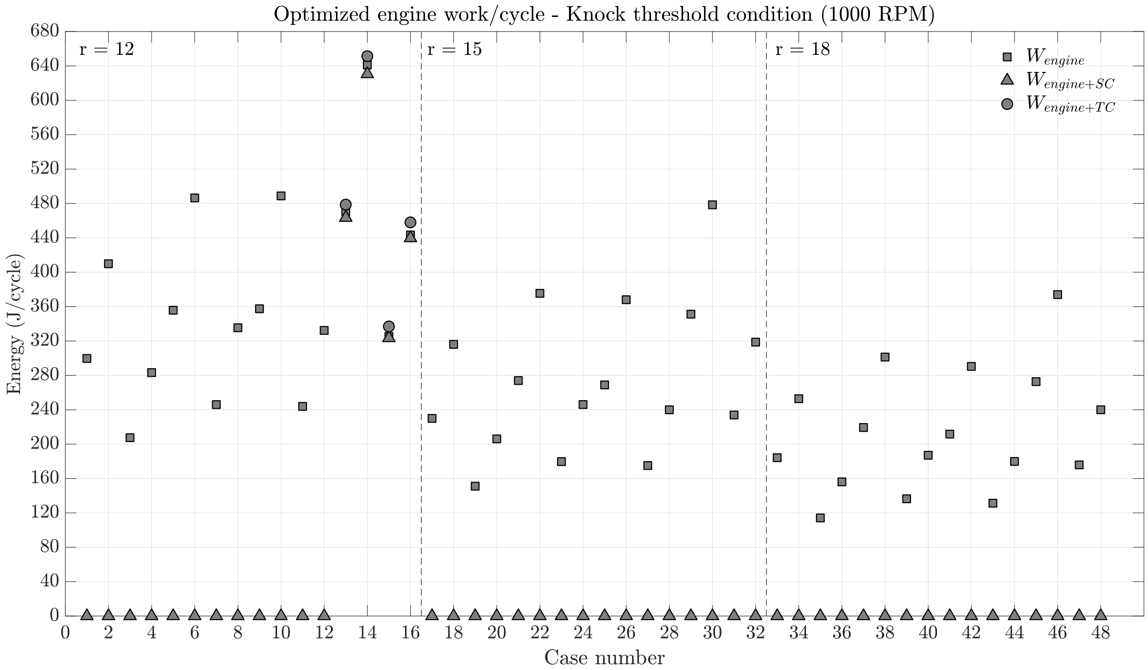

Figure E.6 – Optimal engine work with supercharging/turbocharging at 1000 RPM at knock threshold conditions.

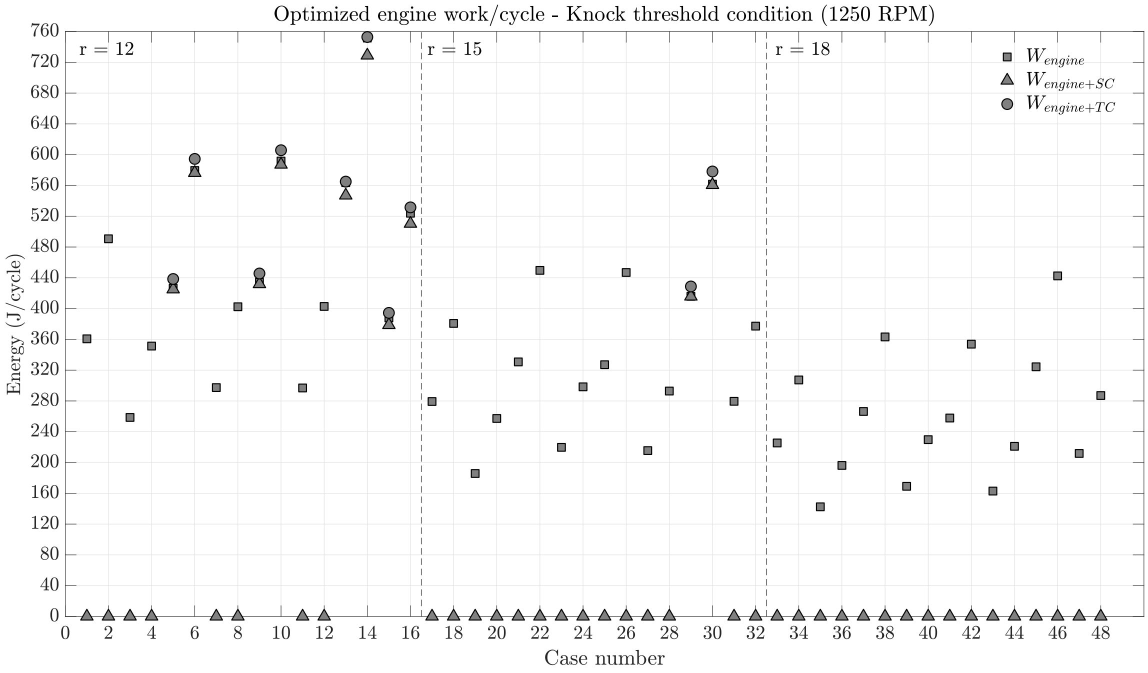

Figure E.7 – Optimal engine work with supercharging/turbocharging at 1250 RPM at knock threshold conditions.

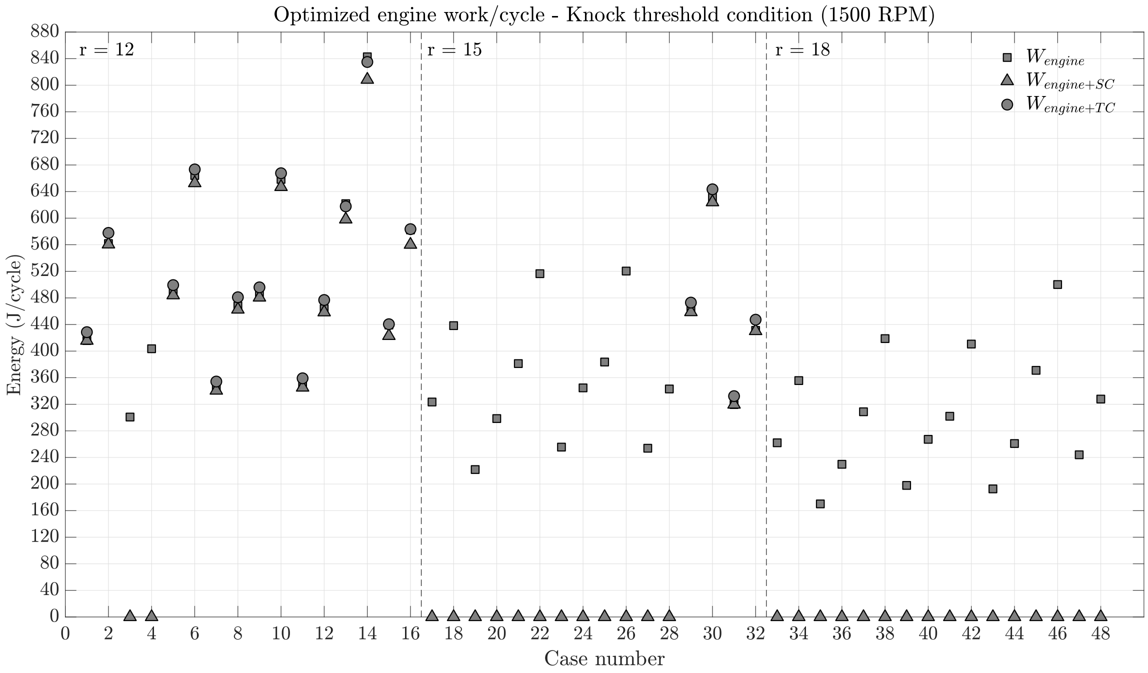

Figure E.8 – Optimal engine work with supercharging/turbocharging at 1500 RPM at knock threshold conditions.

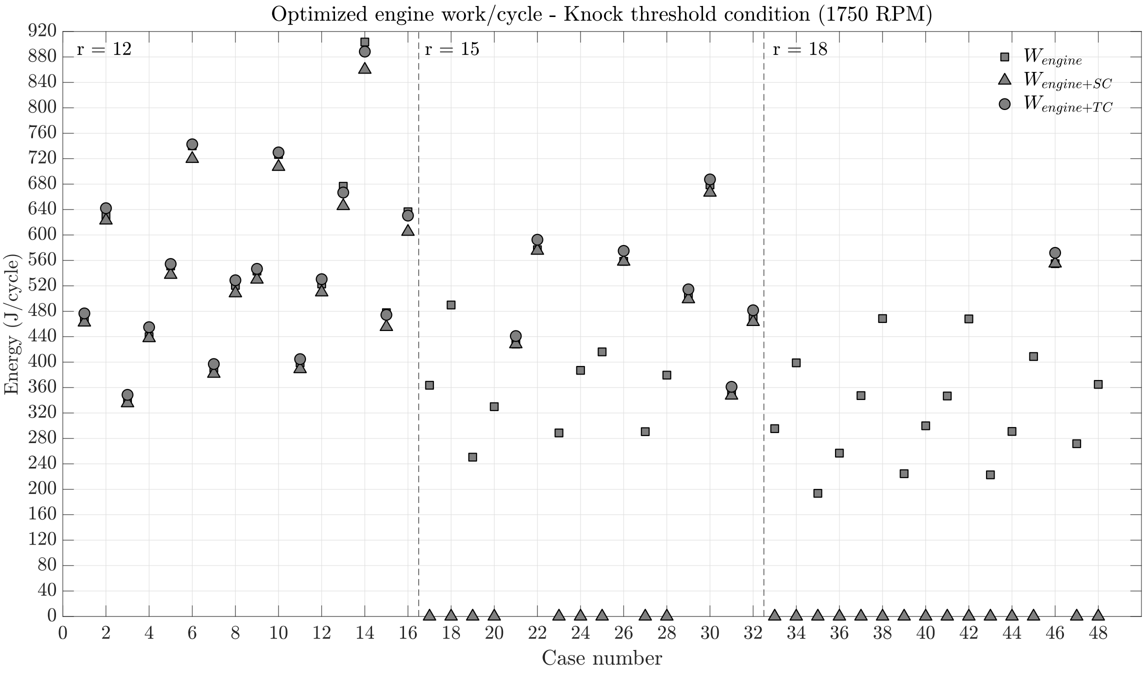

Figure E.9 – Optimal engine work with supercharging/turbocharging at 1750 RPM at knock threshold conditions.

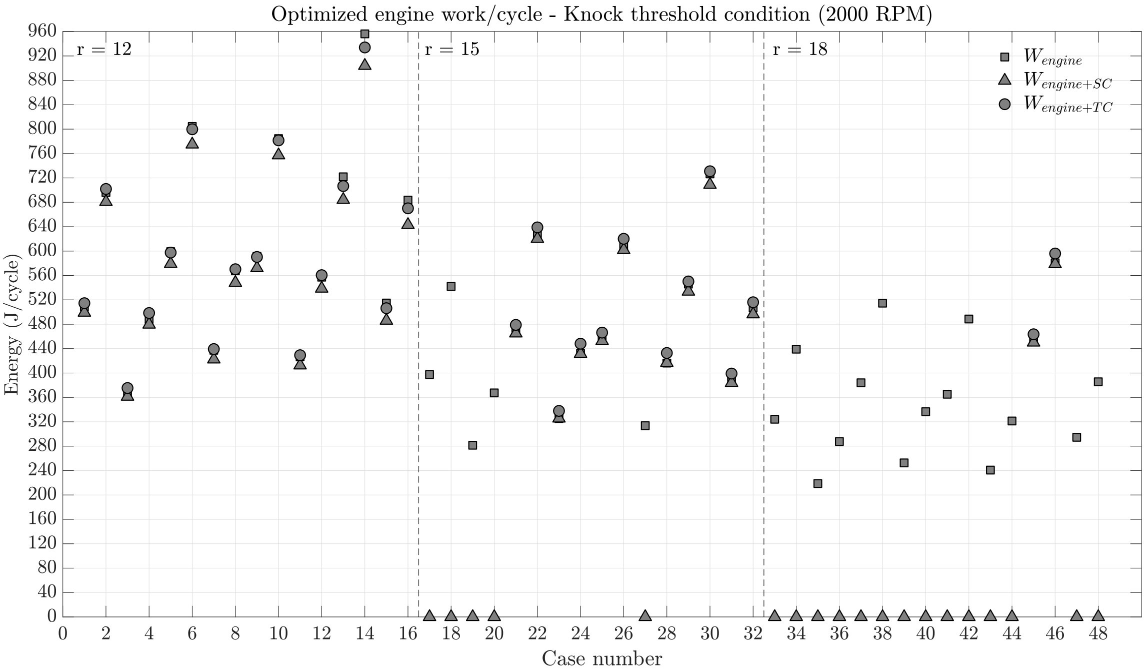

Figure E.10 – Optimal engine work with supercharging/turbocharging at 2000 RPM at knock threshold conditions.